In-situ Surface X-ray Diffraction Studies of Homoepitaxial Growth and Dissolution at Gold Single Crystal Electrodes
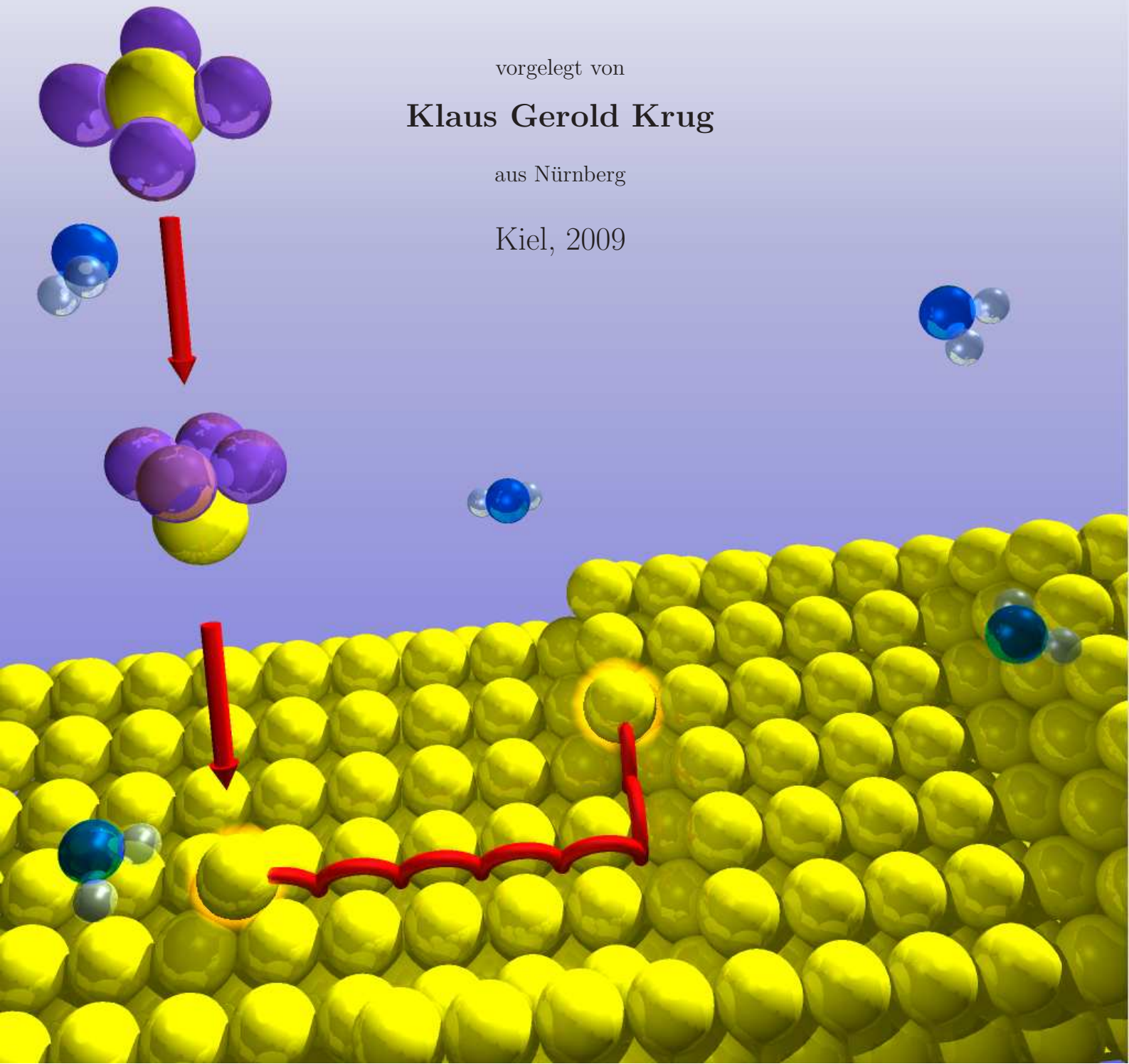
Dissertation

zur Erlangung des Doktorgrades Dr. rer. nat.
der Mathematisch-Naturwissenschaftlichen Fakultät
der Christian-Albrechts-Universität zu Kiel

vorgelegt von

Klaus Gerold Krug

aus Nürnberg

Kiel, 2009

In-situ Surface X-ray Diffraction Studies of Homoepitaxial Growth and Dissolution at Gold Single Crystal Electrodes
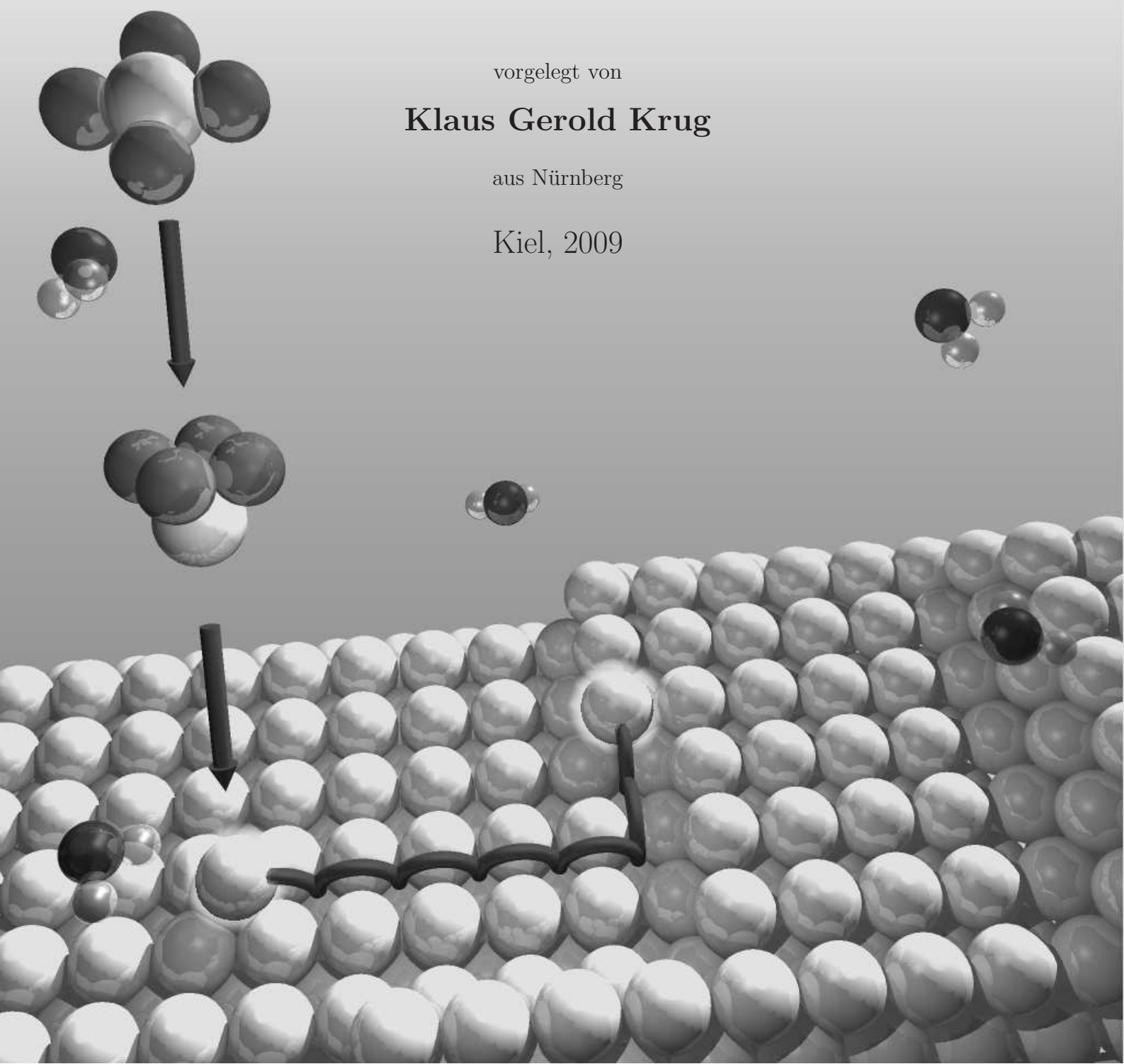
Dissertation

zur Erlangung des Doktorgrades Dr. rer. nat.
der Mathematisch-Naturwissenschaftlichen Fakultät
der Christian-Albrechts-Universität zu Kiel

vorgelegt von

Klaus Gerold Krug

aus Nürnberg

Kiel, 2009

Kurzzusammenfassung

Das homoepitaktische Wachstum und das elektrochemische Auflösen von Goldeinkristallelektroden wurde in chlorhaltigen Elektrolyten in-situ mittels oberflächensensitiver Röntgenbeugung untersucht. Hierzu wurde eine neuartige elektrochemische Röntgentransmissionszelle mit Elektrolytaustauschsystem entwickelt, welche die Aufnahme hochqualitativer elektrochemischer Daten parallel zu einer strukturellen Charakterisierung der elektrochemischen Grenzfläche ermöglicht. Unter Verwendung dieses Aufbaus wurden bislang einzigartige Studien zur Elektrodeposition und zur elektrochemischen Auflösung unter realistischen Reaktionsbedingungen durchgeführt. Dies liefert einen detaillierten Einblick in die komplexen Beziehungen zwischen der Struktur der Fest/Flüssig Grenzfläche, dem Wachstums- bzw. Auflöseverhalten und der resultierenden Oberflächenmorphologie.

Homoepitaktisches Wachstum wurde im diffusionslimitierten Potentialbereich, d.h. bei konstanter Abscheiderate, als Funktion zentraler Abscheideparameter (Elektrodenpotential und Goldkonzentration) untersucht. Ein besonders interessantes Wachstumsverhalten wurde auf Au(100) Elektroden gefunden. Mit abnehmendem Potential wurde ein Übergang von Stufenflusswachstum zu lagenweisem (2D) Wachstum, welches sich in Form von Oszillationen in der Röntgeninstensität äussert, dann zu dreidimensionalem (3D) Wachstum und schließlich zurück zu lagenweisem Wachstum beobachtet. Das wiederkehrende 2D Wachstum im rekonstruierten Potentialbereich demonstriert die wichtige Rolle der Oberflächenstruktur auf das Wachstumsverhalten. Im Gegenzug übt der Wachstumsprozess einen entscheidenden Einfluss auf die rekonstruierte Lage aus. Die 'hex' Lage komprimiert linear und reversibel in Richtung negativerer Potentiale. Während die potentialinduzierte Bildung der Rekonstruktion in goldfreien Elektrolyten auf dem Einbau von Atomen in die existierende unrekonstruierte Lage beruht, vollzieht sich das Wachstum rekonstruierter Lagen in goldhaltigen Elektrolyten durch Anlagerung von Adatomen an Stufenkanten rekonstruierter Inseln und es existiert keine signifikante kinetische Barriere, die einen energetisch günstigeren lateralen Gitterabstand verhindert. Offensichtlich benötigt eine höhere Kompression eine negativere Oberflächenladung. Desweiteren wurde eine schnelle Bildung der rekonstruierten Phase in goldhaltigem Elektrolyt gefunden, die sich deutlich von der sehr langsamen Kinetik dieses Prozesses in Abwesenheit der Goldspezies in der Lösung unterscheidet. Dies weist darauf hin, dass die Barriere für den Einbau von Goldatomen in die Oberfläche klein ist und dass der Oberflächentransport zu unrekonstruierten Bereichen die Kinetik des Phasenübergangs bestimmt. Ähnliche Studien auf Au(111) Elektroden zeigen nur 3D Wachstum oder nicht-ideales 2D Wachstum und lassen auf eine signifikant höhere Energiebarriere an Stufenkanten schließen. Das Wachstumsverhalten auf Goldelektroden in chlorhaltigen Elektrolyten folgt also dem generellen Trend, der auch bei der Molekularstrahlepitaxie unter Ultra-Hochvakuum-Bedingungen beobachtet wurde.

Komplementär zum Wachstum wurde der inverse Prozess der elektrochemischen Auflösung auf Au(111) Elektroden untersucht. Interessanterweise dominiert das lagenweise Auflösen den Potentialbereich der aktiven Auflösung. Dies zeigt, dass Wachstum und Auflösung nicht notwendigerweise symmetrische Prozesse sind. Der 2D Auflöseprozess manifestiert sich in Oszillationen in der Röntgenintensität und im elektrochemischen Strom. Erstmalig wurden Stromoszillationen aufgrund von lagenweisem Auflösen einkristalliner Metallelektroden beobachtet. Die elektrochemischen Daten und die Röntgendaten können erfolgreich mit einem modifizierten Modell beschrieben werden, das ursprünglich für den Fall des homoepitaktischen Wachstums entwickelt wurde.

Abstract

Homoepitaxial growth and electrodissolution of gold single crystal electrodes in chloride-containing solutions have been investigated in-situ by surface sensitive X-ray diffraction. For this a novel electrochemical hanging meniscus X-ray transmission cell with an electrolyte exchange system was developed which allows to obtain high quality electrochemical data in parallel to a structural characterization of the electrochemical interface. Utilizing the new setup, unique real-time studies of electrodeposition and electrodissolution were performed under realistic reaction conditions (unrestricted mass transport). This provided a detailed insight into the complex relationship between the atomic-scale structure of the solid-liquid interface, the growth or dissolution behavior, and the resulting surface morphology.

Operating in the diffusion-limited potential regime, i.e. at constant deposition rate, homoepitaxial growth was studied as a function of central deposition parameters (electrode potential and Au concentration). A particular interesting growth behavior was found on Au(100) electrodes. With decreasing potential transitions from step-flow to layer-by-layer growth, manifested by layering oscillations in the X-ray intensity, then to multilayer growth, and finally back to layer-by-layer growth were observed. The re-entrant layer-by-layer growth in the reconstructed potential regime demonstrates the important role of the solid surface structure on the growth behavior and on the resulting film morphology. In turn the growth process has a pronounced influence on the 'hex' reconstructed surface layer. The 'hex' layer compresses linearly and reversible towards more negative potentials. While the potential-induced formation of reconstruction in Au-free electrolyte requires the incorporation of adatoms into the existing unreconstructed surface layer the growth of reconstructed layers in Au-containing electrolyte proceeds via attachment of adatoms to step edges of reconstructed islands and no significant kinetic barrier exists for attaining the energetically preferred in-plane spacing. A higher compressed phase apparently requires a more negatively charged surface. Furthermore a rapid formation of the reconstruction was found during Au electrodeposition which differs pronouncedly from the very slow kinetics of this process in the absence of Au-species in the solution. This suggests that the barrier for incorporation of the Au atoms into the surface is low and that the Au surface transport to unreconstructed areas governs the phase transition kinetics. In contrast to homoepitaxial growth on Au(100) electrodes similar studies on Au(111) electrodes provided only indications for 3D growth or non-ideal layer-by-layer growth which indicates a significantly larger step edge barrier on the (111) oriented surface. Thus the growth behavior of Au electrodes in chloride containing solution follows the general trends observed in MBE studies under UHV conditions.

Complementary to homoepitaxial growth the inverse process of electrodissolution has been investigated on Au(111) electrodes. Interestingly the 2D dissolution mode dominates the active dissolution regime which demonstrates that electrodeposition and electrodissolution are not necessarily symmetrical processes. The layer-by-layer dissolution process manifests in X-ray intensity oscillations and in oscillations in the electrochemical current. This is the first report of current oscillations due to layer-by-layer dissolution of single crystal, metal electrodes. Electrochemical data and SXS data can be successfully described by a modified model function which was originally derived for the case of homoepitaxial deposition.

Contents

1 Introduction

For more than 200 years electrodeposition is used for electrowinning and electrofining of metals from natural ores, for galvanic replicas and for decorative, protective and functional coatings. In the second half of the last century electrodeposition found its way into the microelectronics industry. Today galvanic deposition is commonly used for the fabrication of interconnections between microchips and other electronics (flip-chip bonding based on gold solder bumps), for interconnects in ultra large scale integrated (ULSI) chips (copper dual-damascene plating), for the manufacture of magnetic recording devices (e.g. read-write heads), for Micro-Electro-Mechanical Systems (MEMS) and for multilayered alloy coatings. Continuously shrinking feature sizes of those devices make high demands on the deposit morphology and therefore a detailed understanding of the growth processes on atomic-scale is required. Compared to other techniques galvanic deposition allows to create nano-scale structures with extreme height-to-width aspect ratios.

Homoepitaxial growth has been studied only sparsely by in-situ structural methods in electrochemical environment, but was investigated in great detail for growth from the gas phase, e.g. molecular beam epitaxy (MBE). For the latter direct studies by diffraction methods [1,2] strongly helped to clarify the basic kinetic mechanisms which determine thin film growth and to establish the experimental basis for kinetic growth theory [3]. According to these experimental and theoretical studies homoepitaxial growth far from equilibrium is governed by the flux of adatoms to the surface, i.e. the deposition rate, and the rates of intra- and inter-layer transport, which under ultrahigh vacuum (UHV) conditions are functions of temperature and surface structure. Depending upon the relative rates of these processes step-flow growth, layer-by-layer growth, or multilayer growth are observed. Specifically, for homoepitaxial growth on reconstructed Au(111) and Au(100) surfaces under UHV conditions layer-by-layer growth and a more disordered surface reconstruction were reported [2,4,5]. In electrochemical environment the surface transport can be controlled by the applied electrode potential while temperature and deposition rate are kept constant.

To clarify the complex interdependence of surface structure and growth behavior atomic-scale structural data has to be obtained in-situ during deposition and under realistic reaction conditions, which often include high current densities and substantial mass transport in the electrolyte. Unfortunately, under these conditions established structure-sensitive methods for the study of electrochemical interfaces are often only of limited use. In scanning probe microscopy, such as scanning tunneling (STM) and atomic force microscopy (AFM), the local deposition rate in the investigated surface area is substantially reduced due to shielding by the scanning tip [6,7]. Realistic observations of the growth kinetics are therefore only possible for extremely slow reaction-controlled deposition processes. Moreover, scanning probe techniques image surface areas of some $1000\,nm^2$ only. Techniques employing synchrotron X-ray radiation, such as in-situ surface X-ray scattering (SXS) [8,9], do not have such inherent limitations. However, nearly all previous SXS investigations of electrochemical systems were performed in a thin-layer geometry where the electrolyte thickness during the X-ray measurements is confined to several microns by a thin plastic window. Due to the restricted mass transport and the high cell resistance in these thin-layer cells the kinetic behavior is

strongly limited and consequently true in-situ investigations of electrochemical growth processes are not possible. For these reasons SXS measurements have been performed almost exclusively at potentials in the double layer regime, where the deposition rates are very low or vanish. To overcome these drawbacks some recent SXS studies have employed a transmission geometry, where the beam traverses through an electrolyte volume of several mm thickness [8, 10–12]. The electrochemical behavior in this geometry is comparable to that of conventional electrochemical cells. In particular the cell employed in the present studies allows the recording of high quality electrochemical data parallel to structural SXS data. A novel electrolyte exchange system has been developed which allows to initiate or to stop the deposition process. Due to the higher X-ray absorption as compared to 'thin-layer' cells, these experiments are preferentially performed at third generation synchrotron sources that offer sufficient X-ray flux at high photon energies (>15 keV).

This thesis focuses on homoepitaxial deposition and electrodissolution on gold single crystal electrodes. The structure of electrochemical interfaces between the low index gold electrode surfaces and chloride containing electrolytes has been investigated by numerous structure-sensitive methods, including STM and SXS. Thus the surface structure, the adsorbate structure and potential-dependent changes are well-known. Based on these comparatively simple model systems the influence of homoepitaxial growth and electrochemical dissolution on the surface morphology has been studied by SXS. Of particular interest is the dependence of the growth and dissolution behavior on system parameters, such as the deposition (dissolution) rate and the electrode potential. On the one hand, the interface structure, which includes the structure of the electrode surface and that of adlayers formed by adsorbed ionic and molecular species (e.g. anions or additives), clearly affects the energy of surface defects, such as adatoms, small adatom clusters, steps, and kinks as well as the activation energies for surface transport and hence has a pronounced influence on the growth process. On the other hand, the surface structure under deposition conditions may differ considerably from that found under otherwise identical conditions in the absence of deposition.

Prior to the discussion of the SXS results the microscopic structure at electrochemical interfaces, the reaction kinetics at the interface and electrodeposition from metal-complex containing solutions will be introduced in chapter 2. The subsequent chapter 3 deals with growth kinetics, in particular with atomic surface processes and the influence of deposition parameters, such as deposition rate and electrode potential, on the growth behavior. Chapter 4 gives a short overview about surface sensitive X-ray scattering. It will be shown which information about the interface structure can be obtained from scattered X-ray intensity. Experimental techniques and preparation methods will be presented in chapter 5. Since most of the experiments have been performed on Au(100) electrodes the surface structure in UHV and in electrochemical environment will be summarized in chapter 6. The main results of the SXS experiments are divided into five parts and will be presented in the chapters 7 to 11.

Homoepitaxial growth on Au(100) electrodes has been investigated in detail. The chapters 7 and 8 address the lateral surface structure of Au(100) electrodes in Au-free and Au-containing electrolyte, respectively. It is well-known that in anion containing solutions the

Au(100) surface reconstructs negative of a critical potential [13]. The unreconstructed (1×1) phase transforms to a closed-packed, quasi-hexagonal structure, generally termed as 'hex' phase. Prior to initiation of homoepitaxial growth the reconstructed surface was characterized in Au-free 0.1 M HCl solution. The discussion in chapter 7 focuses on in-plane lattice spacings, on the orientation of reconstructed domains with respect to the underlying unreconstructed layer and on the domain structure. Furthermore the kinetics of the (1×1) → 'hex' surface phase transition and the potential-dependence of the reconstructed layer will be analyzed. Whenever possible the results are compared with those of previous studies carried out in UHV and in perchloric acid solution. In a similar manner the reconstructed surface layer was characterized in Au-containing electrolyte. Previous studies performed by our group revealed a pronounced influence of homoepitaxial growth on the lateral surface structure of reconstructed Au(111) electrodes, in particular a linear potential-dependent compression towards more negative electrode potentials [12]. The present study shows that homoepitaxial growth also strongly affects the in-plane structure of the 'hex' reconstructed Au(100) surface.

Besides of the in-plane structure the growth along the surface normal was investigated. An analysis of the scattered X-ray intensity at selected positions in reciprocal space allows us to infer the kinetic growth mode. The results of extensive growth mode studies on Au(100) and Au(111) electrodes, which were performed as a function of the electrode potential and Au concentration in the electrolyte, are presented in chapter 9. Furthermore it is shown that the novel experimental setup facilitates deposition experiments up to deposition rates of some monolayers per minute and during constant flow of electrolyte through the electrochemical cell. The study demonstrates that the structure of the surface has an influence on the resulting film morphology. An influence of the reconstructed Au(111) electrode surface on the deposit morphology has been previously reported by our group [14].

Chapter 10 focuses on the influence of homoepitaxial growth on the (1x1)→'hex' phase transition. In particular SXS measurements of the specularly scattered intensity are presented. A detailed analysis of the surface structure in the initial time period after the potential step allows us to determine if the Au(100) surface first reconstructs and then subsequent layers grow in the reconstructed phase or if the substrate remains unreconstructed while new layers directly grow in the reconstructed phase. Furthermore it will be clarified if under growth conditions only the topmost surface layer is reconstructed. The kinetics of the phase transition in Au-containing solution will be compared to the kinetics in Au-free solution.

Besides of electrodeposition the inverse process of electrodissolution has been investigated. Chapter 11 summarizes the results of electrodissolution studies on Au(111) electrodes in chloride containing electrolytes. The present combined SXS and electrochemical study confirms earlier STM results [15–17] and provides more detailed information about the dissolution process due to a much better time resolution and unrestricted mass transport in the electrochemical cell. In contrast to scanning probe techniques the SXS technique allows us to access the dissolution behavior at high anodic overpotentials where the surface dissolves with a rate of several monolayers per minute. For the first time current oscillations are observed in the active dissolution regime of single crystal metal electrodes.

2 Electrochemical Interfaces

2.1 Structure of the Electrochemical Double Layer

Since the discovery of the electrochemical double layer by Helmholtz, a detailed thermodynamic description of the phase boundary between metals and electrolytes has been developed on the basis of several electrochemical techniques. Here measurements of current, voltage and charge played a central role. The results and theories are explained in many books about electrochemistry [18–20] and will be summarized briefly.

2.1.1 The Helmholtz Model

A planar metal electrode be immersed in an aqueous electrolyte solution. The axis along the surface normal shall be denoted by x with $x = 0$ at the phase boundary. Then, following Helmholtz, the interface can be considered as a simple plate capacitor. The ions in front of the electrode form a plane parallel to the electrode surface which is carrying a total charge q_s. This charge is compensated by an equal excess or deficit charge $q_{Me} = -q_s$ of the electrons in the conducting band of the metal electrode. q_{Me} resides in a very thin layer (< 0.5Å) on the metal surface and can therefore be located at $x = 0$. In contrast, the extension of excess charge on the solution side amounts to some Ångstroms. Because the double layer structure will not change in equilibrium it is termed as rigid double layer. Figure 2.1 depicts the microscopic structure at the interface.

The electrode potential Φ determines the charge on the capacitor plates, i.e. the concentration of anions and cations on the surface. This fact has been proven by several ex-situ and in-situ methods [21–24]. Electrodes which have been removed from the electrolyte with intact double layer at different potentials were transferred into ultra high vacuum (UHV) and analyzed by electron spectroscopy to determine the chemical composition. At very negative (positive) potentials only cations (anions) could be observed.

The capacitance C_H of the double layer depends on the distance d between the surface and the ion layer in front of the electrode:

$$C_H = \frac{\epsilon_0 \cdot \epsilon}{d} \tag{2.1}$$

where ϵ_0 and ϵ denote the dielectric constants in vacuum and electrolyte, respectively. Water molecules have a strong dipole character and they form hydration shells around ions in aqueous solutions. This hydration shell determines the distance d. In the most simple case the hydration shell remains when ions participate in the electrochemical double layer. Such adsorbed ions are bonded to the electrode via long-range electrostatic forces (physisorption), a process termed as *non-specific adsorption*. In this case d is defined by the distance between the surface and the centers of the hydrated ions, the so-called *'outer Helmholtz-plane'* (OHP). For simplicity most models assume the charge to be in the center of the hydrated ion of diameter a, i.e. the OHP is located at $x_{OHP} = a/2$. The described situation applies for strongly hydrated ions, like F^-, ClO_4^- or most of the cations. In contrast, if the ions are weakly solvated, they are able to partially strip off their hydration shell and to chemically

bond to the surface (chemisorption), termed as *specific adsorption*. Typical species showing this behavior are Cl^-, Br^- and I^-. In this case the plane formed by the centers of charge, the *'inner Helmholtz-plane'* (IHP) or *'Stern layer'*, is located closer to the surface than the OHP. A change of the electrode potential causes a reformation of the double layer and a charging current.

At a certain potential Φ_{PZC} called 'potential of zero charge' (pzc) the charges of anions and cations compensate each other resulting in a vanish of excess charge on the electrode surface. For non-specific adsorption the ion concentration in the electrochemical double layer
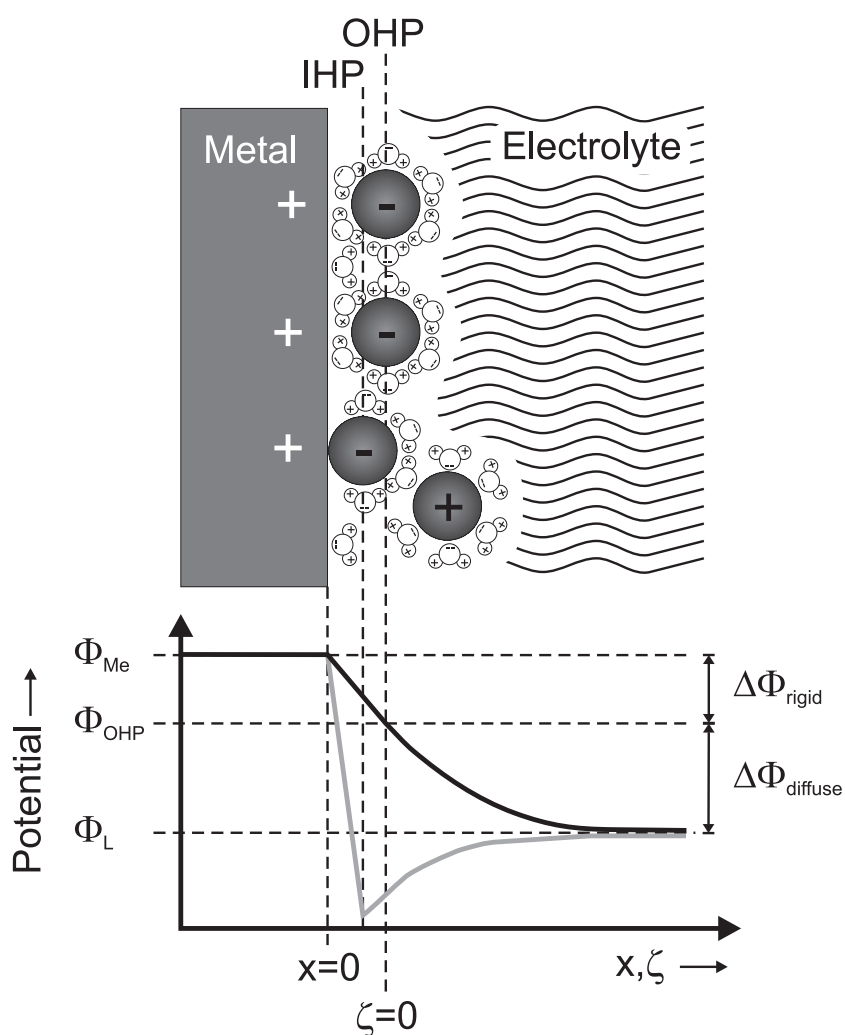
Figure 2.1: Potential gradient across the rigid and diffuse electrolytic double layer. Me denotes the metal electrode, OHP the outer Helmholtz plane, IHP the inner Helmholtz plane, L the liquid solution and ζ the zeta potential. The lines show the potential gradient in absence (black line) and in presence (gray line) of specific adsorption.

at Φ_{PZC} is approximately equal to the concentration inside the electrolyte and the ion coverage of the surface lies in a range of some percent. However, chemical bond of the ions results in higher concentrations on the surface compared to the case of electrostatically bonded ions ('superequivalent adsorption'). This excess charge is compensated by accumulation of counterions in front of the electrode. Especially for the case of specifically adsorbed species the ion concentration in the double layer is higher at the potential of zero charge compared to the electrolyte bulk concentration.

Of particular interest in electrochemical systems is the potential gradient across the interface as it exerts influence on electrode reactions. For the chosen electrode geometry the one-dimensional form of the poisson equation has to be solved, which connects the potential with the charge density.

$$\frac{d^2\phi}{dx^2} = -\frac{4\pi\rho}{\epsilon} \tag{2.2}$$

If the space between OHP and surface is assumed to be charge-free, i.e. $\rho = 0$, equation 2.2 provides a linear gradient between the surface potential Φ_{Me} and the potential Φ_{OHP} at the OHP.

$$\Phi(x) = \begin{cases} \Phi_{Me} + |\vec{E}| \cdot x & x \in [0, a/2] \\ \Phi_{OHP} & x \geq a/2 \end{cases} \tag{2.3}$$

The small distance d between the capacitor plates leads to enormous electrical fields $|\vec{E}|$ which can easily take a value as high as $10^7\,V/m$ [20]. This is high enough to distort electroreactants (see section 2.3.4) and to affect the kinetics of charge transport across the interface. The simple Helmholtz model describes interfaces with highly concentrated electrolytes, such as those employed in the present study (0.1 M HCl), quite well but it fails for low concentrations.

2.1.2 The Gouy-Chapman-Stern Model

For low ion concentrations in the electrolyte the thermal motion of ions has to be considered which results in a diffuse ionic space charge following the Maxwell-Boltzmann distribution (diffuse double layer). In the framework of the Gouy-Chapman model the potential drops exponentially from the potential Φ_{OHP} at the position of the outer Helmholtz plane to Φ_L in the solution bulk. The capacitance C_{GC} of the diffuse double layer is given by

$$C_{GC} = \sqrt{\frac{2z^2e^2\epsilon\epsilon_0 n^0}{kT}} \cosh\left(\frac{ze(\Phi - \Phi_{PZC})}{2kT}\right) \tag{2.4}$$

where e is the elementary charge, k is the Boltzmann constant, T is the temperature and z is the charge transfer number. Since this model is only valid for very diluted electrolytes the Helmholtz-model and the Gouy-Chapman model were combined by Otto Stern. According to the Gouy-Chapman-Stern model the double layer is more accurately described by a combination of a rigid layer and a diffuse layer with a total capacitance C_d of

$$\frac{1}{C_d} = \frac{1}{C_{GC}} + \frac{1}{C_H} \tag{2.5}$$

The gray and the black curve in figure 2.1 depict the potential gradients across the interface in presence and absence of specific adsorption, respectively.

2.2 Galvani Potential of Metal Electrodes

Considering two phases I and II in contact with each other, then the system is in equilibrium if the chemical potentials ($\mu = \mu^0 + RT \ln a$) are equal. In electrochemical environment the electrical potential difference between the electrode and the solution causes an additional electrical work $zF\Phi$ which has either to be applied or which is released when charged particles are added to a phase. Hence, Butler [25] and Guggenheim [26] introduced the electrochemical potential

$$\mu^* = \mu + zF\Phi = \mu^0 + RT \ln a + zF\Phi \tag{2.6}$$

where R is the gas constant, T is the temperature, F is the Faraday constant, a is the chemical activity (which is a measure for the effective concentration), μ^0 is the chemical standard potential ($a = 1$) and z is the charge transfer number. This extension of the chemical potential points to the following definition of the electrochemical equilibrium

$$\mu_i^*(I) = \mu_i^*(II) \qquad \text{for all components } i. \tag{2.7}$$

If a metal electrode with an inner galvani potential Φ_{Me} is immersed in an aqueous electrolyte with an inner galvani potential Φ_L then according to the equations 2.6 and 2.7 the galvani potential $\Delta\Phi = \Phi_{Me} - \Phi_L$ of the electrochemical interface is given by

$$\begin{aligned} \Delta\Phi = \Phi_{Me} - \Phi_L &= \frac{\mu^0_{Me^{z+}} - \mu^0_{Me}}{zF} + \frac{RT}{zF} \ln \frac{a_{Me^{z+}}}{a_{Me}} \\ &= \Delta\Phi_{00} + \frac{RT}{zF} \ln \frac{a_{Me^{z+}}}{a_{Me}} \end{aligned} \tag{2.8}$$

Chemically pure substances like metal electrodes have unit activity, i.e. $a_{Me} = 1$. The constant $\Delta\Phi_{00}$ is the difference between the inner galvani potentials of electrode and electrolyte for $a_{Me^{z+}} = 1$ and termed as *standard galvani potential*. For low concentrations of Me^{z+} in the electrolyte the activity $a_{Me^{z+}}$ can be substituted by the concentration $c_{Me^{z+}}$.

In general the potential Φ_L within the solution is no adequate point of reference as it cannot be determined experimentally. At the same time an instrument would try to measure it, a second metal/electrolyte interface is created. Hence, in order to obtain the galvani potential an additional electrode has to be systematically introduced into the system which on his part has a certain galvani potential with respect to Φ_L. Each interface is then called *half-cell*, and two half-cells in combination form an *electrochemical cell*. The cell voltage in equilibrium, termed as electromotive force (EMF) or open circuit potential (OCP), can be measured if no significant current is forced through the cell. Its value then corresponds to the difference in the galvani potentials of the electrodes. Employing an appropriate, stable reference electrode then equation 2.8 leads to the well-known Nernst-equation

$$\Phi_0 = \Phi_{00} + \frac{RT}{zF} \ln a_{Me^{z+}} \qquad \text{(Nernst equation)} \tag{2.9}$$

which describes the equilibrium potential Φ_0 of a metal ion electrode. Φ_{00} is termed as *standard electrode potential* and equals Φ_0 if the activity $a_{Me^{z+}}$ is unity. The absolute value of

half-cell	electrode reaction	Φ_{00} vs. NHE	Φ_{00} vs. Ag/AgCl
Au/Au$^+$	Au$^+$ + e$^-$ $\rightleftharpoons$ Au	+1.680 to 1.830	1.436 to 1.586
Au/Au^{3+}	Au^{3+} + 3 e$^-$ $\rightleftharpoons$ Au	+1.420 to 1.520	1.176 to 1.276
Au/Au^{2+}	Au^{2+} + 2 e$^-$ $\rightleftharpoons$ Au	+1.400	1.156
	O$_2$ + 4H$^+$ + 4e$^-$ $\rightleftharpoons$ 2 H$_2$O	+1.229	0.985
	AuCl$_2^-$ + e$^-$ $\rightarrow$ Au + 2 Cl$^-$	+1.150	0.906
	AuCl$_4^-$ + 3 e$^-$ $\rightarrow$ Au + 4 Cl$^-$	+0.994 to +1.002	0.750 to 0.758
	AuCl$_4^-$ + 2 e$^-$ $\rightarrow$ AuCl$_2^-$ + 2 Cl$^-$	+0.926	0.682
	O$_2$ + 2 H$_2$O + 4 e$^-$ $\rightleftharpoons$ 4 OH$^-$	+0.401	0.157
Ag/AgCl/Cl$^-$	AgCl + e$^-$ $\rightleftharpoons$ Ag + Cl$^-$	+0.244	0

Table 2.1: Standard potentials of important gold redox reactions versus NHE at 25°C and versus Ag/AgCl (3 M KCl).

the standard potential depends on the employed reference electrode. For metal electrodes in electrolytes containing ions of the same species the Nernst-potential determines the border line between metal deposition and metal dissolution.

Electrochemists are often interested in redox reactions which proceed at only one of the electrodes, the so-called *working electrode* (WE). Since the measured or applied cell potential always includes or influences both electrodes a reliable potential of the working electrode is only assured if the electrode in the second half-cell has a well defined and 'fixed' galvani potential. Electrodes which fulfill this demand are called *reference electrodes*. Because of rapid achievement of the equilibrium potential and high reproducibility the normal hydrogen electrode (NHE) has been arbitrarily chosen to be the origin of the potential scale with the standard potential $\Phi_{00}(NHE) \coloneqq 0$. However, often the NHE electrode is inconvenient for experiments so that potentials are usually measured with respect to alternative reference electrodes. A very common and compact reference electrode is the Ag/AgCl electrode in saturated 3 M KCl solution, which is shifted by +0.244 V versus NHE. Ag/AgCl has been employed in all present studies and as far as not explicitly quoted all potentials are referred versus Ag/AgCl in the following. Table 2.1 summarizes some standard potentials of important gold redox reactions.

2.3 Non-Equilibrium and Electrode Reaction Kinetics

While thermodynamic solely predicts the equilibrium state, a kinetic approach focuses on reaction directions and on reaction rates in order to describe non-equilibrium states. Nevertheless, to be correct the kinetic equations must contain the thermodynamic form in the limit of equilibrium. In particular, for an electrode reaction the kinetic theory has to predict the Nernst equation. Furthermore, in the range of non-equilibrium it is required that the theory explains the observed dependence of current on potential under various circumstances. Below, a kinetic treatment of the interface at non-equilibrium conditions is presented. First the

activated complex theory and afterwards the current-overpotential relationship, the diffusion-limited deposition and the deposition from metal complexes will be outlined.

2.3.1 Activated Complex Theory

Arrhenius discovered in 1889 experimentally that most rate constants k of solution-phase reactions vary with temperature T in the following way

$$k = A\exp(-E_A/RT) \tag{2.10}$$

where E_A describes an energy which can be interpreted as activation barrier. The prefactor A is called frequency factor and it is imagined as attempt frequency to overcome E_A. Focusing on electrochemical interfaces the educts (products) in the solution phase in front of the electrode and the products (educts) on the electrode surface reside in potential minima, i.e. they present stable states. The energy of all intermediate states is higher, especially at the maximum called state of the *activated complex*. Consequently an electrochemical reaction proceeding in either of the two reaction paths along the reaction coordinate has to pass an activation barrier and the corresponding rate depends on the barrier height in the particular direction. At equilibrium the activation barrier in forward direction - from the solution state to the surface state - shall be denoted by $E_{A,f}$ and the barrier in backward direction - from the surface state to the solution state - by $E_{A,b}$. By applying an additional potential difference $\Delta\Phi$ the balance of the energy barriers changes and one of the reaction directions gets favored
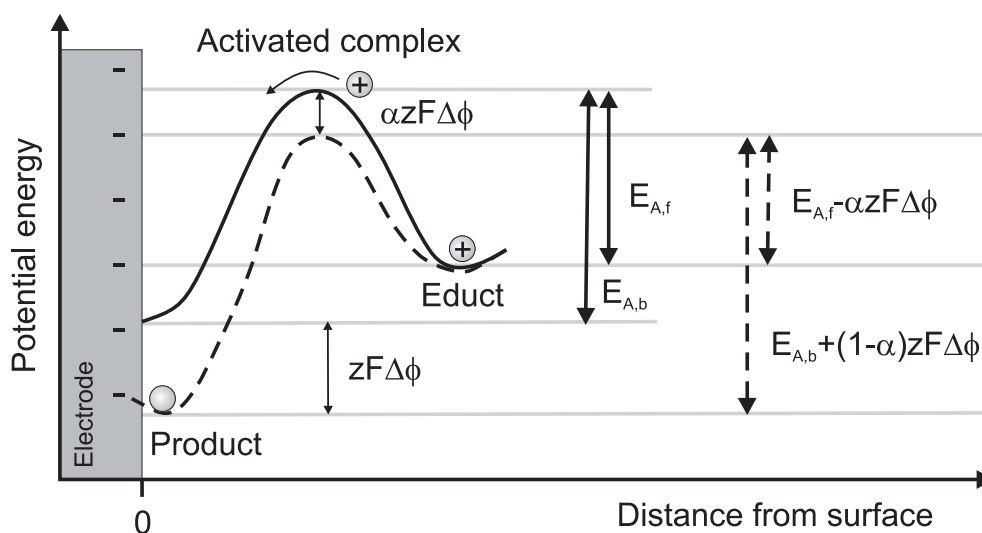
Figure 2.2: Potential energy surface at an electrochemical interface explained on the basis of metal deposition. Educts in the solution and products on the surface reside in potential minima and have to overcome a potential barrier. The net reaction rate depends on the barrier heights $E_{A,f}$ and $E_{A,b}$ in both reaction directions which can be changed by an applied potential difference $\Delta\Phi$ (dashed curve). The activated complex is the configuration of maximum free energy.

compared to the other. Without loss of generality, the barrier in forward direction may be lowered by an amount $\alpha z F \Delta \Phi$, while the barrier in backward direction will be increased by $(1 - \alpha)zF\Delta\Phi$. Then the reduction of the species will be the favored reaction while the oxidation reaction is partly hindered. Figure 2.2 illustrates the situation on the basis of metal deposition. It was found phenomenologically that changes in the forward and backward barrier are coupled by a parameter α which is called the asymmetry parameter. In many systems α takes a value of approximately 0.5 but it basically can vary in the range between zero and unity.

2.3.2 Current-Overpotential Relationship

If an electrochemical cell is operated as electrolytic cell then the system is pertubated by imposition of an external voltage. The difference between the applied potential $\Phi_{applied}$ and the equilibrium potential Φ_{Eq} is called *overpotential* η. In general η is the sum of different partial overpotentials.

$$\eta = \Phi_{applied} - \Phi_{Eq} = \eta_E + \eta_R + \eta_D + ... \tag{2.11}$$

Central in electrode reaction kinetics and always present in electrochemical systems is the electron transfer overpotential η_E. It is determined by the inhibited velocity of charge transfer through the electrode/electrolyte interface and equates to $\Delta\Phi$ in the activated complex theory. η_E is to a great extend dependent on the chosen electrode material. Further contributions to η may arise from limited mass transport of reactants from the solution bulk to the surface ('diffusion overpotential' or 'concentration overpotential', η_D) or from insufficient velocity of coupled reaction steps before or after the electron transfer step (reaction overpotential, η_R). Examples for the latter are adsorption and desorption processes. The overpotential belonging to the slowest process dominates η, i.e. it represents the rate determining step. We consider the case that the total overpotential is mainly determined by η_E, i.e. $\eta \approx \eta_E$, and that other contributions are negligible. If the redox reaction

$$Ox + ne \underset{k_b}{\overset{k_f}{\rightleftharpoons}} Red \tag{2.12}$$

takes place at the electrode/electrolyte interface, where Ox is the oxidized species, Red is the reduced species, n is the charge transfer number, e is the elementary charge and k_f and k_b are the rate constants of the forward and backward reaction, respectively, then the current density $j(\eta)$ is expressed by the Butler-Volmer equation

$$j(\eta) = j^+ + j^- = j_0 \left(\exp\left[\frac{\alpha n F}{RT}\eta \right] - \exp\left[-\frac{(1-\alpha)nF}{RT}\eta \right] \right) \tag{2.13}$$

with

$$j_0 = nFk_0c_{red} \exp\left(\frac{\alpha n F}{RT}\Phi_{Eq} \right) = -nFk_0c_{ox} \exp\left(\frac{(1-\alpha)nF}{RT}\Phi_{Eq} \right) \tag{2.14}$$

Herein, j^+ and j^- denote the anodic and cathodic current densities, respectively, j_0 the exchange current density, F the Faraday constant, R the gas constant, T the absolute temperature and α the asymmetry parameter. The Butler-Volmer equation does not completely
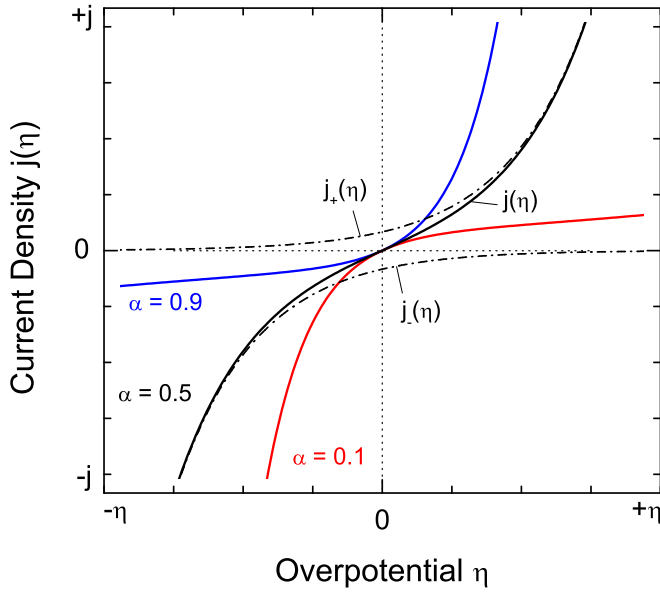
Figure 2.3: Illustration of the current-overpotential relationship according to the Butler-Volmer equation. Curves for asymmetry parameters $\alpha = 0.1$, 0.5 and 0.9 are depicted as well as the partial anodic (j_+) and cathodic (j_-) current densities for $\alpha = 0.5$.

describe kinetic processes at the electrochemical interface, but gives a first quantitative approximation. Figure 2.3 depicts equation 2.13 for different asymmetry parameters α.

If η is equal to zero then the current density vanishes and the system is in equilibrium with $j_E^- = -j_E^+ = j_0$. Charge transfer through the double layer occurs with identical rates in both directions and the Nernst equation can be derived by evaluation of equation 2.14. At non-vanishing overpotentials equation 2.13 has two limiting cases

1. At low overpotentials ($|\alpha F \eta / RT| \leq 0.2$) the exponent of equation 2.13 can be linearized and a linear $j_{ET} - \eta$ relationship of the form

$$j(\eta) = j_0 \frac{nF}{RT} \eta. \tag{2.15}$$

   is found which solely depends on j_0 but not on α.

2. At high overpotentials ($|\alpha F \eta / RT| \gg 1$) one of the partial currents becomes negligible and equation 2.13 transform to

$$j(\eta) = j_0 \exp\left(\frac{\alpha F \eta}{RT}\right) \qquad \text{or} \qquad j(\eta) = j_0 \exp\left(-\frac{(1-\alpha)F\eta}{RT}\right) \tag{2.16}$$

   which are *Tafel equations* of the general form

$$\eta = m \cdot \log\left(\frac{j}{j_0}\right) \tag{2.17}$$

   where m is the *Tafel slope*. The Tafel slopes m_a and m_c for anodic and cathodic overpotentials, respectively, are defined as

$$m_a = \frac{2.3RT}{\alpha nF} \qquad \text{or} \qquad m_c = \frac{2.3RT}{(1-\alpha)nF} \tag{2.18}$$

2.3.3 Effects of Mass Transfer and Diffusion Limited Deposition

To separate the influence of diffusion on the charge transfer through the double layer from other possible transport processes an electrochemical model system shall be considered in which the transfer is solely coupled to diffusion. A simplified case to discuss and of relevance for the present study is the cathodic deposition of an electrochemically active species 'A' of concentration c_0 within an unstirred solution of higher concentrated support ions. If no current flows then the ion concentration is constant all over the electrolyte, particularly the same near the electrode surface as in the solution bulk. By applying a negative overpotential to the cell the reducing reaction gets more favorable and cations close to the surface adsorb. As direct consequence the ion concentration decreases from c_0 to c_s in the surrounding of the electrode. The diffusion of ions from the solution bulk to the electrode determines the shape of the evolving concentration gradient profile. Figure 2.4(a) outlines the time development of the diffusion layer until equilibrium is achieved for the cases of low (curve ②c) and high (curve ③c) overpotentials.

In the early stage of impressing a voltage on the electrode the thickness δ_N of the gradient layer, also termed as 'Nernst diffusion layer', is comparatively narrow (curve ②a). With time the profile extends into the electrolyte until steady state conditions are accomplished (curve ②c). δ_N is defined as intersection of the concentration profile tangent with the horizontal line of c_0.

$$\delta_N = \frac{c_0 - c_s}{(\partial c / \partial x)_{x=0}} \tag{2.19}$$

The stationary thickness of the Nernst layer strongly depends on the hydrodynamic conditions near the electrode. In unstirred electrolytes microscopic convections compensate
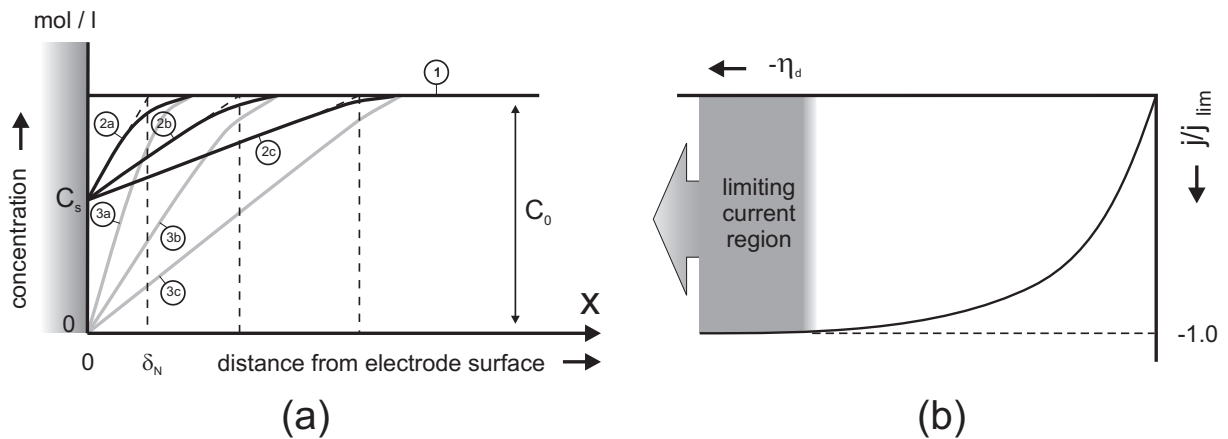
Figure 2.4: (a) Time-dependent concentration gradient for electrochemical deposition of active species in unstirred solution (a = after some seconds, c = after some minutes): ①: without current flow ②a-②c: after initiation of current flow ③a-③c: after initiation of limited current flow. (b) Dependence of the normalized cathodic current density j/j_{lim} on the diffusion overpotential η_d

density differences. This effect limits δ_N to 0.5 mm and equilibrium is reached after a time of approximately 30 to 60 s. In contrast, an equilibrium under electrolyte flow conditions is obtained within 0.1 to 1 s (dependent on the flow rate) where an artificial flow supplies the diffusion layer with additional ions of the concentration c_0. In the latter case the thickness of the Nernst diffusion layer can be lowered to 10^{-3} mm. As it will be seen in section 9.7 the deposition rate indeed increases significantly when the electrolyte is forced to flow over the electrode surface.

c_s, i.e. the cation concentration on the electrode surface, is determined by the value of the overvoltage η_D. The higher the overvoltage the smaller is the cation concentration c_s ($\lim c_s \to 0$, curve ③). Using Fick's first law of diffusion and equation 2.19 the electrochemical current density is given by

$$j = nFD\left(\frac{\partial c}{\partial x}\right)_{x=0} = nFD\frac{c_0 - c_s}{\delta_N} \tag{2.20}$$

where D is the diffusion coefficient of A in the solution, F is the Faraday constant and n is the number of transferred electrons in each reaction step. Besides of c_s and δ_N equation 2.20 contains only constants. Therefore, considering a time-independent diffusion layer (δ_N constant) and high overpotentials ($c_s \approx 0$), the current density reaches a limit value j_{lim} of

$$j_{lim} = \frac{dq}{dt} = nFD\frac{c_0}{\delta_N} \tag{2.21}$$

The range where j equals j_{lim} is called the 'limiting current region'. Electrochemical reactions in this potential regime proceed extremely fast and the system overvoltage η is almost equal to the diffusion overvoltage η_D. The latter can be obtained by use of the Nernst-equation:

$$\eta_D = \frac{RT}{nF}\ln\frac{c_s}{c_0} \tag{2.22}$$

Combining equations 2.20, 2.21 and 2.22 the relationship $\eta_D(j_{lim})$ is given by

$$\eta_D = \frac{RT}{nF}\ln\left(1 - \frac{j}{j_{lim}}\right) \tag{2.23}$$

as schematically shown in figure 2.4b. The relationship described by equation 2.23 is of major importance for investigations of epitaxial growth from solution. Operating within the limiting current region allows to deposit ions from a solution of concentration c_0 with constant deposition rate independent of the chosen electrode potential. Consequently, potential-dependent processes on the electrode surface, e.g. surface transport, can be studied without being coupled to a change in deposition rate. Helpful in terms of X-ray measurements is the change of coverage θ with time t. Considering metal electrodeposition with a charge transfer of n electrons for each deposited metal atom then the relationship between charge q and coverage θ is given by

$$q = \theta \cdot N_{ML} \cdot n \cdot e_0 \tag{2.24}$$

where N_{ML} is the number of atoms in one monolayer. Replacing dq in equation 2.21 by $dq = N_{ML} \cdot n \cdot e_0 \cdot d\theta$ yields the time-dependence of θ in the limiting current region

$$\frac{d\theta}{dt} = \frac{N_A \cdot D}{N_{ML} \cdot \delta_N} \cdot c_0 = \frac{j_{lim}}{n \cdot e_0 \cdot N_{ML}} \tag{2.25}$$

2.3.4 Cathodic Deposition of Metal Complexes

In contrast to strong electrolytes in which metal species (e.g. lithium, sodium and potassium) are present as positively charged cations, weak electrolytes often contain negatively charged metal complexes (e.g. silver or gold complexes). In order to understand how these complex anions can be deposited cathodically even though electrode and ion complex carry charge of the same polarity, the driving forces for ion transport must be considered. In electrochemical environment basically three mechanisms of ion transport exist. The first mechanism is the transport by 'migration' due to the electric field, the second mechanism is the transport by 'diffusion' which arises due to the concentration gradient evolving in front of the electrode and the third mechanism is 'convection'. The sum of all contributions gives the total ion transport $\dot{n}_i$.

$$\dot{n}_i = \dot{n}_{i,\text{diffusion}} + \dot{n}_{i,\text{migration}} + \dot{n}_{i,\text{convection}} \tag{2.26}$$

Applying Faradays law to equation 2.26 results in the Planck-Nernst equation which describes the current density, here given in the one dimensional form

$$j_i = j_{i,m} + j_{i,d} + j_{i,c} = -z_i F \left(\underbrace{c_i u_i \frac{\partial \Phi}{\partial x}}_{\text{migration}} + \underbrace{D_i \frac{\partial c_i}{\partial x}}_{\text{diffusion}} - \underbrace{c_i \cdot v}_{\text{convection}} \right) \tag{2.27}$$

where z_i denotes the number of transferred electrons per reaction step, F is the Faraday constant, c_i is the concentration of the species i in the solution, D_i is the diffusion constant of i in solution and u_i is the ionic mobility. In stagnant solution the convection term can be neglected and a closer look at equation 2.27 reveals that under conditions where $\partial c/\partial x$ dominates over $\partial \Phi/\partial x$, i.e. the diffusion is more pronounced than migration, negatively charged ions like metal complexes can move to the cathode against the electrostatic repulsion force. Experimentally these conditions are fulfilled in most of the cases since electrolytes are chosen to have good conductivity which decreases the potential gradient. According to the literature, the concentration of the supporting electrolyte should be at least 100 times higher than the concentration of the metal complex [18].

In reference [27] the author describes a possible interfacial mechanism for gold electrodeposition from solutions containing gold cyanide complexes. Au(CN)_2^- ions which approach the Helmholtz layer will become polarized in the electric field of the cathode. The original distribution of ligands gets distorted in a way that the diffusion of the complex into the Helmholtz layer is assisted. Once within the Helmholtz layer, the complex decomposes stepwise following the overall reaction

$$\text{Au(CN)}_2^- \rightleftharpoons \text{Au}^+ + 2\,\text{CN}^- \tag{2.28}$$

and the freed metal cation is deposited on the cathode. For the latter steps the polarization of the complex is of major importance. Without the influence of polarization the mass action law predicts the equilibrium in reaction 2.28 far to the left and an exceedingly low concentration of Au^+ ions. Once they are deposited the adatoms migrate over the surface and
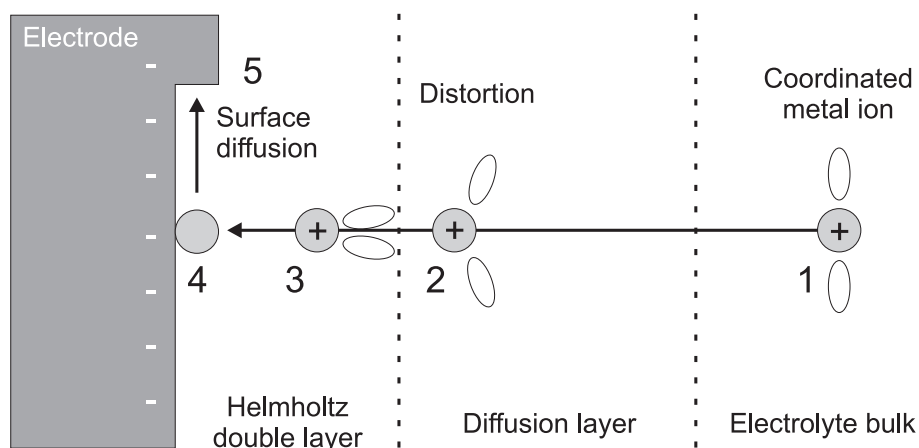
Figure 2.5: Schematic diagram of deposition process. 1: The metal ion in its ligand field, 2: The ligand field becomes distorted, 3: The metal ion is stripped from its ligand field, 4: The metal ion is neutralized, 5: The metal atom migrates to the nearest growth point. (from [27])

become either incorporated to step-edges or participate in the formation of nuclei. Figure 2.5 shows a schematic diagram of the considered deposition process. Gold electrodeposition from other gold complexes is thought to occur in a similar manner.

2.3.5 Electrodeposition from Tetrachloroaurate(III) Solution

Compared to other metals gold exhibits a relatively high electronegativity which led to the suggestion to term is as pseudohalogen. The affinity to attract bonding electrons manifests in numerous gold oxidation states occurring in a variety of synthesized gold complexes. Basically, oxidation states from (-I) to (V) have been reported. Of these six states gold prefers the oxidation states Au(I) and Au(III), historically known as 'aureous' and 'auric' gold, respectively. These states are also the preferred states in solution. Au(II) and Au(IV) have been as well found in solution but only as intermediate states, disproportioning into Au(I) and Au(III) or to metallic gold [28]. The stability of Au(I) depends on complexing agents. In absence of complexing agents it disproportionates, forming both Au(0) and Au(III).

Gold is unreactive in pure water as can be seen from the high positive standard reduction potentials for Au^+ ($E_0 = 1.83\,V$) and Au^{3+} ($E_0 = 1.52\,V$) which both are more positive than the potential required for the reduction of oxygen ($E_0 = 1.229\,V$). Strong oxidizing acids are ineffective at dissolving gold in the absence of complexing ligands. However, if ligands L, such as cyanide, chloride and thiosulfate ions are present, stable complexes of the form

$$Au^+ + 2L \quad = \quad AuL_2^+ \tag{2.29}$$
$$Au^{3+} + 4L \quad = \quad AuL_4^{3+} \tag{2.30}$$

Ligand	$AuL_2^+ \to Au(0)$		$AuL_4^{3+} \to Au(0)$		$AuL_4^{3+} \to AuL_2^+$	
--------	$E_0\,[V]$	$\log K$	$E_0\,[V]$	$\log K$	$E_0\,[V]$	$\log K$
H_2O	1.830	0	1.520	0	1.400	0
Cl^-	1.154	11	1.000	26	0.921	16
Br^-	0.959	15	0.854	34	0.805	20
SCN^-	0.662	20	0.636	45	0.623	26
I^-	0.578	21	0.560	49	0.560	29
CN^-	-0.611	39	-0.100	82	0.100	44

Table 2.2: Standard reduction potentials (NHE) at 298 K and stability constants for Au(I) and Au(III) complexes in aqueous environments.

can be formed. Besides of the properties of the complexing ligand, the stability of those complexes mainly depends on the donor atom of the ligand that is bonded directly to the gold atom. Generally, stability tends to decrease when the electronegativity of the donor atom increases, which gives rise to a stability order $I^- > Br^- > Cl^- > F^-$ for gold halide complexes. Further, Au(III) favors hard (more electronegative) electron donor ligands such as halides, while Au(I) favors soft electron donor ligands. The stability of gold halides and other gold complexes can be inferred from table 2.2.

Gold cyanide complexes exhibit the highest stability. This is the reason why industrial leaching of gold from natural ores is usually carried out by cyanide. Cyanide and sulfite are also the dominating species in industrial electroplating baths. However, in the present study gold-chloride complexes have been used for mainly two reasons. First, because the electrochemistry of single crystal gold electrodes within chloride containing solutions is well studied and second because of their less toxicity. Moreover, gold chloride complexes have the advantage that they are more easily reduced to metallic gold. All employed electrolytes were prepared from an ultrapure Hydrogen Tetrachloroaurate(III) solution (Chempur, 40% gold). Dimeric gold-chloride complexes transform into Tetrachloroaurate(III) anions in aqueous solutions containing excess chloride and thus are not present in the employed electrolytes. Tetrachloroaurate(III) anions are square planar species and the most stable gold-chloride complex in solution. The standard potentials versus NHE for a variety of Au(I) and Au(III) complexes are summarized in table 2.1. Diffusion constants D for $AuCl_4^-$ in different HCl solutions are given in table 2.3.
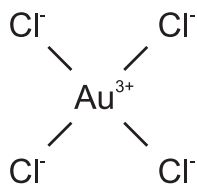
Electrolyte	Temperature T	Diffusion Constant D
0.25 M HCl	25 ± 0.1 °C	$1.1 \pm 0.1 \times 10^{-5}\,cm^2\,s^{-1}$
1.00 M HCl	25 ± 0.1 °C	$1.2 \pm 0.1 \times 10^{-5}\,cm^2\,s^{-1}$
1.00 M HCl	20 ± 0.1 °C	$9.1 \pm 0.7 \times 10^{-6}\,cm^2\,s^{-1}$

Table 2.3: Chemical structure of Tetrachloroaurate and diffusion constants in HCl solutions as measured by Chen et. al via capillary method. [29]

3 Crystal Growth

In this chapter the basic mechanisms involved in the growth and nucleation on solid metal surfaces with defined crystallographic orientation are described. In particular, we will focus on the influence of deposition parameters, such as temperature, electrode potential and deposition flux, on the resulting film morphology. It is clear by definition that crystal growth is impossible at equilibrium conditions since all atomic processes take place with equal rates in two opposite directions. Consequently, at equilibrium growth and dissolution of the crystal are balanced and the net growth equals zero. Thus, crystal growth must be treated as a non-equilibrium kinetic phenomenon. In terms of thermodynamics, growth can only be considered very close to equilibrium and must be treated as a quasi-equilibrium process. Growth proceeds on a planar or quasi-planar crystal surface in contact with a gas phase containing atoms of the same species if the chemical potential for sublimation, μ_{eq}, is smaller than the chemical potential μ of the vapor. Hence, the difference $\Delta\mu = \mu - \mu_{eq}$ is the driving force for crystal growth. In electrochemical environment the Nernst equation describes the equilibrium which is characterized by equity of the electrochemical potentials of both contacted phases. Here the driving force for crystal growth, i.e. the difference $\Delta\mu$ in the electrochemical potentials of atoms in the electrode and the electrolyte, respectively, is controlled by applying an overvoltage η of appropriate sign to the electrode.

3.1 Thermodynamic versus Kinetic Growth Modes

It is generally accepted that crystal growth on surfaces close to thermodynamic equilibrium conditions proceeds via three possible growth modes which have been first addressed by Bauer in 1958 [30]. These growth modes divide the resulting film morphology into three classes and have their origin in a different balancing of interfacial and surface free energy. Following Bauers wetting condition

$$\Delta\gamma = \gamma_f + \gamma_i - \gamma_S \tag{3.1}$$

where γ_f, γ_i, γ_S are the surface free energies of the film surface, substrate and film-substrate interface, respectively, a formal distinction of the growth modes is possible depending on the sign of $\Delta\gamma$: If $\Delta\gamma \leq 0$ the growth proceeds via layer-by-layer growth (Frank-van der Merwe growth), while it proceeds via 3D island growth (Volmer-Weber growth) if $\Delta\gamma > 0$. Besides of these two growth modes an intermediate third growth mode called Stranski-Krastanov exists, where a transition from 2D to 3D growth occurs at a critical film thickness. The latter predominantly appears in heteroepitaxial systems where a significant lattice misfit between the grown film and the substrate exists. However, in the case of homoepitaxial deposition the thermodynamically preferred growth mode is layer-by-layer growth.

In contrast, if crystal growth proceeds far from equilibrium the deposit morphology is the result of the complex interplay of various atomic diffusion processes which happen on a time scale predetermined by the deposition flux. In this situation the thermodynamic picture of a balance between the free energies does not hold anymore and a different framework for description of the film growth is required. However, in real systems a clear separation between

energetic and kinetic effects is not always possible and the border line is blurred. The latter together with the high complexity of such systems often hampers a full description of thin film growth by considering individual atomic processes. For this reason preferably simple model systems, e.g. homoepitaxial deposition, are studied to identify basic kinetic growth mechanisms. Particularly in the context of homoepitaxial growth the thermodynamic concepts are not useful as they simply predict layer-by-layer growth and the occurrence of different growth modes must therefore be fully ascribed to true kinetic effects.

On (single) crystal surfaces several atomic processes take place. Two of them will be considered here: 1st) diffusion of adatoms on a flat terrace, also called *intralayer* mass transport and 2nd) diffusion of adatoms across a step edge onto a lower terrace, also called *interlayer* mass transport. The relative rate of those two processes results in three different kinetic growth modes found in homoepitaxy, termed as step-flow growth, layer-by-layer growth and multilayer growth (figure 3.1). Step-flow growth is the most simple way to grow a flat film and is characterized by pure intralayer transport. The mass transport is so rapid that adatoms reach step edges before they have the chance to meet each other and to form stable nuclei. This growth mode is usually present close to equilibrium. However, if the system is far from equilibrium the growth is determined by nucleation on the terraces and subsequent, simultaneous growth of adatom islands. In this case the intralayer transport plays a minor role and the interlayer transport becomes decisive for the resulting film morphology. One can distinguish two extreme cases. If every adatom deposited on an island (or terrace) reaches the step-edge and subsequently jumps to the lower layer then the growth proceeds via ideal layer-by-layer growth. During the deposition process the surface morphology 'oscillates' between a flat surface (if the topmost layer has full coverage) and a rough surface (if the topmost layer has only fractional coverage) dependent on the deposited amount of atoms. In the other extreme interlayer transport is completely inhibited. Adatoms stay on their island and the surface starts to grow rough as further nucleations take place. This growth mode
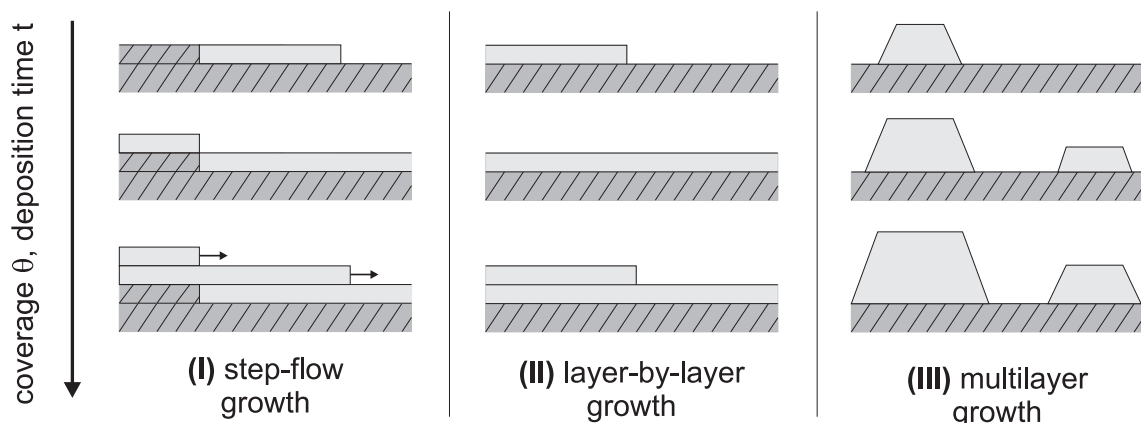
Figure 3.1: Schematic representation of three common kinetic growth modes. The amount of deposited material (coverage θ) increases from the top to the bottom of the sketch.

is termed ideal multilayer growth or 3D growth. The number of exposed layers increases with increasing deposition time and the layer height follows a Poisson distribution [31]. It is important to notice that any real growth far from equilibrium will proceed in between these two extremes.

In order to quantify the influence of deposition parameters on the growth behavior, in particular the dependence of the growth mode on deposition rate, electrode potential and substrate temperature, and to understand the transitions between different kinetic growth modes the role of atomic surface processes as well as the role of surface properties have to be attended.

3.2 Atomic Processes on Surfaces

The growth of a crystal always proceeds in several steps whereas each of those steps can become rate determining. In the initial step atoms are brought from an outer phase to the single crystal surface, i.e. adatoms are formed. This can be done either from the gas phase or from the liquid phase (typically an aqueous solution or metal melt). In both cases the amount of deposited material per time defines the deposition rate R.

Once an adatom is formed the systematic incorporation into the crystal bulk has to follow in order to grow the crystal epitaxially. Modern theories that explain the growth process have been introduced in the beginning of the last century [32, 33]. Burton, Cabrera and Frank describe the crystal growth by successive attachment of adatoms to energetically favorable kink sites at monatomic step edges [34]. That these sites exist and that they play an important role not only in the equilibrium but also in the growth and evaporation of a crystal was first shown by Kossel [35] and Stranski [36]. They termed kink sites as 'repetitive steps' or 'half crystal positions', respectively. The first expression describes that for each incorporation of an adatom in a kink site a new kink site next to the incorporated atom arises which has the same properties as the previous site. Hence, growth proceeds preferentially one dimensionally along step edges. The second expression points out that regardless of structure and range of interatomic forces, an atom in this site has exactly half the environment of a bulk atom. Thus, to take away an atom from a kink site affords only *half* of the work that would be needed to extract it from the bulk. Basically kink sites can be considered as sites of growth or dissolution of the crystal and they represent the final state of the transfer of an atom from the ambient to the crystal. Formally kink sites are treated as surface defects which together with the density of other defects such as adatoms, vacancies and step edges give the degree of surface roughness. Figure 3.2a illustrates some defects on a singular face of a crystal with a simple cubic lattice.

Adatoms are located at minimum energy adsorption sites of the potential energy surface (PES). In the case of metal-on-metal growth adsorption sites generally correspond to the continuation of the bulk stacking sequence such as fourfold hollow sites on a squared fcc(100) surface or threefold hollow sites on a hexagonal fcc(111) surface. Adatoms may undergo transitions between two adjacent adsorption sites if the energy provided by thermal fluctuations is large enough to overcome the activation barrier E_m at the saddle point between neigh-
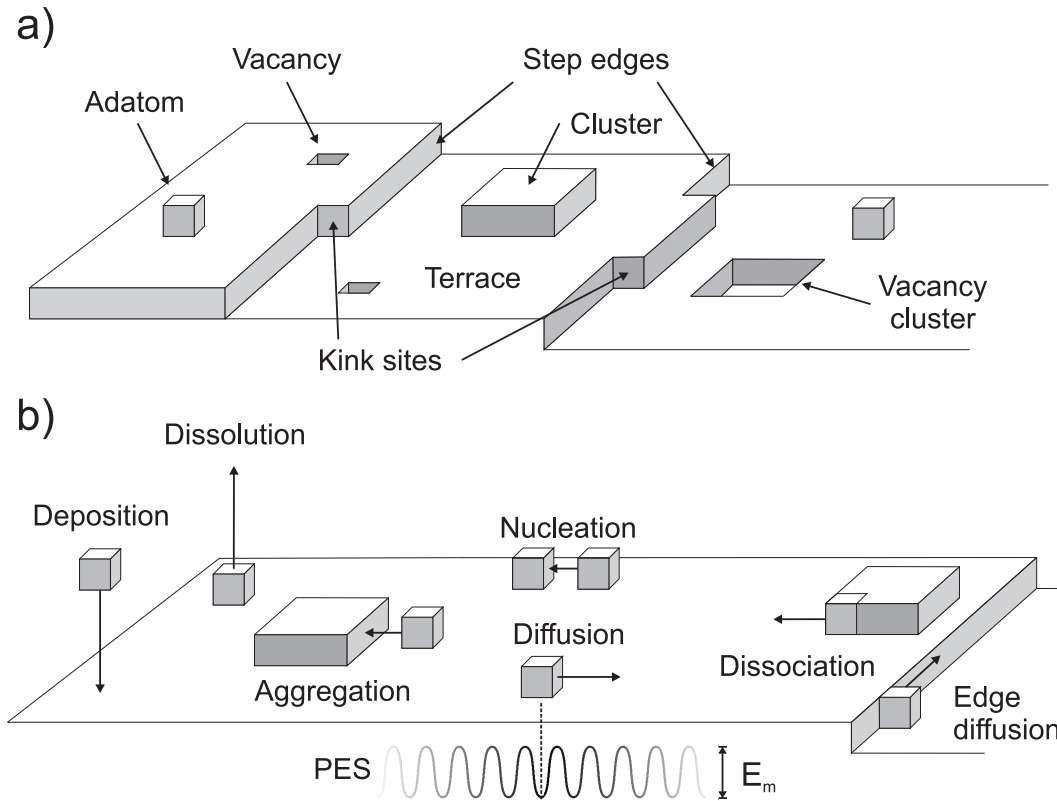
Figure 3.2: a) Model of a real metal surface showing different kind of defects. b)
Atomic processes in the kinetics of 2D film growth. Far from equilibrium desorption
and dissociation can be neglected. Exemplary the potential energy surface (PES)
with activation barrier E_m is depicted.

boring sites. In this way single adatoms may diffuse randomly[1] over the surface until they
take part in one of several processes which are depicted in figure 3.2b. Far from equilibrium
desorption and dissociation processes can be safely neglected.

It has been found that two basic mechanisms exist for thermally activated terrace diffusion.
Adatoms either travel across the surface via jump mechanism (figures 3.3a) or via exchange
mechanism (figures 3.3c) [37–40]. In both cases the diffusion frequency is described by an
Arrhenius expression of the form

$$\nu = \nu_0 \cdot \exp(-E_m/kT) \tag{3.2}$$

where E_m is the activation energy for diffusion and ν_0 is the attempt frequency. ν_0 corre-
sponds to the typical frequency of lattice vibrations ($\approx 10^{12}$ - 10^{13} Hz). These two processes
are not restricted to terrace diffusion but also occur at step edges (figures 3.3b and 3.3d).
Step edges feature another interesting characteristics. Early UHV field ion microscope ex-
periments revealed that adatoms from the two sides of a step do not incorporate into the

---

[1]The picture of randomly diffusing adatoms in only valid if $kT \ll E_m$

step with equal probability [41]. Obviously, an additional potential barrier of the height ΔE_{ES} must exist for adatoms at step edges, called Ehrlich-Schwoebel barrier (ESB), that prevents atoms from crossing the step, either above or below it [41, 42]. Capture anisotropy is frequently used to reveal the ES-barrier. Further evidences are the persistence of small vacancy islands or holes in the surface and widening of island free zones at ascending steps while such zones cannot be observed at descending steps. The Ehrlich-Schwoebel barrier is illustrated in figure 3.3e.

Up to now the physical origin of the enhanced potential barrier at step edges is still controversial. The most probable explanation is that the ESB for an adatom next to a downward step-edge is related to the coordination of the transition state. This gets support from a theoretical surface-embedded-atom method (SEAM) study which predicts different barriers for 'A-steps' and 'B-steps' on Ag(111) surfaces [43]. In contrast to UHV, where numerous systems are known to exhibit an ESB, no direct evidence for such a barrier in electrochemical environment has been reported for a long time. This posed the fundamental question if the ESB has a counterpart at solid/liquid interfaces. Y. He et al. found in 2002 that the island decay rates of gold islands on reconstructed Au(111) surfaces in 0.1 M perchloric acid are strongly correlated to the position of the islands relative to step edges and suggested the existence of an ESB [44]. This interpretation got additional support by the simultaneously observed persistence of surface vacancies. One year later Haftel and Rosen utilized the surface-embedded-atom-model (SEAM) to calculate the potential-dependent variations
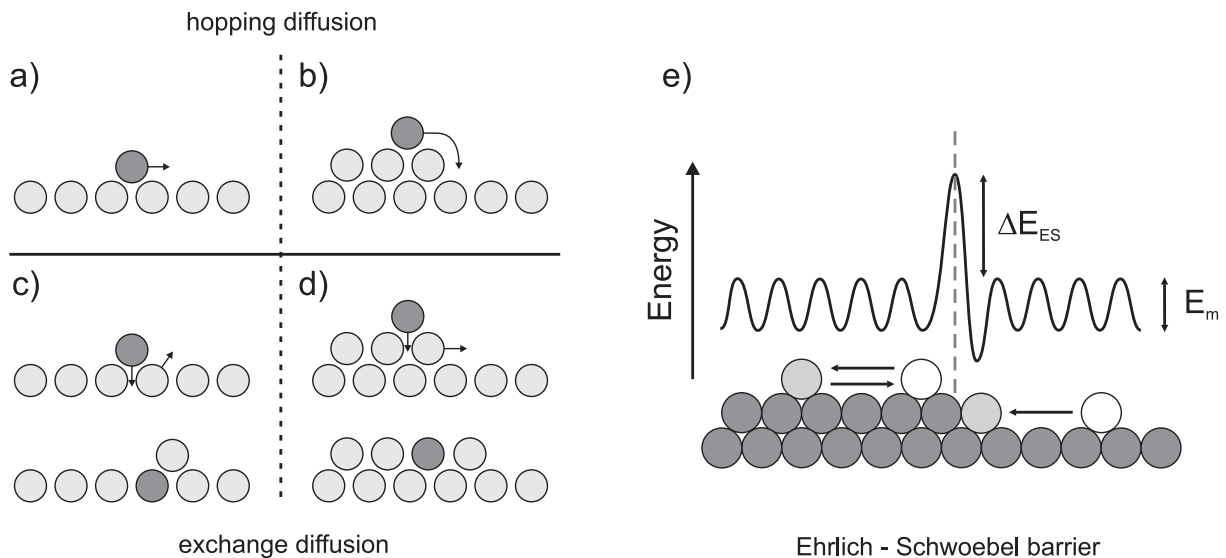
Figure 3.3: Adatoms diffuse over the surface either by a hopping mechanism (a) or by an exchange mechanism (c). Both diffusion types are also observed at step edges (b and d). The activation energy for an adatom to migrate over a step edge is by an amount of ΔE_{ES} higher than the activation energy E_m for terrace diffusion. This additional barrier (schematically shown in e) is called Ehrlich-Schwoebel barrier.

of terrace-diffusion barrier (TDB) and ESB for Ag adatoms migrating on low indexed Ag electrode surfaces in $0.1\,\mathrm{M}$ $HClO_4^-$ [43]. These studies predict that the ESB on Ag(111) surfaces should be much more sensitive to changes in the electrode potential than the TDB. For Ag adatoms migrating on Ag(100) a much weaker dependence of the ESB on the electrode potential is predicted compared to the Ag(111) results. Even though the authors concluded that the variation is not insignificant and has to be attended.

3.3 Dependence on Deposition Parameters and Growth Mode Transitions

The height of the additional step edge barrier ΔE_S is a central quantity to understand the different growth modes observed far from equilibrium as it controls the amount of interlayer mass transport. It is useful to describe the probability for adatoms to cross a step edge by a transmission factor s defined as

$$s = \exp(-E_S/kT) \tag{3.3}$$

where k is the Boltzmann constant and T the temperature. The transmission factor takes a value of $s = 1$ if the step edge barrier vanishes and $s = 0$ if the barrier is infinitely high. Indeed, an infinitely high barrier leads inevitably to ideal multilayer growth. However, the opposite case that a vanishing barrier would coercively lead to ideal layer-by-layer growth is incorrect. This is related to the fact that nucleation on a layer takes always place before the layer is completed and can be understood as follows: In the initial stage of monolayer growth deposited atoms diffuse over the surface until they meet and form stable nuclei. After some deposition time the nuclei density will be saturated, i.e. the probability of an adatom to reach an existing nucleus is much higher than to form a new nucleus within uncovered areas. At the time when saturation sets in (at low coverages) the surface is covered by a constant number of smaller islands which grow in size as new material is deposited. As long as islands do not coalesce every adatom on top of an island has a mean free path high enough to reach the island edge and, provided that no barrier prevents it to jump across the edge, no nucleation occurs on top of the islands. The situation changes in presence of island coalescence as merging islands form larger areas which on the other hand enhances the nucleation probability in the second layer. As a consequence any surface following the layer-by-layer growth mode will grow rough after deposition of many layers, i.e. it shows a certain degree of multilayer growth. A clear qualitative distinction between both growth modes is impossible for real systems.

In order to classify the growth behavior into different growth modes, criteria that quantify the amount of interlayer mass transport or the film roughness are required. One of manifold possibilities is the *submonolayer criterion*. The latter makes use of the critical coverage θ_c at which nucleation on top of growing islands sets in and allows to quantify the interlayer mass transport. Different growth modes are then defined by comparison of this θ_c with a certain fixed value. Based on nucleation theory and typical values for capture numbers and nuclei sizes Rosenfeld et al. [1] determined a critical coverage of $\theta_c = 0.66$. This

is a value where island coalescence is typically observed (θ_{coal}), so that the following two conditions qualitatively define the regimes of 2D and 3D growth

$$2\text{D growth} \qquad \Leftrightarrow \qquad \theta_C > \theta_{\text{coal}} \tag{3.4}$$

$$3\text{D growth} \qquad \Leftrightarrow \qquad \theta_C < \theta_{\text{coal}} \tag{3.5}$$

Based on this definition and nucleation theory Rosenfeld et al. derived two expressions which more quantitatively describe the transition lines between 2D and 3D growth and between 2D growth and step-flow growth, respectively [1]. The obtained relations are supposed to hold for deposition from the gas phase as well as from the solution phase. According to Rosenfeld the transition line between 2D and 3D growth is defined by

$$R = \lambda_0^{2(i+2)/i} \cdot \exp\left(-\frac{E_i/i + E_m + E_s \cdot 2(i+2)/i}{kT}\right) \tag{3.6}$$

where R is the deposition rate, λ_0 is a constant related to island separation, i is the size of the critical nucleus, E_i is the binding energy of the critical cluster, E_m is the activation energy for terrace diffusion, k is the Boltzmann constant and T is the temperature. The 2D to step-flow transition line is defined by

$$R = \left(\frac{\lambda_0}{L}\right)^{2(i+2)/i} \cdot \exp\left(-\frac{E_i/i + E_m}{kT}\right) \tag{3.7}$$

where L is the step separation. An interpretation of the transition lines is clear for deposition from the gas phase since all energies (i.e. E_i, E_m and E_s) are fixed and only the temperature varies. Hence, in an Arrhenius plot all transition lines are straight as depicted in figure 3.4. In the case of $\Delta E_s > 0$ (figure 3.4a) the transition lines have to cross as their slope is different (cp. equations 3.6 and 3.7). At constant deposition rate and increasing
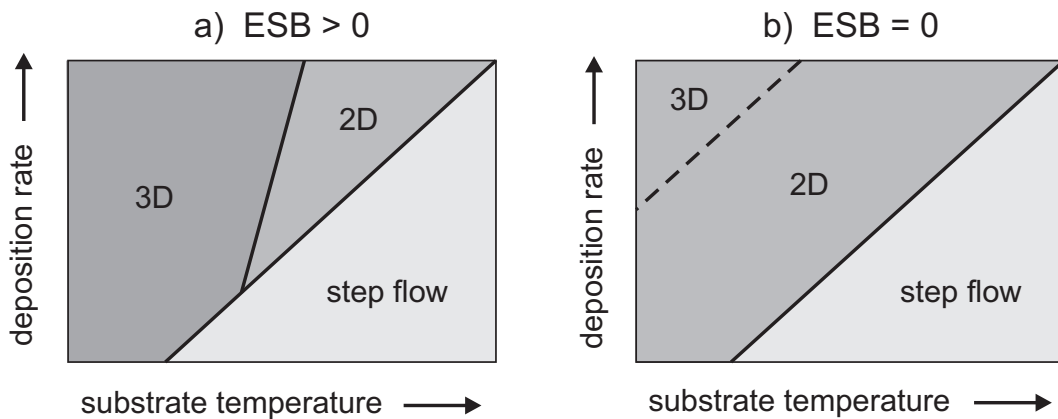
Figure 3.4: Growth mode diagrams with transition lines for the two cases that a) $\Delta E_S > 0$ and b) $\Delta E_S = 0$. The theoretical study in reference [1] indicates that 3D growth cannot be observed if the step edge barrier vanishes as marked by a dashed line.

temperature one either observes the sequence 3D → 2D → step-flow growth or the sequence 3D → step-flow growth. On the other hand, if the step edge barrier vanishes, i.e. $E_s = 0$, then the transition lines run parallel. Only 2D and step-flow growth are observed in this case.

For deposition from the solution phase the situation is much more complex. While in electrodeposition studies the temperature T is generally fixed the energies E_i, E_m and E_s are potential-dependent. Hence, the shape of the transition lines is determined by the sum of up to three potential-dependent energies. The todays knowledge about the potential-dependence of these energies is extremely limited so that the shape of the transition lines cannot be predicted but only inferred from experiments. Such a growth mode study will be presented in chapter 9.

4 Theory of Surface X-ray Diffraction

In the last 30 years surface sensitive X-ray diffraction turned out to be a valuable instrumental technique in order to characterize surfaces. Pioneering work has been for example carried out by L.G. Parratt [45], J. Als-Nielsen [46], H. Dosch [47], S.K. Sinha [48], I.K. Robinson [49], R. Feidenhans'l [50] and by W.C. Marra and P. Eisenberger who performed in the late 70th and early 80th of the last century the first glancing angle X-ray diffraction measurements on metal and semi-conductor surfaces under UHV conditions [51, 52]. In contrast to other surface sensitive scattering techniques (e.g. LEED or He-scattering) X-rays only weakly interact with matter because of the low scattering cross section. Therefore multiple scattering effects can be neglected and a kinematical approach is sufficient to analyze the data. On the other hand the large penetration depth is especially useful to investigate electrochemical interfaces as simultaneously the structure on the solution side as well as on the electrode side can be studied. In contrast to scanning probe techniques like STM or AFM surface X-ray scattering is able to access buried structures below the electrode surface, e.g. an unreconstructed bulk structure below a reconstructed surface layer or the surface structure below an adlayer. Furthermore structures which are invisible for STM and AFM, such as an enhanced positional order of water molecules, can be resolved. However, due to the small amount of atoms residing in the surface layer, typically in the order of 10^{15} atoms per cm^2, the scattered intensity is very low compared to the much larger intensity scattered by the crystal bulk. The problem is exacerbated by scattering from species in the solution bulk which contributes to the background intensity. Hence, in order to resolve the surface structure the X-ray source has to fulfill a couple of requirements. First, the X-ray beam must be of high brilliance to provide sufficient statistics and reasonable counting times. Second, the penetration depth has to be limited in order to reduce the strong signal from the crystal bulk. As demonstrated by Marra and Eisenberger the latter is achieved by grazing incidence angles of the X-ray beam with respect to the surface plane which simultaneously demands highly collimated beams. X-ray beams with those properties are generated by powerful third generation synchrotron sources.

The following sections will give a brief overview of surface X-ray diffraction. Basic principles of X-ray scattering and scattering from crystal surfaces can be found in many solid state text books [53, 54]. Details on surface diffraction are found in several excellent reviews, describing the technique in general [50, 55–57] and in the context of electrochemical interfaces [58–60].

4.1 Surface Sensitivity

Special geometries allow to separate the weak surface signal from the strong bulk signal. Eisenberger and Marra demonstrated in 1979 that the surface sensitivity is considerably enhanced for X-rays with very small incident and exit angles with respect to the surface plane [51]. This effect is strongly related to the complex refractive index

$$n = 1 - \delta - i\beta \tag{4.1}$$
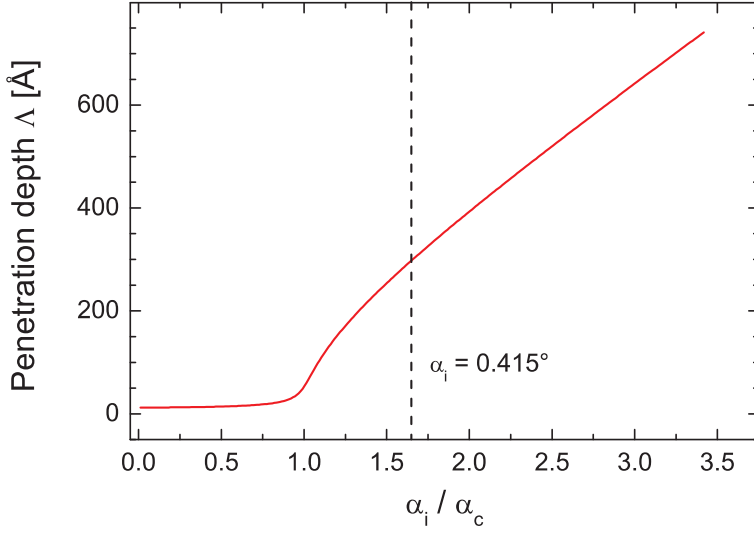
Figure 4.1: X-ray penetration depth Λ calculated for gold and a photon energy of 18.2 keV. The critical angle for 18.2 keV is $\alpha_c = 0.252°$. The dashed line marks the incident angle α_i used in the performed SXS experiments corresponding to a penetration depth of approximately 300 Å or ≈ 220 atomic layers.

which in the case of X-rays is smaller than unity for most materials. This is a direct consequence of the high radiation frequency which lies beyond the resonance of electronic polarization. The complex part β and the real part δ are dependent on the radiation properties and on the properties of the penetrated medium

$$\delta = \frac{\lambda^2}{2\pi} r_e \rho_e \qquad \text{and} \qquad \beta = \frac{\lambda}{4\pi} \mu_x \tag{4.2}$$

where λ is the wavelength, r_e the Thomson radius of the electron, ρ_e the electron density of the material and μ_x the linear absorption coefficient. If the incident angle α_i is smaller than a critical angle α_c, given by

$$\alpha_c \approx \sqrt{2\delta} \tag{4.3}$$

then total external reflection occurs. As a consequence of interference between the incoming and the reflected wave an evanescent wave travels parallel to the surface and is strongly damped into the crystal bulk. The penetration depth Λ is given by

$$\Lambda = (\sqrt{2}k)^{-1} \cdot \left((2\delta - \sin^2 \alpha_i) + \sqrt{(\sin^2 \alpha_i - 2\delta)^2 + 4\beta^2} \right)^{-1/2} \tag{4.4}$$

$$\approx (\sqrt{2}k)^{-1} \cdot \left(\sqrt{(\alpha_c^2 - \alpha_i^2)^2 + 4\beta^2} + \alpha_c^2 - \alpha_i^2 \right)^{-1/2} \tag{4.5}$$

and depends on the incident angle. Here $k = 2\pi/\lambda$ is the wave number. Equation 4.5 is depicted in figure 4.1 for gold and a photon energy of 18.2 keV. The penetration depth at an incident angle of $\alpha_i = 0.415°$, which has been preferentially used in the present measurements on Au(100) surfaces, is about 300 Å and corresponds to ≈ 220 atomic layers.

4.2 X-ray Diffraction from Single Crystals

We consider a cubic crystal which is characterized by the lattice vectors $\vec{a}_1 = (a_1, 0, 0)$, $\vec{a}_2 = (0, a_2, 0)$ and $\vec{a}_3 = (0, 0, a_3)$ in real space and the according lattice vectors $\vec{a}_1^*$, $\vec{a}_2^*$ and

$\vec{a_3^*}$ in reciprocal space. In a diffraction experiment the incident wave with a wave vector $\vec{k_i}$ impinges on the surface and is scattered into another direction described by the wave vector $\vec{k_f}$. The scattering process is considered to be elastic, i.e. $|\vec{k_i}| = |\vec{k_f}| = k = 2\pi/\lambda$, where k is the wave number and λ is the wave length. Furthermore, we neglect multiple scattering effects. The kinematical approach is applied in this and all following sections. The scattering vector $\vec{q}$ is defined by

$$\vec{q} = \vec{k_f} - \vec{k_i} = (q_1, q_2, q_3) \tag{4.6}$$

or in terms of the Miller indices H, K and L

$$\vec{q} = H \cdot \vec{a_1^*} + K \cdot \vec{a_2^*} + L \cdot \vec{a_3^*} \tag{4.7}$$

If the scattered radiation is monitored at a fixed position in reciprocal space, the intensity I is proportional to the square modulus of the structure factor $F(q_1, q_2, q_3)$ of the crystal.

The structure factor of the unit cell, $F_u(\vec{q})$, is defined by

$$F_u(\vec{q}) = \sum_{j=1}^{N} f_j(\vec{q}) \cdot e^{2\pi i \vec{q} \cdot \vec{r_j}} \tag{4.8}$$

where $f_j(\vec{q})$ is the atomic scattering factor and $\vec{r_j}$ is the position vector of the atom j in the unit cell. The summation is carried out over all N atoms in the unit cell. For an infinite crystal diffracted intensity is exclusively observed if the scattering vector $\vec{q}$ equals a reciprocal lattice vector or, which is equivalent, if the three Laue conditions

$$\vec{q} \cdot \vec{a_1} = 2\pi H \qquad \vec{q} \cdot \vec{a_2} = 2\pi K \qquad \vec{q} \cdot \vec{a_3} = 2\pi L \tag{4.9}$$

are simultaneously fulfilled. In the case of finite crystals the reflections are broadened by an amount inversely related to the dimension of the diffracting region of the crystal. The intensity I of a finite crystal is given by

$$
\begin{aligned}
I \propto |F(q_1, q_2, q_3)|^2 &= \left| \sum_{j_1=1}^{N_1} \sum_{j_2=1}^{N_2} \sum_{j_3=1}^{N_3} \sum_{j}^{N} f_j(\vec{q}) \cdot e^{2\pi i \vec{q} \cdot (\vec{r_j} + j_1 \vec{a_1} + j_2 \vec{a_2} + j_3 \vec{a_3})} \right|^2 \\[2ex]
&= \underbrace{\left| \sum_{j}^{N} f_j(\vec{q}) \cdot e^{2\pi i \vec{q} \cdot \vec{r_j}} \right|^2}_{|F_u(\vec{q})|^2} \cdot \left| \sum_{j_1=1}^{N_1} \sum_{j_2=1}^{N_2} \sum_{j_3=1}^{N_3} e^{2\pi i \vec{q} \cdot (j_1 \vec{a_1} + j_2 \vec{a_2} + j_3 \vec{a_3})} \right|^2 \\[2ex]
&= |F_u(\vec{q})|^2 \cdot \frac{\sin^2(\frac{1}{2} N_1 q_1 a_1)}{\sin^2(\frac{1}{2} q_1 a_1)} \cdot \frac{\sin^2(\frac{1}{2} N_2 q_2 a_2)}{\sin^2(\frac{1}{2} q_2 a_2)} \cdot \frac{\sin^2(\frac{1}{2} N_3 q_3 a_3)}{\sin^2(\frac{1}{2} q_3 a_3)} \\[2ex]
&= |F_u(\vec{q})|^2 \cdot (N_1 N_2 N_3)^2 \qquad \text{for large values of } N_1, N_2 \text{ and } N_3
\end{aligned}
\tag{4.10}
$$

where N_1, N_2, N_3 are integer numbers describing the number of unit cells in direction of the real space lattice vectors $\vec{a_1}$, $\vec{a_2}$ and $\vec{a_3}$, respectively. If the crystal is infinitely large, i.e. in the limit N_1, N_2 and $N_3 \to \infty$, the according Bragg diffraction peaks are perfect δ functions.

The scattered intensity for a certain reflection depends on the diffraction geometry and on radiation properties. In order to compare the intensity of two reflections, which are located at different positions in reciprocal space, corrections have to be applied. If the crystal is rotated through the reflection condition and I_0 is the integrated intensity of the resulting intensity profile then the corrected intensity I_c is given by

$$I_c = K \cdot G(\theta) \cdot L(\theta) \cdot P(\theta) \cdot A \cdot I_0 \tag{4.11}$$

where θ is the Bragg angle of the reflection, K is a constant, $G(\theta)$ is the geometry correction factor, $L(\theta)$ is the Lorentz correction factor, $P(\theta)$ is the polarization correction factor and A is the absorption correction factor. Correction factors for different diffraction geometries are given in many books about X-ray diffraction [53]. The correction factors for a 6-circle diffractometer, which was also used in the present studies, are given in [61] and summarized in table A.3 of appendix A.3.

4.3 X-ray Diffraction from Surfaces - Crystal Truncation Rods

At the crystal surface ($z = 0$, if the z-direction points along the surface normal) the translation symmetry of the bulk is broken and the electron density is described by a step function (Heaviside function) of the form

$$\rho(z) = \begin{cases} \rho_0 & : & z \leq 0 \\ 0 & : & z > 0. \end{cases} \tag{4.12}$$

which equals ρ_0 within the crystal and which vanishes outside. The structure factor $F(\vec{q})$ is the Fourier transform of the electron density $\rho(\vec{r})$ in the crystal

$$F(\vec{q}) = \int_V \rho(\vec{r}) \mathrm{e}^{-i\vec{q}\cdot\vec{r}} \mathrm{dV} \tag{4.13}$$

where the integration is carried out over the coherently illuminated volume V. The structure factor F of the truncated crystal is the Fourier transform of the electron density step function (4.12) convoluted with the Fourier transform of the infinite crystal. This operation is depicted in figure 4.2. The result are diffuse streaks of intensity of the form

$$I \propto |F(2\pi H/a_1, 2\pi K/a_2, q_3)|^2 \quad = \quad |F_u(\vec{q})|^2 \cdot N_1^2 \cdot N_2^2 \cdot \frac{\sin^2(\frac{1}{2}N_3 q_3 a_3)}{\sin^2(\frac{1}{2}q_3 a_3)} \tag{4.14}$$

$$\underset{N_3 \to \infty}{\longrightarrow} \quad |F_u(\vec{q})|^2 \cdot N_1^2 \cdot N_2^2 \cdot \frac{1}{2\sin^2(\frac{1}{2}q_3 a_3)} \tag{4.15}$$

perpendicular to the surface, the so-called crystal truncation rods (CTR) [49]. These CTRs connect the bulk Bragg reflections and are only existent at positions where the in-plane Miller indices H and K satisfy the selection rule. The intensity near each of the Bragg reflections decays by a factor $\propto \mathrm{q}_z^{-2}$ (the Fourier transform of the step function described by equation 4.12 is $1/\mathrm{q}_z$) along the L-direction and takes a minimum at halfway positions
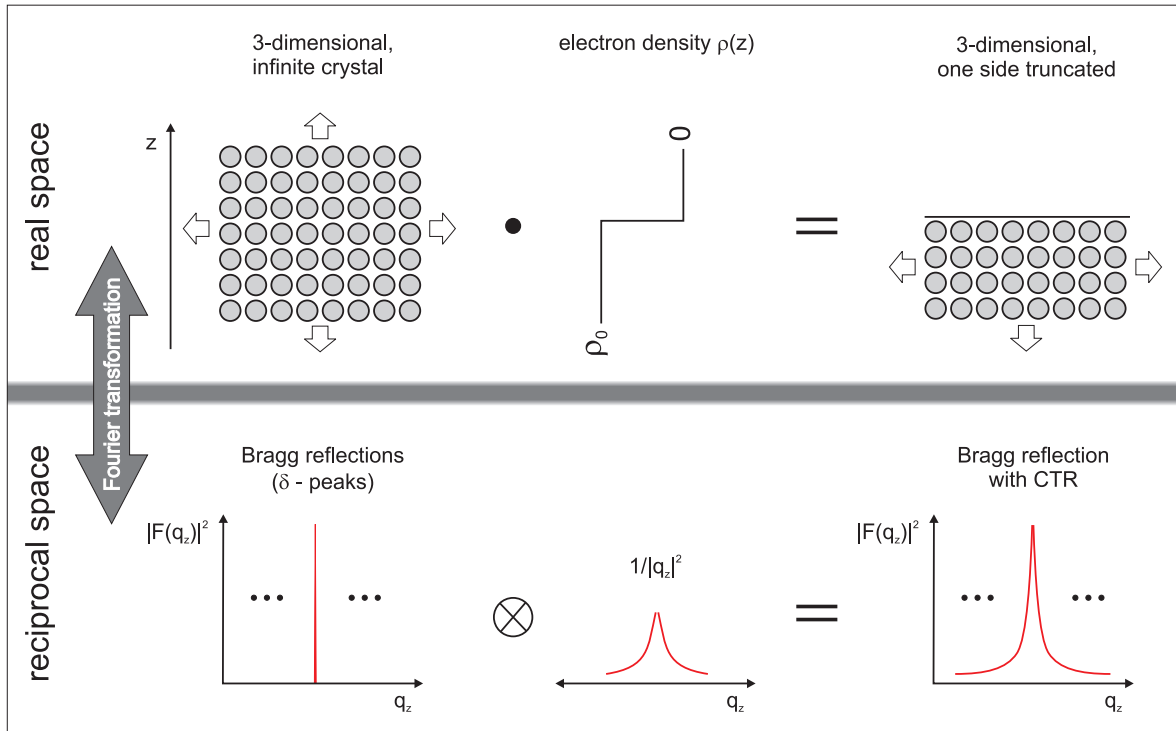
Figure 4.2: Principal explanation for the origin of crystal truncation rods. In real space the one side truncated crystal can be described as multiplication of the infinite crystal structure with an electron density step function $\rho(z)$. In reciprocal space the infinite crystal lattice produces Bragg-reflections with the shape of δ functions. The multiplication operation of the infinite crystal with $\rho(z)$ in real space equates to a convolution of the δ-peaks with the Fourier transform of $\rho(z)$ in reciprocal space ($\propto 1/|q_z|^2$). The result are Bragg-reflections which exhibit extended tails of intensity towards lower and higher q_z. For clarity only one Bragg-reflection is shown.

between two Bragg-peaks which are termed as *anti-Bragg* positions. The intensity between two Bragg peaks varies over several orders of magnitude. Anti-Bragg positions are very sensitive to structural changes at the surface. It is a commonly employed procedure to monitor time-dependent changes in the surface structure or surface morphology by intensity-time transients at anti-Bragg positions. The so-called *specular* CTR has no in-plane component ($H = K = 0$) and thus depends solely on the atomic positions in the direction normal to the surface. In contrast *non-specular* CTRs have an additional dependence on H and K and are therefore sensitive to the atomic arrangement within the surface plane.

The exact intensity distribution between two Bragg reflections is strongly influenced by surface properties and by the surface morphology, e.g. by surface roughness, by relaxation of the first atomic layer, by thermal vibration of atoms, by surface reconstruction or by adsorbate layers. Some characteristic specular CTR intensity curves are shown in figure 4.3 for an ideally terminated Au(100) surface and for relaxated and rough surfaces, respectively. These CTRs were simulated with the Ana-Rod software package of E. Vlieg [62]. The most

striking feature of the reflectivity profile for the relaxed top layer is the asymmetry of the intensity between two Bragg peaks. The asymmetry increases as the order of the Bragg peak increases. Furthermore, the asymmetry increases as the top layer expands and it reverses if the top layer contracts.

In a typical CTR experiment the intensity is monitored by rocking scans at a sufficient amount of positions along a crystal truncation rod. For data analysis each intensity profile is integrated and necessary correction factors are applied. The resulting CTR is then fitted on the basis of real space models for the atomic arrangement at the surface or interface.

4.3.1 X-ray Diffraction from Rough Surfaces

In order to quantify the influence of surface roughness on the diffracted intensity the roughness itself has to be quantified. One of manifold possibilities to do this is the 'β-model' which was first introduced by I.K. Robinson [49]. In this model the occupancy of the first layer (indexed by $n=1$) added on top of the perfectly terminated surface is described by the value β ($0<\beta<1$). Further layers added on top (indexed by $n=2,3,\ldots$) have the occupancy β^n where n is the number of the n-th layer. This definition is not restricted to random distributions of atoms within the layers but it is also applicable to terraced structures. According to Robinson the degree of surface roughness described by the value of β can be expressed as root-mean square roughness σ_{rms}

$$\sigma_{\mathrm{rms}} = \frac{\sqrt{\beta}}{1 - \beta} \cdot d_\perp \tag{4.16}$$

where $d_\perp$ is the lattice spacing perpendicular to the surface [49]. Following this model, the diffracted intensity I from a rough surface is given by

$$I \quad \propto \quad |F(2\pi H/a_1, 2\pi K/a_2, q_3)|^2 \tag{4.17}$$

$$= \quad |F_u(\vec{q})|^2 \cdot N_1^2 N_2^2 \left| \sum_{j=-\infty}^{0} \beta^{-j} e^{iq_3 a_3 j} + \sum_{j=1}^{\infty} \alpha^j e^{iq_3 a_3 j} \right|^2 \tag{4.18}$$

$$\underset{\alpha \to 1}{\longrightarrow} \quad |F_u(\vec{q})|^2 \cdot N_1^2 N_2^2 \frac{1 - \beta^2}{1 + \beta^2 - 2\beta \cos(q_3 a_3)} \cdot \frac{1}{4\sin^2(\frac{1}{2}q_3 a_3)} \tag{4.19}$$

where α is an attenuation parameter ($0<\alpha<1$) which accounts for the finite penetration into the crystal. The truncation rod of a rough surface exhibits a lower intensity than that for a smooth surface (dashed line in figure 4.3), with the biggest proportional difference halfway between the Bragg positions, i.e. in anti-Bragg position. This effect increases with L.

4.3.2 X-ray Diffraction from Reconstructed Surfaces

If the topmost surface layer is reconstructed then the bulk crystal is covered by a 2-dimensional structure described by a separate set of lattice vectors and an electron density which differs from the electron density within the bulk. The situation is the same for a bulk terminated crystal which is covered by an adsorbate layer. The total structure factor is given by the

interference sum of contributions from the surface layer and from the crystal bulk, i.e.

$$F_{sum}(\vec{q}) = F_{\text{surf}}(\vec{q}) + F_{\text{bulk}}(\vec{q}) \tag{4.20}$$

The 2-dimensional, reconstructed surface layer (or adsorbate layer) gives rise to additional crystal truncation rods, also termed as superstructure CTRs. These rods are as well perpendicular to the surface but they show a distinct characteristics compared to bulk CTRs. First no Bragg reflections are observed since the 2-dimensional structure has no periodicity along the L-direction. The electron density in z-direction is approximately described by a delta function resulting in an infinitely broad Fourier transform. Thus, in contrast to the bulk CTRs the intensity is homogeneously distributed along the rods. The amount of diffracted intensity along superstructure rods is only affected by the atomic scattering factor, by surface roughness and by thermal vibrations (Debye-Waller). Second, if the reconstructed surface layer is incommensurable with the bulk structure then the superstructure CTRs are located at separate reciprocal space positions with fractional Miller indices, i.e. they do not overlap with bulk truncation rods.
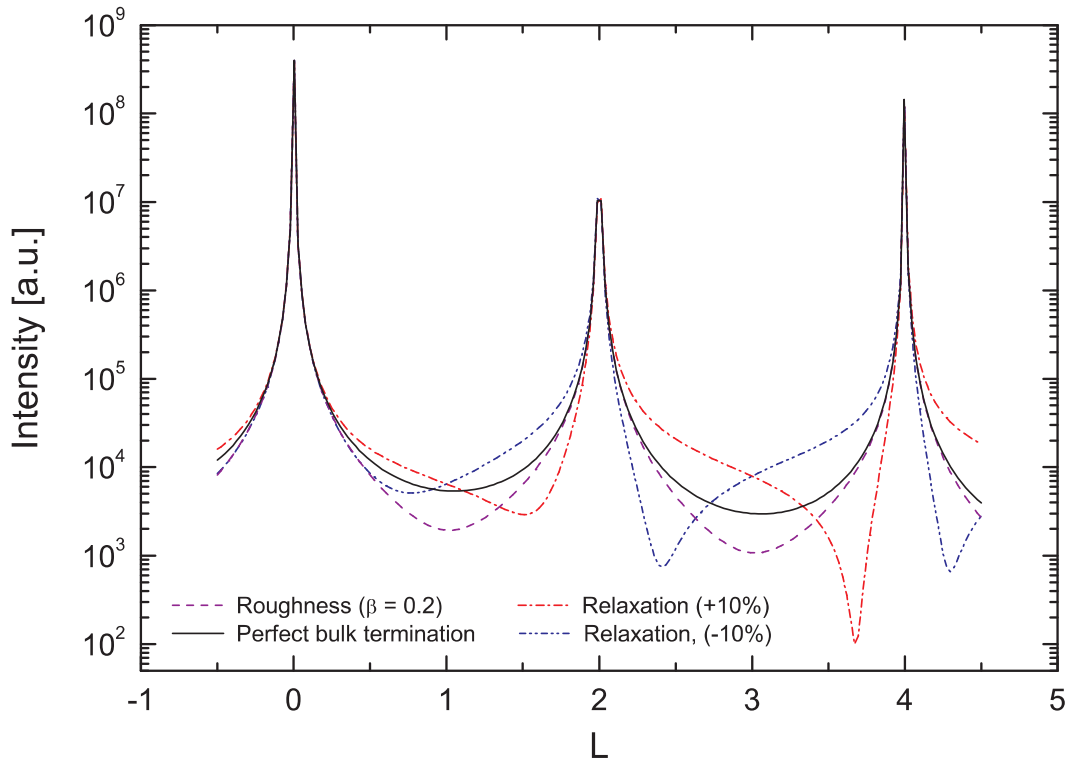
Figure 4.3: Specular crystal truncation rods ($H = K = 0$) for different Au(100) surfaces. The solid curve shows the intensity of a perfectly terminated, flat surface. The two dash dotted curves show the intensity for a relaxation of the top most surface layer by -10% and +10%, respectively. If the surface is rough then the intensity at each position along the CTR (L) is lower than the intensity of the perfectly terminated surface (dashed curve, β-model with $\beta = 0.2$).

4.4 Debye-Waller Factor

Atoms in a crystal lattice are not at definite positions but they are subject to thermal vibrations, i.e. they oscillate about average positions. This atomic motion strongly influences the diffracted intensity, weakening crystalline reflections on the one hand and increasing the amount of diffuse scattering on the other. Moreover the intensity decreases with increasing length of the scattering vector $\vec{q}$. The atomic displacement factor for an atom j can be written as

$$e^{-\frac{1}{(4\pi)^2} \cdot B_j \cdot \vec{q}^2} \tag{4.21}$$

where $B_j = 8\pi^2 < (x_j - \overline{x_j})^2 >$ describes the displacement from the equilibrium position. The Debye-Waller factor in (4.21) considers that the atomic displacement is isotropic, i.e. that B_j is a scalar. In this case the structure factor of the unit cell takes the form

$$F_u(\vec{q}) = \sum_{j=1}^{N} f_j(\vec{q}) \cdot e^{-\frac{1}{(4\pi)^2} \cdot B_j \cdot \vec{q}^2} \cdot e^{2\pi i \vec{q} \cdot \vec{r}_j} \tag{4.22}$$

For further refinements, especially for surface atoms, an anisotropic displacement factor has to be considered where B_j has to be replaced by a tensor.

5 Experimental Techniques

5.1 Beamline ID32 and Diffractometer

The predominant part of the experiments presented in this work has been carried out at beamline ID32 of the European Synchrotron Radiation Facility (ESRF) in Grenoble. This beamline is optimized for surface and interface studies by X-ray diffraction and suitable for our investigations on solid-liquid interfaces. A principle sketch of the beamline is shown in figure 5.1.
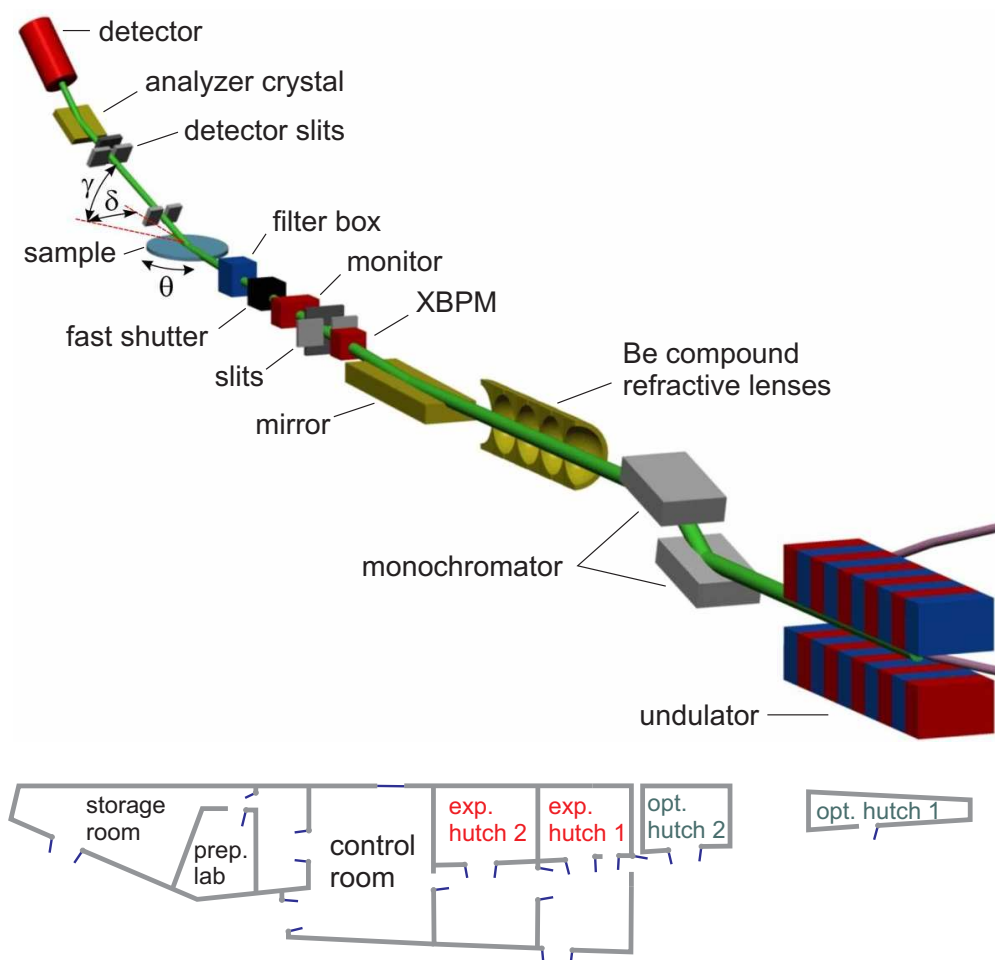
Figure 5.1: Principle sketch of the beamline ID32 at the European Synchrotron Radiation Facility (by courtesy of Dr. Tien-Lin Lee).

The synchrotron radiation, provided by an undulator in the electron storage ring, is monochromized by a pair of Si(111) crystals. Both crystals can be rotated synchronously around a common axis to adjust the photon energy. By tracking simultaneously the gap between both crystals the beam height is kept on a constant level. Subsequently and in dependence of the chosen energy the monochromated beam is focused by an array of up to 16 two-dimensional

beryllium refractive compound lenses (CRL). Higher harmonics of the monochromator are suppressed by an X-ray mirror which is coated with three stripes of different materials (SiO2, Ni and Pd whereas Pd replaced the formerly mounted Ru). For the studies presented here X-ray energies between 18 keV and 22 keV have been used in combination with 16 CRLs and the Pd (Ru) mirror. At an incident angle of 0.1° in reflectivity geometry the Pd (Ru) mirror attenuates radiation with energies > 24 keV (> 22 keV). Due to the thermal load on the optical components the beam position slightly drifts with time. In our early experiments we readjusted the monochromator manually by optimizing the signal on a photo diode. Later on an X-Ray beam positioning monitor (XBPM) had been installed which automatically stabilizes the beam by a feedback loop connected with the monochromator. Appendix A.1 summarizes the characteristics of the X-ray source and provides informations about the X-ray optics at ID32 present at the time when the measurements were carried out.

The monochromized and focused beam enters the experimental hutch (EH 1) and is targeted on a sequentially arranged assembly of a pair of slits, an ionization chamber, a fast shutter and an attenuator, before it impinges on the sample surface. The pair of slits, consisting of a vertical (vg) and a horizontal slit (hg), respectively, defines the cross section of the beam. For our relatively small samples with 4 mm surface diameter we preferentially chose a vertical slit size of 50 μm. Directly behind the slits an ionization chamber monitors the beam
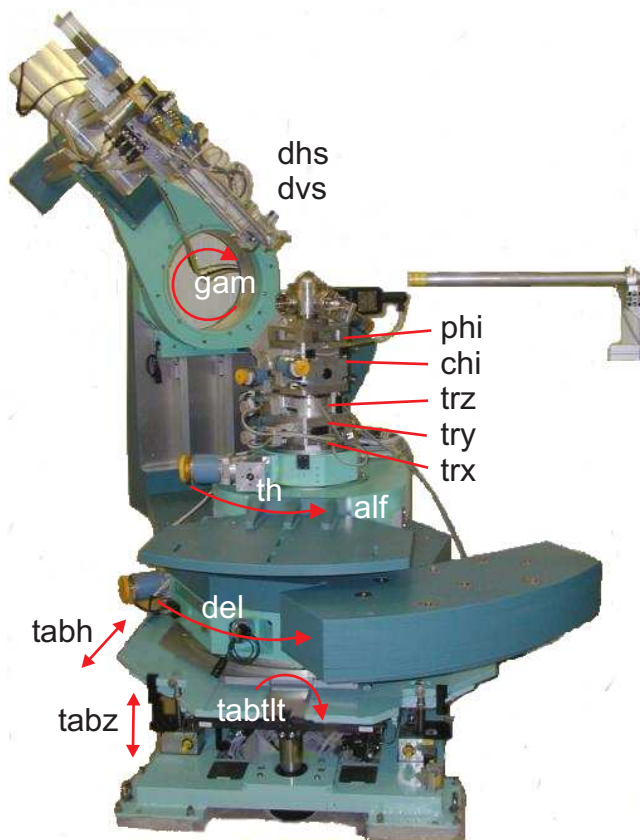
Figure 5.2: Six-circle diffractometer at beamline ID32. The mounted 'Huber tower' allows to position the sample by three translatorial ('trx', 'try' and 'trz') and three rotational motors ('th', 'chi' and 'phi'). The detector position is defined by the motors 'gam' and 'del'.

intensity and allows to normalize the detector intensity to the intensity of the incident beam. In order to avoid beam damage the beam is additionally blocked by a fast shutter when no data are taken, e.g. during motor movement. Especially in electrochemical systems the X-ray beam potentially creates photoelectrons at the sample surface as well as it is able to induce chemical reactions within the electrolyte (radiolytic effects). Since the generation of photo-electrons comes along with a charge transfer through the solid-liquid interface the measured electrochemical current increases by a constant amount during irradiation. Therefore, the fast shutter had to be disabled for some experiments, e.g. when current-time transients were recorded. The intensity of the X-ray beam is reduced by an attenuator system to prevent detector saturation. The system allows to select attenuators manually but also provides the possibility to use automatic filter control. The diffracted intensity is detected by a Cyberstar point detector which is mounted in a distance of approximately 1 m away from the sample. At the detector flight tube end that is faced towards the sample guard slits with a fixed aperture of $1(H) \times 5(V)\,mm^2$ reduce contributions to the background intensity originating from diffuse scattering. The detector resolution is determined by the widths of two slits placed directly in front of the detector. Here aperture sizes between 0.5 mm and 5 mm in horizontal (dhs) and in vertical (dvs) direction are available. An additional graphite analyzer crystal in front of the detector suppresses fluorescence X-rays that might be emitted from the sample.

All surface X-ray experiments have been performed with a computer controlled six-circle diffractometer from Huber and by use of the SPEC[1] control software. The sample has been mounted on a 'Huber tower' with several degrees of freedom for sample positioning. By use of the three motors 'trx', 'try' and 'trz' the sample is translationally positioned in space. Additionally the sample can be rotated about its surface normal by the motor 'theta' or tilted by use of the motors 'phi' and 'chi'. The latter two motors have a hardware limit of ± 15°. The pivots of all turning circles must coincide in one pivot point that lies 170 mm above the center of the mounting plate. For in-plane measurements the whole goniometer can be tilted by the motor 'tabtlt' such that a defined incident angle of the beam is achieved. The detector position is set by two turning circles, called 'delta' and 'gamma', where 'delta' rotates the detector about the surface normal (in-plane) and 'gamma' in direction of the surface normal (out-of-plane). In-plane measurements have been carried out as follows: first the sample was aligned and the motors 'phi' and 'chi' frozen. Then the table has been tilted to set a fixed incident angle of the beam. During data acquisition the only moving motors were 'theta', 'delta' and 'gamma'. For reflectivity measurements 'delta' has been fixed to the center of the primary beam and data has been acquired by synchronous movement of 'gamma' and 'phi' ('chi', respectively) in order to maintain the reflectivity condition. Figure 5.2 shows the diffractometer with all motors.

5.2 The In-Situ Hanging-Meniscus X-ray Transmission Cell

For in-situ SXS measurements in transmission geometry a novel electrochemical cell with electrolyte exchange system has been developed. Although the setup resembles earlier 'hang-

---

[1]UNIX-based software package for instrument control and data acquisition, 'Certified Scientific Software'

ing meniscus' geometries commonly used in single crystal electrochemistry (e.g. [8, 63]) our design offers a much higher flexibility in controlling the electrolyte and has proven to be perfectly suited for electrodeposition experiments. In the following we will first introduce the cell design and later on discuss its appliance in X-ray experiments. The pump exchange system will be explained separately in section 5.3.

The electrochemical cell employed in all transmission SXS experiments within this project is schematically shown in figure 5.3a. A volume of approximately 1 ml electrolyte is hold by chemical inert parts of ™KEL-F[2], ™Teflon and glass. The ™KEL-F parts form two separated compartments. In the upper compartment an electrolyte inlet and a liquid bridge (filled with supporting electrolyte) leading to a Ag/AgCl (3M KCl) reference electrode (RE) are incorporated. To avoid ion contamination the reference electrode is additionally separated from the cell by two micropore glass frits (Microelectrodes Inc.). The lower compartment contains a platinum counter electrode (CE), an electrolyte outlet and a glass capillary ($\varnothing_{inner}$ = 3 mm). RE and CE were incorporated in the inlet and outlet of the cell, respectively, to minimize the uncompensated IR-drop. From the upper cell compartment a thin ™Teflon tube is leading through the lower compartment to the end of the glass capillary serving at the same time as Luggin capillary for the RE.

Between the glass tube and the single crystal a free-standing meniscus (volume $\approx 50\mu l$) of almost cylindrical shape is established by injection of electrolyte. Figure 5.3b shows a closeup view of the meniscus. In order to fill the cell each outlet is connected to a manual three-way valve which, dependent on the valve position, allows to fill the cell by a connected syringe, to remove air from the valve and tube or to close the outlet (e.g. during preparation of the cell). The electrochemical cell and the sample holder are both screwed into an eloxated aluminium housing with ™Kapton window as seen in figure 5.3c. A fine thread for the electrochemical cell allows to adjust the distance between the lower end of the glass capillary and the sample surface, i.e. the height of the meniscus. Distances of up to ≈ 5 mm allow to create a stable meniscus. Due to the small dimensions of our samples (4 mm diameter) the meniscus is extremely stable and the cell can be operated in arbitrary spatial orientations, i.e. in horizontal (ESRF) or even vertical geometry (HASYLAB) on an X-ray diffractometer. In total, experiments have been performed for more than 10 h in this cell without breaking the meniscus and without contamination of the electrolyte solution. The aluminium holder is fixed by two screws to the residual setup and can be easily transfered to the preparation lab where the sample and the electrochemical cell are prepared. For electrochemical measurements it is important to minimize the oxygen concentration within the electrolyte as the oxygen reduction reaction gives rise to rather large unwanted contributions to the electrochemical current. Hence a constant flow of nitrogen gas is used to keep the compartment containing the meniscus oxygen-free. To slow down evaporation of the meniscus, the nitrogen gas is additionally moistened by Milli-Q water before it is fed into the compartment. The oxygen concentration of the electrolyte itself is lowered by degasing with N_2 in the electrolyte reservoirs before it is pulled into the syringe of the exchange system.

---

[2]PCTFE, PolyChloroTriFluoroEthylene
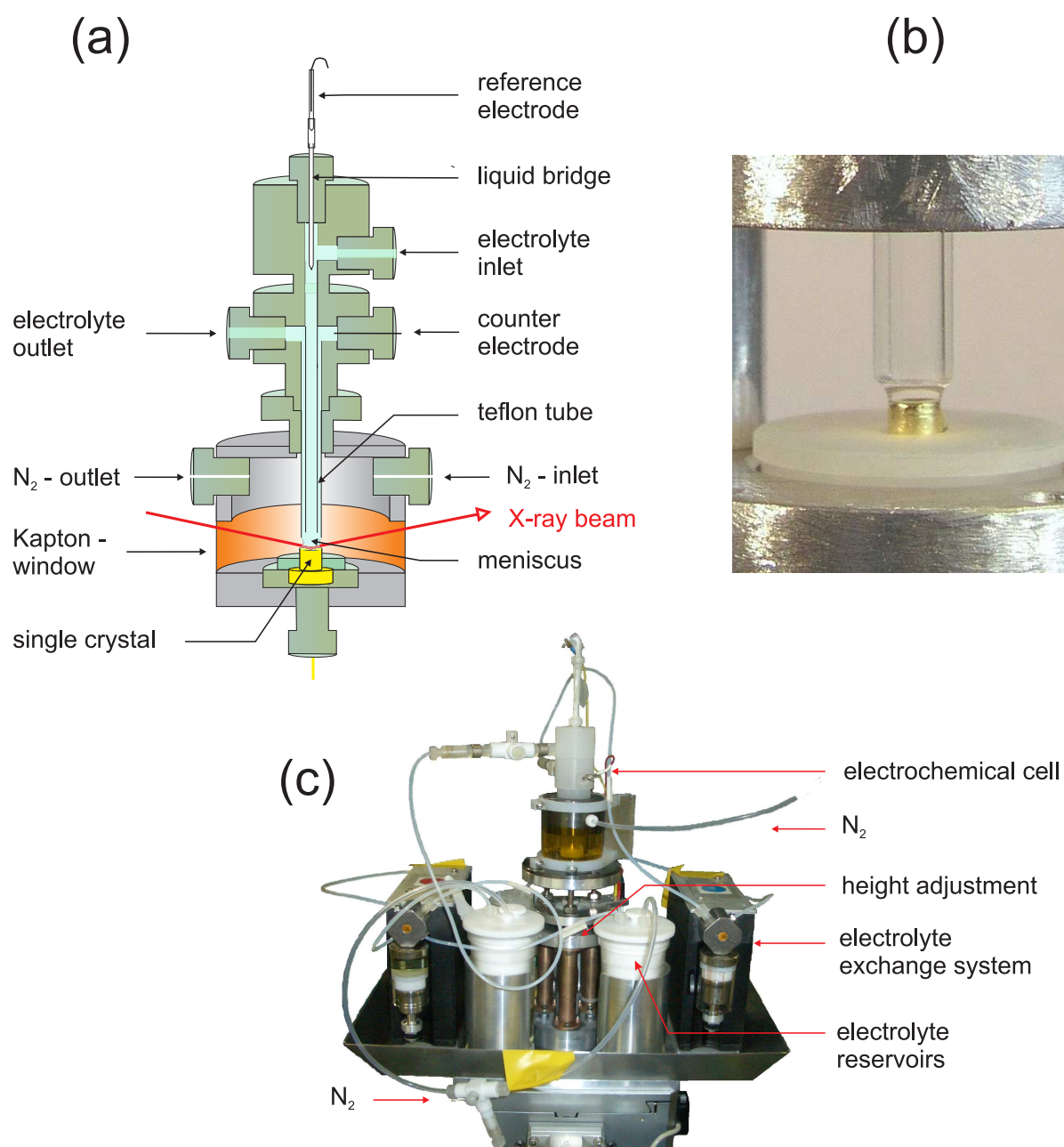
Figure 5.3: (a) Schematic drawing of the electrochemical cell with single crystal working electrode, Ag/AgCl reference electrode and Pt counter electrode. (b) Closeup view of the electrolyte meniscus, established between the glass capillary and the single crystal working electrode. (c) Experimental setup on the X-ray diffractometer containing the electrochemical cell, the electrolyte reservoirs and the electrolyte exchange system.

The resistance of this cell is low as the following estimation shows. We assume that the cell is filled with aqueous 1M HCl solution which has a specific conductivity of $\sigma = 0.3322\,\Omega^{-1}\text{cm}^{-1}$. Together with a sample surface area of $A = 0.125\,\text{cm}^2$ and a distance of $d_{RE} = 0.3\,\text{cm}$ between the sample surface and the lower end of the ™Teflon Luggin capillary the cell resistance R_{cell} is

$$R_{\text{cell}} \approx \frac{d_{\text{RE}}}{\sigma \cdot \pi \cdot (0.5 \cdot d_s)^2} = 7\,\Omega \tag{5.1}$$

During SXS measurements the X-ray beam penetrates the meniscus from the side as symbolized by the red arrow in figure 5.3a. The geometry around the meniscus provides almost 360° access around the surface normal for the incident beam, only restricted by a small post that connects the bottom with the top of the aluminium holder. This 'hanging meniscus' cell geometry has been successfully applied in earlier and up-to-date surface sensitive X-ray studies [12, 64, 65] and is for several reasons perfectly suited for electrodeposition experiments: First, it provides nearly unrestricted mass transport from the solution to the surface and allows to obtain high-quality electrochemical data parallel to the diffraction experiments. Even at high current densities (several mA cm^{-2}) or during gas evolution (e.g. in the hydrogen evolution regime) data has been successfully acquired. In particular the unrestricted mass transport of our cell design is a great advantage over thin-layer X-ray cells. Moreover a slow diffusion of charge into the central region of the electrode surface after potential jumps has been reported for thin-layer cells which is connected with a disturbing time delay of surface processes such as surface phase transitions [66]. This delay does not exist in our cell geometry. Second, electrolyte outlets in both cell compartments allow to exchange the electrolyte homogeneously during the experiment by a remote-controlled pump system. Investigations of the growth behavior are not restricted to stagnant solution but can also be accomplished at a defined constant electrolyte flow through the cell. Third, the X-ray beam passes through the meniscus and is therefore only scattered by the sample and the electrolyte solution avoiding strong, non-uniform contributions to the background from plastic X-ray windows as they are commonly used in thin-layer SXS cells. Moreover, problems caused by beam damage (e.g. cell leakage, contamination of the electrolyte) are avoided because the electrolyte is not in contact with additional window material.

Besides of the crystal structure and the chosen X-ray energy the maximal accessible range in L-direction is determined by the dimensions of the transmission cell and the ± 15° hardware limits of the motors 'phi' and 'chi'. The latter is sufficient to measure all in-plane reflections and allows e.g. recording of the specular Au(111) CTR up to $L = 4$ at photon energies of 20 keV. The transmission cell itself allows incident and exit angles up to about 30°. Important for X-ray investigations at solid-liquid interfaces is the transmittivity of the electrolyte. For a meniscus of a strongly diluted electrolyte with a total diameter of $d = 4\,\text{mm}$ the intensity I after central penetration is given by

$$I = I_0 \cdot e^{-\mu_w \cdot d} \tag{5.2}$$

where I_0 is the intensity of the incident X-ray beam and μ_w the energy dependent absorption coefficient of water. For the used photon energies of 10 keV (HASYLAB), 18.2 keV (ESRF) and 22.5 keV (ESRF) the transmissions are 13%, 70% and 81%, respectively.

5.3 The Electrolyte Exchange System

SXS experiments were performed on gold electrodes in contact with different electrolytes. In order to facilitate an exchange of electrolyte during the SXS measurements, which is for example important to replace Au-free by Au-containing electrolyte, an electrolyte exchange system was constructed on the basis of commercially available syringe pump modules. The electrolyte exchange system consists of two motor-driven syringe pumps (Hamilton, model PSD/3) which are mounted next to the electrochemical cell on the X-ray goniometer. Each pump carries one replaceable set of a syringe and a four-way selector valve with internal parts made from ™KEL-F and glass. Via serial interface both, the position of the syringe as well as the position of the four-way valve can be remotely set by a PC, placed in the control room during the SXS experiments. In- and outlet of the electrochemical cell are connected via ™Teflon tubes with pump 1 and pump 2, respectively. Pump 1 is preferentially used to fill the electrochemical cell while pump 2 is used to remove electrolyte. Additionally each pump is connected via ™Teflon tubes to a common waste bottle and to several electrolyte vessels. All connections, the electrolyte flow and the nitrogen gas flow are schematically shown in figure 5.4. The fluid delivery speed of the pumps ranges from 0.5 to 3600 seconds per full stroke. Hence using a 12.5 ml syringe (like in the present work) the minimum flow rate of electrolyte is limited to $3.5\,\mu$l per second. In principal the flow rate can be further lowered by
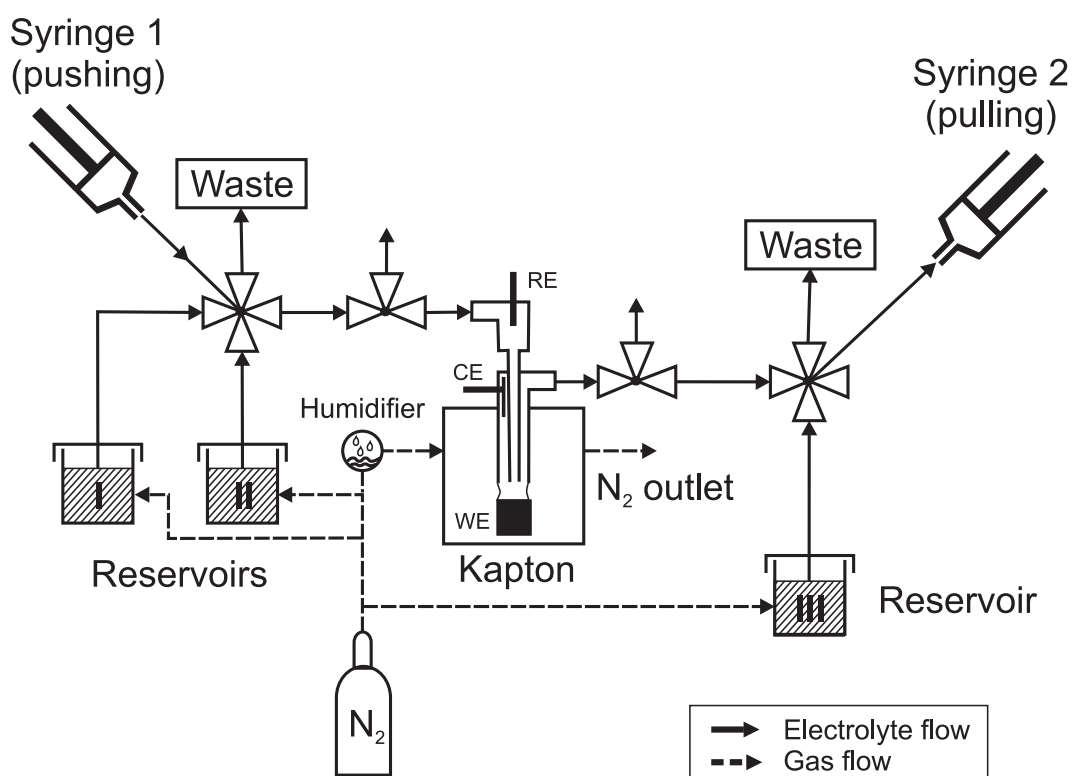
Figure 5.4: Diagram of electrolyte flow and gas flow through the electrochemical X-ray transmission cell and the electrolyte reservoirs.

the use of smaller syringes but only on the cost of electrolyte capacity. The resolution of the pumps depends on the amount of steps of the stepper motor and constitutes maximal 30000 increments per full stroke, i.e. about 8 steps per second at the lowest flow rate. Thus the system allows a quasi-continuous exchange of the electrolyte in the electrochemical cell. In order to operate the pumps a LabVIEW based software has been developed. This software allows to drive each pump separately to add or remove electrolyte in the cell or to drive both pumps synchronously to replace the solution in the cell with the electrolyte solution in reservoir I and II, respectively. Reservoir III is needed to remove air from the ™Teflon tube which connects the cell outlet with pump 2. It furthermore allows to facilitate a back and forth exchange. The maximum flow rate of the setup is restricted by the cell design, i.e. by the stability of the meniscus. We tested flow rates of up to $100\,\mu l\,s^{-1}$ in 0.1 M HCl solution and found no significant influence on the shape of the meniscus. In addition to a complete electrolyte exchange, the pump system is used to adjust the size of the meniscus with μl precision, which is necessary to compensate the loss of solution due to evaporation. The construction of the cell (both cell compartments are connected to each other solely by the electrolyte in the meniscus) ensures that the injected electrolyte is transported directly into the meniscus close to the surface, i.e. that the electrolyte is rapidly replaced. Our experiments demonstrate that this setup allows long term measurements, including several electrolyte exchanges, without contamination of the electrolyte by the electrolyte exchange system.

5.4 Electrochemical Setup

For electrochemical measurements we employed a common three electrode configuration consisting of a single crystal working electrode, a platinum counter electrode and a Ag/AgCl reference electrode. The RE is ideal non-polarizable and has a fixed galvani potential at low current density. In order to achieve low current density the RE is connected via high input impedance so that the main current flows through the CE. To prevent characteristic electrode reactions at the CE its dimensions ($A \approx 100\,\mathrm{mm^2}$) have been chosen to be about eight times larger than the sample surface ($\approx 12.5\,\mathrm{mm^2}$).

The electrochemical cell has been operated as galvanic cell by use of a remote controlled potentiostat that was placed within the experimental hutch. In early studies we applied an analog potentiostat from BAS (Voltammograph CV-27) in combination with an I/O interface from National Instruments (NI DAQPad-6015). This instrument has been replaced by a digital potentiostat from Iviumstat in more recent studies. Both setups allow full potential control of the sample from a PC within the control room and to obtain high quality electrochemical data, such as cyclic voltammograms and current transients, parallel to the X-ray experiments. In contrast to the BAS potentiostat the Iviumstat handles by default potentiostatic as well as galvanostatic control of the sample (figure 5.5b). When the cell is controlled potentiostatically the potential between the WE and the RE is kept constant by an operational amplifier and the current response of the system is recorded. Under galvanostatic control the current through the WE is kept constant by use of an additional resistor and changes of the potential are recorded.
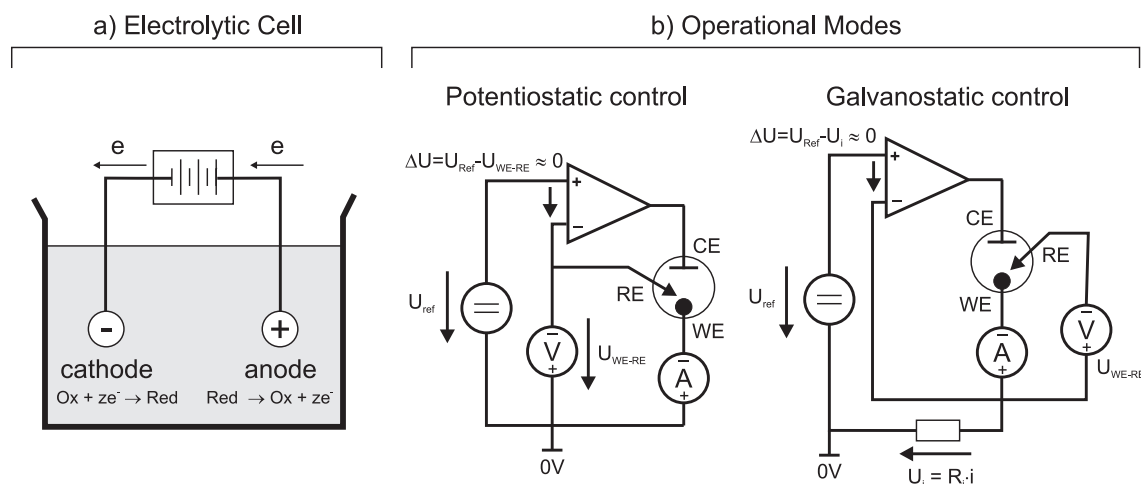
Figure 5.5: a) Electrolytic Cell b) Simplified electronic circuits to realize potentiostatic control and galvanostatic control of the electrochemical cell.

Alternative to the potentiostat software, the electrode potential can be directly controlled by the diffractometer software SPEC via analog voltage signal (pseudo motor 'Pot'). This is especially useful to perform potential jump experiments in combination with SXS experiments where the electrochemical experiment is triggered by the diffractometer software. Furthermore it is possible to utilize analog input channels at the potentiostats to record direct voltage signals from the X-ray detector rate meter and from the monitor. In doing so the time-resolution of the X-ray experiments could be significantly improved (subsecond time-resolution).

5.5 Surface Preparation of Gold Single Crystal Electrodes

All Au(100) and Au(111) single crystals were purchased from Mateck with a specified roughness smaller than $0.03\,\mu$m, a miscut smaller than $0.1°$ and a purity of 99.999%. The crystals are hat-shaped with a total height of 6 mm, a brim of 2 mm and a surface diameter of 4 mm. We employed different surface preparation techniques dependent on the surface quality.

5.5.1 Surface Preparation of New Samples

Following a commonly employed procedure, newly received crystals were heated in an oven for at least 24 hours at 850 °C to recrystallize the surface. Subsequently the surface was flame annealed or if necessary electropolished in a further step. This method produced satisfactory surfaces with a mosaic spread of $< 0.2°$ as determined by X-ray reflectivity measurements. More recently ordered samples have been sputtered with Argon in a vacuum chamber (10^{-4} mbar). Figure 5.6 shows a series of detector rocking scans in reflectivity geometry recorded at an incident angle of $1°$ after several sputter and annealing cycles of a new Au(111) single crystal (12 mm surface diameter). The first intensity profile (figure 5.6a) was taken after 5 min immersion in Caro acid, followed by two sputter and annealing (630 °C)
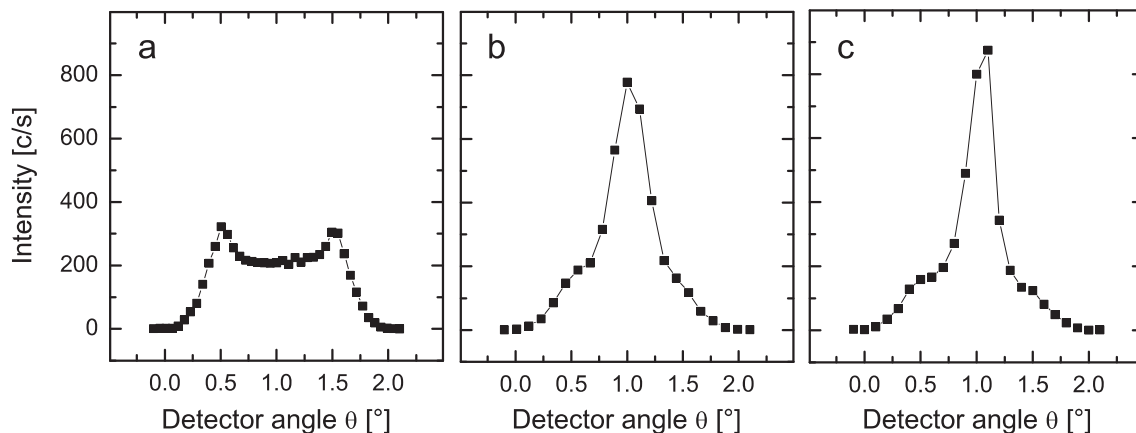
Figure 5.6: Detector rocking scans of a Au(111) single crystal (12 mm surface diameter) recorded at an incident angle of 1° in reflectivity geometry after several Argon sputtering and annealing cycles performed within a vacuum chamber (10^{-4} mbar). a) Surface condition of the freshly delivered sample after 5 min in Caro acid, 15 min annealing at 630 °C, 15 min sputtering at 8 μA/1000 V, 15 min annealing at 630°, 30 min sputtering at 8 μA/1000 V and final 30 min annealing at 670 °C. b) Same sample after 8 additional cycles of sputtering and annealing, each with 15-20 min annealing at 750 °C and 20 min sputtering at 10 μA/1000 V. c) Sample after 7 additional sputtering and annealing cycles, each with 15 min annealing at 800 °C and 15-20 min sputtering at 10 μA/1000 V.

cycles and a final annealing for 30 min at 670 °C. Two pronounced Yoneda wings indicate a large contribution of diffuse scattering to the intensity while no specular peak is observed. Initial surface roughness is typical for new samples and probably related to industrial surface finish processes. A second characterization of the same sample has been carried out after 8 more sputter and annealing (750 °C) cycles. The obtained intensity profile (figure 5.6b) shows a specular peak with a FWHM of ≈ 0.4° and reduced diffuse scattering. Further sputter and annealing cycles at an elevated temperature of 800 °C resulted in a more intense specular peak with a lower FWHM of ≈ 0.3° (figure 5.6c).

5.5.2 Surface Preparation by Flame Annealing

Before each experiment the samples were rinsed with Milli-Q water and flame annealed in a butane gas flame for approximately 5 to 10 minutes at light yellow glow (approx. 800 °C). This procedure was originally developed for the preparation of platinum and it is known to remove surface adsorbates and to flatten the surface on atomic scale by the high mobility of surface adatoms at elevated temperatures [67]. A subsequent characterization by X-ray reflectivity at small incident angles showed, that surfaces prepared in this manner exhibit at least 800×800 Å^2 wide terraces. The mosaic spread was < 0.2°. After the crystals reasonably cooled down in air (2-3 minutes) they were immediately transfered into the electrochemical cell. In order to protect the surface from contaminations contact between the electrolyte

and the surface has been established as quick as possible. The cell was afterwards moved from the preparation lab to the hutch, mounted on the goniometer and connected to the N_2 gas system, to the potentiostat as well as to the electrolyte exchange system. Prior to the X-ray experiments a first electrochemical characterization was done by cyclic voltammetry to assure the cleanness of the system. As indicator for the latter the characteristics of the reconstruction peak and of the chloride order-/disorder peaks were used. During X-ray alignment and at times when no data was acquired the samples in Au-free electrolyte were preferentially kept at holding potentials in the reconstructed potential regime (-0.2 V vs. Ag/AgCl). This allows the surface to establish a well reconstructed surface phase which was the objective of subsequent investigations. In Au-containing solution the Au(100) sample was preferentially kept at a holding potential of ≈ 0.6 V where the growth proceeds via step-flow mode so that the surface remains sufficiently smooth over longer time periods (see chapter 9).

5.5.3 Surface Preparation by Electropolishing and Mechanical Polishing

After several deposition experiments the electrode surface became optically rough and showed a decrease in X-ray intensity of in-plane reflections as well as along the crystal truncation rods. In these cases the single crystals were electropolished in a solution containing ethylene glycol, ethanol and hydrochloric acid (33%) at the ratio of 2.5 : 1.5 : 1. As counter electrode we used a sheet of platinum with a surface area of $\approx 6 \, cm^2$. The temperature of the solution was kept at 60 °C. Several polishing cycles were performed for about 10 to 20 seconds each at currents of about 1.8 A to 2.2 A. While immersing the crystal in the polishing solution it was steadily moved along its surface normal with the surface faced towards the platinum electrode. After each polishing cycle the surface was thoroughly rinsed with Milli-Q water and occasionally checked by an optical microscope. This method usually provided good results if the crystal was of good quality before the deposition experiments. In the case of Au(111) very good surfaces could be obtained by applying extremely high currents in the range of 7 A to 8 A for comparatively short times of about 5 seconds. If electropolishing could not improve the surface quality to a sufficient extent mechanical polishing by hand was applied. Starting by sand paper with a grain size of 30 μm (grit size 800) the surface was successively polished down. The procedure with sand paper ended with a grain size of 6.5 μm (grit size 4000). Afterwards polishing cloth in combination with aluminum dispersions ranging from 5 μm down to 0.03 μm were used. To remove remaining aluminum particles the surface was shortly electropolished in a final step. In total this procedure removed some μm up to several 100 μm.

5.6 Preparation of Electrolytes

All electrolytes were prepared from ultrapure chemicals and ultrapure water (Milli-Q, 18.2 MΩ, impurities 8 ppb). Gold-containing electrolytes were mixed from a $HAuCl_4$+aq. solution (Chempur, 40% gold). Supporting electrolytes were prepared from ultrapure HCl (Merck Ultrapur, 30%) and ultrapure H_2SO_4 (Merck Ultrapure, 96%). Nitrogen gas, to purge the cell and the electrolyte, was from Air Liquide with a specified purity of 99.9995% (N 5.5).

5.7 Cleaning of Electrochemical Cell and Glassware

All parts of the setup which were in direct contact with the electrolyte had been immersed to Caro acid (mixture of H_2SO_4 and H_2O_2 at the ratio of $3:1$) for at least two days. Afterwards the glassware, i.e. the electrolyte reservoirs, beakers and flasks were cooked in Milli-Q water for several times. To avoid deformations of the materials and to remove the Caro acid, ™KEL-F and ™Teflon parts, such as the electrochemical cell, were put within a beaker (filled with Milli-Q water) for several times at low temperatures ($60\,°C$) in an ultrasonic bath. Syringes, valves and ™Teflon tubes were several times flushed with Caro acid and subsequently flushed with Milli-Q water. Gold amounts on the counter electrode which became apparent after long deposition experiments were stripped electrochemically. Afterwards the CE was first flame-annealed and then immersed in Caro-Acid.

6 Surface Structure of Gold Single Crystal Electrodes

The low index surfaces of gold single crystals exhibit interesting properties which predestine them as substrate for a huge variety of experiments. Besides of excellent chemical stability all low index gold surfaces reconstruct at sufficiently elevated temperatures in UHV or at appropriate potentials in solution. In the following we will first discuss the general phenomenon of surface reconstruction. Then we will focus on the reconstructed phase of Au(100) in UHV and in electrochemical environment, in particular on the very complex atomic mechanisms during the surface phase transition. Experiments on Au(111) electrodes have been mainly carried out in the unreconstructed potential regime and the surface structure will be briefly discussed in chapter 11.

6.1 Surface Reconstruction

Preeminent characteristics of surfaces is the abrupt discontinuity of the crystal translation symmetry. Atoms which reside within the topmost surface layer exhibit forces which are significantly different to those acting on atoms within the crystal bulk. This is most evident under ultra high vacuum (UHV) conditions where the coordination number of surface atoms is simply decreased. In many cases this anisotropy induces a lateral rearrangement of atoms such that a new surface phase with lower free energy is created, a process termed as *surface reconstruction*.

Surface reconstruction has been observed at many interfaces between solids and UHV. In particular, the low index surfaces of the 5d metals platinum and gold [68] are known to exhibit a pronounced reconstruction. Thus, specifically for these systems detailed information about the structure and stability of the reconstructed surface phase have been obtained by various instrumental methods. Additional systematic studies revealed that very small amounts of surface adsorbates can cause a phase transition between the reconstructed and unreconstructed phase [69, 70] showing likewise that the energy difference between the two phases is small. This effect, also called 'lifting' of the reconstruction, is induced by different adsorption enthalpies on the unreconstructed and on the reconstructed surface, respectively. For the same reason, the existence of surface reconstruction in electrochemical environment was for a long time subject of controversial discussions. The presence of adsorbed ions or solvent molecules in the electrochemical double layer was initially thought to prevent surface reconstruction [71]. However, on the basis of ex-situ methods Kolb et al. could prove the existence of surface reconstruction on gold electrodes in contact with electrolyte [13, 72–75]. At electrode potentials where no specific adsorption of anions takes place the reconstructed phase was found to be stable. Furthermore Kolb could show that the transition between reconstructed and unreconstructed surface can be reversibly controlled by the applied electrode potential [73, 76]. A stable reconstructed surface at more negative potentials than a critical potential lifts towards more positive potentials and it is reformed by the opposite potential sweep direction. Interestingly, nowadays a couple of theoretical studies predict that the lifting of the reconstructed Au(100) surface at positive potentials might be solely induced by surface charges without the need of a chemically adsorbed species [77–79].

In the last quarter of the previous century new structure sensitive methods have been developed which provide powerful tools to investigate solid-liquid interfaces in-situ. Surface sensitive X-ray scattering (SXS) [80,81] and scanning tunneling microscopy (STM) [82–88] confirmed earlier ex-situ results and could furthermore help to partly clarify the atomic mechanisms during the phase transition [89,90]. Besides of experimental studies also various theoretical works deal with the reconstruction phenomenon. Calculations based on density functional theory (DFT), embedded atom method (EAM) and molecular dynamical (MD) simulations were performed to model reconstruction and to shed light on the underlying mechanisms in agreement with experimental results [91–93].

6.2 Surface Structure of Au(100) in UHV

Early UHV studies in the late 60s of the last century show that clean Au(100) surfaces, which usually should exhibit a (1×1) structure according to crystal truncation, are hexagonally reconstructed after proper sample preparation by thermal annealing [69,94]. In order to induce an irreversible transition from the metastable, unreconstructed surface phase to the reconstructed phase, a temperature of about 100 °C is needed as measured by low energy electron diffraction (LEED) [95]. The hexagonal arrangement is the closed-packed form of the surface with lower energy compared to the more open (1×1) structure. This results in an excess of $\approx 25\%$ gold atoms in the reconstructed phase. Since atoms in the reconstructed topmost layer reside at different places over the underlying unreconstructed crystal lattice the surface becomes corrugated. Along the crystals $[110]_c$-direction a corrugation periodicity with a period of approximately 14.5 Å has been found. However, in the perpendicular $[\bar{1}10]_c$-direction the height modulation extends over a longer range, giving rise to a rather large unit cell [69,80]. Historically, a surface unit cell of (5×20) has been inferred from early LEED investigations [96]. Today, various structure-sensitive techniques report the existence of many larger and incommensurate (5×M) unit cells so that the reconstruction is more generally described as 'hex' reconstruction. However, often the (5×20) structure is considered as an *average* structure. In this context it is interesting to mention that theoretical simulations of different (5×M) configurations revealed very close surface energies for the range $20 < M < 35$ with an energy difference of merely 0.1 meV/Å^2 [97,98]. Indeed, UHV-TEM studies of Dunn et al. indicate that for less defective Au(100) surfaces the extension of the unit cell in 'x20' direction is not fixed, but varies from domain to domain and even within domains [99]. This effect has been explained by local accomodations to strains. According to high resolution electron microscopy and ion channeling data a substantial buckle along the 'x5' direction would lead to a significant bulk strain field. This strain field acts differently on centers and edges of large domains. These kind of fluctuations were also found in other studies [5]. Structural variations within 'hex' domains would explain why bulk crystal truncation rods were found to be sensitive to the reconstructed layer (see chapter 9) even though the 'hex' layer is incommensurable.

An average relative height difference of atoms within the reconstructed phase has been inferred from He scattering and from X-ray scattering and led to values of 0.5 Å and 0.56 Å, respectively [100,101]. Theoretical works of Ercolessi, Parinello and Tosatti confirm this
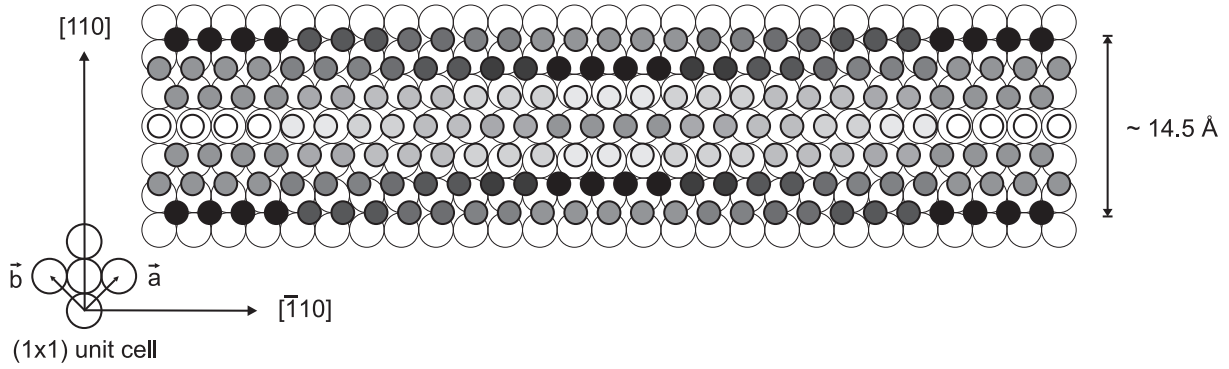
Figure 6.1: Model of the reconstructed phase of Au(100). The modulation of the reconstructed surface (small circles) on top of the unreconstructed surface (large circles) is depicted by different shades of gray. The lighter the shade the higher is the position of the atom. (according to Behm et al.).

average corrugation height and furthermore predict a displacement maximum of 0.8 Å for atoms on on-top positions (which is close to 0.84 Å in a hard sphere model) [102]. The dimensions of the unit cell have been determined as $a = (2.763 \pm 0.002)$ Å, $b = (2.766 \pm 0.005)$ Å and $\gamma = (120.03 \pm 0.1)°$. Comparing this size with the nearest-neighbor distance of 2.885 Å within the (111) plane of the bulk, the atomic distances are compressed by 4.2% in direction of $\vec{a}$ and 4.3% in direction of $\vec{b}$. The compression can be expressed as an area contraction related to the unreconstructed bulk structure, the so-called surface strain ϵ:

$$\epsilon = \frac{A_{rec} - A_{1\times1}}{A_{1\times1}} = \frac{2.763\,\text{Å} \cdot 2.766\,\text{Å} \cdot \sin 60° - (2.885\,\text{Å})^2}{(2.885\,\text{Å})^2} = -20.48\% \qquad (6.1)$$

where A_{rec} denotes the area per atom in the reconstructed surface phase and $A_{1\times1}$ the area per atom in the underlying bulk phase. Applying the same formalism on the atom fractions per unit area, i.e. $\sigma_{rec} = 1/A_{rec}$ and $\sigma_{1\times1} = 1/A_{1\times1}$, then the excess mass density $\Delta\sigma$ in the reconstructed phase

$$\Delta\sigma = \frac{\sigma_{rec} - \sigma_{1x1}}{\sigma_{1x1}} = 25.76\% \qquad (6.2)$$

is obtained. As neighboring gold atoms are aligned within rows along $[\bar{1}10]_c$ the observed periodicity of 14.5 Å in perpendicular direction corresponds to a width of about 6 atomic rows on top of 5 densely packed atom positions of the unreconstructed, squared lattice. This structure can be easily seen in STM images even without atomic resolution by means of 14.5 Å wide 'reconstruction stripes'. To simplify matters the direction along the rows shall be denoted by 'x20' and the perpendicular direction by 'x5'.

Determined by the fourfold symmetry of the squared Au(100) substrate, the hexagonal reconstructed surface layer consists of domains which are oriented 90° in respect to each other. The atomic rows within these domains are either parallel aligned to one of the close-packed $\langle 110 \rangle$ directions of the underlying lattice or rotated by $\pm 0.8°$ [103]. On well prepared surfaces

wide domains of sizes up to several $1000\,\text{Å}^2$ exist. Figure 6.1 shows a structure model of the unrotated, reconstructed surface on top of the unreconstructed phase. For simplification only a section of the complete unit cell is shown.

Island/Substrate	$\Delta E_{Surface}$ (meV/Å^2)
(1×1) / (5×28)	8.01
(5×28) / (1×1)	1.35
(5×28) / (5×28)	3.99

Table 6.1: The change in surface energy ($\Delta E_{Surface}$) for three prototype island structures on Au(100) calculated by MD simulations [104].

Some experiments (e.g. performed by He diffraction, positive ion channeling spectroscopy (PICS), SXS and STM) let conclude that only the topmost layer of Au(100) reconstructs, the underlying atomic substrate layers are assumed to be rigid and to remain in the unreconstructed bulk structure [64, 69, 105]. These observations get strong support from MD simulations in which the change in surface energy, $\Delta E_{\text{Surface}}$, has been calculated for a single (5×28) reconstructed island either on top of an unreconstructed (1×1) structure or on top of a reconstructed (5×28) structure. A reconstructed island on an unreconstructed layer was found to stand for the most favorable configuration in energy [104]. Nomura et al. furthermore calculated the change in surface energy for an unreconstructed island on top of a (5×28) reconstructed layer and found an even higher change in $\Delta E_{\text{Surface}}$ due to the presence of the island. The calculated energies are summarized in table 6.1. The same study provides a reasonable explanation for the transformation from the (5×28) reconstructed phase to the unreconstructed (1×1) phase underneath Au islands based on a release of the stress associated with the contracted reconstructed surface. It is believed that corrugated rows pop up as the edge of the island being afterwards incorporated into the island. A top-layer expansion of 20% was determined by SXS studies [101, 106].

6.3 Surface Structure of Au(100) in Solution

Under electrochemical conditions the reconstruction was basically found to resemble the UHV structure depicted in figure 6.1. The periodicity in 'x5' direction and the maximum corrugation height were inferred as $14.5 \pm 0.5\,\text{Å}$ by STM [89] and $0.5\,\text{Å}$ by SXS [80], respectively. Furthermore the existence of $\pm 0.8°$ rotated domains could be confirmed [80]. Figure 6.3a shows a cyclic voltammogram of Au(100) in $0.1\,\text{M}$ HCl which was recorded on the X-ray goniometer prior to the present X-ray experiments. This CV is in agreement with the literature [73]. The peak at $\approx 0\,\text{V}$ in the anodic sweep is related to the lifting of the reconstruction. This potential is usually called the critical potential. At potentials more negative than the critical potential the surface is reconstructed, at potentials more positive than the critical potential the surface is unreconstructed. STM images of both phases are shown in figure 6.3a. Additionally two sharp current peaks at $\approx 0.6\,\text{V}$ appear which are related to an ordering/disordering phase transition of a chloride adlayer. Recent STM investigations reported the ordered chloride adlayer, which is present at electrode potentials $> 0.6\,\text{V}$, to be an uniaxially, incommensurate $c(\sqrt{2} \times p)R45°$ structure with p ranging between 2.3 to 2.5

dependent on the electrode potential [107]. The characteristics of Au(100) in Au-containing solution will be discussed in section 6.5.

Detailed STM studies in $0.1\,\text{M}$ H_2SO_4 demonstrated that the quality of the reconstructed phase strongly depends on the preparation procedure [89, 108, 109]. Thoroughly annealed surfaces which were immersed in electrolyte under potential control negative of the critical potential exhibited terraces with wide, well ordered reconstructed domains. In addition, no monoatomar islands have been seen. Insufficient annealing on the other hand had a strong negative influence on the ordering and coverage of the reconstruction. Especially, unreconstructed regions emerged within the reconstructed surface coming along with a high density of domain boundaries. A similar negative effect on the surface quality of the reconstructed phase has been observed when contact between the annealed electrode and the electrolyte has been established without potential control, i.e. at OCP. After a subsequent change into the reconstructed potential regime many monoatomar reconstructed islands appeared which destroyed the long range order of the reconstructed phase [82, 110]. Additionally, the density of holes and smaller embedded unreconstructed regions is increased. The exactly same topography occurs when an originally well ordered reconstruction exists at potentials negative of the critical potential and the potential is once cycled into the unreconstructed regime and back. With further amount of cycles the quality of the reconstructed phase continuously degrades but approaches a limit value [111]. The origin of the degradation is strongly related to the growth mechanism of the reconstructed phase which will be explained in the next section. A comprehensive review article about surface reconstruction at metal-electrolyte interfaces, including all low index gold surfaces, has been published by D.M. Kolb [112].

6.4 Kinetics of the Au(100) Surface Phase Transition

The kinetics of the (1×1)↔'hex' phase transition is very complex and involves substantial mass transport of gold atoms. Both reconstruction lifting and potential-induced formation of the reconstructed phase of Au(100) electrodes in aqueous solutions has been studied in detail by various experimental techniques. In particular Video-STM studies provided a deep insight in the atomic mechanisms [90, 113]. We will summarize previous results briefly.

6.4.1 Lifting of Reconstruction

Lifting of the reconstruction, i.e. the 'hex'→ (1×1) transition, has been extensively studied by in-situ STM and SXS at Au(100) electrodes in aqueous H_2SO_4 solution [89, 108], in aqueous $HClO_4$ solution [82, 110, 114] and in halide containing solutions [80, 115]. The phase transition proceeds via nucleation of the unreconstructed phase at domain boundaries along the 'x5' direction (either within terraces or at step edges) and subsequent quasi-one-dimensional growth of the unreconstructed phase along the 'x20' direction. Often the growth advances in blocks covering up to 10 reconstruction stripes. According to this, initially highly patterned surfaces with many small reconstructed domains lift faster and more homogeneously than those consisting of wide domains with long extension in the 'x20' direction. The growth rates along 'x20' are strongly potential-dependent and have been found to range from some $100\,\text{Å}$
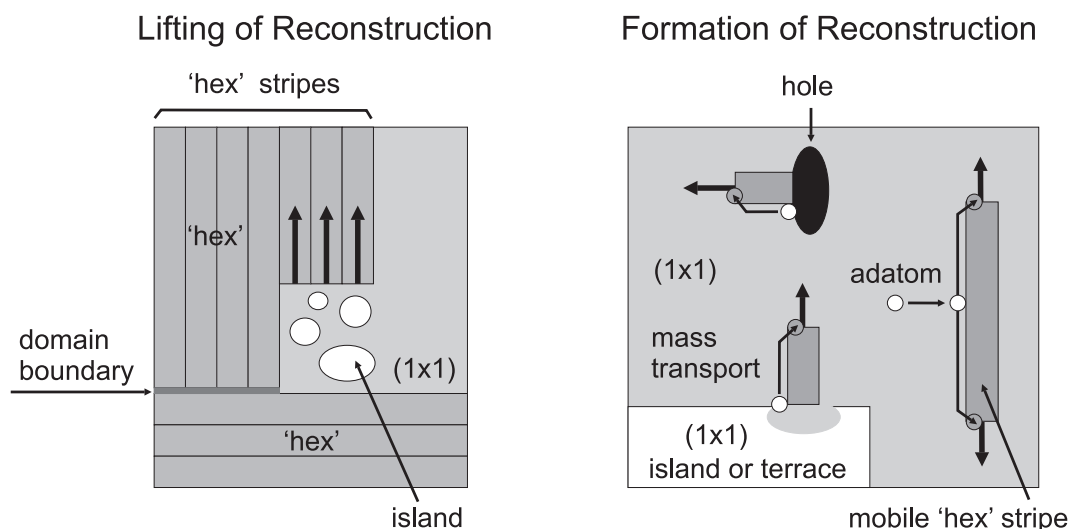
Figure 6.2: Schematic illustration of the atomic mechanisms involved in the formation and lifting process of the reconstructed Au(100) surface. The light and dark gray areas represent unreconstructed and reconstructed surface areas, respectively, within the same surface layer. White areas depict unreconstructed islands and atoms on top.

per minute at lower positive overpotentials to some $1000\,\text{Å}$ per minute at higher positive overpotentials with respect to the critical potential. These rates correspond to reconstruction lifting times ranging from some minutes to some milli-seconds. Thus, reconstruction lifting is generally a very fast process. Near the critical potential the nucleation was found to be heterogeneous and the propagation velocity along 'x20' to be constant. At higher positive potentials STM images gave hints for the existence of instantaneous, homogeneous nucleation. At the progressive front of (1×1) growth the excess atoms leave the reconstructed phase and form small unreconstructed islands which subsequently merge by Ostwald ripening. Reformation of islands involves substantial surface mass transport of gold atoms between the islands. As the transport affects only unreconstructed areas it does obviously not influence the speed of the phase transition. After the lifting process is completed the surface coverage by islands equals 25%, i.e. it accords to the excess of gold atoms in the former reconstructed layer. A model of the described mechanism is depicted in figure 6.2.

6.4.2 Formation of Reconstruction

The formation of the reconstructed phase, i.e. the (1×1)→'hex' transition, proceeds similar to the lifting process by nucleation at step edges and subsequent quasi-one-dimensional growth of single, 5 atomic rows broad reconstruction stripes along their 'x20' direction. With respect to the underlying (1×1) layer the stripes are aligned with one of the close-packed ⟨110⟩ directions, i.e. conform to the orientation of reconstruction domains. In contrast to the reconstruction lifting, now an additional amount of 25 % gold atoms has to be incorporated into the surface. By video-STM investigations [90, 113] three sources for these atoms have

been identified: islands, single diffusing adatoms and atoms at the rim of surface defects (vacancy islands). Nevertheless, independent of the source there is always substantial mass transport involved which shows that formation of the reconstructed surface is a highly complex process. The predominant part of atoms is provided by higher, unreconstructed islands. Single atoms leave the island, move along the beforehand nucleated reconstruction stripe by 1D surface diffusion and become incorporated at the (growing) end [90, 113]. Theoretical DFT calculations show that this path is energetically favorable (see [113]). Less often reconstruction stripes nucleate within (1×1) terraces. If so, the stripe grows by attachment of single adatoms which are subsequently transported to one stripe end. Such isolated reconstruction stripes have been found to be extremely mobile in the longitudinal as well as in the transversal direction. Complete domains are formed by successive attachment of those mobile stripes and by nucleation and growth of further stripes along already existing stripes and domains, respectively. In rare cases mobile stripes encounter hole defects in the (1×1) structure and get pinned to them. In a similar manner as for islands atoms around the defects contribute to the growth of the stripe and leave larger holes within the reconstructed surface layer. All described growth mechanisms are depicted in figure 6.2. The fact that stripes are growing simultaneously in perpendicular directions explains the decreased surface quality which is obtained after potential cycles between reconstructed and unreconstructed phase. Besides the amount of small domains the amount of holes and remaining unreconstructed areas increases with each cycle.

Obviously, in the case of reconstruction formation the mass transport as well as the nucleation rate determine the speed of the phase transition. Growth rates of single reconstruction stripes up to 700 Å per minute could be estimated by STM [89]. Thus, compared to the speed obtained for reconstruction lifting the formation of reconstruction is a rather slow process. The probability for nucleation scales with the availability of possible nucleation sites. Hence for a certain surface coverage by islands (terraces) the surface reconstructs the faster the smaller the average island size is. This has been proven by fast potential jump experiments from the reconstructed phase into the unreconstructed phase and back, where the reconstruction was finished within some minutes [111]. However, in the presence of larger islands full completion of the phase transition takes a time of 20 to 40 minutes [89].

6.5 Electrochemical Characterization During Homoepitaxial Growth

Prior to each electrodeposition or electrodissolution experiment the electrochemical system has been characterized by cyclic voltammetry. These measurements were carried out while the system was mounted on the X-ray diffractometer. Figure 6.3a shows a cyclic voltammogram (CV) of Au(100) in 0.1 M HCl obtained in the SXS cell at 20 mV/s. This CV is in agreement with the literature [73] and demonstrates that the SXS cell is suited for high quality electrochemical measurements. Pronounced peaks attributed to the lifting of reconstruction and to the chloride order/disorder transitions are observed.

In the following chapters we will focus on structural studies during Au electrodeposition. A corresponding cyclic voltammogram, taken in 0.1 M HCl + 0.5 mM AuCl$_4$ solution, is shown
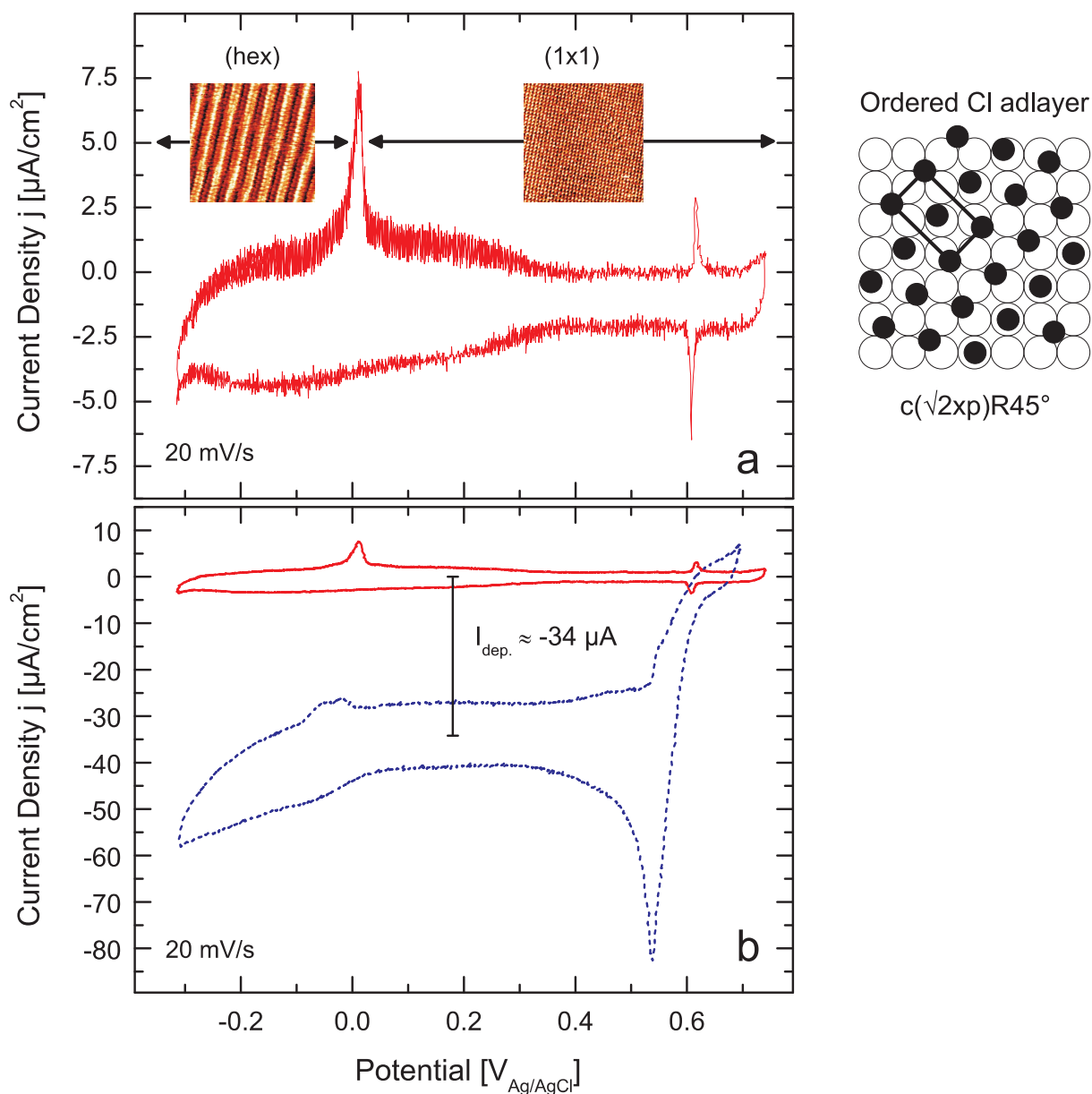
Figure 6.3: a) Cyclic voltammogram of Au(100) in 0.1 M HCl recorded with a potential sweep rate of 20 mV/s. Lifting of the reconstruction occurs at ≈ 0 V in positive sweep direction. The insets shows high resolution STM images of the unreconstructed (1×1) structure and the reconstructed 'hex' structure. At ≈ 0.6 V two sharp peaks arise which belong to the ordering-disordering phase transition of the $c(\sqrt{2} \times p)R45°$ chloride adlayer. b) Two cyclic voltammograms of Au(100) in 0.1M HCl (solid line) and in 0.1 M HCl + 0.5 mM HAuCl$_4$ (dashed line), obtained in the SXS cell at 20 mV/s.

in figure 6.3b (dashed line). At potentials negative of the $Au/AuCl_4^-$ equilibrium potential an increasing Au deposition current is measured that approaches a constant diffusion-limited value at potentials negative of $\approx 0.6\,V$ (the slight increase in current below $0.1\,V$ is attributed to oxygen reduction, caused by incomplete deoxygenation of the electrolyte in this experiment). In addition, the peak corresponding to the lifting of the 'hex' reconstruction is visible, albeit weaker than in Au-free solution. The latter can be explained by the shorter residence time in the regime of the 'hex' phase and the increased surface roughness, caused by the Au electrodeposition.

According to equation 2.25 the measured current density of $j \approx$ -34 $\mu A\,cm^{-2}$ during electrodeposition corresponds to a deposition rate of $R = 3.52\,ML\,min^{-1}$. Within the same electrolyte and within the diffusion-limited potential regime potential step experiments were performed while the scattered X-ray intensity was monitored at a fixed point in reciprocal space (typically in anti-Bragg position). Stepping the potential into the regime of layer-by-layer growth results in intensity oscillations from which the deposition rate R can be inferred (see section 9.2). For a potential step from $0.6\,V$ to $0.25\,V$ layering oscillations with an average period of $T \approx 17\,s$ have been determined. This oscillation period corresponds to a deposition rate of $R \approx 3.5\,ML\,min^{-1}$ which is in perfect agreement with the deposition rate obtained from the electrochemical current density.

Table 6.2 summarizes the averaged X-ray oscillation periods $\overline{T}$ with according deposition rates R, the current densities j_{lim} of electrochemical measurements and the current densities $j_{lim}(R)$ calculated on the basis of R for different nominal concentrations c of $AuCl_4$ in the electrolyte. All deposition experiments presented in the following chapters (8 to 10) were performed within these electrolytes. Electrochemical data and X-ray data are in good agreement as can be seen by comparison of j_{lim} and $j_{lim}(R)$. For the concentrations in the range between $0.05\,mM$ and $0.5\,mM$ data was acquired directly after an electrolyte exchange, i.e. the Au concentration in the meniscus droplet accords to the nominal concentration in the solution bulk. In contrast, the data in $1.0\,mM$ and $2.0\,mM$ Au containing solutions were taken some minutes subsequent to an electrolyte exchange and thus the Au concentration in the meniscus droplet is less than the nominal concentration due to depletion. Especially, the oscillation periods T for $1.0\,mM$ $AuCl_4$ solution yield deposition rates of 3.21 to $3.83\,ML\,min^{-1}$ which are very similar to the rates obtained in $0.5\,mM$ $AuCl_4$ solution. For this reason the structural data presented in chapter 10 will be associated with an Au concentration of $0.5\,mM$ $AuCl_4$. The consistency of electrochemical data and SXS data will be analyzed in more detail in section 9.7 which also includes a constant electrolyte flow through the electrochemical cell.

c [mM]	Beamtime month/year	Dataset	Scan Number	$\overline{T}$ [s]	R [ML min^{-1}]	Range R [ML min^{-1}]	j_{lim} [μA cm^{-2}]	$j_{lim}(R)$ [μA cm^{-2}]	Chapter
0.05†	ESRF, 06/2005	ausau3	364	386.0	0.16	0.16	n/a	-1.5	8
0.1†	ESRF, 06/2005	ausau6	37, 41, 45, 64, 74, 78	157.9	0.38	0.33 - 0.38	n/a	-3.7	9.3 to 9.6
0.1†	ESRF, 03/2006	ausau5	33	185.0	0.33		-3.6	-3.2	
0.2†	ESRF, 06/2005	ausau5	89	116.3	0.52		n/a	-5.0	
0.2†	ESRF, 06/2005	ausau5	98, 104, 122, 130, 134, 140	95.2	0.63	0.52 - 0.63	n/a	-6.0	9.3 to 9.6
0.5†	ESRF, 06/2005	ausau3	378	14.9	4.03		n/a	-38.8	
0.5†	ESRF, 06/2005	ausau3	383	14.8	4.06		n/a	-39.1	
0.5†	ESRF, 06/2005	ausau7	44, 48, 51, 57, 61, 64, 70, 73, 76, 85, 88, 91	15.0	4.01	4.01 - 4.06	-34.0$^\clubsuit$	-38.8	9.3 to 9.6
1.0*	ESRF, 03/2006	ausau7	609	18.7	3.21	3.21 - 3.83	-31.8	-30.9	10
1.0**	ESRF, 04/2007	ausau2	166	15.7	3.83		-43.8	-36.9	
2.0***	ESRF, 03/2006	ausau6	200306-ts12	7.9	7.60	7.60	-68.3	-73.1	9.9

Table 6.2: Deposition rates R and diffusion-limited current densities j_{lim} inferred from X-ray intensity oscillations in the layer-by-layer growth regime and from current transients, respectively. c is the nominal concentration of AuCl$_4$ in the electrolyte. The oscillation period $\overline{T}$ is the average over the first two oscillation periods in a single X-ray time transient or the average over several X-ray time transients. For comparison with j_{lim} the current density $j_{lim}(R)$ has been determined from the deposition rate R. Structural and electrochemical data was taken †) directly after electrolyte exchange, *) 72 min after exchange, **) ≈ 5 min after exchange and ***) ≈ 35 min after electrolyte exchange. The diffusion-limited current density denoted with $^\clubsuit$ was obtained by a cyclic voltammogram measured in the end of the experiment (figure 6.3b).

7 In-plane Structure of Au(100)-Electrodes in Aqueous 0.1 M HCl Solution

The in-plane structure of Au(100) electrodes in aqueous 0.1 M hydrochloric acid solution with and without gold has been investigated by surface sensitive X-ray scattering (SXS) at beam line ID 32 of the European Synchrotron Radiation Facility (ESRF). Most of the experiments were performed at a fixed photon energy of $E = 18.2 \, \text{keV}$ which corresponds to a wavelength of $\lambda = 0.681 \, \text{Å}$. To set the grazing incident angle α_i of the beam with respect to the surface plane the whole goniometer was tilted by $0.415°$. This value is close to the critical angle $\alpha_c(18.2 \, \text{keV}) = 0.2518°$ of gold as determined by

$$\alpha_c = \lambda \cdot \sqrt{\frac{N \cdot r_e \cdot Z}{\pi}} \qquad (7.1)$$

where N denotes the atomic volume density, r_e the atomic radius and Z the atomic number of gold. Incoming angles slightly above the critical angle ensure on the one hand that the recorded intensity by the detector is sensitive to the in-plane structure and it avoids on the other hand strong, unwanted contributions from a long-range surface waviness as they would arise at smaller angles for less perfect crystal surfaces. The illuminated surface area was adjusted by presample slits. Here, horizontal and vertical slit sizes of 0.25 mm and 0.05 mm, respectively, define in combination with α_i and a surface diameter of 4 mm the footprint size of 1 mm² on the sample. This stripe-like shape of the footprint ($4 \times 0.25 \, \text{mm}^2$) in direction of the primary beam allows to move the spot on the sample by horizontal translation scans and to probe the area of best surface quality. Furthermore the influence of waviness in the narrow illuminated direction perpendicular to the beam is reduced. On the detector side, a horizontal slit size of 1 mm and a vertical slit size of 3 mm have been chosen. These slits were found to provide the best signal to noise ratio. The wider vertical detector slit allows to collect more scattered signal intensity while the narrower horizontal detector slit is necessary to improve the in-plane resolution. Some additional experiments were performed at an X-ray energy of 22.5 keV corresponding to $\lambda = 0.551 \, \text{Å}$ under use of identical slit sizes. Very first measurements were carried out at beam line BW 2 at Hasylab in Hamburg using an X-ray energy of 10 keV. In the following the experimental conditions (photon energy and slit sizes) will be given in form of footnotes for each of the described experiments.

As convenient coordinate system for the X-ray measurements the conventional cubic gold unit cell has been chosen with two perpendicular lattice vectors $\vec{a}$ and $\vec{b}$ within the surface plane and a third lattice vector $\vec{c}$ along the surface normal ($a_c = |\vec{a}| = |\vec{b}| = |\vec{c}| = 4.08 \, \text{Å}$). The corresponding reciprocal lattice vectors are parallel to the real space vectors ($\vec{a}^* \| \vec{a}$, $\vec{b}^* \| \vec{b}$ and $\vec{c}^* \| \vec{c}$) with a reciprocal lattice length of $a_c^* = |\vec{a}^*| = |\vec{b}^*| = |\vec{c}^*| = 1.54 \, \text{Å}^{-1}$. The scattering vector $\vec{q}$ is represented in terms of the Miller indices (H, K, L), where

$$\vec{q} = H \cdot \vec{a}^* + K \cdot \vec{b}^* + L \cdot \vec{c}^* \qquad (7.2)$$

This convention gives rise to an L-value of 0.087 for the chosen incoming angle $\alpha_i = 0.415°$ in reflectivity geometry ($H{=}K{=}0$) and $E{=}18.2 \, \text{keV}$. In the following, all positions in the reciprocal space, in particular the positions related to the reconstructed surface, are referred to this coordinate system.

7.1 In-plane Structure of Au(100) Surfaces

The left side of figure 7.1 depicts the real space geometry of the reconstructed Au(100) surface phase on top of the unreconstructed bulk structure in an aspect ratio which conforms to a 25% higher packing density within the reconstructed layer. For simplicity the figure shows only the orientation of the 'x20' direction along the crystal $[\overline{1}10]_c$ direction. The reader has to keep in mind that the same reconstructed structure exists in form of 90° rotated domains as well as in form of two slightly rotated domains. The two vectors $\vec{a}$ and $\vec{b}$ define the squared bulk structure, the vectors $\vec{a}_h^*$ and $\vec{b}_h^*$ define the structure of the reconstructed surface phase. Based on the fact that no shearing of the reconstructed surface phase has been reported in the literature, the dimensions of the reconstructed surface are well-defined by the two netplane distances $d(\Delta_1)$ and $d(\Delta_2)$. More precisely, the $d(\Delta_1)$ netplane distance provides information about the extension in 'x5' direction and the $d(\Delta_2)$ distance predominantly about the extension in 'x20' direction. The right side of figure 7.1 shows an in-plane reciprocal space map ($L=0$) according to the real space structure discussed above. Each point represents a rod of scattering normal to the surface originating either from the unreconstructed bulk

Real space   Reciprocal space
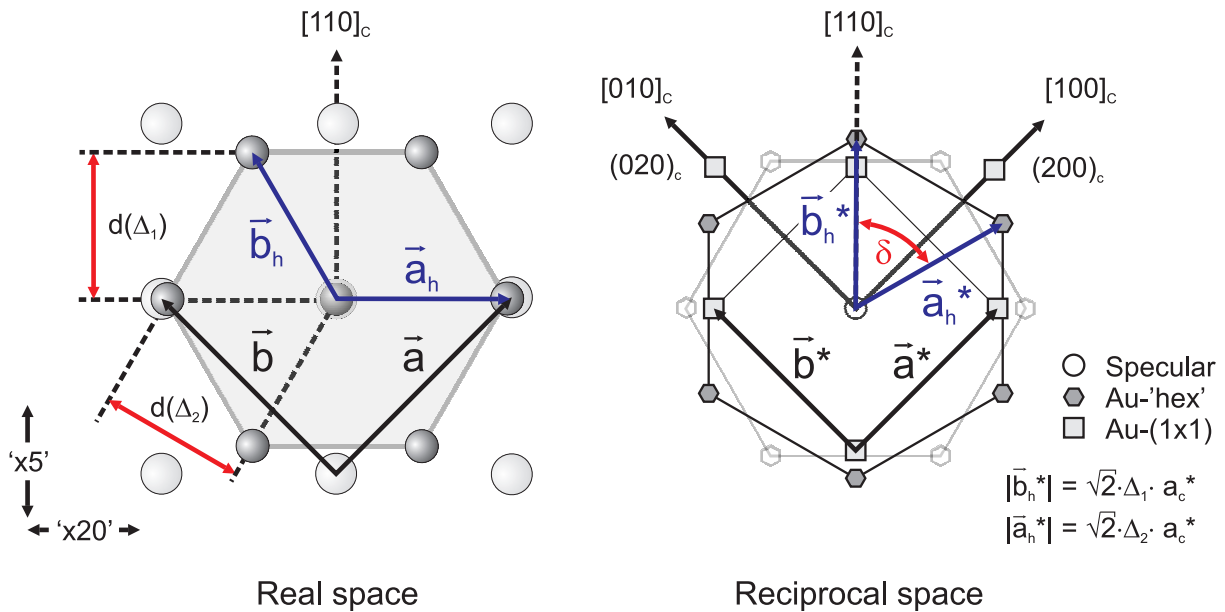
Figure 7.1: In-plane structure of the unrotated, reconstructed Au(100) surface. The left figure shows the real space structure of the hexagonally reconstructed layer (dark atoms) on top of the unreconstructed substrate lattice (bright atoms) for one of the two possible domain orientations. The vectors $\vec{a}$ and $\vec{b}$ define the unreconstructed surface unit cell, $\vec{a}_h^*$ and $\vec{b}_h^*$ the reconstructed surface unit cell. The right figure shows the according reciprocal space map. Each point represents a rod of scattering normal to the surface. The lengths of the two first order reciprocal space vectors, $|\vec{b}_h^*| = \sqrt{2} \cdot \Delta_1 \cdot a_c^*$ and $|\vec{a}_h^*| = \sqrt{2} \cdot \Delta_2 \cdot a_c^*$, are linked to the netplane distances $d(\Delta_1)$ and $d(\Delta_2)$ in real space, respectively.

phase ($\square$) or from the 2-dimensional, reconstructed surface phase ($\bigcirc$). The origin of this map, i.e. the $(0,0,0)$ position ($\bigcirc$) is the intersection of the specular rod with the surface plane. As a consequence of the centered atom in the chosen surface unit cell, every second reflection of the squared bulk structure is forbidden. If the diffraction indices H and K are both even and $L \approx 0$ then the scattering vector $\vec{q}$ fulfills the diffraction condition, i.e. $\{200\}$ are allowed bulk Bragg-reflections and high intensities are measured. However, scattering vectors corresponding to one of the $\{110\}$ netplanes point to anti-Bragg positions on the according crystal truncation rod and are consequently much weaker in intensity. The two-dimensional, hexagonal reconstructed surface layer gives rise to a set of separate crystal truncation rods. According to the threefold symmetry of the reconstructed phase the reciprocal space pattern remains hexagonal. In figure 7.1 the positions of the reconstruction rods are illustrated for the two possible domain orientations with respect to the substrate. Rods belonging to domains aligned to the $[110]_c$ direction are shown by semi-transparent symbols while the rods belonging to domains aligned to the $[\overline{1}10]_c$ direction are represented by solid symbols. In order to determine the structure of the reconstructed surface layer the peak positions and intensity profiles were measured at mainly two positions in reciprocal space. Of particular advantage is the reconstruction rod situated at $(\Delta_1, \Delta_1, 0)$, i.e. at the first order reciprocal lattice vector $\vec{b}_h^*$. It lies close to the $(1,1)$ bulk rod and allows to monitor the intensity from both, the surface and the bulk phase, by one narrow (and fast) radial scan along the $[110]_c$ direction. Moreover, as $(1,1,0.09)$ is in anti-Bragg the intensities at both positions are of the same order of magnitude. The length $\sqrt{2} \cdot \Delta_1 \cdot a_c^*$ of the attributed scattering vector $\vec{b}_h^*$ is linked to the netplane distance $d(\Delta_1)$ in real space. Information about the second netplane distance $d(\Delta_2)$ were obtained at $(\sqrt{2} \cdot \cos 15° \cdot \Delta_2, \sqrt{2} \cdot \sin 15° \cdot \Delta_2, 0.09)$, which belongs to 90° rotated domains. At this point we intentionally selected a symmetry equivalent reflection (to $\vec{a}_h^*$) on perpendicular oriented domains in order to improve the time resolution of the measurements by shortening the motor travel time from one reflection to another and to avoid the illumination of completely different surface areas. In the following, information about the in-plane structure have been obtained by two types of scans. Radial scans along the direction of $\vec{q}$ were performed to determine the dimensions of the reconstructed unit cell. Additional azimuthal rocking scans around the surface normal (Θ-scans) were utilized to probe the orientation of domains with respect to the (1×1) substrate structure.

7.2 Literature Review

Before we focus on present SXS results, we will briefly discuss the results of previous SXS studies which were carried out by several groups for Au(100) surfaces in UHV and in electrochemical environment.

7.2.1 In-plane Structure of Au(100) in UHV

The in-plane structure of Au(100) electrodes in UHV has been investigated in detail by SXS [101, 103, 106, 116]. According to these studies the surface unit cell of the reconstructed layer is defined by the reciprocal lattice parameters $\Delta_1 = \Delta_2 = 1.206 \pm 0.001$ [103, 116]. In fact the study of Mochrie et al. determined a slightly smaller value for Δ_2, i.e. a quasi-hexagonal

unit cell. However, the authors emphasized that within experimental errors the unit cell is hexagonal with $\Delta_1=\Delta_2$. In contrast to scanning probe techniques SXS is sensitive to more than a single surface layer, i.e. it allows to determine the rotational orientation of reconstructed domains with respect to the (1×1) bulk structure. Temperature dependent X-ray studies in UHV revealed in the temperature range from 300 K to 970 K an evenly distributed coexistence of distorted-hexagonal domains which are aligned or rotated by ± 0.81° relative to the $[110]_c$ direction, respectively [116]. Upon elevating the temperature above 970 K the scattered intensity of the rotated domains abrupt vanished, while that of the aligned domains persisted up to a surface disordering transition[1] at $T = 1170$ K. The rotational transition at 970 K was found to be reversible with a small hysteresis of about 10 K (width of transition). Slow cooling of the Au(100) sample resulted in a perfect reconstructed phase consisting exclusively of ± 0.8° rotated domains, while a rapid cooldown led to a mixture of rotated and unrotated domains. Interestingly, subsequent to an intermittent rapid quench to $T = 800$ K, azimuthal scans recorded at $T = 1170$ K featured domains rotated by ±0.3° in addition to aligned and ±0.81° rotated domains. Apparently additional local energy minima exist for rotation angles between 0° and 0.81° and the final surface condition strongly depends on the thermal sample pretreatment.

The existence of differently rotated Au(100)-'hex' phases is substantiated by theoretical studies which predict only slightly larger energies for rotated overlayers compared to the energies of unrotated overlayers [117]. In this context it has been suggested that the rotation of the top atomic layer observed at the Au(100) surface is the same phenomenon as the Novaco-McTague rotation found for rare gas monolayers on the basal plane of graphite [69]. Y. Okwamoto et al. presented a zero temperature phenomenological theory in order to show that the Novaco-McTague theory is able to explain the variety of hexagonal reconstruction and the extremely small rotation angles observed for fcc(100) surfaces of iridium, platinum and gold under UHV conditions [118]. Furthermore the Au(100) surface in UHV has been theoretically modeled by molecular dynamics (MD) simulations. Ercolessi, Tosatti and Parrinello parametrized a many-body 'glue-model' and could predict the bulk melting temperature of $T_M = 1337$ K [97]. Based on the same model further calculations have been carried out by X.Q. Wang in order to explain the rotational and surface-disordering transition [98]. The simulation starts with a purely aligned phase at $T = 0$ K and predicts ± 0.7° rotated domains at elevated temperatures in agreement with experimental results. Moreover the transition temperatures could be quite precisely calculated. An additional interesting influence of the heating speed on the resulting surface condition has been found. While the model predicts rotated domains after instantaneous heating from $T = 0$ K to $T = 300$ K a simulation of slow continuous heating results exclusively in aligned domains.

7.2.2 In-plane Structure of Au(100) in Electrochemical Environment

First SXS measurements on reconstructed Au(100) surfaces in contact with electrolyte were carried out by B.M. Ocko and coworkers [80]. They determined reciprocal lattice parameters of $\Delta_1 = 1.205 \pm 0.002$ and $\Delta_2 = 1.200 \pm 0.005$ in 10 mM $HClO_4$ solution ($E = $ -0.4 $V_{Ag/AgCl}$).

---

[1](1×1) high-temperature structure

As observed for low temperatures in UHV rotated domains were found in the reconstructed phase of Au(100) electrodes [80]. Moreover these studies found for the thermally formed reconstruction, present on the surface after immersion of the Au(100) sample under potential control sufficiently negative of the critical potential, solely 'hex' domains that were aligned along the $[110]_c$ direction. Successive potential cycles into the unreconstructed phase and back always resulted in ±0.8° rotated domains[2], whereas the amount of aligned domains was strongly decreased, indicating an irreversible rotational transition in Au-free $HClO_4$ solution. It is important to realize that this behavior differs from the temperature-dependent, reversible rotational transition observed under UHV conditions.

Apparently, reconstructed domains on Au(100) surfaces seem to favor the local energy minimum of the 0.8° rotated phase if the reconstruction is induced by a change in electrode potential. This might be related to the increasing amount of smaller domains coming along with an increased density of domain boundaries and to surface defects. This idea gets support from STM observations which were carried out under UHV conditions [4]. Due to the crystallographic mismatch between a reconstructed terrace and the neighboring unreconstructed (1×1) bulk structure (the latter existing below a second higher reconstructed terrace) kinks are formed. The sequence of these kinks is correlated with the rotation of the reconstructed domain. S. Günther proposed that at lower temperatures the presence of step edges energetically favors the rotated phase. Upon elevating the temperature thermal motion of the kinks sets in and the interaction between reconstructed domains and the step edges becomes reduced. This results in a cross over from the rotated to the aligned phase. Hence, the aligned phase is assumed to be the energetically favorable phase on Au(100) surfaces with wide terraces and a low density of step edges. However, in the presence of many small terraces the increased amount of step edges and kinks favors rotated, reconstructed domains.

7.3 In-plane Structure of Au(100) Electrodes in Au-free 0.1 M HCl

Prior to the electrodeposition experiments, the Au(100) electrode surface was characterized by cyclic voltammetry and subsequently by SXS in Au-free 0.1 M HCl solution. We first focus on the domain structure, i.e. on the orientation of reconstructed domains with respect to the unreconstructed bulk structure and on the average size of reconstructed domains. Lattice parameters will be analyzed in the sections 7.5 and 7.6. Figure 7.2 shows a typical azimuthal in-plane rocking scan recorded[3] at $(\Delta_1, \Delta_1, 0.09)$ and at an electrode potential of -0.2 V. The latter had been applied 70 minutes prior to the scan in order to ensure a well established reconstructed surface phase. Intensity profiles recorded at reconstruction rods rotated by 60° agree with the scattering observed at $(\Delta_1, \Delta_1, 0.09)$. This rotational symmetry of reflections clearly indicates that the peak splitting arises from rotated, hexagonal domains and not from a significant shearing of the surface structure.

---

[2]Fig. 3 in [80] shows rather domains rotated by ±0.7° than domains rotated by ±0.8°

[3]ESRF, E = 18.2 keV, presample slits: vg = 0.05 mm and hg = 0.25 mm, detector slits: dvs = 3 mm and dhs = 1mm
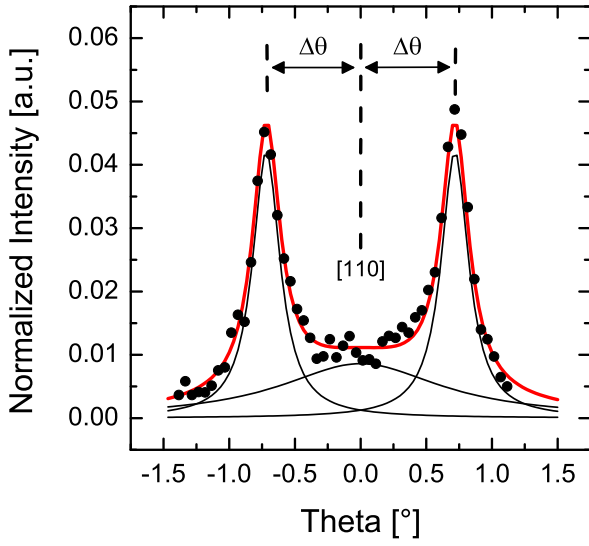
Figure 7.2: Azimuthal rocking scan of Au(100) in 0.1 M HCl recorded at $(\Delta_1, \Delta_1, 0.09)$ and at an electrode potential of E = -0.2 V. The bold solid line shows the best fit to the data (filled circles) based on a sum of three Voigt profiles for the $\Delta\theta = \pm 0.72°$ rotated domains and domains aligned to the $[110]_c$ direction (thin lines).

In figure 7.2 two distinct peaks are recognizable, clearly revealing the presence of rotated domains with preferred in-plane rotation angles of $\Delta\Theta = \pm 0.72°$ relative to the $[110]_c$ axis. This surface condition is in agreement with SXS measurements of Ocko et al [80]. In contrast to the latter no surface condition dominated by aligned domains could be observed in the present study since contact with the electrolyte was always established at open circuit potential (OCP), i.e. in the potential regime of the unreconstructed surface. Furthermore we did not find any indications for preferred rotation angles that significantly differ from a $\Delta\theta = \pm 0.72°$ rotation in Au-free 0.1 M HCl solution.

7.3.1 Model Function for Azimuthal Intensity Profiles

For a quantitative analysis the azimuthal scans were fitted by a sum of three Voigt profiles, located at $0°$ and $\pm\Delta\theta$ to represent the contributions of the aligned and rotated domains, respectively. The mirror symmetry of the azimuthal rocking curve with respect to $\Theta = 0°$ allows to describe the two profiles for rotated domains by an identical amplitude, Lorentz width and rotation $\Delta\Theta$ with respect to the $[110]_c$ direction. The appropriate model function is given by

$$I(\theta) = BG + SLOPE \cdot \theta + \frac{\sqrt{2\pi}}{\sigma} \cdot \int_{-\infty}^{\infty} e^{-0.5 \cdot x^2/\sigma^2} \cdot \left(\underbrace{\frac{A_r}{1+T_L^2} + \frac{A_r}{1+T_R^2}}_{\text{rotated}} + \underbrace{\frac{A_a}{1+T_M^2}}_{\text{aligned}} \right) dx \qquad (7.3)$$

with

$$
\begin{aligned}
T_L &= [\theta - x - (\theta_0 + \Delta\theta)]/\sigma_r \\
T_R &= [\theta - x - (\theta_0 - \Delta\theta)]/\sigma_r \\
T_M &= [\theta - x - \theta_0]/\sigma_a
\end{aligned}
$$

where BG and $SLOPE$ are the parameters for background and slope of the total intensity profile, respectively, A_r and A_a are the amplitudes of the rotated and aligned profiles, respectively, σ is the full width at half maximum (FWHM) of the gaussian, θ_0 is the θ value of the profile center, and σ_r and σ_a are the lorentzian FWHM of the rotated and aligned profiles, respectively. The latter quantities and the rotation angle $\Delta\theta$ define the complete parameter set of the fit procedure. The gaussian part of the Voigt profiles describes the instrumental resolution. Its FWHM, σ, has been determined as follows. First all profiles that were recorded at the same reciprocal space position have been fitted by use of σ as *free* fit parameter. Then the obtained σ values were averaged and the fit was repeated for each profile with $\overline{\sigma}$ as *fixed* parameter. This method provided better fits to the data than σ values calculated by an estimation of the in-plane resolution dependent on instrumental parameters (appendix A.4). In general the calculated values were about twice as large as values received by the aforementioned procedure and led to fits with significantly higher χ^2 values. For an improved time resolution of the measurements the intensity in azimuthal rocking scans was usually recorded close to the $[110]_c$ axis. In these cases the background has been constrained by values obtained from radial scans along $\vec{q}$. The data analysis has been carried out in the C-plot[4] software by use of the χ^2 minimization method.

7.3.2 Size of Reconstructed Domains and Orientational Distribution

For the azimuthal scan shown in figure 7.2 full widths at half maximum of $0.254° \pm 0.05°$ and $1.49° \pm 0.5°$ have been determined for rotated and aligned domains, respectively, i.e. the distribution of the rotated domains is considerably narrower. This finding is in qualitative agreement with observations in UHV which provided values of $0.16°$ to $0.18°$ for aligned domains and $0.09°$ to $0.14°$ for rotated domains [103]. Because of the twofold influence on the width of the peak profile, which is given by the angular rotation distribution of domains on the one hand and by the domain size on the other hand, no definite value for the latter can be obtained. However, the FWHM of radial scans through the $(\Delta_1, \Delta_1, 0.09)$ reflection $(\Delta q \approx 0.0349 \cdot a_c^*, \sigma_G = 0.0045 \cdot a_c^*)$ provides a correlation length of $L \approx 110$ Å as estimated by the Scherrer equation

$$L = \frac{0.94 \cdot \lambda}{\Delta(2\theta) \cdot \cos\theta} = \frac{0.94 \cdot 2 \cdot \pi}{\Delta q} \approx \frac{2\pi}{\Delta q} \tag{7.4}$$

where λ is the wavelength, $\Delta(2\Theta)$ is the FWHM of the intensity profile and θ is the scattering angle. In this calculation the FWHM $\Delta(2\theta)$ has been obtained from the derivative of q given by

$$\Delta q = \left|\frac{\partial q}{\partial 2\theta}\right| \Delta(2\theta) = \left|\frac{4\pi}{\lambda} \cdot \cos\frac{2\theta}{2} \cdot \frac{1}{2}\right| \Delta(2\theta) \tag{7.5}$$

The correlation length of ≈ 110 Å is at least a factor of three smaller than the correlation length of ≥ 300 Å which has been found in the studies of Ocko et al. [80]. This discrepancy may be explained by a different history of the samples before the SXS experiments. While Ocko et al. determined the correlation length directly after thermal annealing and electrolyte contact at -0.2 $V_{Ag/AgCl}$, i.e. without destroying the thermally formed reconstruction, the electrodes

---

[4]C-plot, Scientific Graphics and Data Analysis package from CSS (Certified Scientific Software)

in the present studies had been contacted at OCP and afterwards several times potential-induced reconstructed and lifted during the characterization via cyclic voltammetry. Hence, a decrease in domain size and a simultaneous decrease in correlation length must be expected. An alternative fit with only two Voigt profiles for rotated domains and disregard of aligned domains results in a reasonably higher χ^2 value and the fitting curve does not match well around $\Delta\theta = 0°$. Moreover, separate integration of the intensity profiles for the rotated and aligned domains in figure 7.2 provides values of 0.031 and 0.014 (a.u.), respectively. Thus, the analysis clearly shows that the contribution of unrotated domains is not negligible. Nevertheless, further experiments revealed that the amount of aligned domains depends on the sample history and on the thermal pretreatment. In a second and independently performed experiment rocking curves were obtained which could be perfectly fitted without any contribution from aligned domains showing that in this case almost exclusively rotated domains exist (see figure 7.3b).

7.4 Formation Process of the Reconstructed Phase

The time behavior of the (1×1) → 'hex' surface phase transition in 0.1 M HCl has been studied[5] by potential steps from 0.55 V in the unreconstructed potential regime to -0.2 V in the reconstructed potential regime. Subsequent to the potential step a consecutive series of intensity profiles was recorded at $(\Delta_1 , \Delta_1 , 0.09)$ in radial direction through the peak of -0.72° rotated domains. Figure 7.3a shows every fifth of those scans. The time-dependence of the intensity and the change in the FWHM of the profiles are shown as circles in the figures 7.3c and 7.3d, respectively. Each data point in 7.3c represents the background subtracted, integrated intensity of one profile normalized to an integrated intensity obtained after 6570 seconds, i.e. it is normalized to a saturation value. The experimental values have been fitted by an exponential function of the form

$$I(t) = I_0 + A \cdot \exp(-t/\tau) \tag{7.6}$$

where $I(t)$ is the integrated intensity, t is the time and I_0, A and τ are constants. In this manner a time constant of $\tau_{\mathrm{rad}} = 982\,\mathrm{s}$ has been found for the intensity raise in radial profiles. Parallel to the formation of the reconstructed phase, the FWHM of the radial intensity profiles continuously decreases (figure 7.3d). Equation 7.6 yields a time constant of $\tau_{\mathrm{FWHM}} = 483\,\mathrm{s}$ which is about half of the time constant found for the integrated radial intensity. This difference is most likely related to the modality of the reconstruction process (section 6.4). A saturation value 2.5 times smaller than the initial value shows that the average domain size of the reconstructed phase in 'x5' direction increases with time. In detail the correlation length approximately doubles from 78 Å ($\Delta q = 0.04936 \cdot a_c^*$ for t = 124 s) to 185 Å ($\Delta q = 0.02072 \cdot a_c^*$ for t = 2148 s) according to equation 7.4. A correlation length of 185 Å corresponds to a width of about 13 reconstruction stripes. Indeed, STM pictures of potential-induced, reconstructed Au(100) surfaces either recorded in 0.1 M sulfuric acid [89] or in a mixture of 0.1 M sodium sulfate + 1 mM hydrochloric acid [119] show domains of almost comparable average size in 'x5' direction (figure 7.4).

---

[5]ESRF, E = 22.5 keV, presample slits: vg = 0.01 mm and hg = 0.25 mm, detector slits: dvs = 1 mm and dhs = 1mm
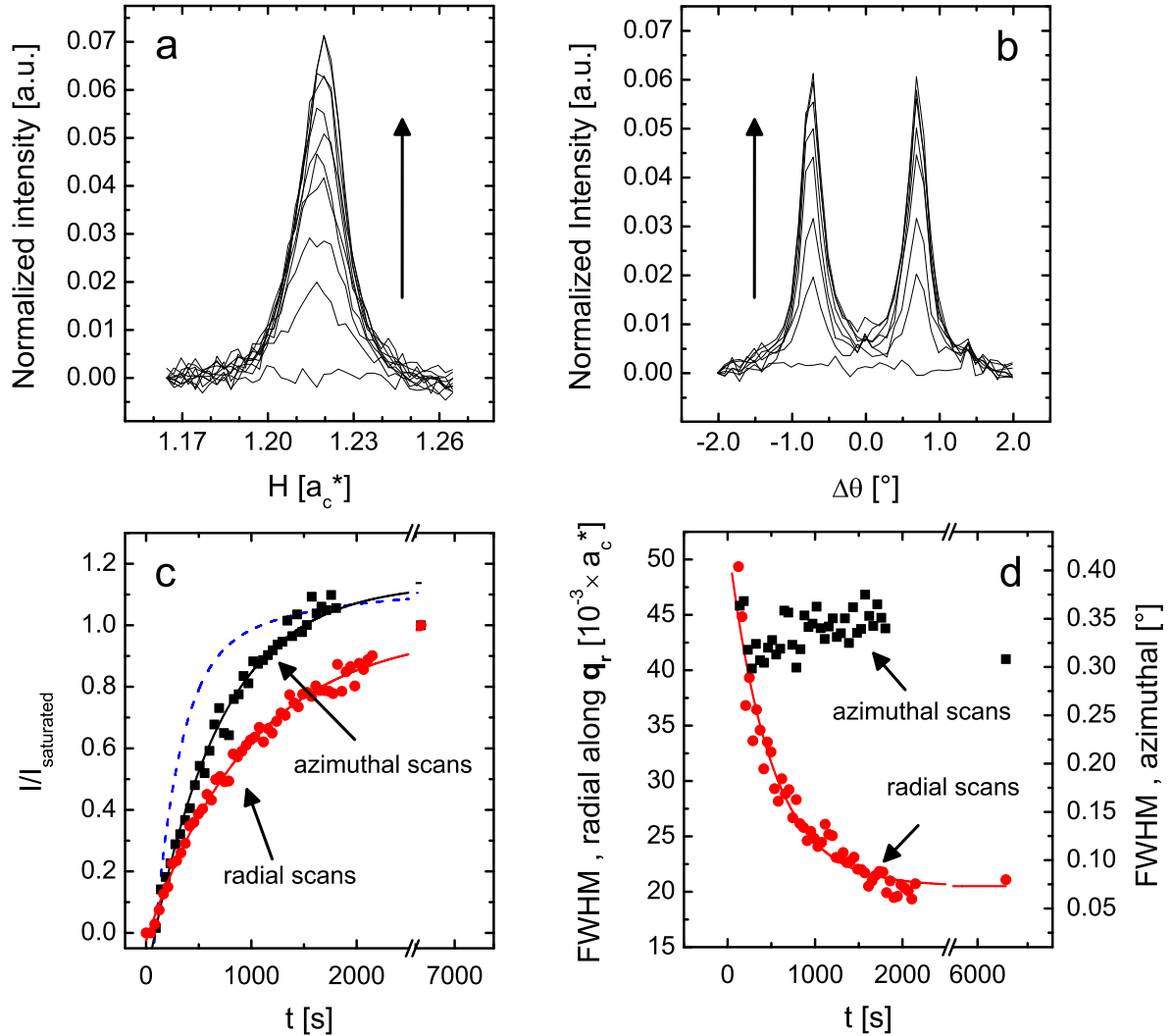
Figure 7.3: The four graphs show the formation of the reconstructed phase after a potential step from $0.55\,\mathrm{V}$ to $-0.2\,\mathrm{V}$ monitored by a consecutive series of in-plane scans at $\vec{b}_h^* = (\Delta_1, \Delta_1, 0.09)$. **a)** Reconstruction peak of $-0.72°$ rotated domains monitored in radial direction along $\vec{q}_r$ (○). The intensity is plotted versus the H component of the scattering vector. **b)** Series of azimuthal rocking scans (□). **c)** Time-dependence of the integrated intensity of the data shown in the graphs a and b. The integrated intensity has been normalized to a saturation value obtained from a different experiment after 6570 seconds at $-0.2\,\mathrm{V}$. The dashed line shows the total integrated intensity at $\vec{b}_h^*$. **d)** Time-dependence of the FWHM of rotated domains obtained from the scans shown in the graphs a and b. Solid lines show exponential fits to the data.

1000×1000 Å², E = -0.5 V$_{SCE}$ 4200×3800 Å², E = -0.15 V$_{SCE}$
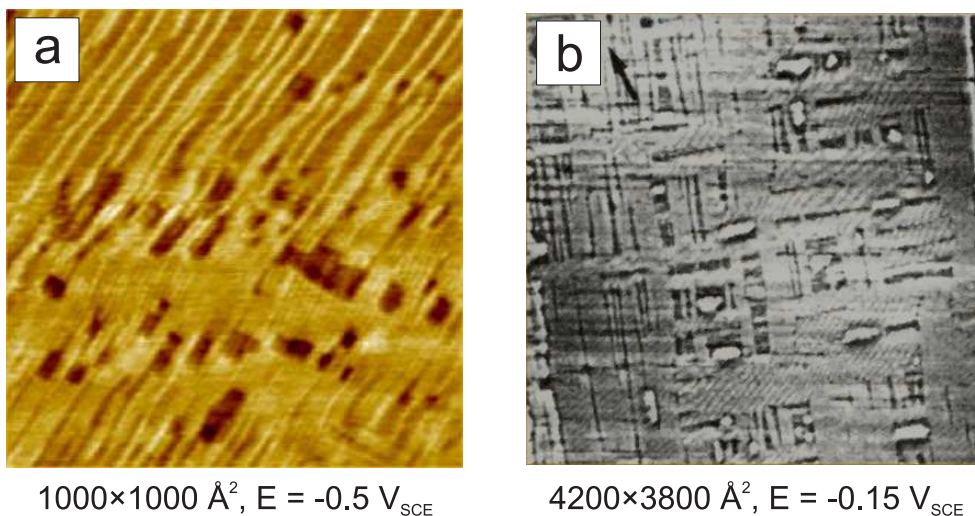
Figure 7.4: STM images of potential-induced, reconstructed Au(100) surfaces recorded in a) 0.1 M NaSO$_4$ + 1 mM HCl (ref. [119]) and b) 0.01 M H$_2$SO$_4$ (ref. [89]).

Subsequent to this measurement the potential has been stepped back to 0.55 V in the unreconstructed potential regime. Fifteen minutes later we repeated the potential step experiment to -0.2 V at the same reciprocal space position with azimuthal scans instead of radial scans. Figure 7.3b shows every fifth of the recorded azimuthal rocking curves. From the averaged peak intensities and the averaged FWHM of the left and the right peak, respectively, an integrated intensity has been obtained for each azimuthal scan. The results are presented as squares in figure 7.3c, again normalized to a saturation value obtained after 6570 seconds. Since the saturation values stem from earlier potential step experiments some of the normalized intensities of the azimuthal scans are greater than unity. An exponential fit to the data provides a time constant of $\tau_{azim} = 670$ s. The time constants τ_{rad} and τ_{azim} are not comparable since both directions influence each other. In this regard the 30% smaller time constant in azimuthal direction may be related to the exponential decrease of the radial FWHM (i.e. an intensity increase in the peak maximum) which potentially results in a faster azimuthal intensity increase. As well it is possible that during the 15 minutes resting time at 0.55 V prior to the second potential step experiment the island ripening did not proceed to the same degree as in the previous experiment where the resting time constituted 18 minutes. Consequently the mass transport of adatoms takes place on shorter length scales and the surface reconstructs faster. However, since STM studies in sulfuric acid reported several hundred Ångstrom wide islands 10 min after lifting of the reconstruction [89] this effect cannot be pronounced, in particular if the accelerating effect of chloride on the Au adatom mobility is considered. Squares in figure 7.3d show the time-dependence of the averaged FWHM of both rotated peaks. The width exhibits no significant change and stays more or less constant with time. Apparently, the angular orientation distribution of rotated domains does not noticable change during the formation process of the reconstructed phase. Expectedly the increase in correlation length in 'x20' direction has no influence on the profile shape.

In order to obtain the total integrated intensity $I(t)$ at $\vec{b}_h^*$ we multiplied the exponential fit curve of the integrated azimuthal intensity with the fit curve of the radial FWHM. The result is plotted as dashed line in figure 7.3c. This $I(t)$ curve is approximately exponential with a time constant of $\tau \approx 360\,\text{s}$. The intensity strongly increases from $t = 0$ to $t \approx 800\,\text{s}$ before it approaches a saturation value. Thus, in accordance with the STM investigations in 0.01 M H_2SO_4 the formation of the reconstructed phase proceeds comparatively slow in gold-free electrolyte and it takes several minutes until the reconstructed phase is formed [89]. After approximately 17 minutes 90% of the saturation value is achieved in reasonable agreement with time spans of 20 to 40 minutes reported in [89]. Obviously the well-known accelerating effect of chloride on the surface mobility of gold adatoms [120–123] does not noticable influence the speed of the surface phase transition. This is most probably related to the fact that chloride is predominantly desorbed at such negative potentials. According to the STM study the surface before the potential steps must be assumed to be covered by large unreconstructed gold islands. The initial intensity observed at $(1\,,1\,,0.09)$ decreases on a similar time scale as the reconstruction peak forms (not shown here).

In contrast to the UHV studies no strong central peak is observed in the azimuthal profiles. The intensity distribution within the HK-plane $(L = 0.09)$ should therefore be given by two rotational symmetric (or elliptic) Lorentz-profiles separated by an angle $2\Delta\theta \approx 1.44°$ from each other. From a mathematical point of view each intensity profile obtained in the radial direction through the splitted reconstruction peak should exhibit the same FWHW
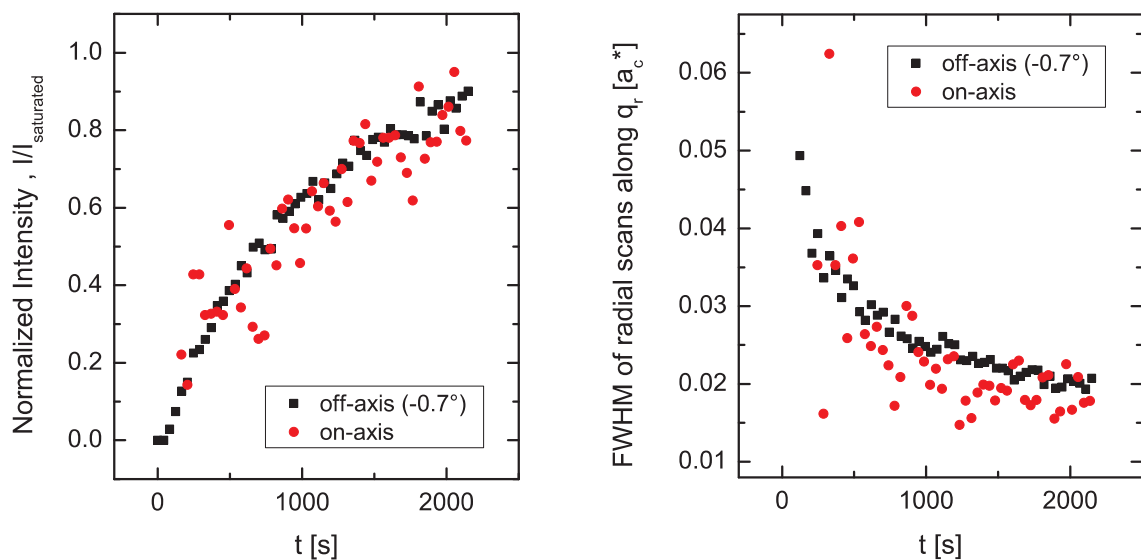
Figure 7.5: Time-dependence of a) the normalized integrated intensity and of b) the FWHM of radial intensity profiles alternatingly recorded along the $[110]_c$ direction (circles) and through the -0.7° rotated peak (squares) after a potential step from 0.5 V in the unreconstructed potential regime to -0.2 V in the reconstructed potential regime. Displayed values have been determined by Voigt-profile fits and by numerical integration of the latter.

independent of the angle being enclosed by the scattering vector $\vec{q}$ and the $[110]_c$ direction. The same holds for the time-dependent increase in the integrated radial intensity subsequent to a potential step from the unreconstructed potential regime to the reconstructed potential regime. In order to prove this the potential step experiment from 0.5 V to -0.2 V was repeated and an additional series of radial profiles was recorded along the $[110]_c$ direction, i.e. through the center of the splitted peaks. The two graphs in figure 7.5 summarize the results for scans through the peak of -0.7° rotated domains ('off-axis') and for scans in $[110]_c$ direction ('on-axis'). Obviously the integrated radial intensity and the radial FWHM exhibit the same time-dependence in both directions. Hence, provided that there is no significant contribution of aligned domains 'on-axis' and 'off-axis' scans are to the same degree qualified to determine the correlation length in 'x5' direction. However, SXS in-plane studies of Au(100) in UHV by Gibbs et al. revealed that for a sample temperature of $T = 840$ K aligned domains give large contributions to the scattered intensity at $\vec{b}_h^*$. The intensity belonging to aligned domains has almost rotational symmetry about the surface normal, while intensity belonging to rotated domains is elongated in radial direction. A profile analysis provided values of $0.0017\, a_c^*$ and $0.003\, a_c^*$ for the radial FWHM of unrotated and rotated peaks, respectively. Thus the correlation length of rotated domains is about half the correlation length of unrotated domains. This demonstrates that under UHV conditions the average domain size in 'x5' direction of rotated domains is significantly smaller than those for unrotated domains. A similar trend has been found for homoepitaxial electrodeposition on Au(100) electrodes and will be discussed in more detail in the next chapter.

7.5 Surface Structure of the Reconstructed Phase at Constant Electrode Potential

In this section the surface structure of the 'hex' phase at $E = -0.2$ V is discussed quantitatively and the results will be compared with the structure of other interfaces. Figure 7.6 summarizes the time-dependence of Δ_1 and $\Delta\theta$ after stepping the potential from 0.55 V to -0.2 V. The squares represent Δ_1 and were obtained from the series of radial scans recorded through the intensity peak of -0.72° rotated domains (figure 7.3a). Since the intensity is very weak in the initial time period after the potential step only profiles recorded after $t = 960$ s allow to extract Δ_1. Values for $\Delta\theta$ are the result of fits to the azimuthal data (figure 7.3b) using the model function given in equation 7.3. Parallel to the formation of the reconstructed phase neither the preferred rotation angle nor the dimension of the reconstructed surface structure in 'x5' direction significantly changes with time in Au-free electrolyte and at a fixed potential of -0.2 V in the reconstructed potential regime. Moreover it is obvious that 'hex'-domains are already rotated by ±0.72° in the initial time period after the potential step where only a small fraction of the electrode is covered by the reconstructed phase. At $E = -0.2$ V the preferred rotation angle is 0.718° ± 0.006° and the average value of Δ_1 is 1.2053 ± 0.0005. The latter perfectly agrees with Δ_1 = 1.205 ± 0.002 obtained by Ocko et al. in 0.01 M perchloric acid [80] and moreover it resembles the value of Δ_1 = 1.206 ± 0.001 found in UHV studies [103, 116]. For Δ_2 no complete scan series was recorded but single scans provide a value of Δ_2 = 1.198 ± 0.001. As before, this value is close to 1.200 ± 0.005
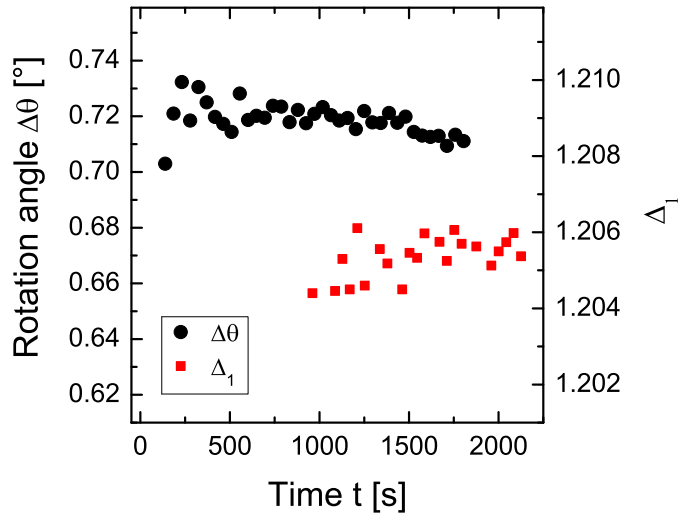
Figure 7.6: Time-dependence of Δ_1 and $\Delta\theta$ for Au(100) electrodes in 0.1 M HCl subsequent to a potential step from 0.55 V to -0.2 V at $t = 0$. Initially weak intensity profiles in radial direction allow to determine Δ_1 only after a time of 960 seconds.

in 0.01 M HClO$_4$ [80]. Compared to UHV, where a value of $\Delta_2 = 1.206$ was found, the reconstructed phase in electrochemical environment appears to be slightly expanded in 'x20' direction. The surface unit cell, defined by $\Delta_1 = 1.2053$ and $\Delta_2 = 1.198$, allows to calculate the surface strain ϵ and the excess mass density $\Delta\sigma$ of the reconstructed layer with respect to the (1×1) bulk structure. According to appendix A.2 the area A_{hex}, occupied by one atom in the reconstructed phase, is given by the expression

$$A_{\text{hex}} = \frac{a_c^2}{\Delta_1 \cdot \sqrt{4 \cdot \Delta_2^2 - \Delta_1^2}}. \tag{7.7}$$

This yields an area of $A_{\text{hex}} = 6.6695\,\text{Å}^2$ per surface atom in the reconstructed surface layer. The area of the unreconstructed bulk structure amounts $A_{1\times1} = 8.3232\,\text{Å}^2$ per atom. Hence the surface strain ϵ of the reconstructed phase in 0.1 M HCl is

$$\epsilon = \frac{A_{\text{hex}} - A_{1\times1}}{A_{1\times1}} = -0.199 \tag{7.8}$$

and the reconstructed Au(100) surface exhibits an area contraction of about 20% with respect to the (1×1) bulk structure. In a similar manner the excess mass density $\Delta\sigma$ is inferred. The fraction of atoms per unit area is given by $\sigma_{hex} = 1/A_{\text{hex}}$ and $\sigma_{1\times1} = 1/A_{1\times1}$. Thus for $\Delta\sigma$ one obtains

$$\Delta\sigma = \frac{\sigma_{hex} - \sigma_{1\times1}}{\sigma_{1\times1}} = 24.79\%. \tag{7.9}$$

The hexagonal reconstructed Au(100) surface in 0.1 M HCl contains an excess of 24.79% atoms compared to the (1×1) bulk termination of the electrode surface. Structural data for the two interfaces Au(100)/UHV and Au(100)/0.01 M HClO$_4$ as well as for the present system are summarized in table 7.1. The similarity of the structural data in both electrolytes is remarkable. In contrast, the reconstructed Au(100) surface in UHV contains about one additional atom per hundred atoms in the unreconstructed (1×1) substrate layer. Since Δ_1 is almost identical for the three considered interfaces, the compression of the Au(100) surface in UHV has to be mainly attributed to a contraction of the unit cell in 'x20' direction.

Au(100) in:	UVH	0.01 M HClO$_4$	0.1 M HCl
E	-	-0.4 V$_{Ag/AgCl}$	-0.2 V$_{Ag/AgCl}$
Δ_1	1.206 ± 0.001	1.205 ± 0.002	1.2053 ± 0.0005
Δ_2	1.206 ± 0.001	1.200 ± 0.005	1.1980 ± 0.0010
d(Δ_1)	2.3922 Å	2.3942 Å	2.3936 Å
d(Δ_2)	2.3922 Å	2.4042 Å	2.4082 Å
ϵ	-20.61%	-20.03%	-19.90%
$\Delta\sigma$	25.96%	25.05%	24.79%
$\Delta\theta$	0.81°	0.80°	0.72°

Table 7.1: Structural data for the reconstructed Au(100) surface in UHV [103,116], in 0.01 M HClO$_4$ [80] and in 0.1 M HCl. The table contains the electrode potential E, the unit cell parameters Δ_1 and Δ_2 in reciprocal space, the real space netplane spacings d(Δ_1) and d(Δ_2), the surface strain ϵ, the excess mass density $\Delta\sigma$ and the rotation angle $\Delta\theta$.

7.6 Potential-Dependence of Au(100)-'hex' in 0.1 M HCl

After this first structural characterization at $E = $ -0.2 V the electrode potential was step-wise varied from -0.4 V to 0 V and back in steps of 50 mV in order to probe the potential-dependence of the reconstructed surface phase. At each potential intensity profiles were recorded in radial and azimuthal direction through the two first-order reconstruction peaks $\vec{a_h^*}$ and $\vec{b_h^*}$. Figure 7.7a summarizes values for Δ_1 and Δ_2 obtained from Voigt-profile fits to the radial profiles. In the potential regime between -0.15 V and -0.4 V the reciprocal lattice parameters Δ_1 and Δ_2 are almost constant indicating a potential-independent size of the re-constructed surface unit cell. Towards more positive potentials, in particular for $E \geq $ -0.1 V, sufficiently pronounced radial intensity profiles in the anodic sweep direction reveal an in-crease of Δ_1, i.e. a compression of the reconstructed surface in 'x5' direction. Simultaneously a decrease in the radial FWHM (figure 7.7b), i.e. an increase in correlation length, as well as a small increase in the radial integrated intensity (figure 7.7c) is observed. The maximum of scattered intensity is achieved in the anodic potential sweep before the reconstruction is lifted at ≈ 0 V. An identical behavior has been reported in SXS studies of Au(111) electrodes in 0.1 M NaF [124]. According to Ocko et al. the intensity increase close to the critical potential, coming along with an increased domain size and a higher compression within the reconstructed surface layer, may be explained by an ordered array of reconstructed domains with different orientations which reduces the strain energy of the underlying substrate. This conclusion has been drawn from similar effects observed on Si(111) surfaces [125]. The az-imuthal intensity profiles have been fitted by a sum of three Voigt-profiles in order to obtain the potential-dependence of the rotation angle $\Delta\theta$. The results are summarized in figure 7.7d. The rotation angle is potential-independent in the entire potential regime of the recon-structed phase. In particular azimuthal profiles recorded directly after intermittent lifting of the reconstruction at 0 V feature two peaks rotated by 0.72°. This behavior clearly demon-strates that potential-induced reconstructed Au(100) electrode surfaces in Au-free electrolyte consist of predominantly rotated domains and confirms the finding of Ocko et al. that the
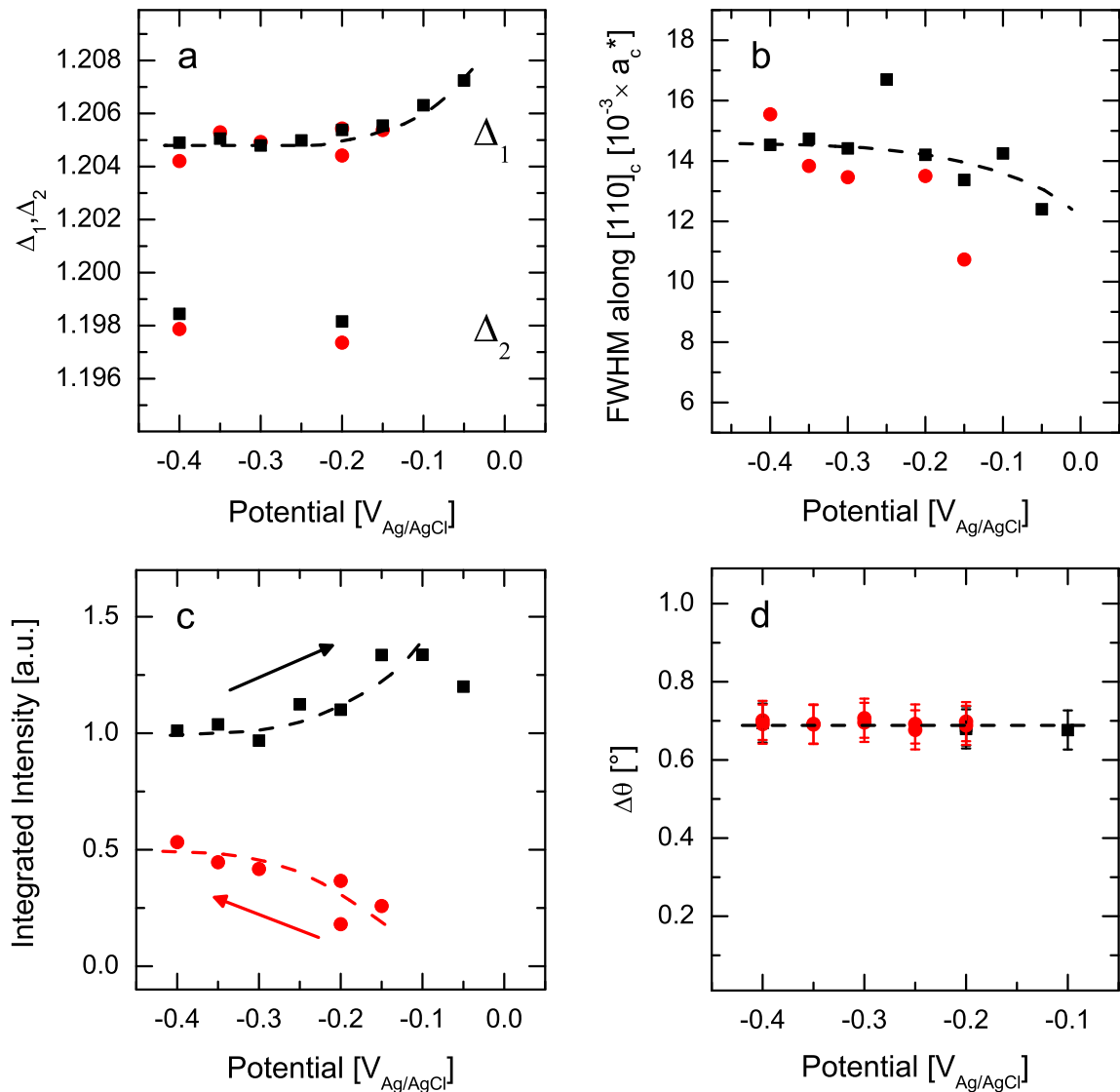
Figure 7.7: Potential-dependence of a) Δ_1 and Δ_2, of b) the FWHM recorded along the $[110]_c$ direction at $(\Delta_1, \Delta_1, 0.09)$, of c) the integrated intensity of the radial intensity profiles and of d) the rotation angle $\Delta\theta$ measured on reconstructed Au(100) electrodes in 0.1 M HCl. Squares symbolize values according to an anodic potential sweep, circles accord to a cathodic potential sweep. Dashed lines depict the potential-dependence in the data.

rotational transition from aligned to rotated domains is irreversible in solution. Error bars for $\Delta\theta$ have been fixed to 0.05°.

In summary, the analysis of the potential-dependence demonstrates that the reconstructed phase in 0.1 M HCl is almost static. Only for potentials $>$ -0.1 V a small compression of the surface phase has been found. The potential- and time-dependence of the FWHM in radial direction is weak indicating that the formation of larger domains is strongly hindered by the modality of the reconstruction formation process.

7.7 X-ray Voltammetry

In the previous sections the potential has been changed in comparatively large steps of $\Delta E \geq$ 50 mV followed by a characterization of the surface structure. This procedure results in extended holding times at each potential so that obtained data reflects the saturated surface structure. Another approach to study the phase transition is to cycle the potential quasi-continuously with a constant, comparatively low sweep rate and to monitor the intensity at a fixed position in reciprocal space that is sensitive to the reconstructed phase. This method is often referred to as X-ray voltammetry (XRV) and the resulting data is commonly termed as cyclic diffractogram (CD) [126, 127]. Such a cyclic diffractogram obtained with a sweep rate of 2 mV/s at the reciprocal space position $(\Delta_1, \Delta_1, 0.09)$ is shown in figure 7.8. The potential cycle starts with a well established reconstructed phase at -0.4 V as indicated by a high initial X-ray intensity and proceeds towards more positive potentials. In the anodic sweep up to 0.2 V the intensity first increases analog to the small increase in integrated intensity observed in the saturation values of the previous potential sweep experiment (section 7.6). The maximum in intensity is achieved at $E \approx$ -50 mV close to the critical potential of reconstruction. Subsequently, between -30 mV and +20 mV, the intensity rapidly drops to zero which is caused by the lifting of reconstruction. On the back cycle from
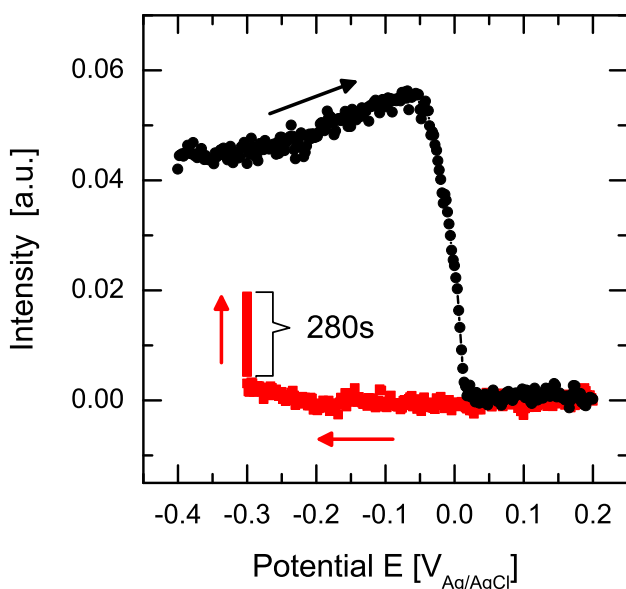
Figure 7.8: Cyclic diffractogram of Au(100) in 0.1 M HCl. The intensity was monitored at $(\Delta_1, \Delta_1, 0.15)$ parallel to potential cycles in positive sweep direction ($\bigcirc$) and negative sweep direction ($\square$) with a sweep rate of 2 mV/s.

0.2 V to -0.3 V the intensity recovers very slowly even in the reconstructed potential regime. At -0.3 V the potential cycle was stopped and a time scan monitored the time-dependence of the intensity. Including the potential cycle time between 0 V and -0.3 V the surface is 45 % reconstructed after 430 seconds. Thus, the observed intensity increase is in reasonable agreement with the data obtained in the potential step experiments.

7.8 Summary

The present chapter focused on the in-plane structure of Au(100) electrodes in Au-free 0.1 M HCl solution. At a constant electrode potential of $E = $ -0.2 V in the reconstructed potential regime reciprocal lattice parameters of $\Delta_1 = 1.2053 \pm 0.0005$ and $\Delta_2 = 1.1980 \pm 0.0010$ were determined which accord to an excess mass density of $\Delta\sigma = 24.79\%$ and a surface strain of $\epsilon = $ -19.90% with respect to the unreconstructed (1×1) bulk structure. These values resemble structural data found by Ocko et al. for Au(100) electrodes in 0.01 M HClO$_4$ [80] and they are furthermore close to the structural data carried out for Au(100) surfaces under UHV conditions [103, 116]. In 0.1 M HCl the netplane spacing perpendicular to the reconstruction stripes is almost identical to the spacing in UHV while the 'hex' structure appears to be expanded in direction of the reconstruction stripes. Reconstructed domains are preferentially rotated by an angle of $\Delta\theta = 0.72°\pm0.05°$ with respect to the $[110]_c$ direction. This finding agrees with earlier observations in 0.01 M HClO$_4$ and a similar rotation angle of 0.8° has been as well found in UHV for temperatures below $T = 970$ K. While the UHV studies reported a temperature-dependent reversible rotational transition from aligned to rotated domains and vice versa, the transition is irreversible under electrochemical conditions. This was found by Ocko et al. for Au(100) electrodes in perchloric acid and could be confirmed for Cl⁻ containing electrolyte. Subsequent potential studies revealed that almost in the entire potential regime of the reconstructed phase, more precisely between -0.15 V and -0.4 V, neither the size of the surface unit cell nor the rotation angle $\Delta\theta$ exhibits a pronounced potential-dependence. For potentials $\geq$-0.1 V a small compression of the reconstructed surface layer has been found similar to those observed for Au(111) electrodes in 0.01 NaF solution. Once the surface is reconstructed the average domain size in the 'x5' direction (perpendicular to the reconstruction stripes) does not change with potential which is expected due to the modality of the reconstruction formation process. The (1×1) → 'hex' surface phase transition in 0.1 M HCl is a comparatively slow process in agreement with earlier STM studies in 0.01 M HClO$_4$ [89]. The electrode surface was found to be 90% reconstructed approximately 17 min after a potential step into the reconstructed potential regime.

8 In-plane Structure of Au(100) in Au Containing Electrolyte

In this chapter the influence of homoepitaxial growth on the lateral structure of the 'hex' reconstructed Au(100) electrode surface is discussed. While homoepitaxial growth on Au(100) surfaces has been investigated under UHV conditions via STM [4, 5], no structure sensitive Au/Au(100) deposition study under electrochemical conditions has been reported so far. The first real-time in-situ experiment of electrochemical growth under realistic reaction conditions has been previously performed in our group by Ayyad and coworkers who investigated the in-plane structure of Au(111) electrodes in chloride and gold containing solutions using the SXS technique [12]. According to this study an interesting influence of homoepitaxial growth on the lateral surface structure of the reconstructed Au(111) surface was determined: the growth process induces an enhanced compression in the reconstructed layer which increases linearly towards more negative potentials. In a similar manner as Ayyad et al. we performed homoepitaxial growth experiments on Au(100) electrodes. In contrast to reconstructed Au(111) surfaces the 'hex' reconstructed Au(100) layer exhibits a comparatively large surface strain $\epsilon \approx$ -20 % with respect to the unreconstructed (1×1) bulk structure. Furthermore the studies of Ocko et al. [80] and the present surface characterization in Au-free electrolyte (chapter 7) have shown the presence of 'hex' reconstructed domains which are rotated by an angle $\Delta\theta$ about the $[110]_c$ direction of the substrate layer. We will demonstrate that homoepitaxial growth has a pronounced influence on the lateral structure of the reconstructed phase as well as on the orientation of reconstructed domains with respect to the unreconstructed substrate. The reader be referred to the beginning of chapter 7 for the in-plane diffraction pattern of unreconstructed and reconstructed Au(100) electrodes.

The present chapter is divided into the following parts. First, section 8.1 summarizes briefly the results of previous growth studies carried out on Au(100) surfaces under UHV conditions. Then we will discuss growth-induced changes in the lateral structure of the 'hex' reconstructed Au(100) surface. The results will be compared with the 'hex' structure in Au-free electrolyte (chapter 7). Structural changes were monitored in parallel to an electrolyte exchange from Au-free to Au-containing solution while the electrode potential was kept in the reconstructed potential regime. The respective data analysis, presented in section 8.2, focuses on the time-dependence of the reciprocal lattice parameter Δ_1 and on the rotation angle $\Delta\theta$. Subsequent to an exchange, i.e. in stagnant Au-containing solution, the potential-dependence of the lateral structure of the reconstructed Au(100) electrode was determined revealing a similar electrocompression effect as observed for reconstructed Au(111) electrodes [12]. Besides of lattice parameters we will concentrate on the domain structure, i.e. on the size of domains (section 8.3.1) and on the orientation of reconstructed domains with respect to the (1×1) bulk structure (section 8.3.2). Furthermore we will discuss the kinetics of the (1×1) → 'hex' surface phase transition (section 8.5) which leads to a simple model describing the formation of the electrocompressed phase subsequent to potential steps into the reconstruction regime (section 8.6). The chapter concludes with a quantitative analysis of the Au(100) electrocompression effect and a theoretical explanation of the electrocompression phenomenon based on a simple continuum model (section 8.7).

8.1 Homoexpitaxial Growth on Au(100) under UHV Conditions

Homoepitaxial growth on reconstructed Au(100) surfaces is a complex process. According to STM studies under UHV conditions the growth proceeds anisotropic and deposited gold atoms contribute to the formation of reconstruction stripes on top of the reconstructed substrate [4]. The orientation of these reconstruction stripes is specified by the orientation of reconstructed domains in the underlying layer (figure 8.1). More precisely, the 'x20' directions of reconstructed domains in the substrate layer and of deposited reconstruction stripes run parallel. Figure 8.1 shows an UHV-STM image of 0.2 ML gold deposited on a Au(100) surface [4]. The same and further studies indicated an anisotropic diffusion of single adatoms at the perimeter of growing, reconstructed islands with a fast mass transport of adatoms along the 'x20' direction and a slow mass transport along the 'x5' direction [4,128]. Parallel to the deposition process and parallel to the formation of reconstructed islands, covered reconstructed regions in the underlying substrate layer transform back to the (1×1) bulk structure. According to a molecular dynamical simulation of Nomura and Wang an interlayer transport of atoms from the substrate layer to the top layer takes place at the edges of growing domains [104]. Respective atoms participate successively in the growth of the new layer. The same theoretical study suggests that the optimal island is 'quantized' in concord to the 'magic' size of 7, 13, ..., $6n + 1$ (n is an integer) reconstruction stripes and that the formation of a hexagonally reconstructed island on an unreconstructed substrate is energetically favored.
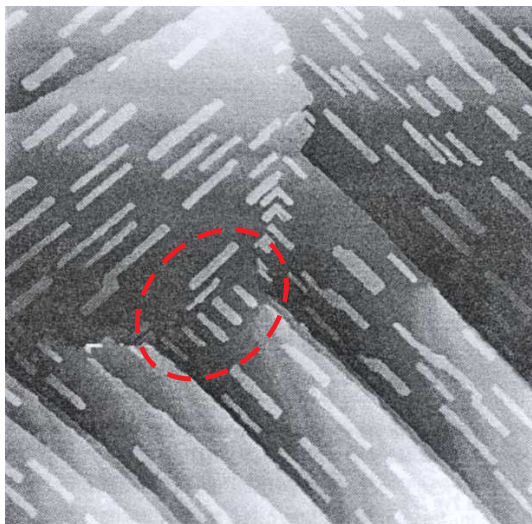
Figure 8.1: UHV-STM image of a reconstructed, stepped Au(100) surface after deposition of 0.2 ML gold (size: 3400Å × 3400Å). Reconstructed Au islands with widths of multiples of one reconstruction stripe are formed which are aligned along the 'x20' direction of underlying reconstructed domains. This indicates strongly anisotropic growth on the reconstructed substrate. The dashed circle points out a domain boundary between two perpendicular oriented domains within the substrate layer. (from [4])

8.2 Structural Changes During Electrolyte Exchange

The in-plane structure of Au(100) electrodes during homoepitaxial deposition has been predominantly studied at the ESRF[1] in Grenoble. Based on the improved instrumental setup,

---

[1]ESRF, E = 18.2 keV, presample slits: vg = 0.05 mm and hg = 0.25 mm, detector slits: dvs = 3 mm and dhs = 1mm

in particular on the homebuilt, remote-controlled electrolyte exchange system, we are able to investigate structural changes during an electrolyte exchange from Au-free to Au-containing solution, i.e. in direct onset of homoepitaxial growth on the unreconstructed or reconstructed electrode surface. After a first characterization in Au-free electrolyte, the pushing syringe of the electrolyte exchange system was filled with electrolyte containing $0.1\,M$ HCl and $50\,\mu M$ HAuCl$_4$. Then the electrolyte in the cell ($0.1\,M$ HCl) was replaced by the Au containing electrolyte at an electrode potential of -0.2 V in the reconstructed potential regime which resulted in the onset of Au deposition onto the reconstructed Au(100) surface. In order to achieve a smooth crossover from Au-free to the Au-containing electrolyte and to ensure that the whole electrolyte in the cell is being replaced an amount of 4 ml has been exchanged with a relatively low flow rate of $5\,\mu l/s$. In doing so the time window was sufficiently extended to monitor structural surface changes by SXS parallel to the exchange procedure.

The electrolyte exchange process from Au-free to Au-containing solution (started at $t=0$) took 800 s. During this time interval the laminar flow of the electrolyte through the cell at $5\,\mu l/s$ (corresponding to a flow of several mm/s parallel to the Au surface) resulted in a reduced diffusion layer thickness and consequently in an increase in the deposition rate by up to a factor of 10 as compared to the rate found in stagnant solution (see section 9.7). The latter has been determined after completion of the electrolyte exchange by a potential jump experiment from $0.5\,V$ in the unreconstructed potential regime to $0\,V$ close to the surface phase transition. Figure 8.2 shows the intensity recorded at the reciprocal space position $(1\,,1\,,0.09)$ parallel to the potential-step experiment. The time-dependent intensity exhibits oscillations which are attributed to layer-by-layer growth. From the average oscillation period, $\overline{T} = 386\,s$, a deposition rate[2] of $\approx 0.16\,ML/min$ is inferred. Taking into account the volume of the upper cell compartment (400 to $500\,\mu l$) and the exchange rate of $5\,\mu l/s$ the onset of deposition initiates with a time delay of $\approx 1.5\,min$ (see below). As soon as the Au-containing electrolyte arrives at the meniscus the Au concentration near the Au(100) surface is identical to the concentration within the replacing electrolyte due to the cell geometry (section 5.2). Hence, in the 800 s time span of electrolyte exchange ($R \approx 1.6\,ML/min$) an amount of gold equivalent to approximately 19 monolayers has been deposited. Nevertheless, even at these enhanced rates the deposition at this potential proceeds via layer-by-layer growth according to results which will be presented in chapter 9. Therefore, the growing Au(001) surface remains sufficiently smooth during the exchange to investigate the changes in the in-plane surface structure in-situ. For this the intensity profile of the $(\Delta_1\,,\Delta_1\,,0.09)$ reflection was monitored parallel to the electrolyte exchange by alternatingly performing in-plane azimuthal (figure 8.3a) and radial (figure 8.3b) scans. Each pair of scans requires approximately 70 s, defining the time resolution by which structural changes due to the onset of Au deposition can be followed. The radial scans, shown in figure 8.3b, exhibit a shift of the reconstruction peak towards larger values, indicating a compression of the reconstructed layer in 'x5' direction. Within the first 300 s after start of the exchange process Δ_1 shifts from Δ_1 = 1.204 in Au-free $0.1\,M$ HCl solution to Δ_1 = 1.208 in the Au-

---

[2]The deposition rate R (given in ML/min) is identical for growth on the reconstructed and on the unreconstructed surface, respectively, since the layer below the reconstructed surface layer transforms back to the (1×1) bulk structure.

Potential-Step Experiment
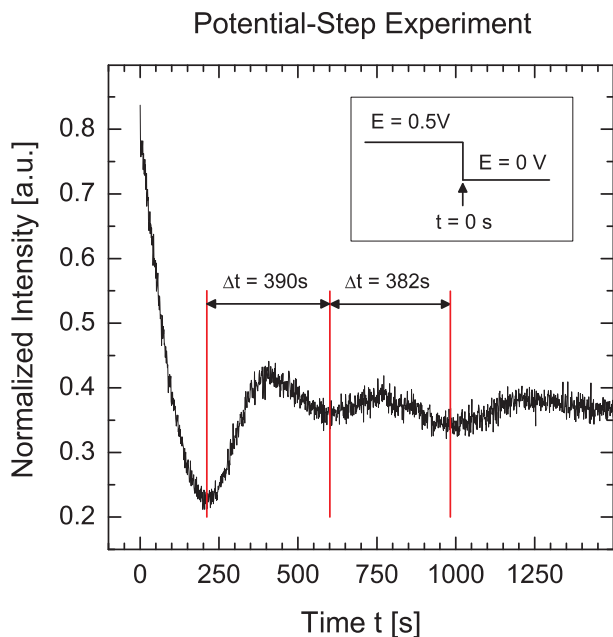
Figure 8.2: Potential-step experiment from 0.5 V to 0 V in order to determine the deposition rate in stagnant 0.1 M HCl + 0.05 mM HAuCl$_4$ solution. The average oscillation period of the layer-by-layer growth oscillations in X-ray intensity is $\overline{T} = 386$ s corresponding to a deposition rate of ≈ 0.16 ML/min.

containing solution. We will see in the following that under the chosen deposition conditions Δ_1 = 1.208 is a typical value for the reconstructed surface phase at an electrode potential of -0.2 V (c.f. figure 8.14a). For $t > 300$ s, i.e. after approximately 5.6 deposited monolayers, Δ_1 stays at the constant saturation value of 1.208. Both trends are marked by solid lines in figure 8.3b. The recorded radial intensity data were fitted by Voigt profiles with a FWHM of σ_G = 0.0045° for the instrumental resolution. This compression phenomenon resembles observations for Au(111) homoepitaxial electrodeposition [12] and will be discussed in more detail in the following sections. In the simultaneously recorded azimuthal scans (figure 8.3a) a decrease of the rotation angle $\Delta\theta$ with ongoing deposition time is observed, suggesting that Au deposition induces an alignment of the 'hex' domains along the $[110]_c$ direction. Moreover this rotation towards the $[110]_c$ axis manifests in an increase of intensity along the $[110]_c$ direction as the shoulders of the intensity profiles of rotated domains overlap and additionally the fraction of aligned domains increases. Only the scans recorded within the first 5 minutes (coverage ≈ 5.6 ML) clearly show peaks of the rotated domains, whereas at later times the peaks merge, indicating a more continuous orientation distribution. Consequently for $t \geq 5$ min the contribution of aligned domains cannot be clearly separated from those of the rotated domains. However, even after 10 minutes (coverage ≥ 13.6 ML) the scans cannot be perfectly fitted by single Voigt-profiles, suggesting that the final state after exchange at -0.2 V contains at least some degree of preferred orientation for rotated domains.

The azimuthal data have been fitted in three different ways in order to determine the time-dependence of the contributing intensity profiles of aligned and rotated domains, respectively. First the data have been fitted with three Voigt profiles as described in the previous chapter. All parameters, i.e. the FWHM and the amplitude of aligned domains, the FWHM and the amplitude of rotated domains and the rotation angle $\Delta\theta$ were free fit parameters. The results of this procedure are presented as 'Fit 1' in figure 8.5. For the intensity profiles
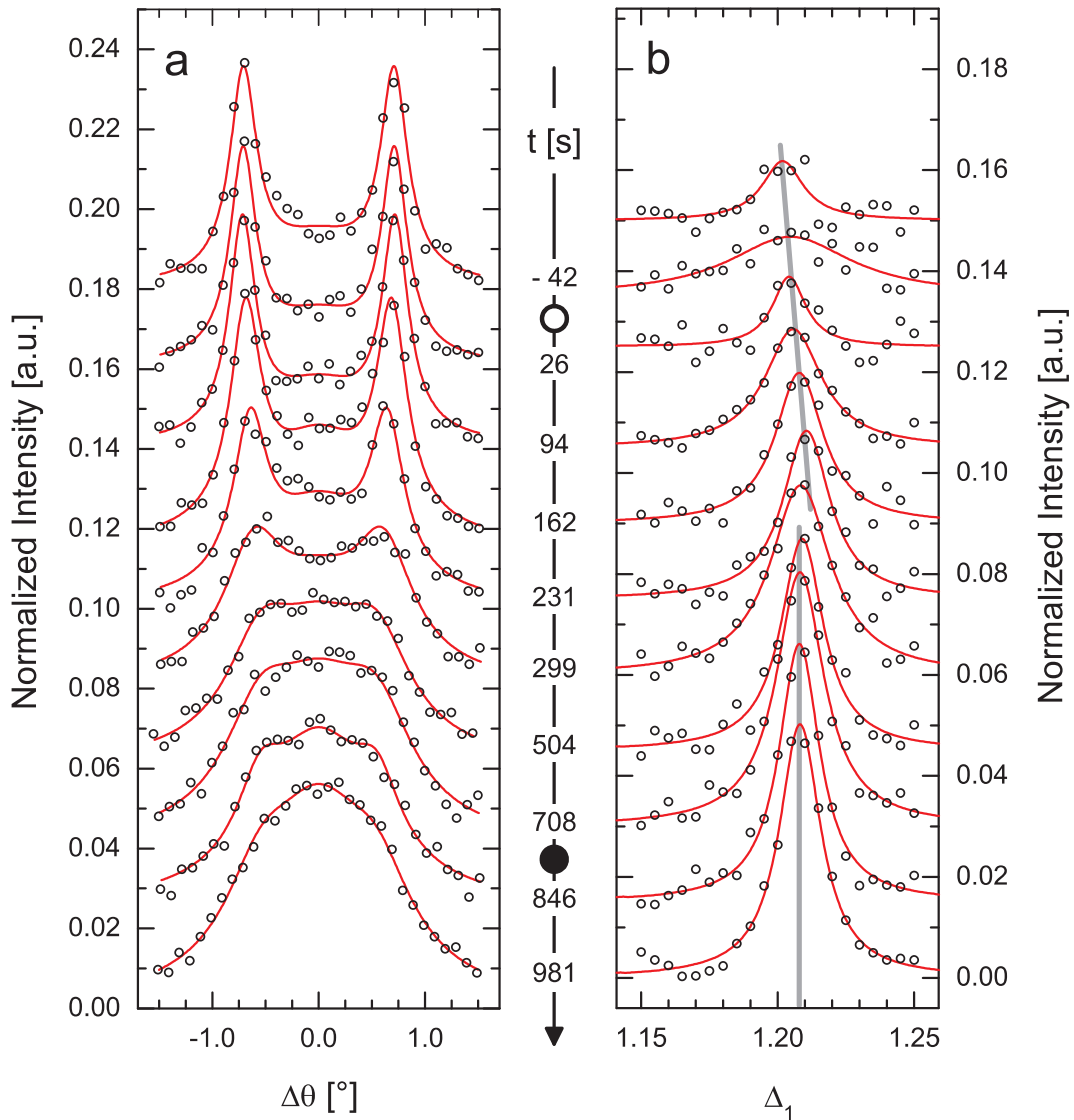
Figure 8.3: Intensity profiles recorded at an electrode potential of -0.2 V during electrolyte exchange from Au-free 0.1 M HCl solution to 0.1 M HCl + 50 μM HAuCl$_4$. Between $\circ$ ($t = 0$ s) and $\bullet$ ($t = 800$s) 4 ml of electrolyte have been exchanged with a speed of 5 μl/s. a) Azimuthal rocking scans across (Δ_1, Δ_1, 0.09). b) Radial in-plane scans along [110]$_c$ through the first order reconstruction rod. The gray solid lines mark the shift observed in Δ_1 during the first ≈ 300 s and the constant Δ_1 after 300 s. For clarity all curves are shifted with respect to each other.

of rotated domains an increase in the azimuthal FWHM from 0.3° to 1° is observed while simultaneously the azimuthal FWHM of the intensity profiles of aligned domains decreases from 1.2° to 0.4°. The integrated azimuthal intensity of rotated domains, given in arbitrary units, increases by a factor of two from 0.04 to 0.08. Since the integrated azimuthal intensity of aligned domains is approximately constant (0.02) the integrated intensity over the

whole azimuthal profile increases with time. In order to obtain the total integrated intensity of the splitted reconstruction peak at $\vec{b}_h^*$ the azimuthal intensity has to be multiplied with the FWHM of radial intensity profiles. The time-dependence of the latter is shown in figure 8.4a. It decreases with time from initially $\approx 0.025\,a_c^*$ at $t = 0$ to $\approx 0.019\,a_c^*$ at $t = 20\,\text{min}$.

The resulting time-dependence of the integrated intensity at the reconstruction peak $\vec{b}_h^*$ is summarized in figure 8.4b. According to this, the total integrated intensity remains constant during the electrolyte exchange. This finding demonstrates that the surface coverage by the reconstructed phase does not change due to the onset of Au deposition. Furthermore it is important to mention that the intensities observed in radial or azimuthal intensity profiles are strongly correlated and that they influence each other. The time-dependent decrease of the FWHM in radial direction along $[110]_c$ and the simultaneously constant integrated intensity indicates an ordering process within the reconstructed surface layer induced by the homoepitaxial deposition process. Indeed, several studies show that the reconstructed surface phase, both in Au-free and Au-containing electrolyte, is not static but subject to a time-dependent in-plane ordering mechanism [64, 89]. In contrast to the studies within Au-free electrolyte the in-plane ordering under deposition conditions appears to proceed on a considerably faster time-scale. This effect is consistent with a smaller degree of surface roughness connected to the layer-by-layer growth mode which potentially results in a lower density of surface defects (especially vacancies) and consequently in an increased order within the reconstructed surface layer. The phenomenon of in-plane ordering will be discussed in more detail in chapter 10.
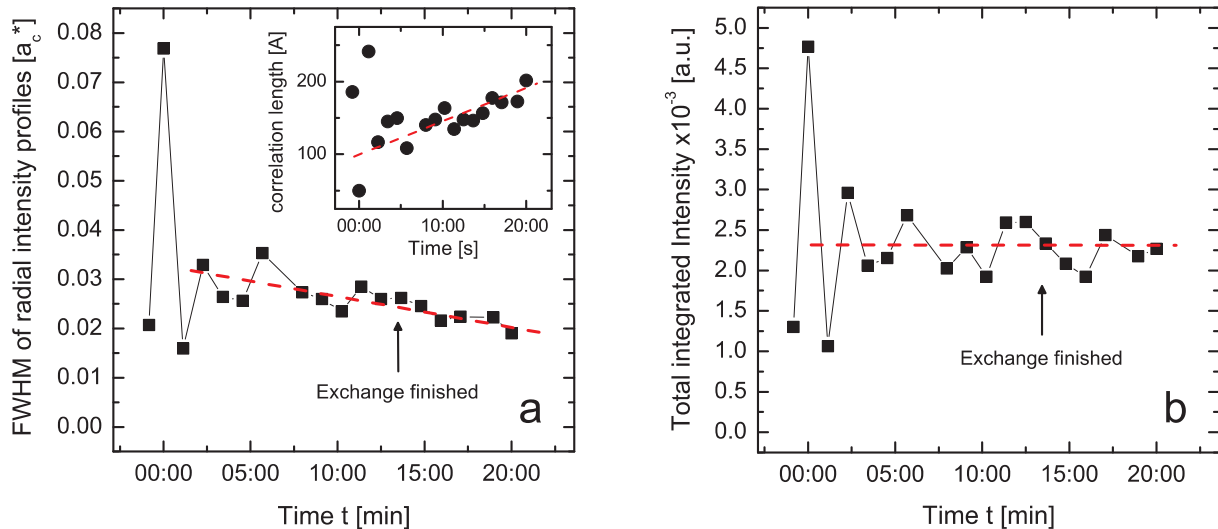
Figure 8.4: a) FWHM of radial intensity profiles across $(\Delta_1, \Delta_1, 0.09)$ recorded parallel and subsequent to an electrolyte exchange from $0.1\,\text{M}$ HCl to $0.1\,\text{M}$ HCl + $0.05\,\text{mM}$ HAuCl$_4$. The inset shows the time-dependence of the according correlation length. b) Total integrated intensity obtained by multiplication of the FWHM in radial intensity profiles with the integrated intensity in the azimuthal profiles.
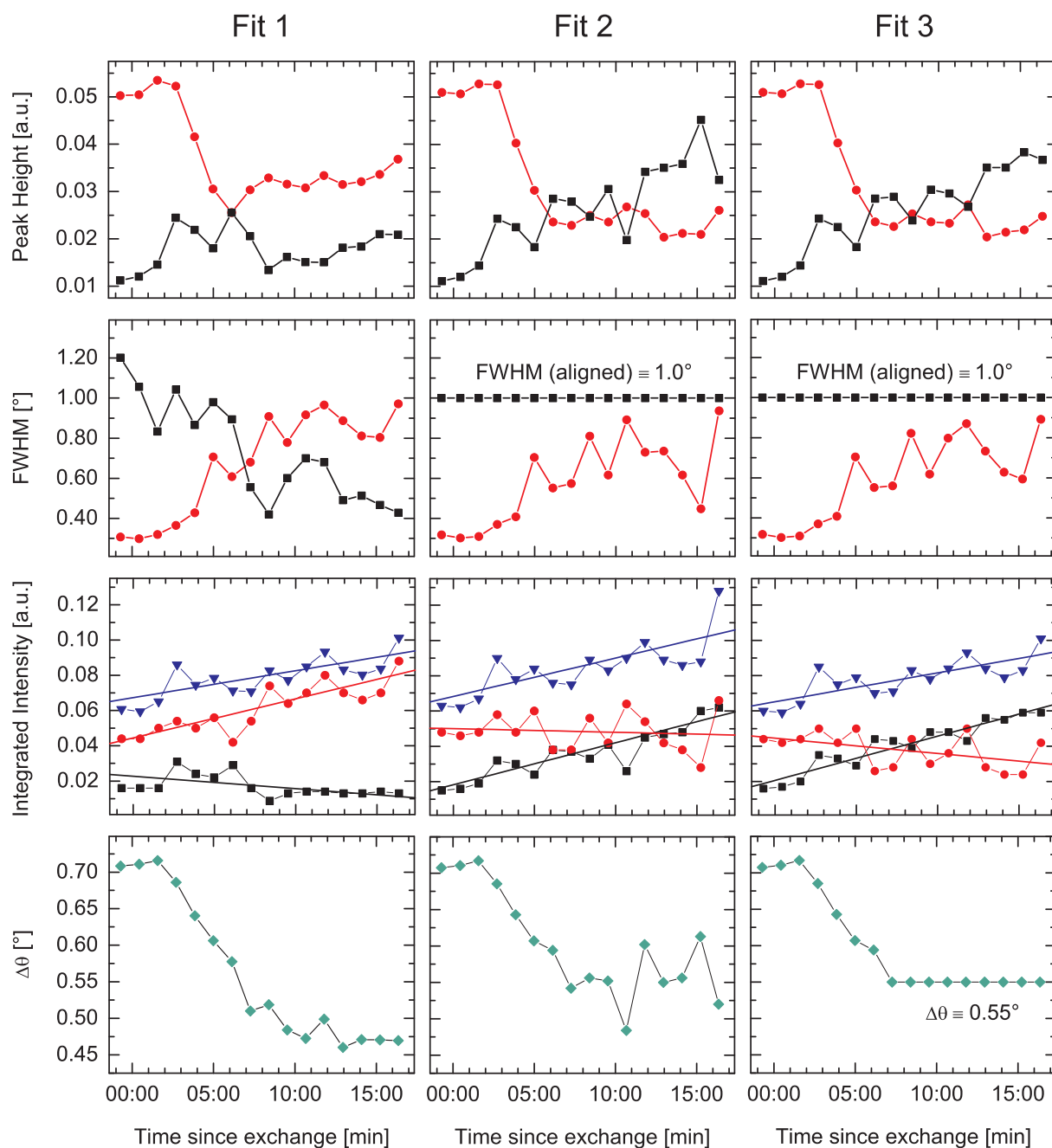
Figure 8.5: Time-dependence of the peak height, the FWHM and the integrated intensity of aligned domains (■) and rotated domains (●) after start of the electrolyte exchange according to three different fit procedures (Fit 1 to 3) applied to the azimuthal SXS data. Additionally the graphs show the total integrated intensity (▼) of the azimuthal profiles and the rotation angle $\Delta\theta$ (◆). Linear fits to the integrated intensities point out the observed trends.

Within the framework of 'Fit 1', the rotation angle $\Delta\theta$ decreases from initially $0.71°$ in Au-free solution to about $0.47°$ for $t \geq 10\,min$ in Au-containing solution. However, merging of all peaks sets in after $5\,min$ and restricts the relevance of the fit for $t > 5\,min$ as the parameters are strongly correlated. In order to reduce the amount of parameters a second fit has been performed, presented as 'Fit 2' in figure 8.5, where the FWHM of the aligned domains has been fixed to $1°$. This value was chosen on the basis of the FWHM in 'Fit 1' which is approximately $1°$ within the first 5 minutes. The time-dependence of the FWHM of intensity profiles of rotated domains is similar to those obtained in 'Fit 1'. In the integrated intensity now a constant value of 0.05 is found for rotated domains while the integrated intensity of aligned domains increases from 0.02 to 0.06. However, the run of total integrated intensity, i.e. the sum of all three peak intensities, is identical with the run found in 'Fit 1'. In the framework of 'Fit 2' the rotation angle $\Delta\theta$ decreases within the first 7 minutes from $0.71°$ to about $0.55°$ in conformity with 'Fit 1'. In the following, i.e. for $t \geq 7\,min$, $\Delta\theta$ varies around $0.55°$ providing no additional information about the time-development of $\Delta\theta$ in view of relatively large errors. For this reason a third fit of the dataset has been carried out by fixing the FWHM of the intensity profiles of aligned domains to $1°$ and by fixing the rotation angle $\Delta\theta$ to $0.55°$ after $t = 7\,min$. The results are presented as 'Fit 3' in figure 8.5. 'Fit 2' and 'Fit 3' are almost identical in the time-dependence of the fitting parameters. In a direct comparison with figure 8.3a the rotation angle $\Delta\theta = 0.55°$ may be interpreted as upper limit of the final rotation angle associated with a larger error of approximately $0.1°$ towards lower angles. In the following we will focus on 'Fit 3' as it allows to describe the data with the smallest amount of parameters.

Quantitative data on the radial peak position Δ_1 and the orientation $\Delta\theta$ of the rotated domains are plotted in figure 8.6 versus time since start of the electrolyte exchange. The Δ_1 values were taken from the Voigt-profile fits shown in figure 8.3b and the $\Delta\theta$ values are identical to those of 'Fit 3'. As the peak profiles along the $[110]_c$ direction have initially
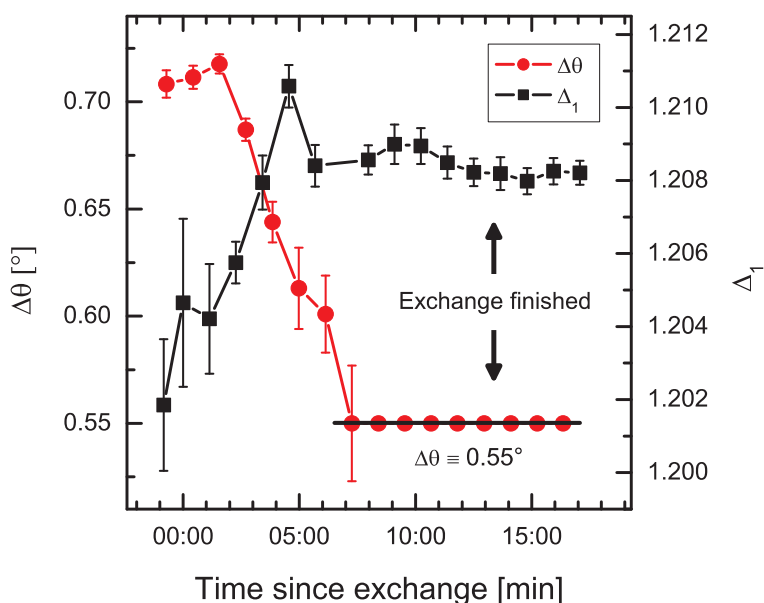
Figure 8.6: Rotation angle $\Delta\theta$ and Δ_1 versus elapsed time since start of the electrolyte exchange ($t = 0$). The exchange-induced changes in both quantities seem to be correlated as both, $\Delta\theta$ and Δ_1, reach after approximately $7\,min$ constant values of $0.55°$ and 1.208, respectively.

low intensity the error bars are correspondingly large for Δ_1. By contrast the error bars for $\Delta\theta$ are initially small as the azimuthal profiles show distinct peaks for the rotated domains but they increase with time once the peaks start merging. The graph shows that Δ_1 and $\Delta\theta$ are approximately constant within the first 1.5 min after initiation of the electrolyte exchange corresponding to an injected volume of $450\,\mu$l. This conforms to the time needed to replace the electrolyte in the upper cell compartment. In the following, i.e. for $t > 1.5$ min, electrodeposition sets in as the Au-containing electrolyte arrives at the meniscus and Δ_1 and $\Delta\theta$ begin to shift. Apparently the exchange-induced rotational transition and the change of compression correlate and reach almost at the same time, i.e. ≈ 7 min after start of the exchange process (coverage ≈ 9 ML), saturation values of $\Delta\theta = 0.55° \pm 0.05°$ and $\Delta_1 = 1.208 \pm 0.001$, respectively. A short time before Δ_1 reaches its saturation value a comparatively large value of 1.2106 is noticeable. The origin of this temporary increase in Δ_1, which can be even seen in the raw data (figure 8.3b), is not clear and has not been reproduced.

8.3 Potential-Dependence of the In-plane Surface Structure During Deposition

The following experiments[3] have been carried out subsequent to the electrolyte exchange in stagnant solution. In order to study the potential-dependence of $\Delta\theta$ and the electrocompression effect during Au electrodeposition the in-plane lattice parameters were measured while changing the potentials from -0.4 V to -0.1 V and back to -0.4 V in steps of 50 mV approximately every 6 minutes. This resting time at each potential corresponds to the deposition of approximately one monolayer. To prevent changes in the Au concentration near the electrode surface $200\,\mu$l of fresh electrolyte have been injected into the meniscus (exchange rate $5\,\mu$l/s) in time intervals of ≈ 12 min, i.e. after every second potential step. The potential sweep procedure has been repeated so that two complete potential cycles were recorded, in the following termed as 'first cycle' and 'second cycle' (depicted in the upper part of figure 8.8). In detail, the anodic and cathodic potential sweeps have been performed as follows. Subsequent to the exchange process the potential was stepped from -0.2 V to -0.3 V followed by the first potential sweep up to -0.1 V in positive sweep direction. At -0.1 V an amount of $500\,\mu$l electrolyte has been exchanged to replenish the Au concentration. This procedure resulted in a vanish of the reconstruction peak even though the electrode potential has been kept in the reconstructed potential regime. According to the growth mode studies in chapter 9 the enhanced deposition rate of 1.6 ML/min during the electrolyte exchange at -0.1 V is supposed to result in 3D growth which probably caused the observed influence of the exchange process on the reconstructed surface phase (cp. figure 9.8). After 12:30 min at -0.1 V the potential has been swept in negative direction to -0.4 V in a second potential sweep. Between the first and the second potential cycle, i.e. between the first cathodic sweep and the second anodic sweep, the footprint of the X-ray beam changed its position on the sample surface and a different surface area has been illuminated. As will be seen below this resulted in a sudden decrease in the FWHM in consecutive radial intensity profiles and in

---

[3]ESRF, $E = 18.2$ keV, presample slits: vg $= 0.05$ mm and hg $= 0.25$ mm, detector slits: dvs $= 3$ mm and dhs $= 1$mm

a sudden intensity increase in consecutive azimuthal intensity profiles, all recorded at the same electrode potential of -0.4 V. In the subsequent two potential sweeps the new position of the footprint on the sample surface was maintained. The third potential sweep in positive direction was initiated after a waiting time of 12:16 min at -0.4 V and ends at -0.05 V where the reconstruction peak along $\vec{b}_h^*$ vanished completely, i.e. the reconstruction is at least partly lifted. In order to avoid degradation of the surface quality a fourth sweep to -0.4 V has been initiated directly after completion of the scans at -0.05 V, i.e. after a holding time of 1:44 min. At each potential radial and azimuthal scans were performed at the two first order reciprocal space lattice vectors $\vec{a}_h^*$ and $\vec{b}_h^*$ of the 'hex' reconstruction.

8.3.1 Potential-Dependence of Radial Scans

Figure 8.7 shows radial intensity profiles recorded at $\vec{b}_h^*$, i.e. along the $[110]_c$ direction, including the $(1, 1, 0.09)$ anti-Bragg position on the $(1, 1)$ bulk rod and $(\Delta_1, \Delta_1, 0.09)$ on the reconstruction rod. The graph clearly shows a shift of Δ_1 towards larger values with decreasing electrode potential, while the positions of the bulk intensity profiles are potential-independent and situated at $\Delta_1 = 1$. Both trends are emphasized by straight lines in the graph. Obviously the dependence of the reconstruction peak position on the electrode potential is reversible. Towards more negative potentials the reconstructed surface layer contracts along the 'x5' direction while it expands in the opposite potential sweep direction. Furthermore the intensity profiles are the more intense the more cathodic the electrode potential. This increase in intensity is caused by the higher driving force for surface reconstruction on more negatively charged surfaces and additionally by the alignment of rotated domains along the $[110]_c$ direction (see below). Profiles recorded at $\vec{a}_h^*$ exhibit a similar behavior but the potential-induced shift in Δ_2 is less pronounced. On this account we desist from plotting the data in a separate graph but refer to the quantitative analysis presented in section 8.7. In the following we analyze the potential-dependence of the radial FWHM and of the integrated intensity at the two first order reconstruction peaks $\vec{a}_h^*$ and $\vec{b}_h^*$. These two quantities provide information about the average size of 'hex' domains and about the coverage of the electrode with the reconstructed phase. It is important to notice that both of the latter are determined by the growth kinetics of reconstructed domains which on the other hand depends on the history of the sample.

The radial intensity profiles of the reference peak and of the two first order reconstruction peaks at $\vec{a}_h^*$ and $\vec{b}_h^*$, respectively, have been fitted by Voigt-profiles. From those fits the potential-dependence of the FWHM has been obtained for each potential sweep. The results are summarized in the figures 8.8a to 8.8c. Values for potentials close to the critical potential are afflicted with larger error bars as the peak profiles are less pronounced. In particular radial intensity profiles taken at potentials > -0.15 V exhibit an high uncertainty in the FWHM and are therefore not considered in figure 8.8.

Radial FWHM of the Bulk Reference Peak. The FWHM of the bulk reference peak at $(1, 1, 0.09)$ increases with time. During the first anodic sweep it constitutes approximately $0.004 \cdot a_c^*$ corresponding to a correlation length of 959 Å as estimated by equation 7.4. This
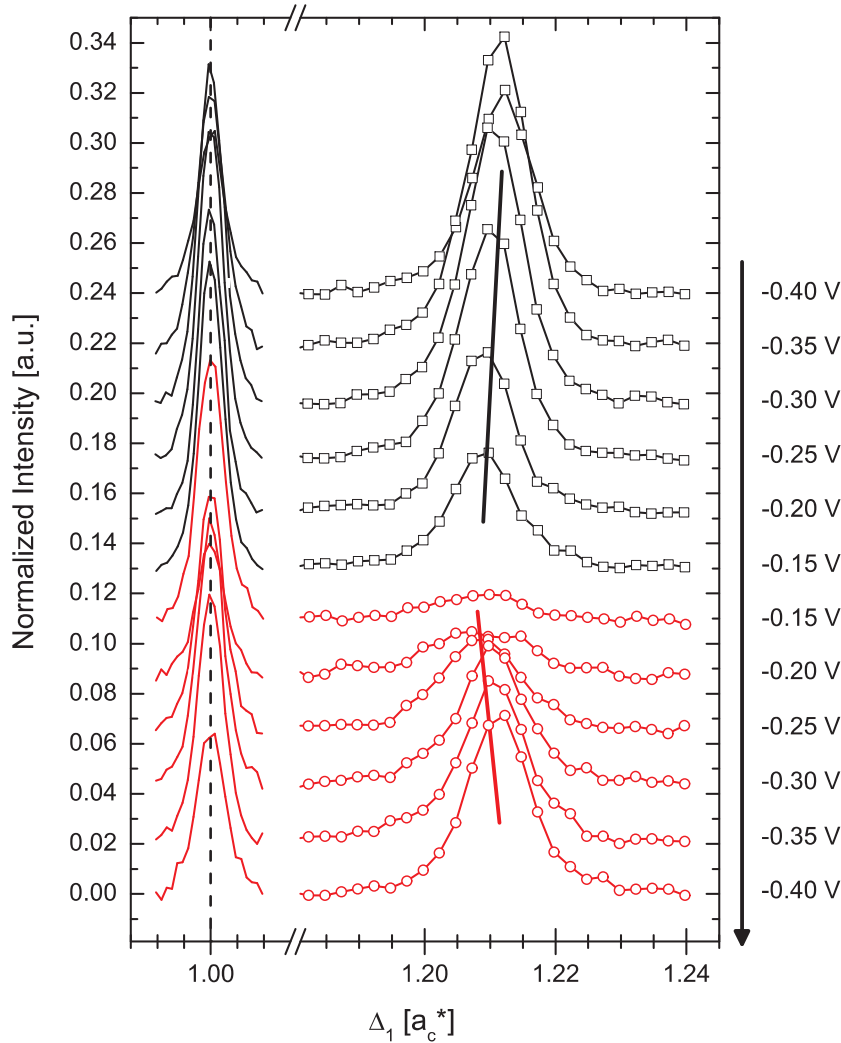
Figure 8.7: Potential-dependence of radial scans across $(\Delta_1, \Delta_1, 0.1)$ of the Au(100) electrode in $0.1\,\mathrm{M}$ $\mathrm{HCl} + 50\,\mu\mathrm{M}$ $\mathrm{HAuCl_4}$. Each scan has been recorded after $50\,\mathrm{mV}$ potential steps into negative or positive direction and in time intervals of approximately 6 minutes. Two solid lines mark the shift observed in Δ_1. The curves are shifted with respect to each other for clarity.

correlation length is comparable with those found for freshly prepared Au(100) crystals (cp. section 5.5). With further potential sweeps the FWHM then increases until it takes a value of $\approx 0.0065 \cdot a_c^*$ in the fourth potential sweep corresponding to a correlation length of $590\,\mathring{\mathrm{A}}$. This decrease in correlation length indicates a decrease in the ordering of the (1×1) structure near the surface being induced by the potential cycling and likely promoted by imperfect layer-by-layer growth.

Radial FWHM of the Reconstruction Peak at $\vec{b}_h^*$. Due to the smaller average domain size in 'x5' direction, the initial FWHM of the reconstruction peak at $(\Delta_1, \Delta_1, 0.09)$ is significantly larger. In the first anodic potential sweep the FWHM is almost constant and a value of $\approx 0.014 \cdot a_c^*$ is found corresponding to a correlation length of $274\,\mathring{\mathrm{A}}$ in 'x5' direction. In the subsequent cathodic potential sweep (performed after electrolyte exchange) a significantly larger FWHM of $0.03 \cdot a_c^*$ is found at -0.2 V indicating the reformation of the reconstructed phase. Towards more negative potentials and parallel to the advancing formation of reconstruction, the FWHM then decreases and takes a value of $0.012 \cdot a_c^*$ at -0.4 V. During the
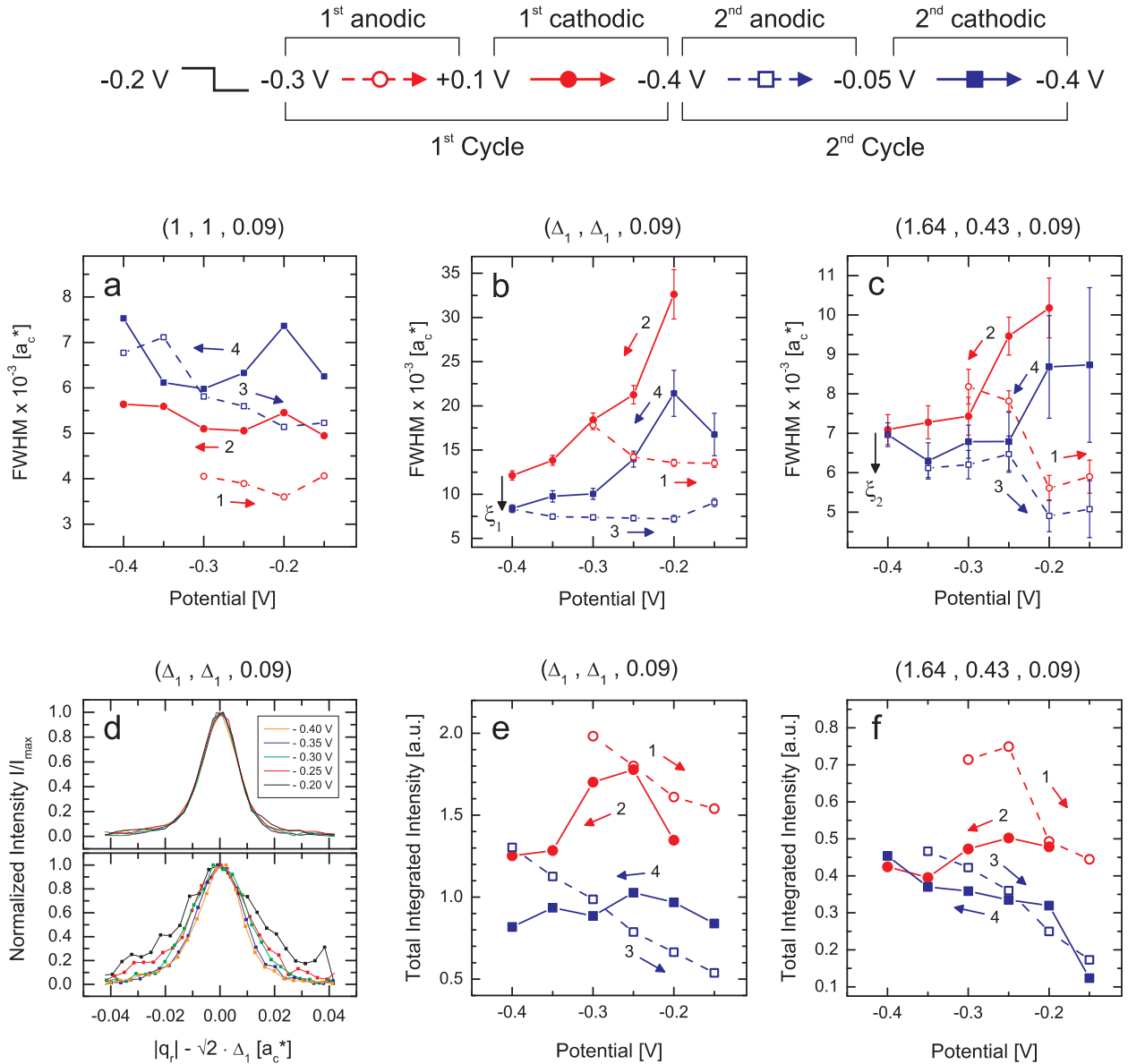
Figure 8.8: Potential-dependence of the FWHM of radial intensity profiles recorded at a) the bulk reference peak, b) the reconstruction peak $\vec{b}_h^*$ and c) the reconstruction peak $\vec{a}_h^*$. Two complete potential cycles are shown ($\circ$ and $\square$), each of them consisting of an anodic sweep from -0.4 V to -0.1 V (open symbols and dashed lines) and of a cathodic sweep from -0.1 V to -0.4 V (solid symbols and solid lines) in steps of 50 mV. At each potential an approximate time of 6 min has been rested corresponding to the deposition of ≈ 1 ML. In figure d radial intensity profiles are shown for the 3rd and the 4th potential sweep at $\vec{b}_h^*$, normalized to the maximum of the peak intensity. Figures e and f summarize the potential-dependence of the total integrated intensity obtained by multiplication of the integrated intensity of azimuthal scans with the FWHM of radial scans for $\vec{b}_h^*$ and $\vec{a}_h^*$, respectively.

resting time at -0.4 V the X-ray beam changed the position on the sample surface. The change in the FWHM caused by this temporary X-ray beam position instability is indicated by an arrow in figure 8.8b and amounts to $\xi_1 \approx 0.004 \cdot a_c^*$. Hence, the surface part being probed after this incident exhibits larger reconstructed domains in the 'x5' direction.

A qualitatively identical behavior in the potential-dependence of the FWHM is found in the second potential cycle. The FWHM remains constant in the anodic sweep, while it again decreases in the cathodic sweep after intermittent (complete or partial) lifting of the reconstruction at -0.05 V. The measured intensity profiles for the latter two potential sweeps have been plotted in figure 8.8d in order to point out the changes in the FWHM. Each intensity profile has been normalized to the maximum peak intensity and the peak position has been subtracted to eliminate the electrocompression related shift. The full widths at half maximum, measured at each potential in the second potential cycle, are shifted by an almost constant amount towards smaller values with respect to corresponding values in the first potential cycle. This constant amount roughly agrees with ξ_1 and shows that the potential-dependence of the FWHM is not only qualitatively but also quantitatively comparable in both potential cycles.

In the anodic sweep of the second potential cycle a constant FWHM of $0.0075 \cdot a_c^*$ is measured. This value corresponds to a correlation length of 511 Å in 'x5' direction, which is about five times larger than the value of 110 Å that has been determined at -0.2 V in Au-free solution. Obviously the homoepitaxial layer-by-layer growth promotes the formation of larger reconstructed domains. This effect will be discussed in more detail below. Interestingly, a similar correlation length of 500 Å (FWHM of $0.005 \cdot a_c^*$) has been found in UHV studies at elevated temperatures of 1147 K where only unrotated domains have been reported [129]. The potential independence of the correlation length in the anodic potential sweeps is identical to the behavior in Au-free 0.1 M HCl solution. Once the surface is to a certain degree reconstructed the average domain size in 'x5' direction appears to be potential-independent in the entire potential regime of the reconstructed phase.

Radial FWHM of the Reconstruction Peak at $\vec{a}_h^*$. The potential-dependence of the FWHM of radial intensity profiles recorded at the second reconstruction peak at $\vec{a}_h^*$ (figure 8.8c) is similar to those observed at $\vec{b}_h^*$. Despite of rather large error bars the FWHM decreases in cathodic potential sweeps, partly caused by the formation of the reconstructed phase. In the anodic sweeps a further decrease towards smaller values is found indicating a continuous time-dependent increase of the correlation length parallel to the potential sweeps within the reconstructed potential regime. Furthermore, because of the sudden change in the illuminated surface area, the first and second potential cycle are again shifted by a constant amount of $\xi_2 \approx 0.001 \cdot a_c^*$ with respect to each other in analogy to the data acquired at $\vec{b}_h^*$ (the only exception is the data point at -0.4 V in the second cathodic cycle). In contrast to the FWHM inferred from radial scans along $\vec{b}_h^*$, the FWHM of radial scans along $\vec{a}_h^*$ does not provide direct information about the average extension of reconstructed domains in 'x20' direction (the normal vector of according netplanes is tilted by 30° with respect to the 'x20'

direction). For example, every decrease in the radial FWHM at $\vec{b}_h^*$ causes a simultaneous decrease of the radial FWHM at $\vec{a}_h^*$ without being linked to a change in domain size along 'x20'. Hence, the observed decrease of the FWHM in cathodic potential sweeps is at least partly caused by the simultaneous increase of domain size in 'x5' direction. However, the further decrease of the FWHM at $\vec{a}_h^*$ in the anodic potential sweeps must be fully attributed to the growth of domains along 'x20' as in this case the FWHM at $\vec{b}_h^*$ is almost constant.

8.3.2 Potential-Dependence of Azimuthal Scans

After this first analysis of the radial intensity profiles we now focus on the potential-dependence of the azimuthal intensity profiles. Prior to the data acquisition of each azimuthal scan the reciprocal lattice vector $\vec{b}_h^*$ has been tracked in order to ensure that the azimuthal intensity profiles were recorded through the intensity maximum in radial direction. The latter is known to shift with each potential step due to the electrocompression effect and has to be accurately set in order to obtain precise information about the rotational orientation of domains and about the total integrated intensity. The azimuthal data, monitored in parallel to the two potential cycles, are plotted in the figures 8.9(1a) and 8.9(2a), respectively. The solid lines show the results of fitting a sum of three Voigt-profiles to the data. In contrast to the situation in Au-free solution the series of azimuthal intensity profiles in Au containing solution clearly indicates a reversible and potential-dependent rotational transition from aligned to rotated domains. A comparison of all azimuthal profiles recorded at -0.4 V shows that the domains are predominantly aligned, i.e. that the width of the profiles is narrower than those for profiles observed at more positive potentials. In particular the intensity profile recorded at -0.4 V in the third potential sweep could be perfectly fitted by a single Voigt profile with a FWHM of 0.88°. This peak width is considerably narrower than the angular range of 1.44° separating two domains rotated by $\Delta\theta = \pm 0.72°$ with respect to the $[110]_c$ direction. In comparison with the smallest FWHM of 0.12° observed in the UHV studies [129] (without growth) the angular distribution under the chosen electrochemical growth conditions is by a factor of 7.3 broader. Hence the alignment of domains with respect to the $[110]_c$ direction does not proceed to the same degree as in UHV at elevated temperatures. The more positive the applied electrode potential the broader are the azimuthal profiles, indicating an increased contribution of rotated domains to the profile shape. This effect is particularly pronounced in the two cathodic potential sweeps after intermittent lifting of the reconstruction close to the critical potential, but it can be as well rationalized in the anodic potential sweeps where small bulges in the profile shoulder are noticeable next to the peak maximum. Thus, the rotational transition is not a pure consequence of the reconstruction lifting between the anodic and the cathodic potential sweeps but moreover an effect which at least partly has to be related to the electrode potential. A quantitative analysis will be given below. It is obvious that intensity profiles at more positive potentials exhibit significant intensity in the center of the profiles ($\Delta\theta = 0$), indicating that not all aligned domains undergo a rotational transition. This behavior is very similar to those in UHV studies where a coexistence of aligned and rotated domains has been found by lowering the sample temperature below $T = 1000\,\mathrm{K}$ [129]. In contrast to the profiles obtained in Au-free solution or under UHV conditions the azimuthal profiles in Au containing solution feature less distinct
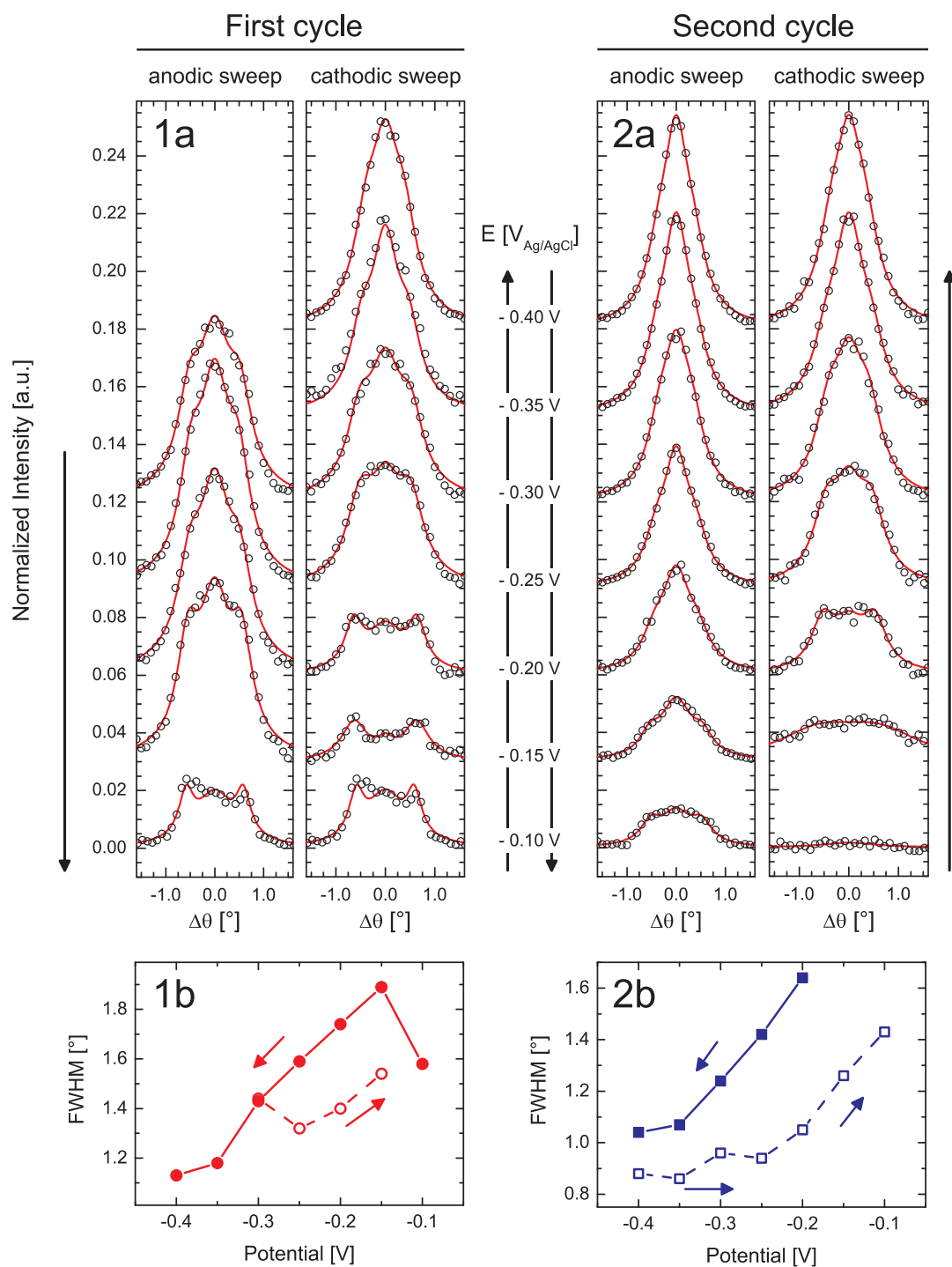
Figure 8.9: The figures 1a and 2a show the potential-dependence of azimuthal rocking scans across $(\Delta_1, \Delta_1, 0.1)$ of the Au(100) electrode in $0.1\,\mathrm{M}$ HCl $+\ 50\,\mu\mathrm{M}$ HAuCl$_4$. Each scan has been recorded after $50\,\mathrm{mV}$ potential steps into cathodic or anodic direction and in time intervals of approximately 6 minutes. The peaks are shifted with respect to each other for clarity. The figures 1b and 2b show the potential-dependence of the pseudo-FWHM which was determined for each intensity profile (see text).

peaks at $\pm\Delta\theta$ which either has to be related to an increased amount of aligned domains or to a general broadening of the three contributing peak profiles. According to figure 8.5 a significant broadening of azimuthal intensity profiles of rotated domains presumably takes place in Au containing solution.

In order to quantify the rotational transition a pseudo-FWHM has been determined for each azimuthal profile. This FWHM is defined by the difference in θ of the intensity values at half maximum of the fitting curve. The results in dependence of the applied electrode potential are shown in the figures 8.9(1b) and 8.9(2b). For both cathodic potential sweeps a monotonic decrease of the FWHM with decreasing electrode potential is found which indicates an continuous alignment of rotated domains along the $[110]_c$ direction, i.e. a decrease of the rotation angle $\Delta\theta$. This rotational transition proceeds parallel to the formation of the reconstructed surface phase, parallel to the increase in domain size and parallel to the electrocompression of the reconstructed layer. Hence, the origin of the rotational transition cannot be uniquely assigned to either of the three effects. For potentials $\leq$ -0.35 V the FWHM appears to be less dependent on the electrode potential since the slope of the decrease apparently flattens in the anodic as well as in the cathodic sweeps. For the anodic potential sweeps a different behavior is observed. Between -0.4 V and -0.25 V the FWHM is almost potential-independent. The intensity profiles in this regime exhibit a similar shape and are reasonably fittable by single Voigt profiles. However, for potentials $E >$ -0.25 V the FWHM monotonically increases with a comparable slope as determined in the cathodic sweeps. Besides of this increase towards more anodic potentials the behavior resembles the potential-dependence of the FWHM in radial direction and may indicate a correlation between the alignment of rotated domains and the size of reconstructed domains. Specifically the partial potential-independence in the anodic sweeps suggests that domains, which are once aligned with the $[110]_c$ direction, aim to persist in this orientation. The latter strongly supports the theory that unrotated domains are energetically favored over rotated domains in agreement with the model proposed by S. Guenther [5] and with the UHV results (alignment at elevated temperatures). On the other hand the monotonic decrease in the cathodic sweeps and the monotonic increase in the anodic sweeps for potentials $>$ -0.25 V suggest a correlation between the alignment of domains and the electrocompression of the reconstructed surface layer (cp. figure 8.13). With the exception of the potential regime between -0.4 V and -0.25 V in the anodic sweeps both of the latter quantities change approximately linearly and reversible with the applied electrode potential. This might implies that the main driving force for the alignment of domains along the $[110]_c$ direction is given by the growth induced electrocompression of the 'hex' reconstructed surface layer. The deviant behavior observed in the azimuthal profiles for potentials $<$ -0.25 V in anodic sweeps then has to be ascribed to the fact that the driving force is insufficient to induce a significant rotation of large domains which are located in the energetically favored aligned orientation.

8.3.3 Potential-Dependence of the Total Integrated Intensity

Information about the degree of reconstruction, i.e. about the coverage of the electrode surface by an ordered reconstructed phase, is given by the total integrated intensity at the

reciprocal space positions $\vec{a_h^*}$ and $\vec{b_h^*}$. The latter is obtained by multiplication of the integrated intensity of azimuthal profiles with the FWHM in radial direction. Figure 8.8e shows the total integrated intensity at $\vec{b_h^*}$ for both potential cycles. A decrease in integrated intensity is observed from initially 2.0 at -0.3 V before the potential cycling to 0.8 at -0.4 V after the last (cathodic) potential sweep. Interestingly the integrated intensity decreases while the correlation length, i.e. the average domain size, is reproduced in each potential cycle. This scenario suggests an continuously increasing amount of structurally disordered regions parallel to the existence of large well-ordered, reconstructed domains. In particular the propagation of disordered regions does not appear to affect the average size of ordered regions. The time-dependent and potential-dependent integrated intensity at the second reconstruction peak $\vec{a_h^*}$ is shown in figure 8.8f. At this reciprocal space position a qualitatively identical behavior is observed confirming the decrease in electrode coverage by the reconstructed phase. In contrast to the intensity at $\vec{b_h^*}$, which does not show a clear tendency in the last cathodic sweep, figure 8.8f indicates a saturation of the intensity in the second potential cycle.

The observed degradation in surface coverage by the reconstructed phase may be attributed to two effects. First, it is known from studies of Au(100) electrodes in Au-free electrolyte that the degree of reconstruction degrades by repeated cycling between the reconstructed and the unreconstructed phase [111]. This effect should be less pronounced in the presence of homoepitaxial growth (see chapter 10) but a certain negative influence on the surface morphology cannot be fully excluded. Second, the homoepitaxial growth is known to proceed via non-ideal layer-by-layer growth as indicated by the decay of time-dependent X-ray intensity oscillations (cp. figure 8.2). Both effects occur at the same time and cannot be clearly separated from each other with regard to the performed experiments. The particularly strong intensity decrease observed in the first cathodic potential sweep most likely has to be attributed to the extensive exchange of $500\,\mu l$ electrolyte at -0.1 V corresponding to $100\,\mathrm{s}$ Au-deposition in the 3D growth mode (deposit equivalent to $\approx 2.7\,\mathrm{ML}$). In contrast to a pronounced surface smoothening of rough surfaces in the step-flow growth regime (section 9.4) the layer-by-layer growth does not seem to be able to flatten substantially roughened surfaces.

8.4 Origin of the Domain Size Increase under Deposition Conditions

Provided that layer-by-layer growth proceeds in a similar manner under electrochemical conditions as in UHV (section 8.1) two mechanisms for an increase in the average domain size are conceivable:

1) Reduction of Surface Defects: A possible decrease of the amount of surface defects induced by homoepitaxial deposition is expected to result in an extension of reconstructed domains. Defects like surface pits and islands are likely overgrown by the deposition of Au atoms, particularly in the layer-by-layer growth regime where the Ehrlich-Schwoebel barrier at step edges is comparatively low. As already discussed in section 6.4.2 EC-STM [88] and

Video-STM [90, 113] studies of the (1×1) → 'hex' surface phase transition revealed that the formation of the reconstructed phase on Au(100) electrodes in Au-free electrolyte is a complex process which involves long-range mass transport of Au adatoms. The formation of the reconstructed phase proceeds via nucleation and unidirectional growth of reconstruction stripes which can grow in two perpendicular directions determined by fourfold symmetry of the unreconstructed substrate. As a consequence comparatively small 'hex' domains are formed. In chloride containing solutions only a little amount of remaining unreconstructed islands but a significant number of surface pits are observed in the reconstructed layer (figure 7.4a). In addition smaller, unreconstructed areas are embedded in the otherwise reconstructed surface layer which in Au-free solution are kinetically hindered to reconstruct due to restricted surface mass transport caused by circumjacent reconstructed domains. However, if growth is started on potential-induced reconstructed surfaces by the injection of Au-containing electrolyte then the deposition process supplies unreconstructed areas with the necessary amount of Au atoms to form reconstruction. Both the reduction of surface defects and the conversion of unreconstructed regions into reconstructed regions facilitate subsequent layers to grow in form of larger reconstructed domains on top of a less defective substrate layer. Figure 8.10 depicts the proposed mechanism. In view of the STM images in figure 7.4 such a mechanism is supposed to result in an increase of domain size by up to a factor of two and has to be considered to contribute to an increase in domain size in the initial stage of deposition, particularly on potential-induced, reconstructed surfaces with a high number of surface defects. According to this model the average domain size is expected to saturate after the deposition of $\theta \leq 0.25\,\text{ML}$. A different situation may be expected if
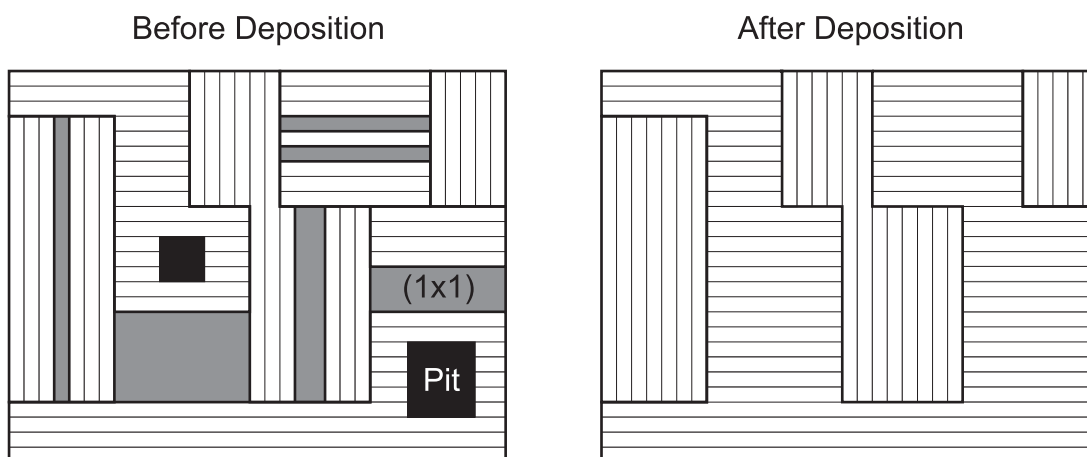
Figure 8.10: Model for layer-by-layer growth in the initial stage of homoepitaxial deposition on Au(100) electrode surfaces ($\theta \leq 0.25\,\text{ML}$) with a high density of surface defects, e.g. present after potential-induced formation of the reconstructed phase. White rectangles symbolize single reconstruction stripes, domain boundaries are indicated by bold lines. Unreconstructed (1×1) regions (gray areas) and surface pits are supposed to be overgrown by Au deposition, resulting in an increase of average domain size after deposition of the first few monolayers.

the reconstructed phase forms subsequent to potential steps into the reconstructed potential regime while the electrode is immersed in Au-containing solution. In this case the number of surface pits and unreconstructed areas should be lower after completion of the reconstruction formation process ($\theta \leq 0.25$ ML).

The potential-dependence of the radial FWHM in 'x5' and 'x20' direction (figure 8.8) indicates that the increase in domain size is not completed after the first deposited 0.25 ML but it proceeds with the deposition of further monolayers. Thus, the filling of surface pits and the supply of unreconstructed surface areas with Au atoms cannot be the only mechanisms causing the increase in domain size in Au-containing solution. According to Video-STM studies of Au(100) in Au-free solution the formation of large reconstructed domains of several hundred Ångstrom in width is assisted by the removal of structural defects via collective dynamic rearrangement processes, in which distorted and misaligned strings reorganize [90]. Restructuring involves changes in the local string orientation, breaking or (re-)connecting of strings and occurs on time scales ≤ 100 ms. These processes play a decisive role in domain ripening, i.e. in the formation of extended 'hex' domains from the initially highly defective reconstructed surface. We will see in chapter 10 that the formation of the reconstructed phase proceeds in a similar manner in Au-containing solution: the 'hex' layer formed on the initially unreconstructed surface after deposition of 0.25 ML gold is rather disordered followed by a slower ripening process. The comparatively large saturation value of the domain size in Au-containing solution suggests that homoepitaxial growth assists the domain ripening process.

2) Growth in the Vicinity of Domain Boundaries: Due to anisotropic growth the domain structure of the growing layer is supposed to be a duplicate of the underlying reconstructed substrate layer provided that growing domains are unable to overgrow domain boundaries which are present in the topmost substrate layer. This situation apparently holds for homoepitaxial growth on Au(100) under UHV conditions at least for $\theta < 1$ ML. In the center of figure 8.1 a domain boundary in the substrate layer is indicated by the orientation of deposited reconstruction stripes. Stripes in the vicinity of the domain boundary seem to be able to attach to it, but they are apparently not able to cross the domain boundary. Thus, subsequent deposited layers will exhibit the same domain structure. This situation might change in the case of electrochemical deposition as the electrode potential influences the terrace diffusion barrier E_d and by this the mobility of surface adatoms. If deposited domains are assumed to overgrow domain boundaries in the substrate layer the average domain size might increase with the amount of further deposited monolayers. Provided that this effect is isotropic, one might expect a benefit for larger domains which will grow on the cost of smaller domains based on the larger perimeter (Ostwald-like behavior). As well this effect could be anisotropic favoring growth of domains either in 'x20' or in 'x5' direction. Detailed studies of island growth in the vicinity of domain boundaries in the substrate layer have not been reported up to now. In this regard the proposed mechanism is speculative.
No definite conclusion about the origin of the domain size increase can be drawn from the performed SXS experiments. Presumably the reduction of surface defects in the initial stage of the $(1 \times 1) \rightarrow$ 'hex' phase transition ($\theta \leq 0.25$ ML) and the growth-assisted domain ripening

in later stages of the deposition process ($\theta \geq 0.25$ ML) account for the predominant part of the increase in domain size. This would as well explain the saturation value of the FWHM observed in 'x5' direction. On the other hand this limit could be as well related to intrinsic surface properties such as the average step edge separation (miscut of the electrode surface). The continuous time-dependent decrease of the FWHM at $\vec{a}_h^*$ might indicate that domain boundaries in the substrate layer are overgrown by the extension of deposited, reconstructed islands in 'x20' direction. UHV studies found significant growth of step edges oriented perpendicular to the 'x20' direction of adjacent reconstructed domains, while step edges parallel to the 'x20' direction grow only moderately [4].

8.5 Kinetics in the Electrocompression Phenomenon

The SXS experiments performed parallel to the electrolyte exchange demonstrate that the compression of the reconstructed surface phase in 'x5' direction does not proceed instantaneously. Moreover it takes a certain time, i.e. a certain deposited amount of gold, until the compression of the reconstructed surface layer is completed. This is indicated by the continuous shift observed in Δ_1 (cp. figure 8.6). Therefore the kinetics of the deposition process plays an important role in the electrocompression phenomenon.

In order to gain a deeper insight in the relationship between the formation of the electrocompressed phase and the kinetics of homoepitaxial deposition an additional experiment is reviewed which shows the time-dependence of Δ_1 after a potential step from 0 V close to the critical potential (i.e. the surface is unreconstructed) to -0.4 V in the reconstructed potential regime. This measurement[4] has been carried out subsequent to the potential cycles and in stagnant 0.1 M HCl + 0.05 mM HAuCl$_4$ solution. Prior to the potential step of interest the electrode potential has been stepped from -0.4 V to 0 V close to the surface phase transition and 200 μl of electrolyte have been injected into the meniscus to replenish the Au concentration. A cyclic diffractogram, obtained with a sweep rate of 2 mV/s in 0.1 M HCl, shows that at an electrode potential of 0 V the intensity at the reciprocal space position $(\Delta_1, \Delta_1, 0.09)$ rapidly drops to the background intensity (cp. figure 7.8), i.e. that the reconstruction is predominantly lifted. This is also apparent in the radial intensity profiles shown in figure 8.11b where the reconstruction peak at $\vec{b}_h^*$ completely diminishes within one single scan after the potential was stepped from -0.4 V to 0 V. Parallel to the subsequent potential step from 0 V to -0.4 V the intensity at the reciprocal space position $(\Delta_1, \Delta_1, 0.09)$ has been repeatedly recorded in radial direction in time intervals of ≈ 45 s. The peak positions, the integrated intensities and the FWHM of those radial intensity curves have been determined by Voigt-profile fits and are summarized in figure 8.11. According error bars for the peak positions have been estimated as 10% of the FWHM of the intensity profiles. In order to improve the time resolution no azimuthal intensity profiles were taken which does not allow to determine the total integrated intensity at the reconstruction peak.

---

[4]ESRF, $E = 18.2$ keV, presample slits: vg $= 0.05$ mm and hg $= 0.25$ mm, detector slits: dvs $= 3$ mm and dhs $= 1$mm
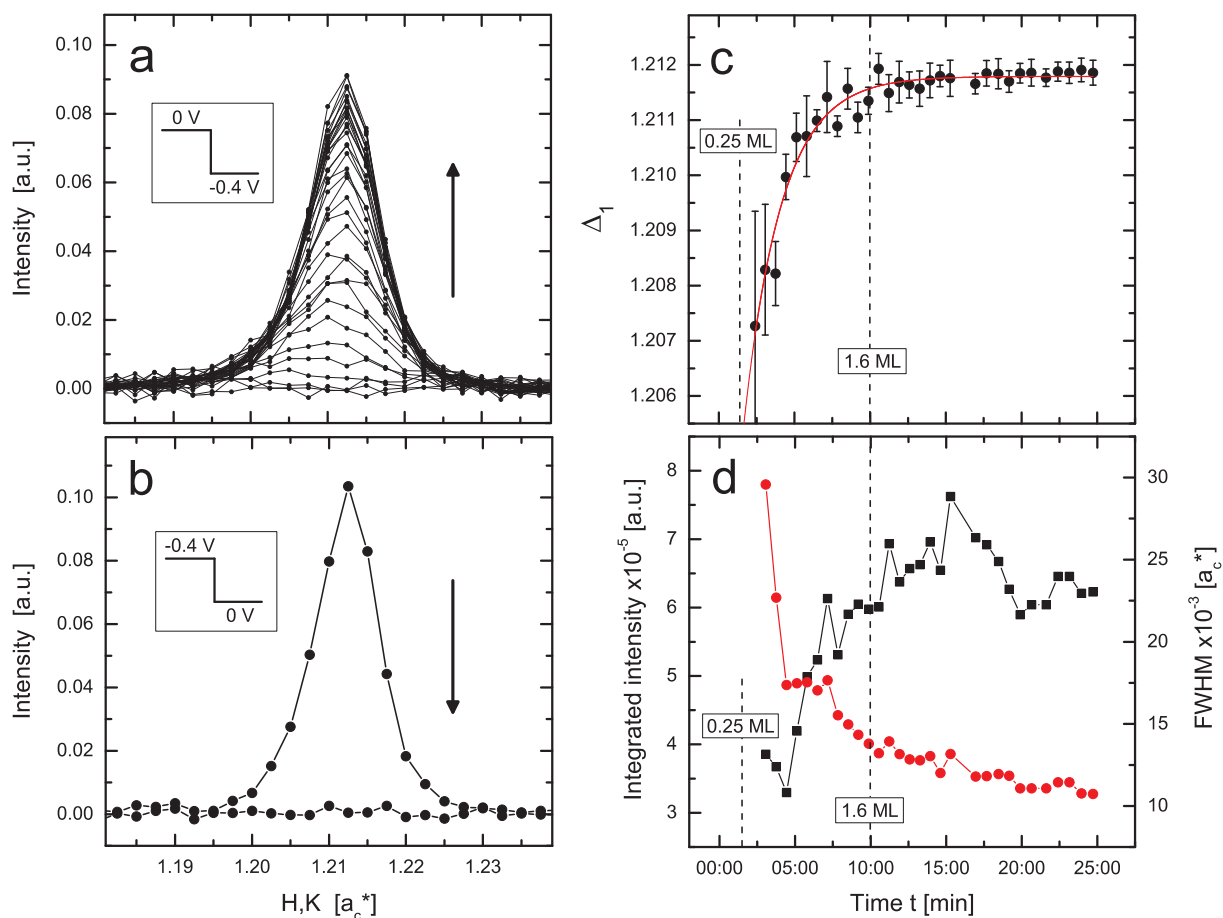
Figure 8.11: The graphs a and c show two potential steps, from a) $0\,\text{V}$ to $-0.4\,\text{V}$ and c) $-0.4\,\text{V}$ to $0\,\text{V}$, in stagnant $0.1\,\text{M}$ HCl $+$ $0.05\,\text{mM}$ HAuCl$_4$ solution. Subsequent to the potential steps at $t = 0$ the intensity has been repeatedly monitored in radial direction at the reciprocal space position $(\Delta_1, \Delta_1, 0.09)$. The two graphs in c and d show the time-dependence of c) Δ_1 and of d) the radial integrated intensity ($\blacksquare$) and the radial FWHM ($\bullet$) as inferred from the series of intensity profiles shown in graph a. The bold line in c shows an exponential fit to the data with a time constant $t = 149\,\text{s}$.

The figures 8.11a and 8.11c show an increase in Δ_1 with time, i.e. a compression of the reconstructed surface layer in 'x5' direction, similar to those observed during the electrolyte exchange (cp. with figures 8.3 and 8.6). The first radial scan recorded directly after change of the electrode potential to $-0.4\,\text{V}$ does not feature any reconstruction peak above the background and confirms that the surface is to a large extent unreconstructed at the time $t = 0$. Within the following $2\,\text{min}$ a broad peak of low intensity emerges which indicates the incipient formation of the reconstructed phase. Unfortunately the peak intensities in this initial time period after the potential step are too low in order to determine the peak position and to draw conclusions about the surface compression. The radial scan taken after $2{:}24\,\text{min}$ is the first intensity profile that allows to obtain information about Δ_1. A value of

$\Delta_1 = 1.2074 \pm 0.002$ is found which is quite similar to the value of $\Delta_1 = 1.2053$ measured at -0.4 V in Au-free solution (cp. figure 7.7), showing likewise that in the initial time period after the potential step (deposit < 0.4 ML) no significant compression of the reconstructed surface occurs. In the preceding deposition process, i.e. between $t = 2{:}30$ min and $t = 10$ min, Δ_1 shifts from 1.207 to a saturation value of 1.212 observed for $t \geq 10$ min (figure 8.11c). The time span of 10 min between the potential step and achievement of the saturation value in Δ_1 corresponds to the deposition of 1.6 ML. This is an interesting result which shows that the compression of the reconstructed surface is completed within the first two deposited monolayers.

The time-dependence of the radial integrated intensity and of the radial FWHM is summarized in the figure 8.11d. The integrated intensity increases with time and approaches a saturation value approximately 10 min after the potential step. Simultaneously the radial FWHM decreases from $0.030 \cdot a_c^*$ at $t = 3{:}04$ min to $0.011 \cdot a_c^*$ at $t = 25{:}00$ min. The latter perfectly agrees to the FWHM that has been found at -0.4 V during the potential cycle experiments. Two processes contribute to the intensity of the reconstruction peak along the $[110]_c$ direction, that is the formation of the reconstructed phase on the one hand and the alignment of rotated domains on the other hand. Thus, the radial integrated intensity on its own is no appropriate measure for the electrode coverage by the reconstructed phase and the time-dependent profile shape in azimuthal direction has to be considered. Unfortunately the latter has not been monitored under identical electrochemical conditions. However, measurements in 0.5 mM $HAuCl_4$ containing electrolyte revealed an exponential-like decay for the azimuthal FWHM after potential steps from 0.55 V to -0.2 V in the reconstructed potential regime (cp. figure 10.5d). Hence, if the integrated intensity in radial direction, shown in figure 8.11b, is multiplied with an exponentially decaying FWHM in azimuthal direction the total intensity at $\vec{b}_h^*$ is expected to saturate at a time $t \ll 10$ min. This implies that the reconstruction formation process is much faster than the electrocompression process. It is evident that the radial FWHM, the radial integrated intensity and the shift in Δ_1 approach saturation values on comparable time scales. In turn saturation of the radial integrated intensity suggests the completion of the rotational transition. This is in agreement with the time behavior of Δ_1 and $\Delta\theta$ in the exchange experiment.

8.6 Simple Model for the Formation of the Compressed Phase

Figure 8.12 illustrates a model which is able to explain the compression behavior observed in the growth experiments of the previous section. Starting point of the consideration is the Au(100) electrode surface in Au containing solution at a potential $E_{(1\times1)}$ in the unreconstructed potential regime (figure 8.12a). At $t = 0$, the electrode potential is stepped to $E_{\text{'hex'}}$ in the reconstruction regime where the growth proceeds via layer-by-layer mode. In the initial time period after the potential step the topmost surface layer reconstructs. In anticipation of chapter 10 the formation of the reconstructed phase occurs on a narrow time scale and the surface is expected to be reconstructed after the deposition of ≈ 0.25 ML by direct incorporation of Au adatoms into the unreconstructed surface layer [64] (figure 8.12b). A deposit amount of 0.25 ML corresponds to a deposition time of ≈ 90 s in the performed

potential step experiment. During the reconstruction formation process none or only little compression of the reconstructed layer is observed, i.e. the final structure of the 'hex' layer agrees with that of a potential-induced, reconstructed electrode surface in Au-free electrolyte. This behavior is expected since at least for low deposition rates (moderate increase of the adatom concentration) the deposition process should not change the modality of the reconstruction formation process.

The small compression observed for $t \leq 90\,\mathrm{s}$ ($\theta \leq 0.25\,\mathrm{ML}$) can be explained on the basis of kinetic limitations which are caused by energy barriers. Since the excess mass density is $\approx 25\%$ higher in the reconstructed 'hex' phase as compared to the unreconstructed (1×1) phase on an average four surface atoms have to rearrange in order to incorporate an additional Au adatom. In the initial time period subsequent to the potential step, where the surface is predominantly unreconstructed and the 'hex' coverage $\theta_{\mathrm{rec}} \ll 1$, surface atoms in the (1×1) phase easily rearrange due to a comparatively low packing density. Accordingly the energy barrier for adatom incorporation is low. However, in the advance of the deposition process the coverage θ_{dep} converges to unity and the energy barrier increases until further incorporations will be unfavorable. This kinetic limitation strongly limits the maximum degree of compression. It is worth mentioning that domain walls and surface defects should have a
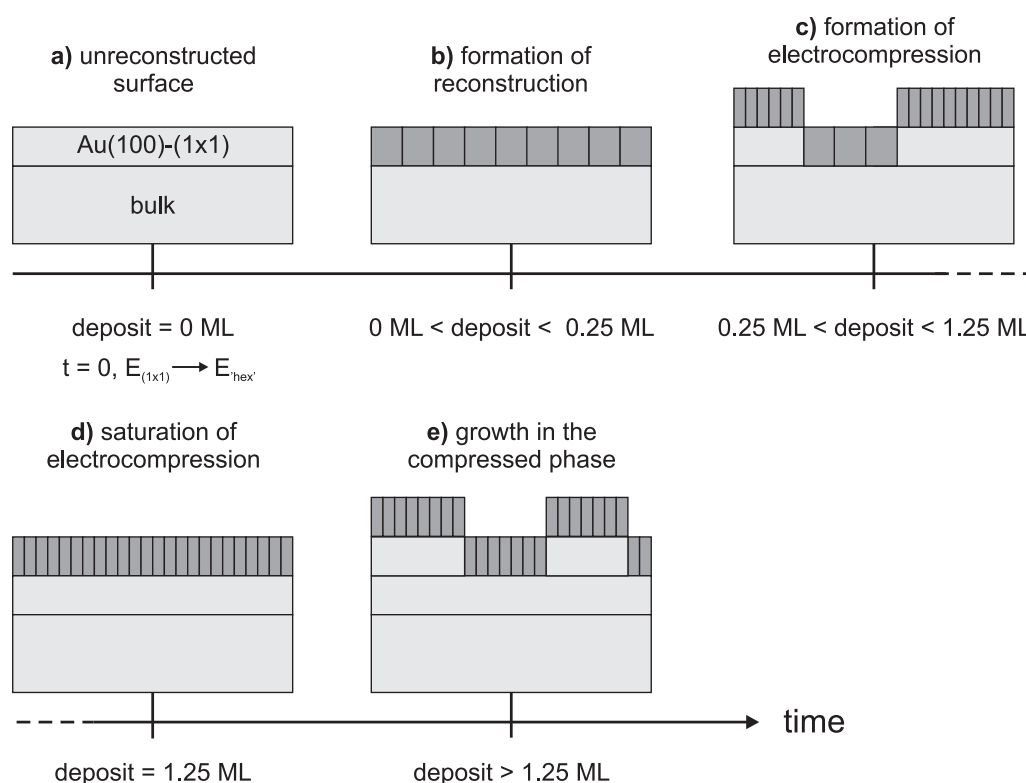
Figure 8.12: Model for the formation of the electrocompressed surface phase in Au containing electrolyte after a potential step from $\mathrm{E}_{(1\times1)}$ in the unreconstructed to $\mathrm{E}_{\mathrm{'hex'}}$ in the reconstructed potential regime.

rather small influence on the compression of the reconstructed phase according to the results of SXS measurements in UHV [129] and in Au free $HClO_4$ [80] solution. The latter two studies report correlation lenghts of $500\,\text{Å}$ and $>300\,\text{Å}$ in 'x5' direction, respectively, and structural lattice parameters of $\Delta_1 = 1.205$ and $\Delta_1 = 1.205 \pm 0.002$. Thus, even though the domain size is three to five times larger than $\approx 128\text{Å}$ in the present study (FWHM of $\geq 0.03\,a_c^*$ for $\theta \leq 0.5\,\text{ML}$, cp. figure 8.11d) no additional compression of the reconstructed layer is observed.

After the reconstruction process of the topmost surface layer is completed growth on top of the reconstructed surface takes place. STM studies of homoepitaxial MBE growth on Au(100) in UHV [5] and SXS studies of homoepitaxial electrodeposition on Au(100) electrodes [64] demonstrated that growing Au islands on top of the reconstructed surface are as well reconstructed. Moreover, theoretical studies [104] and experimental SXS crystal truncation rod measurements [64] revealed that during the deposition process the underlying, reconstructed substrate layer transforms back to the (1×1) bulk structure, i.e. that interlayer transport takes place from the substrate layer to the growing layer. Significant compression of the electrode surface sets in with the growth of the first monolayer on top of the beforehand reconstructed surface (figure 8.12c). In the time span between $t = 90\,\text{s}$ and $t \approx 469\,\text{s}$ the new surface layer grows on top of the reconstructed layer until a total amount $\approx 1.25\,\text{ML}$ is deposited (figure 8.12d). In contrast to the potential-induced formation of the reconstructed phase on the unreconstructed (1×1) surface, which requires the insertion of additional Au atoms into the existing surface layer, the second layer grows unhampered by attachment of adatoms to island step edges since the growing Au islands are not embedded in an ambient atomic layer. Here, no (or at least a lower) barrier for attaining the energetically preferred in-plane spacing exists. The second and subsequent layers grow in the compressed, reconstructed phase (figure 8.12e) with a characteristic, potential-dependent lattice spacing which is predominantly determined by the surface tension in the reconstructed layer and by the interaction with the Au(100) substrate, i.e. by surface stress. According to figure 8.11c the surface compression seems to be a continuous process. However, the SXS data does not allow to decide if the first reconstructed monolayer on the uncompressed, reconstructed layer immediately grows with the potential-dependent minimum in the lattice spacing or if the reconstructed layer successively compresses while the monolayer is formed. This is related to the superposition of scattered intensity originating partially from the continuously disappearing uncompressed 'hex' layer and partially from the continuously forming compressed 'hex' phase in the successive layer. The intensity profiles are symmetric and do not indicate a simultaneous presence of compressed and uncompressed areas.

8.7 Quantitative Analysis of the Electrocompression Effect

In this section the electrocompression effect will be analyzed in more detail. Figure 8.13 summarizes all values for Δ_1 and Δ_2 which were obtained in the four potential sweeps discussed in section 8.3 and additional data recorded within the same electrolyte at beam line BW2 at Hasylab in Hamburg (open circles). In chapter 7 the Au(100) surface structure in $0.1\,\text{M HCl}$ was found to be characterized by $\Delta_1 = 1.205 \pm 0.0005$ and $\Delta_2 = 1.198 \pm 0.001$.
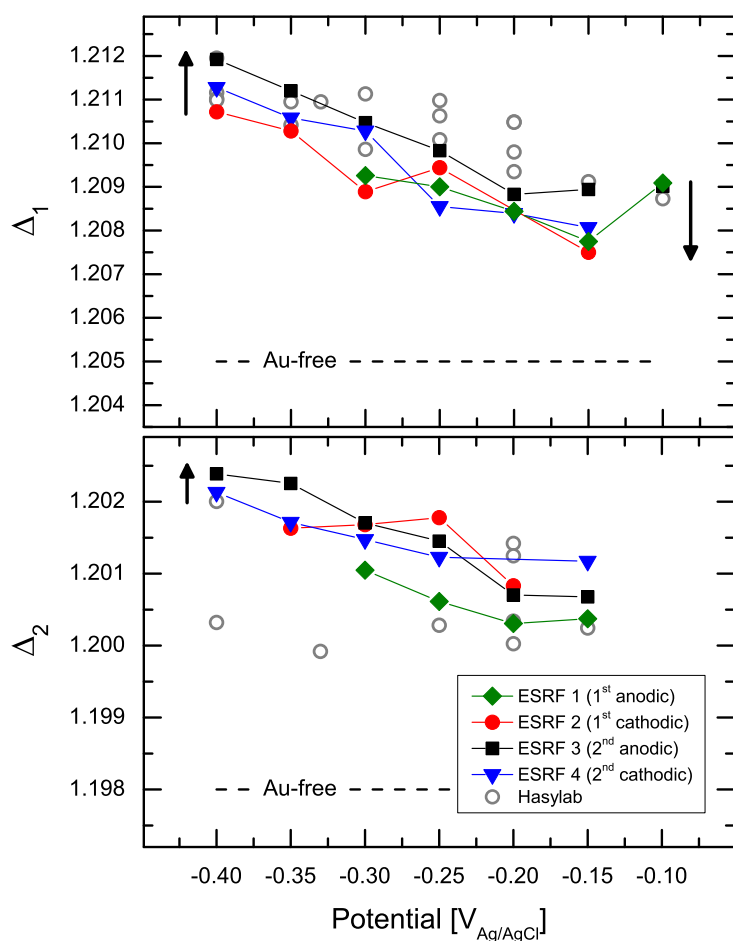
Figure 8.13: Potential-dependence of Δ_1 and Δ_2 in $0.1\,M$ HCl + $0.05\,mM$ HAuCl$_4$ solution according to four potential sweeps performed at the ESRF (solid symbols) and for comparison several potential sweeps recorded at Hasylab (open circles) under identical electrochemical conditions. Arrows mark the shifts at the potential reversal points between two successive potential sweeps due to extended holding times and further compression/expansion of the 'hex' layer. Dashed lines depict the average values of Δ_1 and Δ_2 in Au-free solution.

All data points in the graph show the same qualitative behavior, i.e. Δ_1 and Δ_2 increase towards more negative potentials. We first concentrate on the data of Δ_1 taken at the ESRF. For comparison we determined the slope for each of the four potential sweeps by linear fits to the Δ_1 data and obtained values of $-0.014\,V^{-1}$, $-0.013\,V^{-1}$, $-0.010\,V^{-1}$ and $-0.013\,V^{-1}$, respectively. These slopes are very similar and scatter only slightly around a mean value of $-0.0125\,V^{-1}$. As described above, absolute Δ_1 values are dependent on the kinetics and consequently on the waiting time at single potentials during the potential sweep. This effect results in a small scattering observed for some of the Δ_1 data points, caused by waiting times which differ from the average 6 min mentioned above. In the first anodic sweep ($\color{green}\blacklozenge$) Δ_1 decreases from 1.2093 at -0.3 V to 1.2078 at -0.15 V. The subsequent first cathodic sweep ($\color{red}\bullet$) follows the characteristics of the first anodic sweep and Δ_1 increases from 1.2075 at -0.15 V to 1.2107 at -0.4 V. Between the first cathodic and the second anodic sweep the potential has been kept for 12:16 min at -0.4 V. During this holding time Δ_1 continuously shifted towards larger values (i.e. the surface compresses further in 'x5' direction) until $\Delta_1 = 1.2120$ was reached which is exactly the same saturation value as found in the potential-step experiment (cp. figure 8.11). Besides of being shifted towards larger Δ_1 values the complete second anodic sweep ($\blacksquare$) runs parallel to the two prior sweeps and Δ_1 shifts from 1.2120 at -0.4 V to 1.2089 at -0.15 V. As in this anodic sweep the potential has been swept further to -0.05 V, i.e.

very close to the critical potential, Δ_1 shifts in the beginning of the second cathodic sweep ($\blacktriangledown$) back towards a smaller value of 1.2081 at -0.15 V which is similar to the values observed in the first two potential sweeps. Accordingly the second cathodic sweep is almost identical to the first two potential sweeps. The shifts at the potential reversal points are marked by arrows in figure 8.13. The Δ_1 data recorded at Hasylab demonstrate the reproducibility of the electrocompression effect. All Hasylab data points, which are plotted as gray open circles in figure 8.13, are part of several potential sweeps although it is not explicitly marked for clarity of the graph. Due to the less brilliant X-ray source at Hasylab significantly longer counting times were required for each scan. This results in less pronounced intensity profiles and in more extended time spans (>30 min up to 2 h) between single potential steps, i.e. in a significantly lower time resolution. Consequently the recorded Δ_1 values are all saturation values and they scatter around the values of the third ESRF potential sweep. For identical electrode potentials strongly varying Δ_1 values have been found which in this case has to be attributed to larger errors in the determination of the peak position. For the Hasylab data of Δ_1 these slopes vary between $0.006 \, \text{V}^{-1}$ and $0.011 \, \text{V}^{-1}$, i.e. in a wider range than the ESRF data, but agree with the latter within the errors. The Δ_2 data has been analyzed in an analogous way. Linear fits to the ESRF data provided slopes of $-0.0047 \, \text{V}^{-1}$, $-0.0046 \, \text{V}^{-1}$, $-0.0077 \, \text{V}^{-1}$ and $-0.00375 \, \text{V}^{-1}$, which scatter, with the exception of the third sweep, slightly around a mean value of $-0.0044 \, \text{V}^{-1}$. The influence of the kinetics on Δ_2 at the potential reversal points is as well apparent. The absolute values of Δ_2 vary approximately between 1.2005 at -0.15 V and 1.2023 at -0.4 V. In contrast, the Hasylab data scatters largely in Δ_2 providing therewith no accurate information about the potential-dependent surface compression in the according direction. Nevertheless, the Hasylab values are on the scale of the ESRF values providing likewise confidence in the quantitative data.

Due to the worse statistics of the Hasylab data we desist from merging both datasets. Furthermore we did not merge the data of the different ESRF potential sweeps but concentrated on the third and fourth sweep in which the time spans between consecutive potentials are equally spaced. Although the peak amplitudes and integrated intensities decrease with time the profiles in the last two sweeps were sufficiently pronounced to obtain precise peak positions. The figures 8.14a and 8.14b summarize the results for Δ_1 and Δ_2 at different electrode potentials obtained from Voigt profile fits to the radial scans in the third and fourth potential sweep. Obviously Δ_1 increases linearly with decreasing potential indicating a compression perpendicular to the reconstruction stripes, i.e. in 'x5' direction. The potential-dependence in Δ_2 is less obvious due to small changes and comparatively large error bars. The data obtained during the potential sweeps in cathodic and anodic direction exhibit a small hysteresis in Δ_1 and Δ_2, which is comparable to that found in other electrocompressible, incommensurate metal adlayer structures [130–132] and which at least partly can be attributed to kinetic effects (cp. section 8.5). Since this hysteresis is small compared to the potential-dependent changes in Δ_1 the complete set of Δ_1 data points in both potential sweep directions has been linearly fitted between -0.15 V and -0.4 V. The resulting straight line, plotted in figure 8.14a, exhibits a slope of $0.016 \, \text{V}^{-1}$. In order to emphasize the deposition-induced increase in Δ_1 and Δ_2 the data recorded in Au-free electrolyte has been added by open symbols to figure 8.14.

The interaction of the 'hex' reconstructed layer with the (1×1) substrate layer constricts the amount of possible directions for surface compression. In particular, the close-packed directions of the (1×1) substrate layer (e.g. $[110]_c$) are assumed to be preferential directions due to the alignment of the 'hex' phase. In the following we will consider a) an uniaxial compression along the 'x5' direction and b) a biaxial compression along the 'x5' and the 'x20' direction. We will demonstrate that the experimental data of Δ_1 and Δ_2 can be reproduced by both types of structural deformations. Additional structural changes, e.g. due to a shearing of the 'hex' layer, have been neither reported in previous studies nor does the present study provide a clear evidences.

8.7.1 Uniaxial Compression Perpendicular to the Reconstruction Stripes

We consider an uniaxial compression of the reconstructed surface layer in 'x5' direction. Appendix A.2 demonstrates that a structural change from Δ_1 to $\Delta_{1,U}$ comes along with a (smaller) change from Δ_2 to $\Delta_{2,U}$ and simultaneously with a change in the angle δ between the attributed reciprocal lattice vectors $\vec{a}_h^*$ and $\vec{b}_h^*$. Here the index U denotes structural parameters belonging to the uniaxially compressed phase. Following the derivation in appendix A.2 the value $\Delta_{2,U}$ after uniaxial compression is given by

$$\Delta_{2,U} = \frac{\sqrt{\Delta_1^2 \cdot (4\Delta_2^2 - \Delta_1^2 + \Delta_{1,U}^2)}}{2 \cdot \Delta_1}. \tag{8.1}$$

Provided that the compression in 'x5' direction is known, equation 8.1 allows to calculate the potential-dependence of Δ_2 whereupon the surface structure at a fixed potential is taken as reference point. For the latter we arbitrarily choose the potential of -0.25 V approximately in the center of the investigated potential regime where the surface structure is characterized by $\Delta_1 = 1.2098$ and $\Delta_2 = 1.2015$. Then the $\Delta_{2,U}$ values have been calculated for each potential E based on the $\Delta_{1,U}$ values of the linear fit to the Δ_1 data (solid line in figure 8.14a). The resulting dependence $\Delta_{2,U}(E)$ is shown as dashed line in figure 8.14b. Within the error bars the obtained line fits well to the experimental data of Δ_2 showing that the potential-dependent change in the surface structure is in accordance with an uniaxial compression along the 'x5' direction.

8.7.2 Biaxial Compression Perpendicular and Along the Reconstruction Stripes

In order to estimate the maximum degree of a potentially existing compression along the 'x20' direction a second calculation has been carried out. A compression in the 'x20' direction does not have any influence on the 'x5' direction, i.e. on Δ_1, as depicted in figure 8.15. Therefore, considering a biaxial compression, the surface inevitably has to compress along 'x5' by the amount having found in the experimental data of Δ_1. This yields a basic increase in Δ_2 which accords to the dashed line in figure 8.14b if the best-fit line in 8.14a is assumed to describe the potential-dependence of Δ_1. In the following we disregard the errors in Δ_1. An additional compression along the 'x20' direction will lead to a further increase of Δ_2. As reference point again Δ_1 and Δ_2 at -0.25 V have been chosen. According to appendix A.2
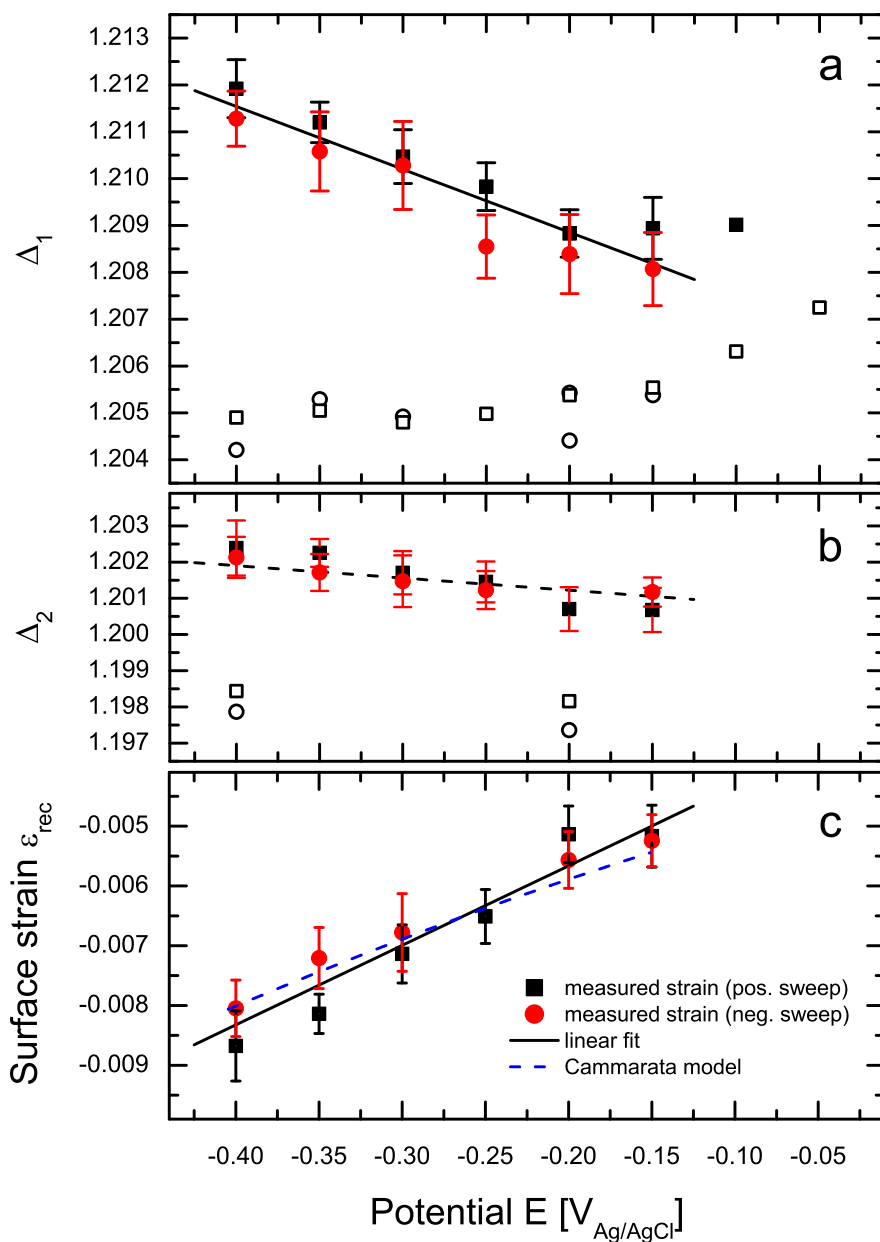
Figure 8.14: The graphs show the potential-dependence of a) Δ_1 b) Δ_2 and c) the surface strain ϵ of the reconstructed phase of Au(100) electrodes in $0.1\,\mathrm{M}$ HCl $+\ 50\,\mu\mathrm{M}$ $HAuCl_4$ solution related to the unit cell area in Au-free $0.1\,\mathrm{M}$ HCl. The solid line in a is the linear best fit, the dashed line in b is the theoretical potential-dependence of Δ_2 as calculated on the basis of the experimentally observed change in Δ_1 provided that the compression is uniaxial along the 'x5' direction. The blue dashed line in c shows the calculated surface strain ϵ determined by use of a simple thermodynamic model which was first proposed by R.C. Cammarata [133]. For comparison the solid line shows the linear best fit to $\epsilon(E)$.

the value of Δ_2 after biaxial compression is given by

$$\Delta_{2,B} = \frac{\sqrt{4 \cdot x^2 \cdot \Delta_2^2 + (y^2 - x^2) \cdot \Delta_1^2}}{2 \cdot x \cdot y} \tag{8.2}$$

where the index B denotes structural parameters of the biaxially compressed phase and where x and y describe the degree of compression at a certain potential E. More precisely, the compression factor x is attributed to the 'x5' direction and is defined by $x = \Delta_1/\Delta_{1,B}$ in reciprocal space, or by $x = d_B(\Delta_1)/d(\Delta_1)$ in terms of real space netplane spacings. The compression factor y is attributed to the 'x20' direction and defined by $y = t^*/t$ as depicted on the right side of figure 8.15. In contrast to x the compression factor y cannot be simply expressed by either of the two netplane spacings.

We estimated the maximum possible compression in 'x20' direction so that the calculated potential-dependence of Δ_2 fits to the experimental data. For this first the compression factors $x(E) = \Delta_1(-0.25\,V) / \Delta_{1,U}(E)$ have been calculated for each potential E where the $\Delta_{1,U}(E)$ values are identical to those of the best-fit line shown in figure 8.14a. Then iteratively a linear run of $y(E)$ has been found so that the calculated line of $\Delta_{2,B}$ according to equation 8.2 lies within the error bars and exhibits maximum slope. The determined slopes for the compression factors x and y are $0.011\,V^{-1}$ and $0.009\,V^{-1}$, respectively. Hence, if the reconstructed surface layer compresses biaxially then the maximum compression in 'x20' direction is 80% of the compression in 'x5' direction. Taking into account the errors in Δ_1 (which were disregarded above) an even larger compression in 'x20' direction may be possible. However, the analysis shows that we cannot exclude a biaxial compression of the reconstructed surface layer since the experimental data of Δ_1 and Δ_2 with according error bars at least allow a biaxial compression with a compression ratio of $y/x = 0.8$.
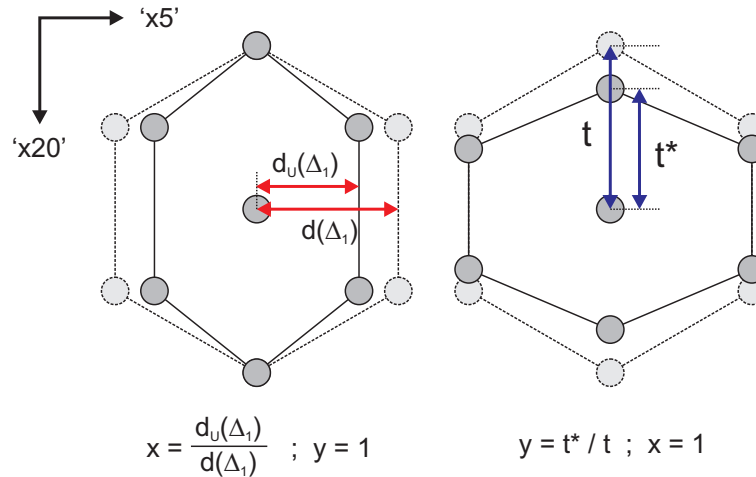
Figure 8.15: Compression along the 'x5' direction (left) and along the 'x20' direction (right) in real space. A compression by the factor x in 'x5' direction influences the netplane spacing $d(\Delta_1)$ as well as $d(\Delta_2)$ while a compression by the factor y along the 'x20' direction influences only $d(\Delta_2)$.

8.7.3 Potential-Dependence of δ

Besides of the potential-dependent changes in Δ_1 and Δ_2 the change in the angle δ between the reciprocal lattice vectors $\vec{a}_h^*$ and $\vec{b}_h^*$ has been analyzed. This angle provides additional information about the compression of the reconstructed surface structure since each type of unit cell distortion causes a characteristic change in δ. In this context it is of particular interest if the potential-dependence of δ is in agreement with an uniaxial or biaxial compression of the 'hex' layer. In order to verify the latter δ has been inferred in two different ways from the experimental data. First we exploit azimuthal scans at $\vec{a}_h^*$ and $\vec{b}_h^*$ and determined the difference in the scattering angles, i.e. $\delta = |\theta_{\vec{a}_h^*} - \theta_{\vec{b}_h^*}|$. This method does not require any information about the lattice distortion. Second, we calculated δ from the lengths of the scattering vectors $\vec{a}_h^*$ and $\vec{b}_h^*$ which were determined by radial scans. In contrast to the prior case we now have to presume a certain unit cell structure. If the unit cell is supposed to be quasi-hexagonal, which is the case for an uniaxially as well as for a biaxially compressed hexagonal structure, then, according to appendix A.2, the angle δ is related to Δ_1 and Δ_2 by the expression

$$\delta = \arccos \frac{\Delta_1}{2 \cdot \Delta_2}. \tag{8.3}$$

The obtained δ values are summarized in figure 8.16. It is obvious that (within the error bars) the potential-dependence of δ from azimuthal scans (■) and the potential-dependence of δ from radial scans (●) are in well agreement[5] for potentials $\leq -0.2\,V$. The strong decrease in δ in the azimuthal data for potentials $\geq$-0.15 V may be attributed to structural effects which occur closer to the critical potential of surface reconstruction. In the according potential regime an increase in Δ_1 was observed in Au-free 0.1 M HCl solution (section 7.6) and in Au-containing solution Δ_1 seems to be less dependent on the electrode potential (figure 8.14a).

In order to compare the potential-dependence of the measured δ values with those expected for uniaxial and biaxial compression two lines have been added to figure 8.16. The dash-dotted line shows δ which has been calculated for an uniaxial compression in 'x5' direction based on the best-fit line in figure 8.14a and on the theoretical line in figure 8.14b. The resulting line perfectly agrees with the values obtained from the radial scans which may indicate that the distortion of the surface unit cell is predominantly uniaxially. Within the error bars and in the potential regime between -0.2 V and -0.4 V the line is furthermore in agreement with the values from the azimuthal scans. The dashed line shows $\delta(E)$ which has been calculated for the maximal possible biaxial compression. Within the error bars also this line is in agreement with the measured data.

In summary, the analysis of the angle δ between the reciprocal lattice vectors $\vec{a}_h^*$ and $\vec{b}_h^*$ does not help to clarify if the compression of the reconstructed surface layer is uniaxial or biaxial. However, since the measured data is well describable by a mere uniaxial compression and since the data points show a clear linear behavior, i.e. the error bars seem to be comparatively large, we suggest that the reconstructed surface layer is rather uniaxially compressed

---

[5]Hasylab data are in quantitative agreement with the ESRF data
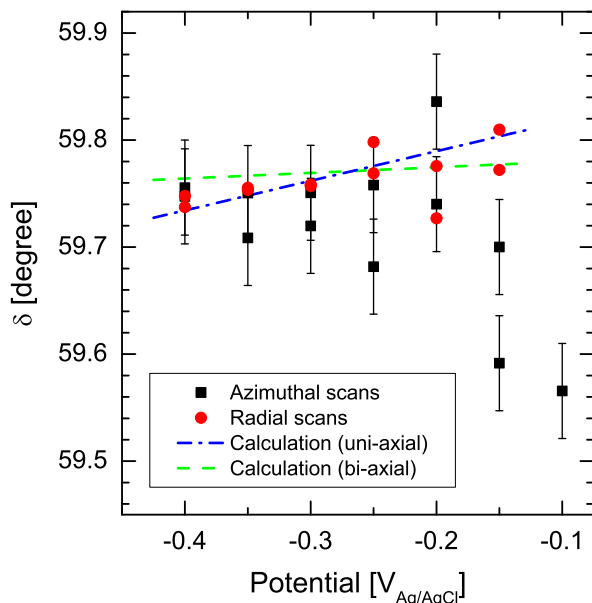
Figure 8.16: Potential-dependence of the angle δ being included by the reciprocal space lattice vectors $\vec{a}_h^*$ and $\vec{b}_h^*$ during Au electrodeposition on Au(100) electrodes in 0.1 M HCl + 50μM HAuCl$_4$ solution. The graph shows δ determined from azimuthal scans (■) and from radial scans (●). In addition two theoretical lines are plotted which presume a mere uniaxial compression (dash-dotted line) and a biaxial compression (dashed line) of the reconstructed surface layer.

than biaxially. In the next section we will presume uniaxial compression in order to apply a simple continuum model.

8.8 Theoretical Explanation of the Electrocompression Effect

The phenomenon of surface reconstruction at single crystal metal surfaces of defined orientation is still the subject of many discussions, especially concerning the driving force for the rearrangement of atoms within the topmost surface layer. Several theoretical works deal with the modeling of surface reconstruction in order to determine criteria which are able to predict if a certain metal surface will reconstruct or not [133–136]. These models are more or less successful in their predictions. However, up to now no model exists that reliably predicts reconstruction for every metal surface. The reason for the difficulties in finding an appropriate theoretical description lies in the often high complexity of the reconstructed surface structure (e.g. large unit cells), the complex interaction of the reconstructed layer with the underlying bulk structure (often incommensurate) and the still not fully clarified influence of two quantities contributing to the driving force, that is the gain in free energy and the release of tensile surface stress. Moreover, from the latter two quantities only the surface stress is measurable, while for the surface energy one has to rely on theoretical calculations. In electrochemical environment the situation is even more complicated since adsorbed ionic species (in particular anions) are known to alter the surface stress. In order to circumvent the complexity on atomic scale, continuum models have been proposed which describe the surface reconstruction based on macroscopic properties such as elastic constants. In the following we will first discuss the role of surface free energy and surface stress in the reconstruction phenomenon and introduce a comparatively successful continuum model which has been proposed by R.C. Cammarata [133, 136]. Then this continuum model will be applied with appropriate modifications to the experimental in-plane data of Au(100) in Au contain-

ing solution in order to explain the electrocompression effect. For more detailed information about surface and interface stresses the reader may be referred to several excellent overview articles [137–139].

8.8.1 Continuum Model for Surface Reconstruction

Following the thermodynamics of surfaces as formulated by Gibbs [140] two quantities describe the total work needed to create a planar solid surface of an area A, that is the surface free energy γ (surface tension) and the surface stress f. γ represents the reversible work per unit area needed to create a new surface and it is a function of the surface strain ϵ. For small strains γ can be expressed as a Taylor series about $\epsilon = 0$, i.e.

$$\gamma(\epsilon) = \gamma_0 + \left.\frac{\partial \gamma}{\partial \epsilon}\right|_{\epsilon=0} \cdot \epsilon. \tag{8.4}$$

In the case of solid surfaces the creation of a new surface is often connected with an elastical deformation which affords an additional reversible work per unit area represented by the surface stress f. This surface stress is a consequence of the broken crystal translation symmetry. Ibach pointed out that the one-sided absence of atoms above the surface results in a charge redistribution near the surface [137, 141]. Transition metals and noble metals typically have an accumulated electronic charge between the atoms in form of a bond charge. For clean metal surfaces bonds can be only established between atoms in the surface layer and the bulk atoms below. Additional charge of missing bonds moves from above the surface into the solid and strengthens the backbonds on the one hand and reduces the bond length between surface atoms on the other hand (figure 8.17a). In this situation the strain ϵ is negative and the surface tends to shrink. The according stress has a positive sign and is called 'tensile' stress. Adsorbate terminated surfaces exhibit a different behavior, especially if the adsorbed species is strongly electronegative. As depicted in figure 8.17b, the charge moves from the backbonds to above the metal surface to establish bonds between atoms in the topmost surface layer and the adsorbate. This causes a positive strain ϵ and the surface tends to expand. The corresponding negative stress is called 'compressive' stress. For most solids f is of the same order of magnitude as γ.

In general f is a tensor $f_{i,j}$ based on the elastic strain tensor ϵ_{ij}. However, for surfaces with high symmetry (threefold or higher rotation axis symmetry), such as (111) and (100) oriented surfaces of cubic metals, the surface stress is isotropic, and can be taken as a scalar f. The latter is related to the surface tension by the Shuttleworth equation [142]

$$f(\epsilon) = \gamma(\epsilon) + \left.\frac{\partial \gamma}{\partial \epsilon}\right|_{\epsilon} \tag{8.5}$$

Equation 8.5 allows to eliminate the derivative $\partial\gamma/\partial\epsilon$ in equation 8.4. Substitution yields the expression

$$\gamma(\epsilon) = \gamma_0 + [\underbrace{f(\epsilon = 0)}_{f_0} - \gamma_0] \cdot \epsilon \tag{8.6}$$
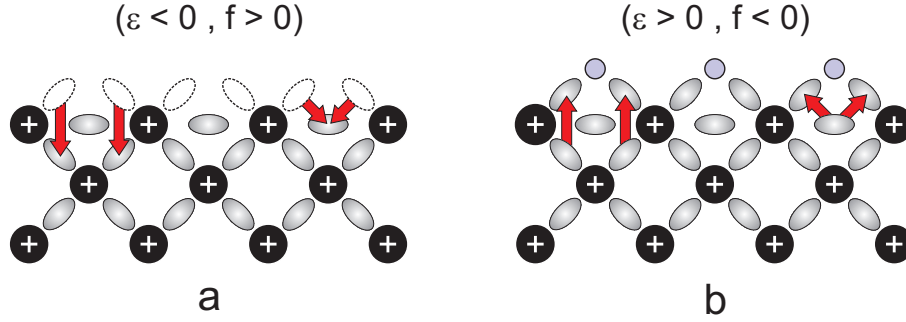
Figure 8.17: a) Bond charge redistribution at a clean metal surface. Bond charge in the missing bonds is redistributed to strengthen the backbonds (left side) and to reduce the equilibrium bond length between surface atoms (right side). This results in 'tensile' surface stress. b) Bond charge redistribution at metal surfaces with strong electronegative adsorbates. Bond charge from backbonds is redistributed to establish bonds with the adsorbates. This results in 'compressive' stress. (from reference [137])

which describes the dependence of the surface tension γ on ϵ using the unstrained (i.e. unreconstructed) surface, characterized by γ_0 and f_0, as reference point. In this consideration the strain-induced change in free surface energy is determined by the term $\Delta F(\epsilon) = \gamma(\epsilon) - \gamma(\epsilon = 0) = (f_0 - \gamma_0) \cdot \epsilon$ which can be seen as the driving force for a change in the surface atom concentration. In order to decide if a surface will reconstruct a criterion is needed that tells how large $\Delta F(\epsilon)$ must be. For these purposes Herring proposed a continuum model which estimates the energy spent by placing atoms in unfavorable binding sites and the energy necessary to create a dislocation [143]. A further extension of this model by Cammarata could surprisingly successful predict surfaces that undergo reconstruction [133]. According to Cammarata the work $\Delta F(\epsilon)$ per unit area needed to introduce an elastic strain in the top monolayer is represented by a sum of three terms (I-III)

$$\Delta F(\epsilon) = \underbrace{\frac{Yh}{2(1 - \nu^2)} \cdot \epsilon^2}_{I} \underbrace{- \alpha G b \cdot \epsilon}_{II} + \underbrace{(f_0 - \gamma_0) \cdot \epsilon}_{III} \tag{8.7}$$

provided that the surface reconstruction is associated with a one-dimensional compression. Term (I) describes the elastic energy of the surface layer that is strained by an amount $\epsilon < 0$ in one direction while the layer is not allowed to deform in the perpendicular in-plane direction. The term contains the Young's modulus Y, the surface layer thickness h and the Poisson's ratio ν. Table 8.1 summarizes some values of Y and ν for differently oriented gold surfaces. Term (II) is associated with the energy of the noncoherent interface between the strained surface atoms and the underlying lattice, i.e. it describes the interaction between the surface layer and the substrate. By analogy with continuum models for epitaxy, this term can be taken as the energy needed to form a periodic row of edge dislocations that accommodates the in-plane misfit strain [133]. Herein G is the shear modulus, b is the Burgers vector and α is given by

$$\alpha \approx [4\pi(1 - \nu)]^{-1} \tag{8.8}$$

Material	Elastic constants $(10^{11}$ Nm$^{-2})$	Elastic compliances $(10^{11}$ m^{2}N$^{-1})$	Surface orientation	Direction	Young modulus Y $(10^{11}$ Nm$^{-2})$	Poisson number ν
Au	$C_{11} = 1.86$	$S_{11} = 2.36$	(111)	all	0.810	0.566
	$C_{12} = 1.57$	$S_{12} = -1.08$	(100)	$< 001 >$	0.424	0.458
	$C_{44} = 0.42$	$S_{44} = 2.38$	(110)	$< 1\bar{1}0 >$	0.81	0.566
			(110)		0.424	0.458

Table 8.1: Young modulus Y and Poisson number ν for different surface orientations calculated in reference [139] based on the elastic constants of reference [144].

The terms I and II are opposing forces which counteract surface reconstruction. Term (III) is the main driving force for reconstruction and regards the change in the surface free energy that results from a change in elastic strain ϵ and concomitant change in the surface density of atoms.

8.8.2 Surface Strain of Au(100) in Au-containing Solution

The surface strain ϵ (as defined in equation 8.9) of the reconstructed Au(100) surface related to the unreconstructed (1×1) bulk structure amounts $\approx$ -20%. For this comparatively large strain the Taylor expansion given in equation 8.4 is not valid since it holds for small ϵ only. Furthermore Grofov showed that the Shuttleworth equation 8.5 for the interface between a solid isotropic electrode and a liquid electrolyte is valid only in the case of an infinitesimal surface deformation [145]. Consequently the model proposed by Cammarata cannot be applied to the reconstructed Au(100) surface using the unreconstructed Au(100) surface as reference. In addition the elastic constants Y and ν are dependent on the surface orientation and they change significantly during the reconstruction formation process from the (1×1) phase to the 'hex' phase. Thus, in contrast to all previous applications of the Cammarata model we refer the structural changes to an alternative reference point which has a surface atom density closer to the reconstructed, compressed surface phase. Since we are interested in the derivative $\partial\epsilon/\partial E$ in the reconstructed potential regime and not in absolute values of the surface strain with respect to the (1×1) bulk structure we are basically free to choose an appropriate 'hex' reconstructed surface structure as reference. Particularly, the following three surfaces are conceivable references:

- Au(100)-'hex' in UHV

- Au(100)-'hex' in Au-free 0.1 M HCl

- Au(100)-'hex' in Au-containing 0.1 HCl at the onset of compression

The potential-dependent surface strain ϵ of the Au(100) surface in Au containing solution with respect to each of the proposed reference surfaces was determined via

$$\epsilon(E) \equiv \frac{A_{hex,Au}(E) - A_{\text{ref}}}{A_{\text{ref}}} = \frac{A_{hex,Au}(E)}{A_{\text{ref}}} - 1 \qquad (8.9)$$
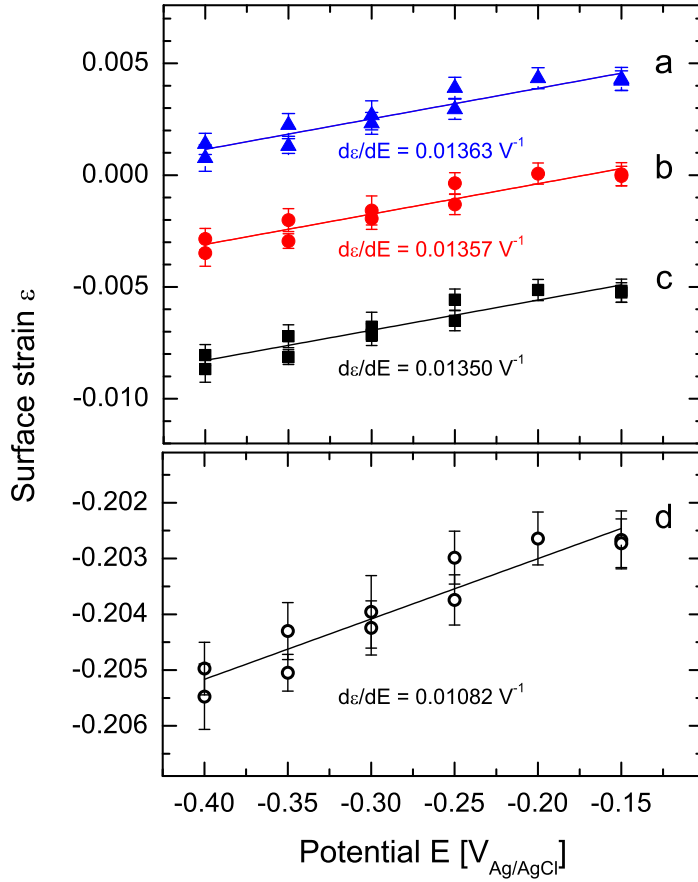
Figure 8.18: Surface strain ϵ of the reconstructed Au(100) electrode in 0.1 M HCl + 0.05 mM HAuCl$_4$ solution with respect to the electrode potential E and different reference surfaces. For the latter the surface structures of a) Au(100)-'hex' in UHV, b) Au(100)-'hex' in 0.1 M HCl + 0.05 mM HAuCl$_4$ at -0.15 V in the onset of compression, c) Au(100)-'hex' in 0.1 M HCl and d) Au(100)-(1×1) bulk termination have been employed.

where $A_{hex,Au}$ is the surface area per atom in Au containing solution and A_{ref} the surface area per atom of the reference surface. In the case of an unsheared, quasi-hexagonal Au(100) surface structure A is obtained by the expression

$$A = \frac{a_c^2}{\Delta_1 \cdot \sqrt{4\Delta_2^2 - \Delta_1^2}} \tag{8.10}$$

where Δ_1 and Δ_2 are the measured reciprocal lattice parameters (see appendix A.2) and a_c is the real space lattice constant of gold (4.08 Å). All determined areas A for the aforementioned reference surfaces and for the Au(100) bulk terminated surface are summarized in table 8.2a. Based on the areas A the surface strain ϵ has been calculated for each potential and for each reference surface. The resulting strains are plotted in figure 8.18. Each set of data points allows to infer the derivative of ϵ with respect to the electrode potential E, the so-called electrostriction coefficient $\partial\epsilon/\partial E$ (table 8.2b). For this straight lines have been fitted to the data and the errors were determined by the lines of minimum and maximum slope within the error bars, respectively. In the case of reconstructed reference surfaces the differences between $A_{hex,Au}$ and A_{ref} are small and the potential-dependence of the calculated surface strains are very similar with a value of $\approx 0.0136 \pm 0.005$ V^{-1}. Thus each of the three proposed reference structures results in almost identical potential-dependent changes in the surface strain within the error bars. In contrast to the latter the difference between $A_{hex,Au}$ and

a) Surface Atom Density			
Surface Structure	Δ_1	Δ_2	Surface Area [$\mathring{A}^2$/atom]
Au(100)-(1×1) bulk termination	-	-	8.32320
Au(100)-'hex' in UHV	1.20600	1.20600	6.60793
Au(100)-'hex' in 0.1 M HCl	1.20502*	1.19796*	6.67084
Au(100)-'hex' in 0.1 M HCl + Au	1.20850†	1.20090†	6.63632
Surface Structure	Stripe Separation p [a_0]		Surface Area [$\mathring{A}^2$/atom]
Au(111)-(1×1) bulk termination	(no stripes)		7.20812
Au(111)-(rec) in 0.1 M HCl	22.45‡		6.90074

b) Surface Strain			
Surface	Reference Surface Structure	$\partial\epsilon/\partial E$ [V^{-1}] measured	$\partial\epsilon/\partial E$ [V^{-1}] continuum model
Au(100)	Au(100)-(1×1) bulk termination	0.0108 ± 0.005	-
Au(100)	Au(100)-'hex' in UHV	0.0136 ± 0.005	≈ 0.0103
Au(100)	Au(100)-'hex' in 0.1 M HCl	0.0135 ± 0.005*	≈ 0.0103
Au(100)	Au(100)-'hex' in 0.1 M HCl + Au	0.0136 ± 0.005†	≈ 0.0103
Au(111)	Au(111)-(1×1) bulk termination	0.0150 ± 0.002	≈ 0.0224
Au(111)	Au(111)-(rec) in 0.1 M HCl	0.0156 ± 0.002	≈ 0.0162

∗ = average between E = -0.15 V and E = -0.4 V , † = determined at E = -0.15 V in 0.05 mM HAuCl$_4$,

‡ = average between E = -0.08 V and E = -0.2 V in the positive potential sweep

Table 8.2: a) Density of Au atoms in unreconstructed and reconstructed surfaces of Au(100) and Au(111) electrodes. The last column lists the area A per surface atom calculated for a quasi-hexagonal, uniaxially compressed 'hex'-layer (equation 8.10 and equation 8.14) and for a perfectly bulk terminated surface. b) Potential-dependent changes in the surface strain ϵ with respect to different reference structures. Continuum model values have been calculated via equation 8.13. Experimental data for Au(111) electrodes were carried out by Ayyad and coworkers [12].

$A_{(1x1)}$ is comparatively large which results in a smaller potential-dependence of the surface strain of ≈ 0.0108 ± 0.005 V^{-1}. For the following analysis we chose the Au(100)-'hex' surface in Au-free 0.1 M HCl solution as reference structure. Similar as in the Frenkel-Kontorova model [146], which was used by Mansfield et al. to explain surface reconstruction on gold single crystals [135], the reconstructed surface is treated like an 'adsorbate' layer.

8.8.3 Continuum Model Applied on Au(100) Reconstruction

In the case of Au(100) surfaces the reconstructed surface layer is fully incommensurate with the underlying unreconstructed bulk. For this reason it seems legitimate to neglect the surface/substrate interaction term in equation 8.7 (term II) so that the surface tension γ_{rec}

of the reconstructed phase is approximated by

$$\gamma_{rec}(\epsilon) = \gamma_0 + \Delta F(\epsilon) \approx \gamma_0 + (f_0 - \gamma_0) \cdot \epsilon + \frac{Yh}{2(1 - \nu^2)} \cdot \epsilon^2 \qquad (8.11)$$

In equilibrium the surface tension γ_{rec} is minimized which defines the corresponding surface strain ϵ_{min}, i.e.

$$\epsilon_{min} = \frac{1 - \nu^2}{Yh} \cdot (\gamma_0 - f_0) \qquad (8.12)$$

In the following we are interested in the potential-dependence of the surface strain. The derivative of equation 8.12 with respect to the electrode potential E is given by

$$\frac{\partial \epsilon}{\partial E} = \frac{1 - \nu^2}{Yh} \cdot \left(\frac{\partial \gamma_0}{\partial E} - \frac{\partial f_0}{\partial E} \right) \qquad (8.13)$$

While $\partial f / \partial E$ is accessible via experiments, $\partial \gamma / \partial E$ can only be obtained by theoretical approach. Figure 8.19a shows the surface tension γ as calculated by a thermodynamic analysis for reconstructed Au(100) electrodes in 10 mM and 100 mM perchloric acid [77]. The data points in 100 mM $HClO_4$ have been fitted well by a polynomial of third order and afterwards the polynomial curve has been derived with respect to the potential E (figure 8.19c). The change of surface stress f with potential E has been measured by Bach et al. for Au(100) electrodes in 0.1 M perchloric acid. The Au(100) surface is reconstructed below ≈ 0 V versus Ag/AgCl. In this potential regime the stress of the (1×1) terminated electrode has a finite slope with $\partial f_{1 \times 1} / \partial E \approx$ -0.12 $Nm^{-1}V^{-1}$ while the stress for the 'hex' terminated electrode is almost constant with $\partial f_{hex} / \partial E \approx 0$ $Nm^{-1}V^{-1}$. The continuous decrease in the surface stress when the potential becomes more positive than the critical potential is due to an increasing number of specifically adsorbed ClO_4^- ions on the surface (supported by the change in pzc). This induces a changeover from tensile to compressive stress and causes the lifting of the reconstruction. In order to model the experimental data the electrostriction coefficient $\partial \epsilon / \partial E$ has been determined via equation 8.13 employing the potential-dependence $\partial \gamma_{hex} / \partial E$ as calculated by Santos et al. for reconstructed Au(100) electrodes in 100 mM $HClO_4$ (figure 8.19c), the potential-dependence $\partial f_{hex} / \partial E \approx 0$ from the surface stress measurements of Bach et al. (figure 8.19b) and the elastic constants[6] $Y = 81$ GPa and $\nu = 0.566$ of a two-dimensional (111) oriented gold surface (table 8.1) with a layer thickness of $h = a_c/3 = 1.36$ Å. This procedure results in a value of $\partial \epsilon / \partial E \approx 0.0103 \pm 0.002$ V^{-1} which is about 76% of the electrostriction coefficient inferred from the experimental electrocompression data (table 8.2). Subsequently $\partial \epsilon / \partial E$ has been integrated over E in order to infer the dependence $\epsilon(E)$. Figure 8.14c summarizes the experimentally determined surface strain values with respect to the 'hex' structure in 0.1 M HCl and the calculated $\epsilon(E)$ curve according to the Cammarata model (dashed line). Since the performed integration over E allows an arbitrary constant being added to $\epsilon(E)$ the theoretical curve has been shifted in ϵ to best comply with the measured data. The calculated model curve fits well to the experimental data within the error bars. The latter were determined by Gaussian error propagation based on the errors in Δ_1 and Δ_2.

---

[6]Here we employ the elastic constants of a (111) oriented surface since we refer the experimental data to the 'hex' structure in 0.1 M HCl.
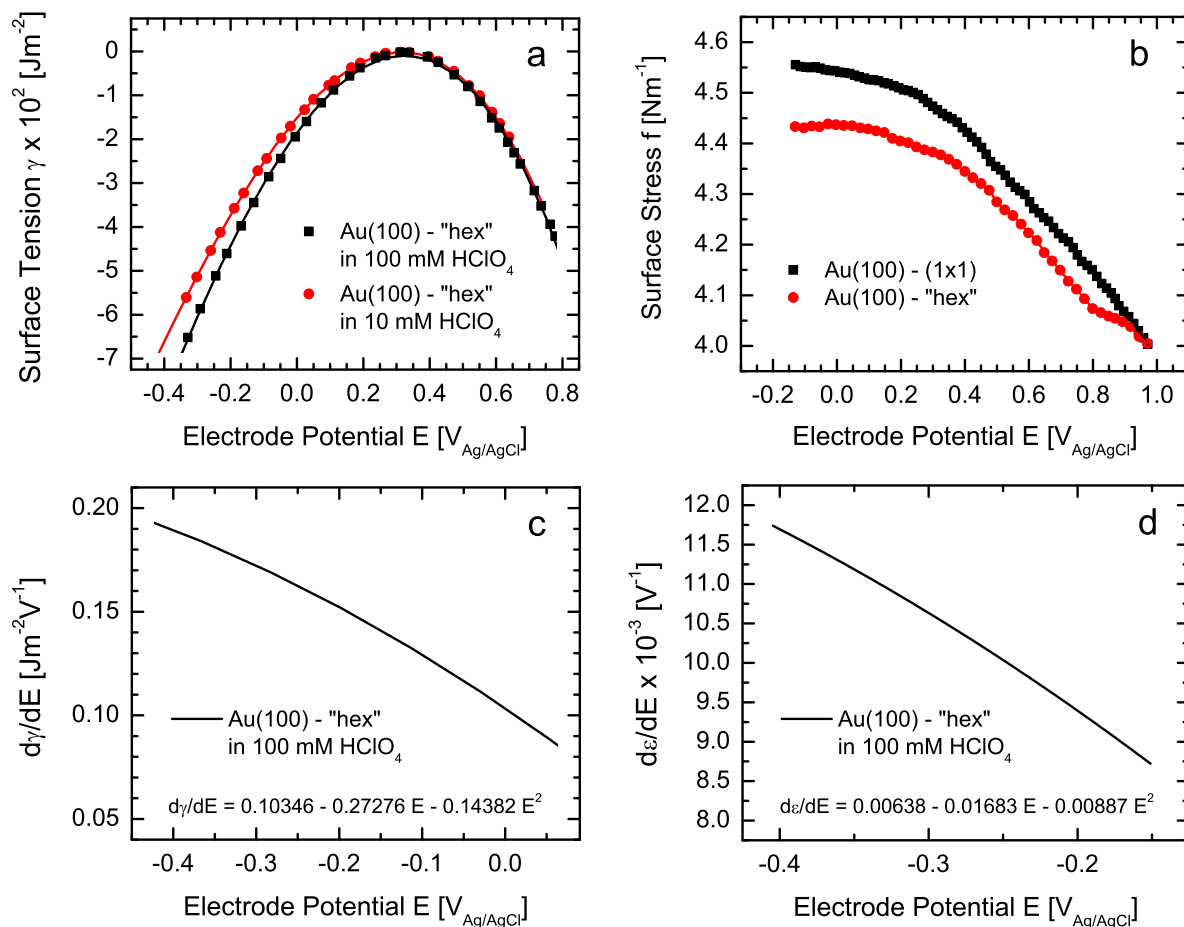
Figure 8.19: a) Surface tensions of reconstructed Au(100) electrodes in perchloric acid solutions calculated by a thermodynamic analysis [77]. b) Surface stress for the initially reconstructed and unreconstructed Au(100) surface measured by the cantilever bending method [147]. The surface stress measurements were carried out in $0.1\,\mathrm{M}$ HClO$_4$ and in positive potential sweep direction. c) Derivative of γ with respect to the electrode potential E. d) Derivative of the surface strain ϵ with respect to E.

The model curve and the measured strain are in good agreement even though the model calculation is based on additional assumptions and on supplemental data. There are several sources for uncertainties. First, the surface/substrate interaction term of equation 8.7 has been neglegted in equation 8.11. It is known from theoretical calculations concerning relaxed and unrelaxed Pt(111) surfaces [148] that a layer expansion of the topmost surface layer is able to alter γ as well as f. Furthermore layer-resolved calculations demonstrate that most of the observed stress is located in the first and second layer [149,150]. Thus the surface/substrate interaction might yield surface energy contributions which are not negligible. Second, Bach et al. stated that their surface stress measurements are not corrected for the effect

of cantilever clamping which is estimated to result in an error of 10% in the surface stress values [137]. Besides of this uncertainty in the measured f values the exact determination of $\partial f/\partial E$ is difficult since the data has to be interpolated into the reconstructed potential regime. Thus $\partial f/\partial E \approx 0$ may be not the best approximation. As well the theoretically calculated dependence $\gamma(E)$ might be afflicted with a noticeable error. Third, in contrast to the present measurements in $0.1\,\text{M}$ HCl containing solution the experimental surface stress data and the theoretical surface energy data were carried out in $0.1\,\text{M}$ perchloric acid which potentially results in a different potential-dependence of f.

In view of the simplicity of the model and of the large amount of uncertainties in contributing quantities the good agreement of model curve and measured data may be coincidental. Nevertheless, the continuum model is able to describe at least the general trend of the observed enhanced surface compression under deposition conditions.

8.8.4 Continuum Model Applied on Au(111) Reconstruction

In-situ SXS experiments on Au(111) electrodes in $0.1\,\text{M}$ HCl and Au containing solution were performed by Ayyad et al. [12]. The reconstructed Au(111) surface[7] exhibits an uniaxial incommensurate $(p \times \sqrt{3})$ structure with three symmetry-equivalent rotational domains (termed as 'striped phase'). The unit cell parameter p, also called stripe separation parameter, is dependent on the electrode potential as can be seen in figure 8.20a. While in $0.1\,\text{M}$ HCl solution p saturates at $\approx 22\,a_0$ at sufficiently negative potential, the data carried out in $0.1\,\text{M}$ HCl + $0.05\,\text{mM}$ HAuCl$_4$ containing solution shows an enhanced linear decrease in p below $0\,\text{V}$, resulting in a significantly smaller stripe separation of $\approx 19\,a_0$ at the most negative potential studied (-$0.5\,\text{V}$). This data demonstrates a potential-dependent, uniaxial and growth-induced compression of the reconstructed Au(111) surface.

In a similar manner as for Au(100) the surface strain ϵ has been determined as a function of the electrode potential. In the case of Au(111) electrodes the area A per surface atom is related to the stripe separation parameter p by the following expression

$$A = \frac{\sqrt{3}a^2}{2}\left[\frac{p}{1+p}\right] \tag{8.14}$$

where $a = 2.885\,\text{Å}$ is the gold nearest neighbor distance. Table 8.2a summarizes the areas A for two employed reference surfaces, that is the unreconstructed (1×1) bulk structure and the reconstructed surface structure in $0.1\,\text{M}$ HCl solution, respectively. Based on the latter and on equation 8.10 the surface strain ϵ of Au(111) in $0.05\,\text{mM}$ HAuCl$_4$ containing solution has been calculated for each potential. Then the electrostriction coefficients have been inferred by fitting lines to the $\epsilon(E)$ data. For the unreconstructed and reconstructed reference surface similar values of $\partial\epsilon/\partial E = 0.015\,\text{V}^{-1}$ and $\partial\epsilon/\partial E = 0.016\,\text{V}^{-1}$ have been found (see table 8.2b).

---

[7]For more detailed information about the reconstructed surface phase of Au(111) the reader be referred to the references [12, 81, 125, 151, 152]
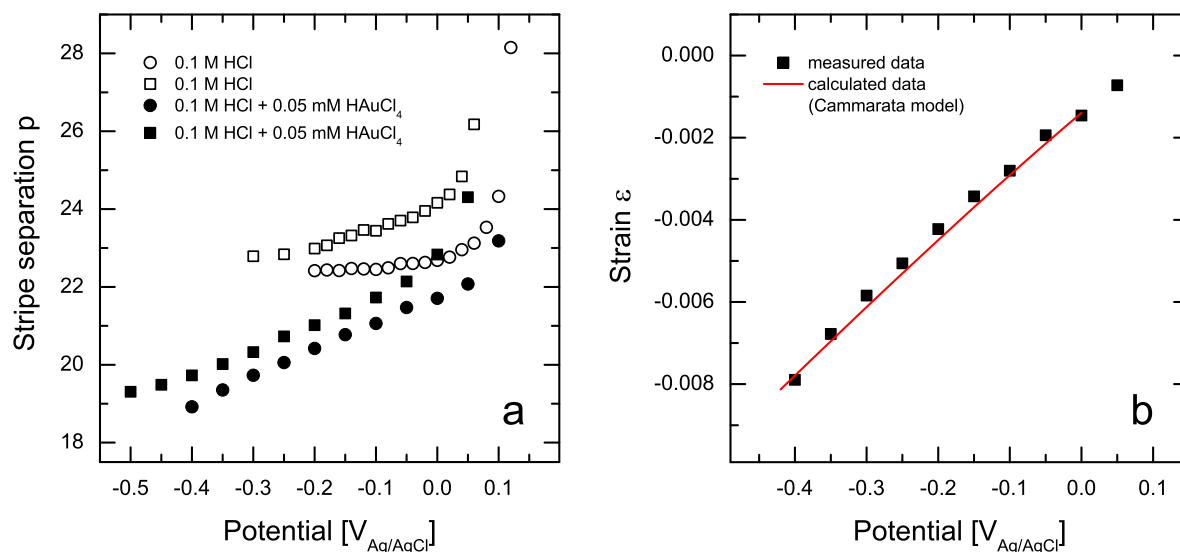
Figure 8.20: a) Stripe separation parameter p of reconstructed Au(111) electrodes as a function of the applied electrode potential. Measurements in Au-containing electrolyte reveal a pronounced linear decrease in p towards more negative potentials which indicates an increased uniaxial compression of the reconstructed surface layer in comparison to the behavior in Au-free solution. From ref. [12]. b) Surface strain ϵ in Au-containing solution determined with respect to the surface structure in Au-free 0.1 M HCl. The solid line shows $\epsilon(E)$ according to the Cammarata model.

In order to apply the Cammarata model we again rely on the results of surface stress measurements of Bach et al. [147] which provide values of $\partial f_{1\times1}/\partial E \approx -0.497\,\mathrm{Nm^{-1}V^{-1}}$ and $\partial f_{rec}/\partial E \approx -0.305\,\mathrm{Nm^{-1}V^{-1}}$ for the unreconstructed and reconstructed Au(111) surface in the reconstructed potential regime, respectively. The derivative of γ with respect to E was obtained from calculations performed by Santos et al. for Au(111) electrodes in 10 mM perchloric acid [77]. For the elastic constants the values of $Y = 81\,\mathrm{GPa}$ and $\nu = 0.566$ were used since the Au(111) surface structure is hexagonal in all surface phases. The layer thickness h for the (111) oriented surface is 2.35 Å. According to equation 8.13 we determined $\partial \epsilon/\partial E$ for the two reference surfaces. With respect to the unreconstructed (1×1) bulk structure a value of $\partial \epsilon/\partial E = 0.022\,\mathrm{V^{-1}}$ was calculated which is about 47% larger than the experimental value of $0.015 \pm 0.002\,\mathrm{V^{-1}}$. However, taking the reconstructed surface in 0.1 M HCl as reference, a value of $0.016\,\mathrm{V^{-1}}$ is found in perfect agreement with the measured data as shown by the potential-dependence of $\epsilon(E)$ in figure 8.20b. Again the reconstructed surface in Au-free electrolyte seems to be the better point of reference.

8.8.5 Conclusions to Electrocompression

In the previous two subsections a continuum model proposed by R.C. Cammarata [133] was successfully applied on SXS in-plane data of Au(100) and Au(111) electrodes in order to de-

scribe the growth-induced and potential-dependent compression in the reconstructed surface layer. In contrast to previous applications of the model we referred changes in the reconstructed surface layer in Au-containing solution to the less compressed, reconstructed surface in Au-free electrolyte and not to the unreconstructed structure of a perfect bulk termination. In doing so the electrocompression effect could be well described by the Cammarata model. At this point we want to emphasize that our approach allows to explain structural changes within the reconstructed potential regime but it provides no information about the role of surface stress and surface energy in the surface phase transition. The potential-dependent changes in the surface strain on both investigated Au surfaces are more than an order of magnitude smaller than those of UPD adlayers on noble metal electrodes [153] which is plausible due to the higher packing density in the reconstructed layers.

Both surfaces have in common that they exhibit a quasi-hexagonal surface structure in the reconstructed potential regime. Moreover these quasi-hexagonal surface layers compress uniaxially towards more negative potentials. However, the fact that the experimentally determined electrostriction coefficients of $\partial \epsilon / \partial E \approx 0.0135 \pm 0.005\,\mathrm{V}^{-1}$ and $\partial \epsilon / \partial E \approx 0.016 \pm 0.002\,\mathrm{V}^{-1}$ for reconstructed Au(100) and Au(111) electrodes, respectively, are very close to each other is presumably not related to the common hexagonal arrangement of atoms in the reconstructed layers. The changes in surface stress and in surface energy are different in the electrocompression of both surfaces. For homoepitaxial growth on reconstructed Au(100) electrodes the surface stress does not markedly change with potential while the surface stress changes noticeable for homoepitaxial growth on reconstructed Au(111) electrodes.

Finally it is noted that at the potential of zero charge (i.e. close to the surface phase transition) where the surface energy and stress should resemble most closely that of the metal-vacuum interface, the compression during electrodeposition is almost identical to that found on clean surfaces under UHV conditions. A higher compression apparently requires a negatively charged surface, which explains why this effect was not observed during homoepitaxial growth in vacuum [2].

8.9 Summary

In this chapter we discussed the in-plane structure of Au(100) electrodes during homoepitaxial deposition in $0.1\,\mathrm{M}$ HCl + $0.05\,\mathrm{mM}$ HAuCl$_4$ solution. In-plane scans which were performed in parallel to an electrolyte exchange from Au-free to Au-containing solution revealed that the homoepitaxial growth induces an enhanced compression of the reconstructed surface layer in 'x5' direction (i.e. perpendicular to the reconstruction stripes) as well as an alignment of $\pm\,0.71°$ rotated 'hex' domains along the $[110]_c$ direction. Both effects are strongly potential-dependent and reversible: the 'hex' layer compresses linearly towards more negative potentials while simultaneously an almost linear rotational transition from rotated domains to aligned domains is observed. Geometrical considerations based on the measured reciprocal lattice constants Δ_1 and Δ_2 of the 'hex' layer show that the potential-dependent compression is in good agreement with an uniaxial compression along the 'x5' direction. However, due to significant error bars in the measured data a biaxial compression cannot

be fully excluded. This entire behavior is in strong contrast to the behavior in Au-free electrolyte where the surface structure is almost potential-independent and predominantly rotated domains are observed. The reversible and linear potential-dependent change in surface compression and in the rotation angle $\Delta\theta$, respectively, suggests a correlation between both effects, i.e. that the rotational transition may be induced by the (presumably uniaxial) compression of the surface layer. In addition to the latter two effects homoepitaxtial growth results in a significant increase in the average domain size in 'x5' direction. Especially at very negative potentials approximately five times larger reconstructed domains are found compared to those in Au free solution. This effect potentially has to be related to a reduce of surface defects and to a ripening process which increases the in-plane order of the reconstructed surface phase. Moreover it is evident that large reconstructed domains prefer the aligned orientation which resembles earlier observations in UHV [5] and which suggests that the aligned phase is energetically favorable.

The formation process of the electrocompressed phase has been investigated in more detail by potential steps into the reconstructed potential regime giving rise to the following conclusions: The first deposited 0.25 ML appear to be directly incorporated in the unreconstructed Au(100) surface which results in a reconstructed and uncompressed 'hex' layer exhibiting a similar structure as potential-induced, reconstructed surfaces in Au-free electrolyte. Here an enhanced surface compression seems to be hindered by kinetic limitations since the initial formation of reconstruction requires the insertion of Au adatoms into the existing surface layer. The compressed phase forms with the deposition of the successive monolayer and is almost completed after a total deposit of 1.25 ML. In this stage of the deposition process the growth proceeds via attachment of adatoms to island step edges and no significant barrier exists for attaining the energetically preferred in-plane spacing. Consequently further layers grow in the electrocompressed phase. A simple theoretical continuum model proposed by R.C. Cammarata [133] is able to explain the electrocompression effect observed on reconstructed Au(100) as well as on Au(111) electrodes in Au-containing 0.1 M HCl solution. In contrast to previous applications of the model we referred growth-induced changes to the reconstructed surface in Au-free electrolyte. The data modeling indicates that the main driving force for electrocompression of Au(111) electrode surfaces is the release of surface stress while for Au(100) electrode surfaces the gain in surface energy seems to be the dominating factor. Although the present study does not allow to identify the driving force for reconstruction on both surface orientations the determined behavior within the reconstructed potential regime is in agreement with the opinion of H. Ibach, C.E. Bach et al. who pointed out that the release of tensile surface stress plays only a minor role in the reconstruction of Au(100) surfaces [137, 147, 154]. A higher compression apparently requires a negatively charged surface, which explains why this effect was not observed during homoepitaxial growth in vacuum.

9 Growth Mode Studies of Au(100)-Electrodes

The growth of crystalline solids in liquid solutions is central not only in natural mineralization but also in current and future technological deposition processes. To clarify the relationship between the atomic-scale structure of the solid-liquid interface, the growth behavior, and the resulting surface morphology (figure 9.1), direct investigations of the interface structure during the growth process are required.
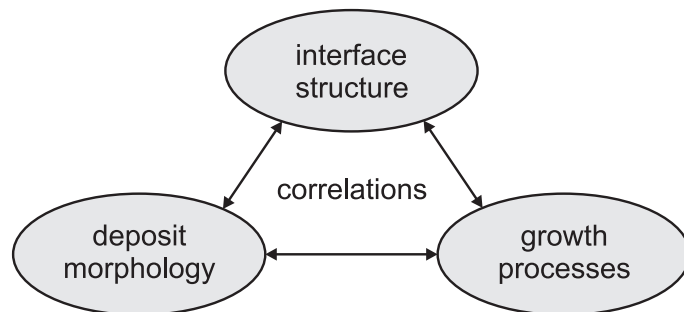
Figure 9.1: Complex relationships at the solid/liquid interface during electrodeposition.

In this chapter I will demonstrate that such investigations are possible by surface X-ray scattering in transmission geometry up to growth rates of several monolayers per minute. An electrochemical system, homoepitaxial Au(100) electrodeposition, was chosen for the study because of the particularly easy control of electrochemical growth processes and the interesting potential-dependent growth behavior. In contrast to crystal growth in solution, growth at the solid-vacuum interface has been investigated in great detail on the atomic scale for the case of molecular beam epitaxy (MBE) of metals and semiconductors by diffraction methods [1, 2]. According to these experimental as well as theoretical studies [3] homoepitaxial growth far from equilibrium is governed by the flux of adatoms to the surface, i.e., the deposition rate, and the rates of intra- and interlayer transport, which are functions of temperature and surface structure. Dependent on the relative rates of these processes step-flow growth, layer-by-layer growth, or multilayer growth are observed. For unreconstructed fcc(100) surfaces step-flow or layer-by-layer growth is found over a wide range of temperatures, indicating highly effective interlayer mass transport [1]. Au(100) exhibits a reconstructed surface layer of hexagonally ('hex') arranged atoms under ultrahigh vacuum (UHV) conditions. STM studies reported layer-by-layer growth with strongly anisotropic islands on this surface [4, 5].

While the previous chapter focused on the in-plane structure of Au(100) electrodes during homoepitaxial deposition, this chapter will address growth in the direction along the surface normal. In more detail, the present surface X-ray scattering study of electrochemical homoepitaxial growth on Au(100) aims at elucidating the influence of the deposition parameters and interface structure on the atomistic growth process and on the resulting atomic-scale film morphology in a similar manner as in previous MBE studies. In electrochemical environment the hex surface reconstruction is only stable negative of a critical (electrolyte-dependent) potential, whereas at more positive potentials the surface is unreconstructed. Furthermore, the surface mobility in the potential regime of the unreconstructed

Au(100) surface was found to increase substantially with increasing potential, in particular, in the presence of Cl⁻ anions [120–123]. According to kinetic growth theory also the growth behavior should therefore depend on potential, as will be shown in this chapter. Deposition was performed at high overpotentials, where the deposition rate is determined solely by diffusion of the metal species ($HAuCl_4^-$) in the electrolyte solution to the metal surface, i.e., can be controlled by the metal concentration in the solution ('diffusion-limited' growth). This procedure allows us to control the potential and the deposition rate independently over a wide range of potentials and growth rates, making it possible to separate the influence of these two effects on the atomic-scale morphology of the deposit [12]. Thus, in contrast to previous MBE studies, where the morphology is monitored after initiation of a constant adatom flux at constant temperature, i.e. at fixed surface mobility, our electrodeposition experiments monitor the morphology at constant (diffusion-limited) flux upon a potential step, i.e. parallel to a change in the surface mobility.

The chapter is divided into the following parts. First we introduce the employed scattering geometry. Then we discuss the growth behavior during electrolyte exchange from Au-free to Au-containing solution followed by systematic growth mode studies based on potential step experiments and interpretation of the results. To our knowledge this is the first study of this kind for growth at solid-liquid interfaces. In addition, experiments during constant electrolyte flow through the cell and experiments at higher deposition rates are presented. In particular, the latter allow us to develop a model for the growth behavior in the initial stage after potential steps into the reconstructed potential regime. The chapter concludes with a brief overview of homoepitaxial growth experiments on Au(111) electrodes which as well were performed in the framework of this project.

9.1 Diffracted Intensity from Au(100) Electrodes

As in the case of the previously discussed Au(100) in-plane measurements, the conventional cubic gold unit cell has been chosen with two perpendicular lattice vectors $\vec{a}$ and $\vec{b}$ within the surface plane and vector $\vec{c}$ along the surface normal. The cubic real space lattice constant is $4.08\,\text{Å}$. Again the scattering vector $\vec{q}$ is represented in terms of the Miller indices (H, K, L) where

$$\vec{q} = H \cdot \vec{a}^* + K \cdot \vec{b}^* + L \cdot \vec{c}^* \tag{9.1}$$

with $\vec{a}^*$, $\vec{b}^*$ and $\vec{c}^*$ denoting the reciprocal lattice vectors, each with a length of $1.54\,\text{Å}^{-1}$. In the present deposition studies potential step experiments have been performed into the unreconstructed as well as into the reconstructed potential regime. Thus, besides of reflections with integer Miller indices from the bulk also reflections with fractional indices are observed from the reconstructed surface layer. The in-plane diffraction pattern is illustrated in figure 9.2a.

The defined real space unit cell gives rise to allowed Bragg reflections if either all Miller indices are even or if all Miller indices are odd. Figure 9.2b shows the first order Bragg reflections in the octant of positive H, K and L values. Due to the abrupt termination of the
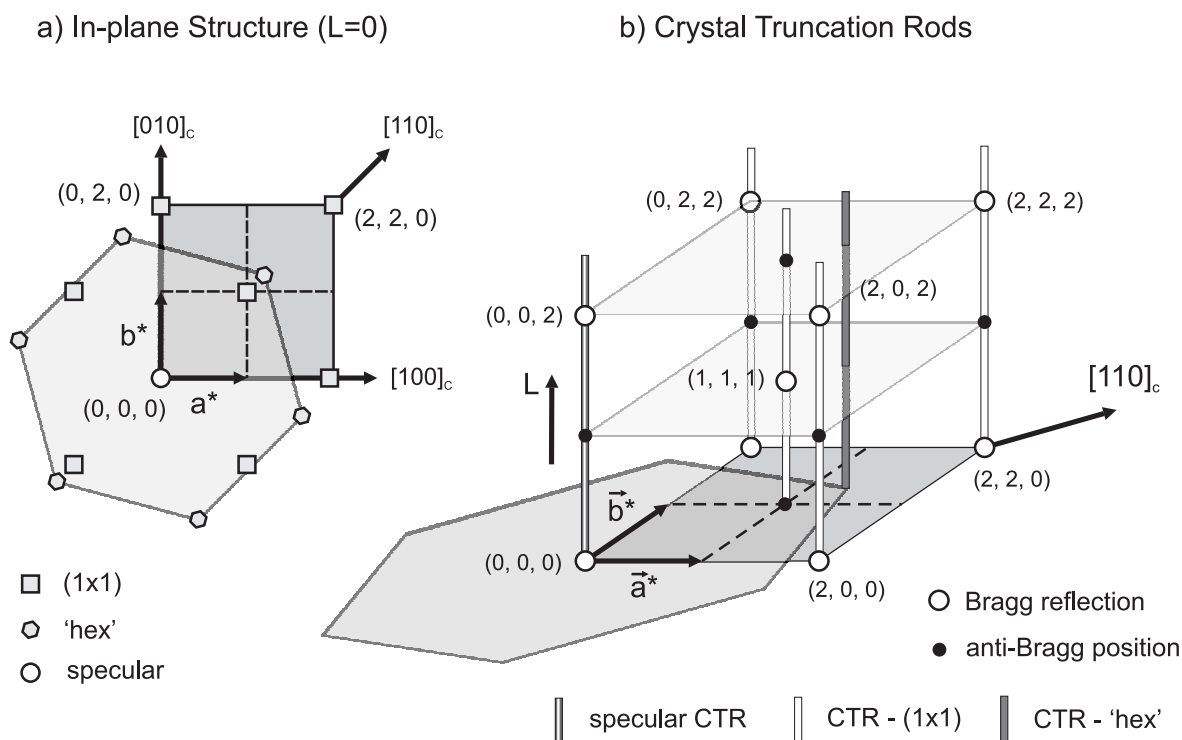
Figure 9.2: a) In-plane structure of reconstructed Au(100) single crystals. Each point represents a rod of scattered intensity along the surface normal, originating either from the (1x1) bulk structure (□) or from the reconstructed surface layer (○). b) Out-of-plane structure. Streaks of intensity connect Bragg reflections (○) in L-direction, the so-called crystal truncation rods (CTR). Half way positions (anti-Bragg) between two Bragg reflections are indicated by filled circles (●).

crystal at the surface additional X-ray intensity is observed in the connection line between two Bragg peaks along the L-direction, the so-called crystal truncation rods (CTR). There are different types of CTRs. The intensity along the specular CTR ($H = K = 0$) contains informations about the electron density profile $\rho(z)$ perpendicular to the surface (averaged over the lateral coordinates x and y) including contributions from the crystal bulk as well as from the reconstructed surface layer. In contrast, non-specular bulk rods, situated at positions where H and K are both even or both odd, are expected to consist solely of scattered intensity from the crystal bulk since the reconstructed surface layer of Au(100) is incommensurable. However, our diffraction studies revealed that non-specular bulk CTRs are sensitive to the reconstructed surface layer which probably has to be attributed to local variations in the structural parameters of the reconstructed layer so that some parts of reconstructed areas give contributions to the scattered intensity in the bulk CTRs (see section 9.9). A similar influence of incommensurate adlayers on the intensity along bulk CTRs was first reported by Toney and coworkers who investigated underpotential electrochemical deposition of Thallium monolayers on Ag(111) electrodes [155]. According to Toney the periodic potential of the substrate creates small amplitude, static displacements in the atomic positions of the thin adsorbed layer (e.g. atoms sitting close to hollow sites of the substrate layer tend to move

towards the hollow site position). These displacements give rise to a spatial modulation in the adlayer which has wave vectors commensurate with the substrate periodicity. On the other hand the reconstructed surface layer gives rise to a set of separate CTRs which are placed apart from the bulk rods in reciprocal space, so-called superstructure CTRs. Because of the two-dimensionality of the 'hex' layer no Bragg reflections are observed in L-direction and the intensity is uniformly distributed along the respective CTRs. Only the atomic form factor of gold gives rise to intensity variations along superstructure CTRs.

The in-situ SXS measurements were performed at beam line ID32 of the ESRF and beam line BW2 of HASYLAB using photon energies of 18.2 and 10.0 keV, respectively. In the following I will present data which was acquired at beam line ID32 because of the much better signal to noise ratio and counting statistics. Nevertheless, it is worth mentioning that all data acquired at Hasylab were consistent with the ESRF data. For the experiments at ID32 we employed horizontal and vertical presample slits with aperture sizes of 0.25 mm and 0.01 mm, respectively. Detector slits with 1 mm horizontal aperture and 3 mm vertical aperture were used as they provided the best signal to noise ratio. The growth behavior was mainly investigated at two positions in reciprocal space, that is $(0 , 0 , 0.7)$ on the specular CTR and $(1 , 1 , 0.1)$ on the non-specular $(1,1)$ rod. Both positions are close to anti-Bragg and thus very sensitive to effects of surface disorder. In particular, the kinetic growth mode is inferred from the time-dependence of the diffracted intensity at these positions (see section 9.2). As will be shown in chapter 10 growth-induced changes in the scattered X-ray intensity are measurable along the whole crystal truncation rod, i.e. the presence of layer-by-layer growth oscillations is not restricted to the anti-Bragg positions, albeit they are most pronounced in anti-Bragg.

9.2 Growth Mode Dependence of the Scattered X-ray Intensity

Growth modes are determined by monitoring the time-dependent scattered X-ray intensity at selected positions in reciprocal space (typically in anti-Bragg) while gold is deposited onto the electrode surface. As illustrated schematically in figure 9.3, each growth mode results in a different characteristic, time-dependent scattered intensity. In case of 3D growth the surface roughness steadily increases with time which leads to a rapid monotonic decay in the measured X-ray intensity. Especially at long deposition times the intensity approaches a very low value close to the background intensity level. For the layer-by-layer growth mode the X-ray intensity behavior is different. The latter is characterized by the successive growth of single monolayers whereas in the ideal case each monolayer has to be completed before growth of the next monolayer starts. Hence, during all times t the electrode surface is either perfectly terminated or covered by one monolayer with fractional coverage. In the X-ray intensity oscillations are observed with a period corresponding to the growth of one monolayer. The oscillation maxima arise from constructive interference of the scattered waves by a perfectly terminated surface and the minima arise from a maximum destructive interference if the surface is covered by exactly half a monolayer. Yet another behavior is observed for step-flow growth. In this growth mode all step edges grow simultaneously. Since in addition to the latter nucleation processes take place on the topmost surface layer the overall surface
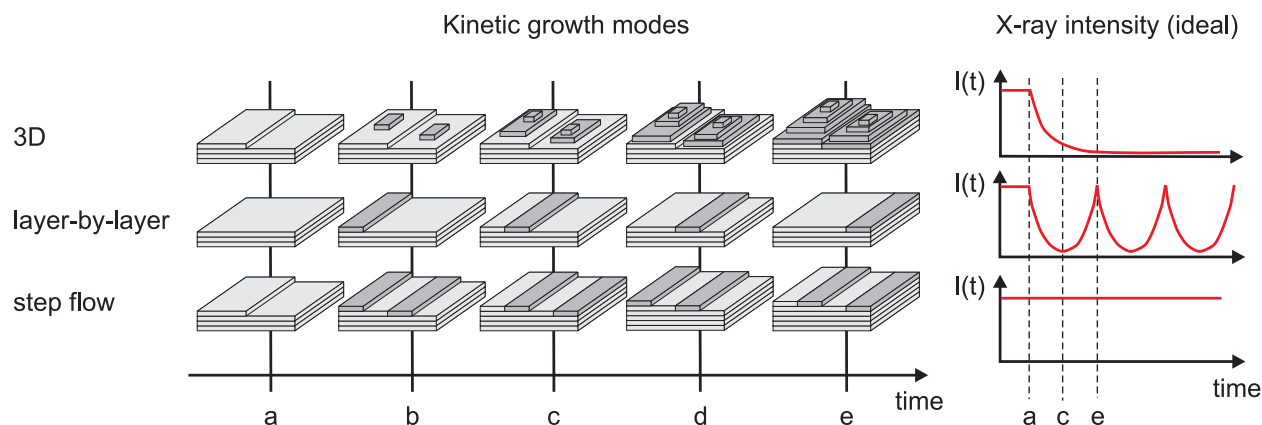
Figure 9.3: Illustration of the three kinetic growth modes and associated theoretical shapes of the time-dependent X-ray intensities $I(t)$ which are observed for growth on an initially smooth surface.

morphology does not change with time. This can be also observed in the diffracted X-ray intensity which is independent of time and on a constant high level. All X-ray intensity curves depicted in figure 9.3 represent the case of ideal growth. Obviously, real crystal growth will never proceed ideally. In particular, for non-ideal layer-by-layer growth the oscillations are damped as the film roughens with increasing film thickness. Additionally the oscillation period may change due to depletion of the metal species within the electrolyte. In any case, oscillations in the scattered intensity indicate steady interlayer mass transport and hence a low step-edge barrier while a monotonically decaying intensity indicates limited interlayer mass transport and a high step-edge barrier.

In order to determine the growth mode by use of the aforementioned procedure, initially smooth surfaces with reproducible statistical properties are required. If potential steps are performed from E_{start} to E_{end} and the initial surface is rough, e.g. due to 3D growth at E_{start}, then it is almost impossible to determine layer-by-layer growth by stepping the potential to E_{end}. Therefore, it is highly desirable that the investigated system exhibits a step-flow growth regime where the surface smoothens before the potential is stepped to different growth regimes. I will show in the following sections that Au(100) provides such a step-flow growth regime which facilitates extensive growth mode studies.

9.3 Growth Behavior During Electrolyte Exchange

Following our commonly employed procedure the Au(100) electrode surface was first aligned and characterized in Au-free 0.1 M HCl solution. Subsequently Au-containing electrolyte was injected into the electrochemical cell. At an electrode potential of 0.5 V the Au-free electrolyte was replaced with an exchange rate of $5\,\mu$l/s by $4000\,\mu$l Au-containing solution consisting of 0.1 M HCl and 0.2 mM $HAuCl_4$. Parallel to this procedure the X-ray intensity

was monitored at the reciprocal space position $(0,0,0.7)$. Since the surface is unreconstructed at 0.5 V the scattered intensity along the specular CTR is solely given by the (1×1) bulk terminated crystal. The time-dependence of the observed X-ray intensity is shown in figure 9.4a. Within the first 60 s after starting the exchange process the monitor normalized intensity remains constant and conforms to the initial intensity of ≈ 0.6 measured at $t=0$. For $t>60$ s, the intensity suddenly decreases indicating an increased amount of surface roughness. The onset of this intensity decrease coincides with the arrival of Au-containing electrolyte in the hanging meniscus droplet near the electrode surface. Deposited Au atoms form nuclei and participate in the growth of preexisting Au islands. After a time of 140 s the intensity takes a minimum of 0.46 corresponding to maximum destructive interference. As the growth proceeds the intensity increases rapidly until a value of 0.54 is reached 340 s after start of the electrolyte exchange. At this point the surface is relatively smooth and the Au island coverage is low. Nevertheless, the original intensity value is not achieved which indicates that the overall surface roughness, induced by the electrolyte exchange, increased. For $t>340$ s the intensity then continuously but slowly increases with an approximately linear slope of $0.002\,\mathrm{min}^{-1}$. The absence of a further intensity decrease indicates a transition from layer-by-layer or 3D growth to step-flow growth. Hence the preferred growth mode at 0.5 V is step-flow growth. The initial decrease in intensity might be attributed to growth of Au islands which were present before the exchange process. After completion of the first monolayer the nucleation rate on top of flat surface terraces is low and due to the lack of capturing Au islands the adatoms diffuse to step edges which results in the observed step-flow growth mode.
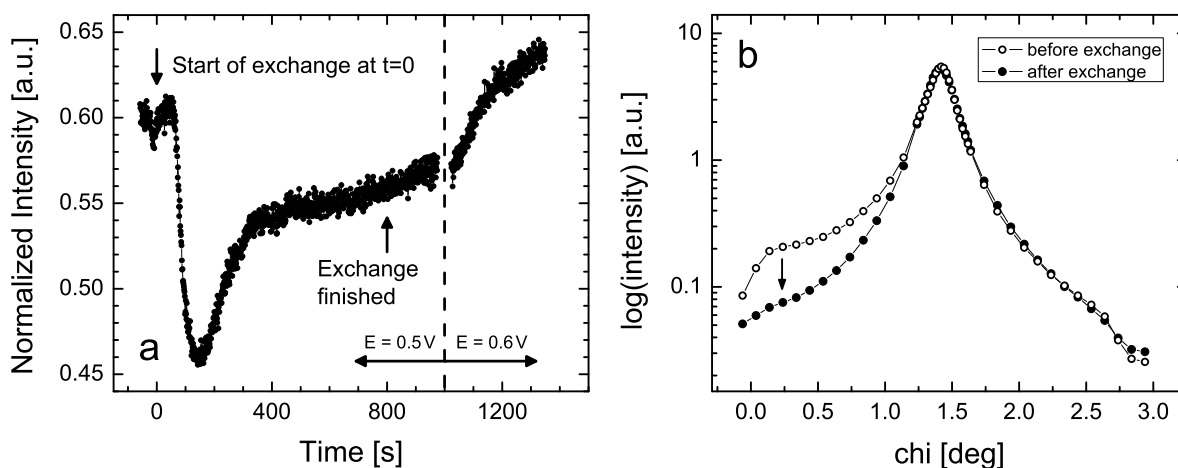
Figure 9.4: a) Intensity at $(0,0,0.7)$ on the specular CTR monitored parallel to an electrolyte exchange from 0.1 M HCl to 0.1 M HCl + 0.2 mM HAuCl$_4$. An amount of 4000 μl was exchanged with a rate of 5 μl/s at an electrode potential of 0.5 V. Subsequently, at $t=1000$ s, the potential was stepped to 0.6 V. b) Sample rocking scan about the 'chi' axis recorded before and after electrolyte exchange from 0.1 M HCl to 0.1 M HCl + 0.2 mM HAuCl$_4$ at an electrode potential of 0.6 V. The arrow indicates a decrease in the diffusely scattered intensity.

Subsequent to the electrolyte exchange the electrode potential has been stepped from 0.5 V to 0.6 V, i.e. closer to the Nernst potential. This potential step results in a further rapid intensity increase. Obviously the step-flow growth is even more pronounced at higher positive electrode potentials. According to the cyclic voltammogram shown in figure 6.3 the potential of 0.6 V is not in the diffusion-limited potential regime and the deposition rate is significantly lower. A lower deposition rate and an enhanced surface mobility of Au adatoms in presence of adsorbed chloride ions promotes step-flow growth and thus results in a smoother electrode surface. It is remarkable that the achieved X-ray intensity at 0.6 V is even higher than the X-ray intensity measured at 0.5 V in Au-free solution, i.e. compared to the X-ray intensity scattered by the freshly prepared electrode surface. Hence the initiated homoepitaxial growth in the step-flow potential regime significantly promotes the surface quality. This can be also seen in sample rocking scans about the 'chi' axis which were performed before and after an electrolyte exchange at 0.6 V. For this the sample was first aligned to reflectivity geometry with $L = 0.3$ where the incident and the exit angle equals approximately 1.42°. Then the electrode was rotated about the 'chi' axis while the detector position was fixed. The measured X-ray intensity profiles are plotted in figure 9.4b. The profile in Au-free solution exhibits pronounced off-specular intensity close to the critical angle for total external reflection which is a sign for a rough electrode surface. However, in the profile recorded after the electrolyte exchange, i.e. in Au-containing solution, the diffusely scattered intensity strongly decreased as indicated by the arrow in the graph. Diffuse scattering in Au-containing solution was investigated in more detail as function of the electrode potential and will be the subject of section 9.8.

9.4 Surface Smoothening at High Positive Electrode Potentials

Anti-Bragg positions are of major importance for growth mode studies since the observed X-ray intensity is very sensitive to changes in the surface morphology. In particular, the intensity is largely influenced by the degree of surface roughness. Figure 9.5a shows an exemplary $I(t)$ curve monitored at the anti-Bragg position $(1, 1, 0.15)$ after a potential step from 0.225 V to 0.6 V for an Au(100) electrode in 0.1 M HCl + 0.5 mM HAuCl$_4$ solution. The diffusion-limited deposition rate in this electrolyte is ≈ 4 ML/min. At 0.225 V before the potential step an intensity of ≈ 0.36 is measured. Subsequent to the potential step to 0.6 V the intensity strongly increases and approaches a saturation value of ≈ 0.94 after $t = 175$ s, corresponding to a total deposit equivalent to 11.7 ML. Obviously the amount of surface roughness is significantly reduced at 0.6 V and the homoepitaxial growth results in a smooth and flat surface. This behavior is typical for the transition from 3D growth or imperfect layer-by-layer growth to step-flow growth. The experiment was repeated in a similar manner for other electrode potentials. Starting at a potential of 0.6 V, where step-flow growth results in a high initial intensity at $(1, 1, 0.15)$, the potential was stepped to different potentials between 0.6 V and -0.4 V, i.e. within the diffusion-limited potential regime. At the latter potentials a certain time was rested, typically between 60 and 200 seconds, until the intensity achieved a saturation value. The potential-dependence of the measured intensities is illustrated in figure 9.5b. For all potentials < 0.6 V the observed intensity is significantly lower than the initial intensity at 0.6 V indicating less perfect crystal growth and an increased surface roughness.
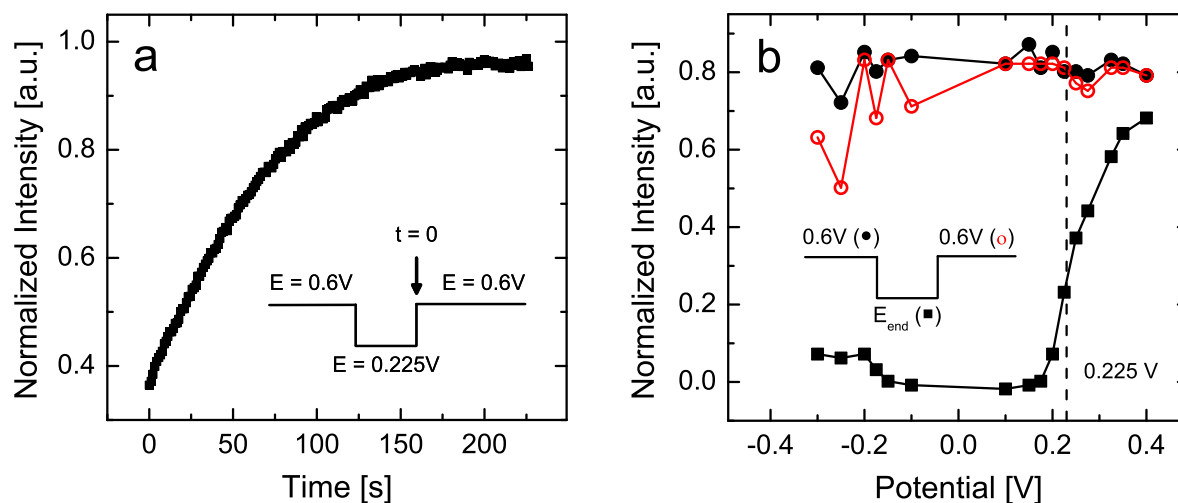
Figure 9.5: a) Time-dependent intensity $I(t)$ monitored at $(1, 1, 0.15)$ after a potential step from $0.225\,\mathrm{V}$ to $0.6\,\mathrm{V}$. The initially low intensity at $0.225\,\mathrm{V}$ significantly increases with time after the potential is stepped to very positive potentials and approaches a saturation value. b) Potential step experiments. The steady state intensity has been determined for the start potential $E_{\mathrm{start}} = 0.6\,\mathrm{V}$ (filled circles), for the end potential $E_{\mathrm{end}} = x\,\mathrm{V}$ (squares, $-0.3\,\mathrm{V} \le x \le 0.4\,\mathrm{V}$) and after the final potential step back to $E = 0.6\,\mathrm{V}$ (open circles). At the potential of $E = 0.6\,\mathrm{V}$ the X-ray intensity fully recovers.

Interestingly a subsequent potential step back to $0.6\,\mathrm{V}$ always results in a strong increase in intensity. In particular, the intensity fully recovers and accords to the initial intensity. This clearly demonstrates that the step-flow growth at $0.6\,\mathrm{V}$ smoothens even very rough surfaces present after deposition of several monolayers in the 3D growth regime. Due to this characteristic the Au(100) electrode was preferentially kept at an electrode potential of $0.6\,\mathrm{V}$ in Au-containing solution at times when no measurements were carried out, e.g. during surface alignment.

9.5 Systematic Growth Mode Studies

In this section systematic growth mode studies are discussed. For the experiments electrolyte solutions of $0.1\,\mathrm{M}\,\mathrm{HCl} + x\,\mathrm{mM}\,\mathrm{HAuCl_4}$ ($x = 0.05,\ 0.1,\ 0.2,\ 0.5$), prepared from suprapure HCl (Merck), $\mathrm{HAuCl_4}$ (Johnson Matthey), and Milli-Q water, were employed, corresponding to diffusion-limited deposition rates of approximately 0.4 to $4\,\mathrm{ML/min}$. All given growth rates in these studies were determined from the time between the first and the second maximum observed in the $I(t)$ curves within the layer-by-layer growth regime. In each experiment the sample was first immersed in Au-free $0.1\,\mathrm{M}\,\mathrm{HCl}$ for alignment and first characterization to ensure a well-ordered 'hex' reconstructed Au surface prior to deposition. Subsequently, the electrolyte was exchanged by Au-containing solution, resulting in the onset of electrodeposition.

To study the growth behavior the scattered intensity was monitored as a function of time at selected reciprocal space positions (typically close to the anti-Bragg positions) along the specular (0,0) and non-specular (1,1) crystal truncation rods (CTR). In-situ studies of the growth mechanism were performed in $HAuCl_4$ containing solution using the following procedure: first, the potential was kept for at least 5 min at 0.6 V, where the Au surface mobility is very high (see below), resulting in rapid smoothening even of very rough surfaces as verified by the complete recovery of the X-ray intensity. Then the Au concentration was replenished by an exchange of 200 μl fresh electrolyte solution and after a waiting time of at least 4 min a potential step to a more negative potential was initiated. Because of the change in surface mobility induced by the potential step, significant changes in the scattered intensity are observed, from which the kinetic growth mode can be inferred. Examples of the scattered intensity as a function of time after the potential step are shown in figure 9.6 for electrolytes containing different $HAuCl_4$ concentrations. At all employed concentrations oscillations in the X-ray intensity are observed that clearly indicate layer-by-layer growth, with each oscillation period Δt corresponding to the deposition of one Au monolayer [1, 2]. These growth
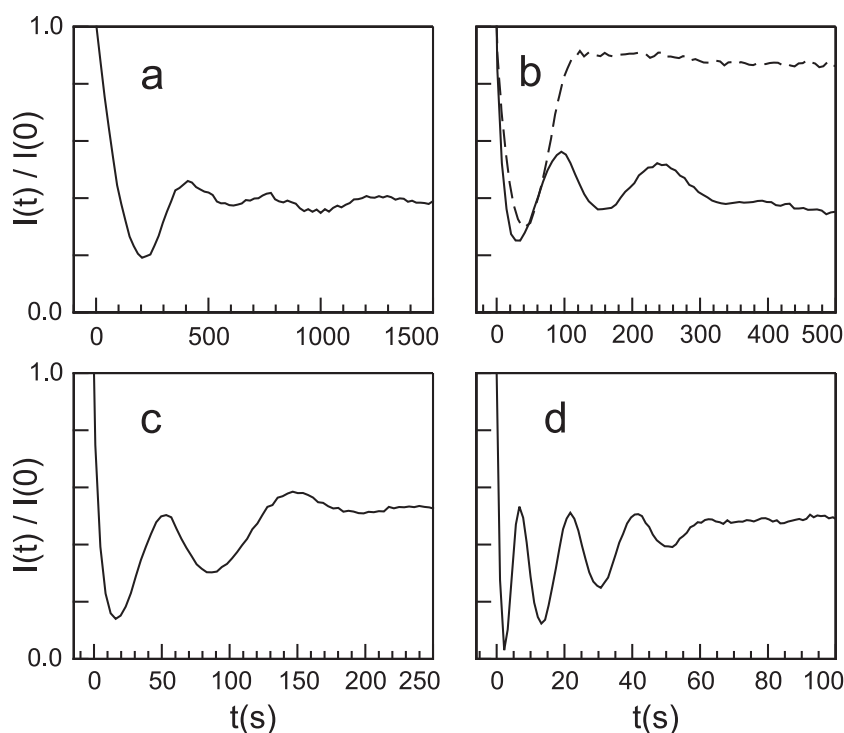
Figure 9.6: In-situ growth experiments on Au(100) in 0.1 M HCl solution containing (a) 0.05 mM, (b) 0.1 mM, (c) 0.2 mM, and (d) 0.5 mM $HAuCl_4$ at a deposition potential of (a) 0 V, (b) 0.05 V (solid line) and 0.2 V (dashed line), (c) 0.10 V, and (d) 0.25 V. The panels show the background-corrected X-ray intensity $I(t)$ as a function of deposition time t, normalized with respect to the saturation value $I(0)$ directly before the potential step at $t = 0$. The data were obtained at reciprocal space positions of (a),(d) $(1, 1, 0.1)$ and (b),(c) $(0, 0, 0.7)$; similar behavior was found at other positions along the CTRs.

oscillations are found in the specular (figures 9.6b and 9.6c) as well as the non-specular (figures 9.6b and 9.6c) CTRs and occur in a wide potential regime. The amplitude of these oscillations decays within typically 3 to 4 periods, approaching an approximately constant value. Overall, this behavior strongly resembles that found in various scattering studies by He scattering, electron diffraction (RHEED, MEED, and LEED), and SXS of MBE growth on (100)-oriented fcc-metal substrates under UHV conditions [1,2]. Similar oscillations could be observed at all $HAuCl_4$ concentrations employed in this study, albeit in somewhat different potential regimes.

As visible in figure 9.6 the oscillation period Δt decreases, i.e., the local deposition rate increases, approximately proportionally to the concentration, as expected for diffusion-limited
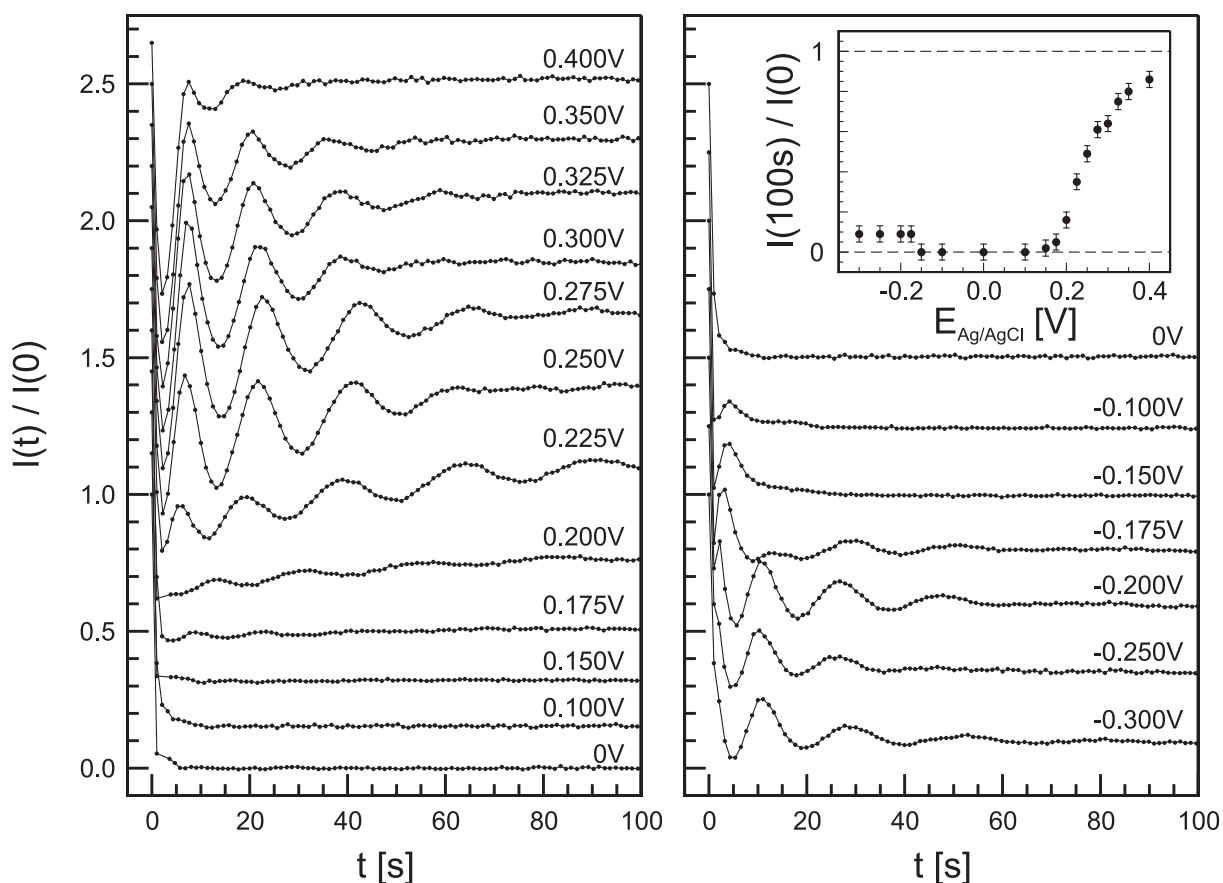
Figure 9.7: Background-subtracted, normalized intensity as a function of deposition time t after potential steps from $0.6\,V$ to different potentials in $0.1\,M$ HCl + $0.5\,mM$ $HAuCl_4$. For clarity, the curves are shifted with respect to each other by a constant offset. The data were obtained at $(1,1,0.1)$ and show step-flow, layer-by-layer, multilayer, and re-entrant layer-by-layer growth (for classification of each curve, see figure 9.8, topmost row of symbols) with decreasing potential. In the inset the steady-state intensity, measured $100\,s$ after the potential step, is plotted as a function of potential.

deposition. The reproducibility of the oscillation periods is limited by (a) the rather slow approach of steady-state hydrodynamic conditions after the exchange (3-5 min), which is also the origin of the slow increase in Δt observed in some of the experiments, and (b) the slow depletion of the Au concentration within the electrolyte, resulting in a 1% decrease in deposition rate per minute. Within the variation of the data the Δt values are in good agreement with the deposition rates obtained from the electrochemical current density (cp. table 6.2). The decay in the oscillation amplitude with time can be attributed to slow surface roughening due to non-ideal layer-by-layer growth. Similar behavior was also found for MBE under UHV conditions. Following the procedure commonly employed in MBE studies [1], the presence of at least one complete period in the oscillations will be associated with layer-by-layer growth in the following.

The response of the scattered intensity $I(t)$, especially the occurrence of growth oscillations, strongly depends on potential. At the most positive potentials (> 0.4 and > 0.1 V in 0.1 M HCl containing 0.1 and 0.5 mM HAuCl$_4$, respectively) the intensity usually first decreases and then recovers, approaching an approximately constant intensity that is comparable to the initial intensity I_0 before the potential step (figure 9.6b, dashed line). The steady-state intensity is obtained precisely after the time Δt, corresponding to the deposition of the first monolayer. This behavior is attributed to Au island nucleation and subsequent 2D growth (i.e., a layer-by-layer growth) of the first monolayer, followed by step-flow growth (see below). After stepping the potential down to more negative values growth oscillations emerge and, at even more negative potentials, disappear again. This is illustrated in figure 9.7 for a series of measurements in 0.1 M HCl + 0.5 mM HAuCl$_4$ solution, where the oscillations are found between approximately 0.4 and 0.2 V. Below 0.2 V $I(t)$ decays rapidly to zero (see figure 10.2, inset), indicating formation of a rough surface via multilayer growth. Interestingly, upon further lowering of the potential growth oscillations reappear negative of -0.15 V (figure 9.7, right panel). As verified by separate studies of the Au(100) in-plane structure, performed in the same in-situ SXS experiments, the onset of this 're-entrant'
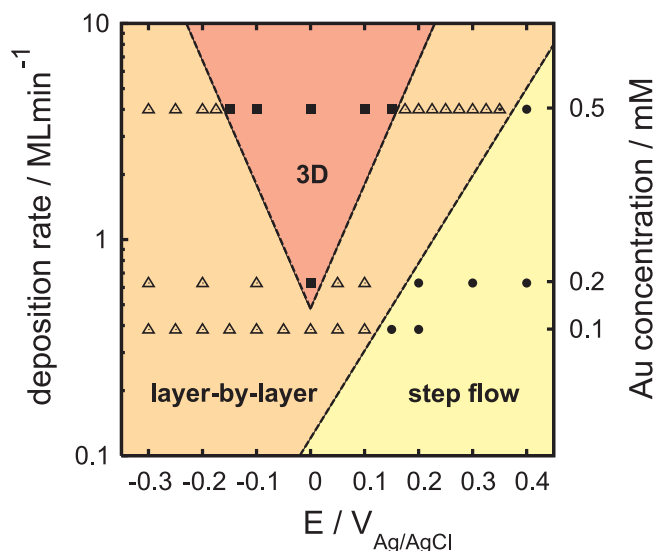
Figure 9.8: Kinetic growth mode diagram for Au/Au(100) in 0.1 M HCl, showing the occurrence of step-flow (filled circles), layer-by-layer (open triangles), and multilayer growth (filled squares) as a function of potential and deposition rate.

layer-by-layer growth coincides with the formation of the 'hex' surface reconstruction on the electrode surface. Analog experiments at deposition rates of ≈ 0.38 and $\approx 0.63\,\mathrm{ML/min}$ (not shown) revealed a similar behavior. However, here the transition from step-flow to layer-by-layer growth is found at more negative potentials (<0.2 and $<0.15\,\mathrm{V}$ at fluxes of ≈ 0.63 and $\approx 0.38\,\mathrm{ML/min}$, respectively) and the multilayer growth regime is limited to a small potential regime around $0\,\mathrm{V}$ at $\approx 0.63\,\mathrm{ML/min}$ whereas it does not occur at all at $\approx 0.38\,\mathrm{ML/min}$. These observations, which are summarized in the kinetic growth mode diagram in figure 9.8, reveal that the growth process and the resulting morphology depend in a complex way on the deposition potential as well as on the deposition rate.

Since the flux is independent of potential in these experiments, the potential-dependent growth behavior has to be related to a potential dependence of the surface transport processes. In the potential regime of the unreconstructed Au(100) surface ($\geq -0.15\,\mathrm{V}$ in $0.1\,\mathrm{M\ HCl}$ + $0.5\,\mathrm{mM\ HAuCl_4}$ solution) a change from multilayer to layer-by-layer, and then to step-flow growth is found with increasing potential, indicating a continuous increase in the surface mobility. The data are in complete agreement with previous studies of surface transport in Au-free solution, where a substantial, often exponential increase in surface mobility with increasing potential was reported [120–123]. This potential effect was attributed to the influence of the electric field of the electrochemical double layer and the chemisorption of anions on the activation energies for surface transport [123]. Specifically, the presence of Cl⁻ anions is known to significantly enhance the surface mobility [120, 122, 156].

9.6 Discussion of the Growth Mode Transitions

Within the framework of kinetic growth theory an increase in the surface transport rate at identical adatom flux F should result in a crossover from multilayer to layer-by-layer to step-flow growth, as indeed found in the experiments in $0.5\,\mathrm{mM\ HAuCl_4}$ containing solution. The potential-dependent 3D-2D growth transition indicates an increased rate of interlayer transport or, more precisely, a decrease in the Ehrlich-Schwoebel barrier E_S for Au adatoms stepping down the Au islands. Support for this comes from in-situ AFM experiments on the decay of multilayer islands on Au(100) in Cl⁻-containing electrolyte, where a pronounced increase in the island decay rate with potential was found [122], indicating likewise enhanced interlayer transport. With decreasing deposition rate the potential regime of multilayer growth is reduced. This again is in accordance with the condition for the 2D-3D transition and can be rationalized by the lower nucleation probability for Au islands at lower flux, resulting in layer-by-layer growth even at lower surface transport rates. More quantitatively, according to rate equation theory and kinetic Monte Carlo simulations the 2D-3D transition line in the growth mode diagram is given (for a critical nucleus size $i = 1$, an adatom diffusion rate on terraces D, and an in-plane lattice constant a) by the condition [157–159]

$$\exp(-\Delta E_S/k_B T) \propto \left(\frac{D}{Fa^4}\right)^{-1/6} \tag{9.2}$$

where $\Delta E_S = E_S - E_D$ is the additional barrier for step-down diffusion, k_B is the Boltzmann constant, T is the temperature and E_D is the activation energy for surface diffusion. At

constant T this condition can be rewritten as

$$\frac{5}{6}E_D - E_S \propto \ln F \tag{9.3}$$

i.e., the critical flux F for the transition from 2D to 3D growth only shifts to higher values, if the Ehrlich-Schwoebel barrier E_S decreases whereas a decrease in the surface diffusion rate E_D (at constant E_S) would even lower F. Hence the observed increase in F towards more positive potentials (figure 9.8) suggests that with increasing potential the Ehrlich-Schwoebel barrier decreases by (at least) a similar amount as the surface diffusion barrier.

The 2D to step-flow growth transition depends on the average step separation, i.e., the surface morphology, and hence is of less fundamental importance. Step-flow emerges when intralayer transport to existing steps is so rapid that all adatoms reach steps prior to nucleation and consequently depends on the diffusion barrier for adatom motion on the terraces, the binding energy of the critical cluster, and the adatom flux [1]. Taking into account the increase in intralayer transport with increasing potential, the transition to step-flow at positive potentials and the dependence of this transition on the deposition rate can be easily rationalized.

The re-entrant layer-by-layer growth in the potential regime of the 'hex' reconstructed surface is in good agreement with the homoepitaxial growth behavior of reconstructed Au(100) under UHV conditions, where at similar deposition rates also a layer-by-layer growth was found [4,5]. It indicates an enhanced surface mobility in the reconstructed as compared to the unreconstructed surface. Indeed, theoretical studies predict considerably lower barriers for adatom surface diffusion on the hexagonal close-packed reconstructed Au(100) surface [113], but no data on the additional barrier at step edges ΔE_S exists, which determines the interlayer transport and consequently the 3D-2D transition. Our experiments suggest that the formation of the 'hex' reconstruction substantially lowers this barrier, in accordance with in-situ AFM observations [121]. However, the atomic-scale growth mechanisms on the reconstructed Au(100) surface are rather complex and cannot be rationalized based on simple kinetic models employed above: first, the critical nucleus size $i > 1$ on reconstructed Au(100) [4] and consequently the simple relationship for the 2D-3D transition given in [157–159] does not hold anymore. Second, molecular dynamics simulations suggest that rather complex collective processes are involved in island nucleation [104]. Third, recent STM studies revealed other, more complex mass transport mechanisms on partly reconstructed Au(100), such as fast adatom transport along the boundaries between reconstructed and unreconstructed surface areas and the quasi-collective motion of elements of the surface reconstruction [90, 113]. More complex models will therefore be necessary to describe growth on the reconstructed surface.

Although the experiments discussed here resemble diffraction studies of MBE growth under vacuum conditions, some important differences to those studies exist. In both cases the high scattered intensity indicates that the initial surface is smooth with large atomically flat terraces. However, whereas conventional MBE growth studies monitor the surface morphology at fixed temperature (i.e., fixed surface mobility) after initiating a constant adatom

flux, our experiments show the response of the morphology at constant (diffusion-limited) flux upon a potential step, i.e., upon a change in surface mobility. This results in an enhanced transient adatom concentration on the Au terraces directly after the potential step until a new equilibrium adatom distribution has developed. The layer-by-layer growth of the first monolayer in the step-flow potential regime may be attributed to this phenomenon. An alternative experimental approach would be electrodeposition experiments that, as in MBE, start at zero flux. This can in principle be done by rapid exchange of Au-free with Au-containing solution at fixed potential.

9.7 Growth Mode Studies During Constant Electrolyte Flow

The combination of employed cell geometry and electrolyte exchange system allows to perform experiments parallel to a well-defined constant flow of electrolyte through the electrochemical cell. The present section aims at the influence of electrolyte flow on the deposition rate R and on the resulting growth modes. Furthermore the consistency of both electrochemical data and X-ray data will be analyzed. In order to compare the growth behavior during electrolyte flow with those in stagnant solution the growth behavior was first characterized in stagnant solution. Figure 9.9a shows the time-dependent intensity $I(t)$ monitored at the reciprocal space position $(1\,,1\,,0.1)$ parallel to a potential step from $0.4\,\mathrm{V}$ to $0\,\mathrm{V}$ in stagnant $0.1\,\mathrm{M}$ HCl $+\ 0.1\,\mathrm{mM}$ HAuCl$_4$ solution. The growth at $0\,\mathrm{V}$ proceeds via layer-by-layer mode and from the oscillation period a deposition rate of $\approx 0.33\,\mathrm{ML/min}$ is inferred. This will be the reference value for the electrolyte flow experiments.

For the measurements at constant electrolyte flow the electrode potential was first kept at $0.5\,\mathrm{V}$ for $100\,\mathrm{s}$ in order to smoothen the surface in the step-flow growth regime and to obtain high initial X-ray intensity at $(1\,,1\,,0.1)$ in anti-Bragg position. Within this time period, more precisely after the elapse of 50 seconds, an electrolyte exchange of $4000\,\mu l$ electrolyte was initiated with a constant flow rate $\mathfrak{F}$. Then the electrode potential was stepped to a certain potential E_{end} while changes in the diffracted X-ray intensity as well as in the electrochemical current were monitored. Figure 9.9b summarizes $I(t)$ curves obtained for three different flow rates of 5.0, 7.5 and $10.0\,\mu l/\mathrm{s}$ at an electrode potential $E_{\mathrm{end}} = 0.25\,\mathrm{V}$ in the unreconstructed potential regime. For all flow rates growth in the layer-by-layer mode is observed. It can be seen that the oscillation period decreases with increasing flow rate. From the first to the second intensity minimum deposition rates of $2.82\,\mathrm{ML/min}$, $3.14\,\mathrm{ML/min}$ and $3.22\,\mathrm{ML/min}$ are obtained for flow rates of 5.0, 7.5 and $10.0\,\mu l/\mathrm{s}$, respectively. Additional $I(t)$ curves with $E_{\mathrm{end}} = \text{-}0.3\,\mathrm{V}$ in the reconstructed potential regime are shown in figure 9.9c for flow rates of 15.0, 17.5 and $20\,\mu l/\mathrm{s}$, respectively. In the initial stage after the potential step to -0.3 V a significantly different behavior is observed compared to potential steps within the unreconstructed potential regime. In detail, the initial, monitor normalized intensity of 0.4 rapidly drops to a value of 0.15 within the first two seconds and recovers very rapidly to 0.4 within the subsequent two seconds before layer-by-layer growth with a larger oscillation period sets in. If these 4 seconds are multiplied with the deposition rate of $\approx 4\,\mathrm{ML/min}$ (see below) then a deposit of $\approx 0.27\,\mathrm{ML}$ is found which may indicate that the intensity decrease is related to the formation of the reconstructed phase. Due to even less pronounced intensity
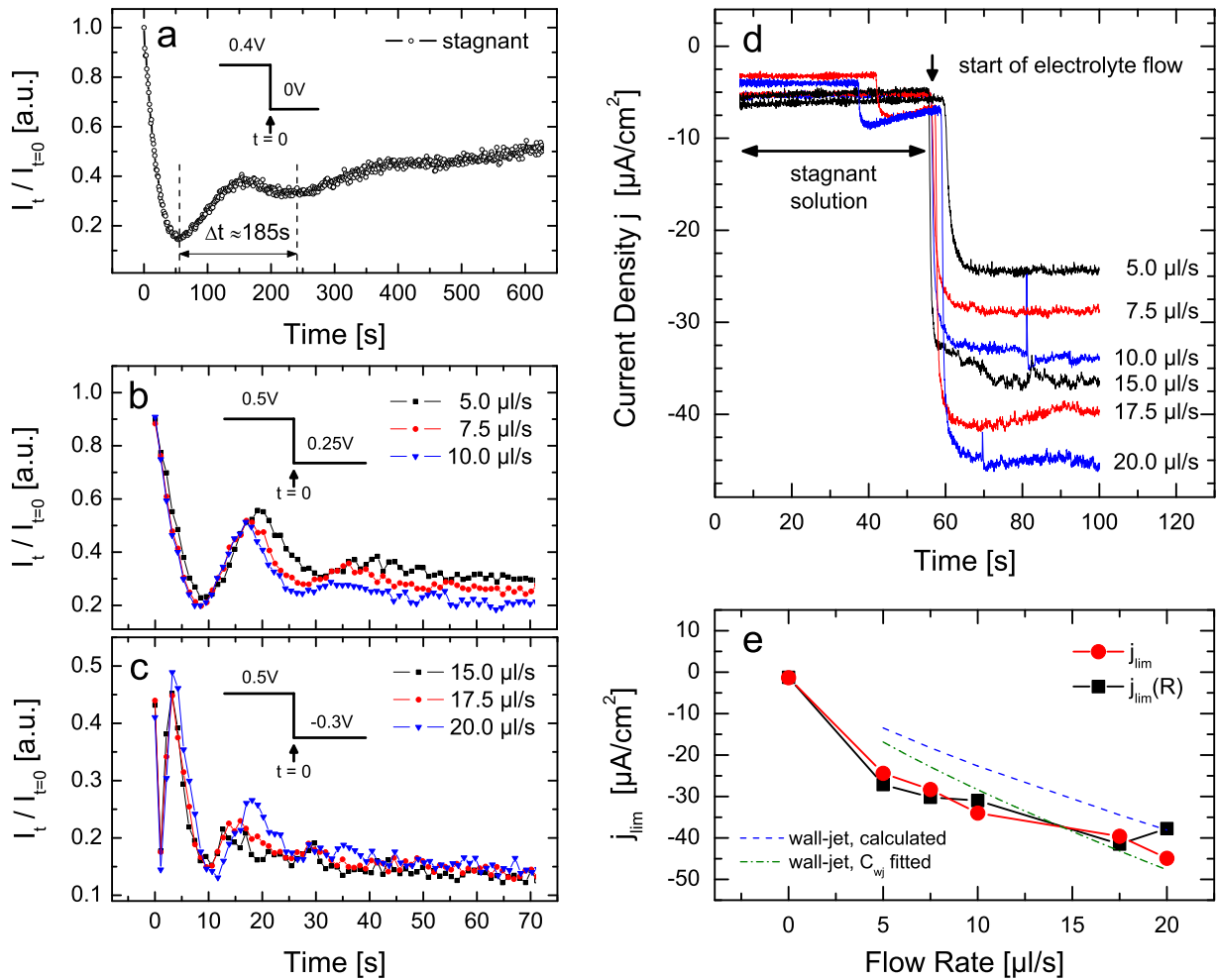
Figure 9.9: Potential step experiments performed on Au(100) electrodes in $0.1\,M$ HCl + $0.1\,mM$ HAuCl$_4$ solution. The potential was stepped from $0.5\,V$ to different potentials E_{end} while time-dependent X-ray intensity transients at $(1,1,0.1)$ and electrochemical current-time transients were recorded. During data acquisition the electrolyte was either stagnant or flowing through the cell with a constant flow rate $\mathfrak{F}$. $I(t)$ was monitored a) in stagnant solution for $E_{end} = 0.05\,V$, b) during constant electrolyte flow with flow rates of 5.0, 7.5 and $10.0\,\mu l/s$ for $E_{end} = 0.25\,V$ in the unreconstructed potential regime and c) during constant electrolyte flow with flow rates of 15.0, 17.5 and $20\,\mu l/s$ for $E_{end} = -0.3\,V$ in the reconstructed potential regime. Figure d) shows current-time transients recorded via potentiostat in parallel to the initiation of electrolyte flow. In figure e) the measured current density j_{lim} is compared with the current density calculated via equation 9.5 whereas R is inferred from X-ray intensity oscillations. The dashed line shows the current-flow rate dependence based on equation 9.6, i.e. assuming an behavior similar to impinging wall-jet electrodes.

oscillations the obtained deposition rates are afflicted with relatively high uncertainties. For flow rates of $17.5\,\mu l/s$ and $20\,\mu l/s$ deposition rates of $4.31\,ML/min$ and $3.92\,ML/min$ have been found. These two values are very similar and may indicate that for the according flow rates a saturation in the deposition rate is achieved, i.e. that the Nernst diffusion layer cannot be effectively further compressed. All deposition rates R inferred from the growth oscillations are summarized in table 9.1.

The higher the electrolyte flow rate $\mathfrak{F}$ through the cell the more compressed is the Nernst diffusion layer δ_N and the higher is the deposition rate R in the diffusion-limited potential regime according to

$$R = \frac{d\theta}{dt} = \frac{N_A \cdot D}{N_{ML} \cdot \delta_N} \cdot c_0 \tag{9.4}$$

where N_{ML} is the number of Au atoms in one unreconstructed monolayer of $1\,cm^2$ unit area, N_A is the Avogadro constant, D is the diffusion constant of $AuCl_4^-$ in the electrolyte and c_0 is the nominal concentration of $AuCl_4^-$ in the solution bulk. Similarly the diffusion-limited current density j_{lim} is dependent on the diffusion layer thickness, i.e.

$$j_{lim} = \frac{n \cdot F \cdot D}{\delta_N} \cdot c_0 = n \cdot e_0 \cdot N_{ML} \cdot R \tag{9.5}$$

where n is the electron transfer number, F is the Faraday constant and e_0 is the elementary electron charge. Figure 9.9d shows the electrochemical current density which was recorded parallel to the onset of electrolyte flow. In accordance to the deposition rate obtained from the X-ray intensity oscillations the steady state current density increases with increasing electrolyte flow rate. In order to compare the electrochemical data with the X-ray data the current density $j_{lim}(R)$ has been calculated from the measured deposition rate R according to equation 9.5. Both the directly measured and the calculated current densities are summarized in table 9.1 and plotted in figure 9.9e. The X-ray data are in good agreement

Concentration c_0 [mM]	Potential E_{end} [V]	Flow Rate $\mathfrak{F}$ [μl/s]	Deposition Rate R [ML/min]	Current Density	
				j_{lim} [μA/cm²]	$j_{lim}(R)$ [μA/cm²]
0.1	0	stagnant	0.33	-3.6	-3.2
2.0	0.55	stagnant	7.60	-68.3	-73.1
0.1	0.25	5.0	2.82	-24.4	-27.1
0.1	0.25	7.5	3.14	-28.3	-30.2
0.1	0.25	10.0	3.22	-34.0	-31.0
0.1	-0.30	17.5	4.31	-39.6	-41.5
0.1	-0.30	20.0	3.92	-44.9	-37.7

Table 9.1: Deposition rates R and current densities j_{lim} determined in stagnant solution and during constant flow of electrolyte through the cell. The deposition rates R have been inferred from X-ray intensity oscillations and the current densities j_{lim} from electrochemical current transients. $j_{lim}(R)$ was calculated via equation 9.5.

with the electrochemical data. Based on equation 9.5 the thickness of the Nernst diffusion layer is estimated. Assuming a diffusion constant of $D = 1.1 \cdot 10^{-5}\,\mathrm{cm^2/s}$ for AuCl4$^-$ as measured in 0.25 M HCl by Chen and coworkers [29] and regarding the number density of atoms $N_{ML} = 1.2015 \cdot 10^{15}\,\mathrm{ML^{-1}cm^{-2}}$ then a diffusion layer thickness of approximately 1 mm is found in stagnant 0.1 mM Au-containing solution. In comparison the diffusion layer at the highest investigated flow rate of $20\,\mu\mathrm{l\,s^{-1}}$ exhibits an estimated compressed thickness of $\approx 0.08\,\mathrm{mm}$.

The employed cell geometry under electrolyte flow conditions resembles an impinging wall-jet electrode. For the latter theoretical and geometrical considerations predict the dependence of current density j_{wj} on the electrolyte flow rate $\mathfrak{F}$ which according to reference [160] is given by

$$j_{\mathrm{wj}}(\mathfrak{F}) = \frac{1.38 \cdot n \cdot F \cdot D^{2/3} \cdot r^{3/4} \cdot c_0}{\nu^{5/12} \cdot d^{1/2}} \cdot \mathfrak{F}^{3/4} \equiv C_{\mathrm{wj}} \cdot \mathfrak{F}^{3/4} \tag{9.6}$$

where n is the charge transfer number, F is the Faraday constant, D is the diffusion constant of AuCl$_4$, r is the sample radius, ν is kinematic viscosity of the solvent (here 0.1 M HCl) and d is the nozzle opening diameter. Inserting $D = 1.1 \cdot 10^{-5}\,\mathrm{cm^2/s}$ from reference [29], $\nu = 10^{-6}\,\mathrm{m^2\,s^{-1}}$ (H$_2$O at 20 °C) and geometrical dimensions of the electrode surface ($r = 2\,\mathrm{mm}$) and the electrochemical cell ($d = 1\,\mathrm{mm}$), respectively, then a proportionality constant of $C_{\mathrm{wj}} = 4.03\,\mathrm{C\,m^{-9/4}\,s^{-1/4}}$ is obtained. The resulting $j(\mathfrak{F})$-curve is shown as dashed line in figure 9.9e. Since the predicted currents are significantly lower than the measured data, the latter has been additionally fitted with C_{wj} as free fit parameter. This procedure yields a proportionality constant of $C_{\mathrm{wj}} = 5.04\,\mathrm{C\,m^{-9/4}\,s^{-1/4}}$ which is about 25% larger than the value estimated before. The according fit curve is shown as dash-dotted line in figure 9.9e. Apparently equation 9.6 cannot accurately describe the measured, flow-dependent current densities. On the one hand this is related to the lack of detailed information about D and ν which affects the theoretical curve. On the other hand the employed cell does not fully match the requirements of an impinging wall-jet electrode. In particular, the nozzle diameter is too large compared to the surface diameter (equation 9.6 presumes $d \ll 2 \cdot r$) and the electrolyte jet does not impinge exactly perpendicular on the electrode surface. Nevertheless, even though equation 9.6 fails to predict the current densities with good accuracy it can explain the qualitative behavior, i.e. that the current density decreases towards higher flow rates.

In order to show that the growth modes during electrolyte flow are in agreement with the growth mode diagram, intensity transients at different potentials E_{end} have been evaluated for the flow rate of $5\,\mu\mathrm{l/s}$. For this the potential was successively stepped from 0.5 V to several potentials E_{end} between -0.4 V and 0.4 V. The obtained $I(t)$ curves were classified into the three kinetic growth modes and have been added to the previously determined growth mode diagram. Deposition rates at different electrode potentials varied in the range between $\approx 2.8\,\mathrm{ML\,min^{-1}}$ and $\approx 3.6\,\mathrm{ML\,min^{-1}}$. The determined average deposition rate at an electrolyte flow of $5\,\mu\mathrm{l/s}$ is $\overline{R} = 3.39\,\mathrm{ML\,min^{-1}}$. As a result of the analysis all inferred growth modes in the investigated potential regime, illustrated by solid symbols in figure 9.10, perfectly agree with the expected growth modes at the increased deposition rate. In summary, the performed experiments demonstrate that the deposition rate R significantly increases
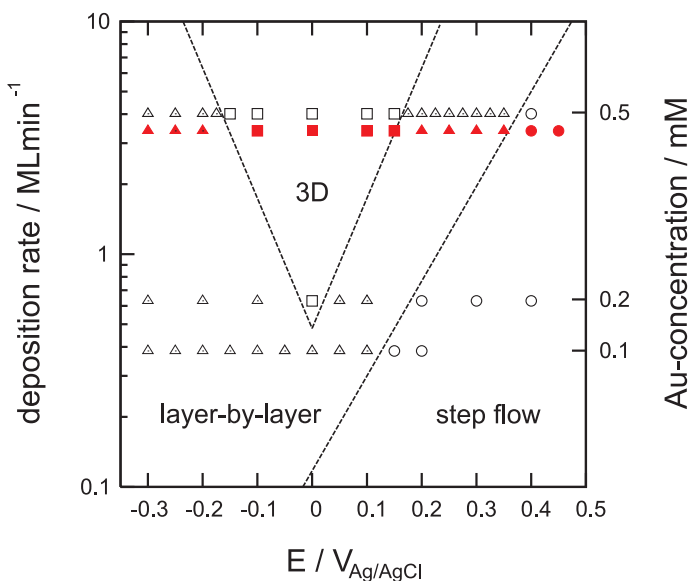
Figure 9.10: Kinetic growth mode diagram for Au/Au(100) in 0.1 M HCl + 0.1 mM HAuCl$_4$, showing the occurrence of step-flow (circles), layer-by-layer (triangles), and multilayer (squares) growth. Solid symbols denote growth modes which were inferred from X-ray time transients while the electrolyte was flowing with a rate of 5 μl/s through the electrochemical cell ($\overline{R} = 3.39\,\mathrm{ML\,min^{-1}}$). Open symbols denote growth modes observed in stagnant solution.

when the Au-containing electrolyte continuously flows through the electrochemical cell. For a nominal Au concentration of 0.1 mM HAuCl$_4$ and a flow rate of 5 μl/s the deposition rate was determined to be approximately 8.6 times higher than in stagnant solution while the Nernst diffusion layer is approximately 8.6 times more compressed. Taking into account the less pronounced shape of measured intensity oscillations then an increase in deposition rate by a factor in the range between 8 to 10 seems to be realistic. The employed procedure may be of particular advantage in the investigation of deposition processes as it allows to control the deposition rate R not only by choice of the Au-concentration c_0 in the solution but also by variation of the flow rate $\mathfrak{F}$.

9.8 Diffuse Scattering

The surface morphology was additionally studied by diffuse scattering in standard geometry (i.e. with the surface normal in the scattering plane). For this growth mode studies were performed on Au(100) electrodes in 0.1 M HCl + 0.2 mM HAuCl$_4$ solution. First, parallel to potential steps from 0.6 V to E_{end}, X-ray intensity transients were recorded at the reciprocal space position $(0 , 0 , 0.7)$ close to anti-Bragg on the specular crystal truncation rod. The resulting growth modes are summarized in the growth mode diagram of figure 9.8 (figure 9.10, respectively). For potentials ≥ 0.2 V step-flow growth was found, close to the surface phase transition at 0 V ($\approx \pm 50$ mV) 3D-growth and in the remaining potential regimes layer-by-layer growth. Subsequent to the recording of the intensity transients rocking scans about the 'chi' axis were performed at the reciprocal space position $(0 , 0 , 0.3)$. The scattering geometry is depicted in the inset of figure 9.11. The X-ray wave, described by the wave vector $\vec{k}_i$, impinges with an incoming angle α_i on the surface. The diffracted wave is described by the wave vector $\vec{k}_f$ which defines the exit angle α_f with respect to the surface plane. Rough interfaces damp the specularly reflected intensity considerably. The 'missing' intensity is diffusely scattered at exit angles $\alpha_f \neq \alpha_i$, i.e. in off-specular directions. After the sample
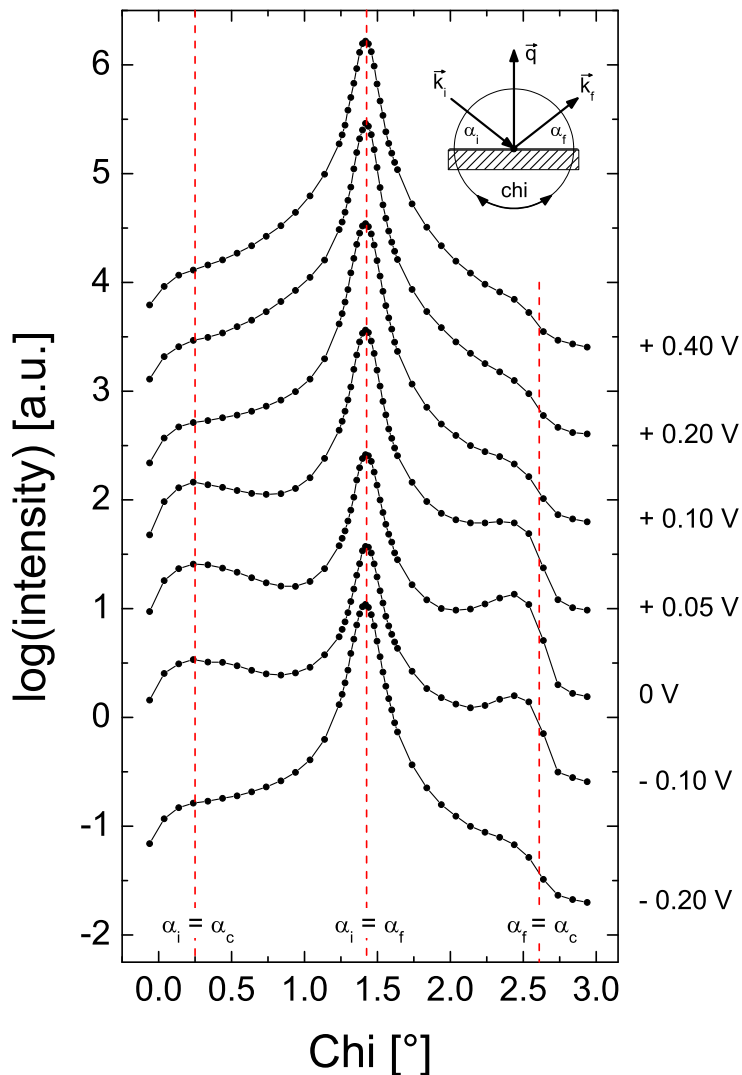
Figure 9.11: Au(100) sample rocking scans about the 'chi' axis recorded in $0.1\,\mathrm{M}$ HCl + $0.2\,\mathrm{mM}$ HAuCl$_4$ subsequent to potential steps from $0.6\,\mathrm{V}$ to different potentials E_{end} at the reciprocal space position $(0\,,0\,,0.3)$. The measured intensity profiles exhibit a resolution limited specular component followed by a broader diffuse component arising from surface/interface roughness. Enhanced scattered intensity is observed for $(\alpha_i = \alpha_c)$ and $(\alpha_f = \alpha_c)$, so-called Yoneda scattering. All curves are shifted with respect to each other for clarity.

was aligned to match the reflectivity condition with $L = 0.3$ the detector was fixed while the sample was rotated about the 'chi' axis. Measured intensity profiles for different potentials E_{end} are shown in figure 9.11. There are two components in the profiles, one which is resolution limited that will be referred to as the specular component, and another broad diffuse component. The diffuse scattering arises from disorder which is correlated over a finite range and exhibits side peaks called 'Yoneda scattering' or 'Yoneda wing' [48,161–163]. In order to emphasize the diffuse component the intensity is plotted in logarithmic scale. Because the data are taken at rather low q_z, the incident or outgoing beam can approach α_c, where the increased electric field at the surface enhances the diffuse scattering of the rough surface.

Closer inspection of the potential-dependent intensity profiles reveals an enhanced diffuse scattering in the vicinity of the surface phase transition, more precisely for potentials between -0.1 V and 0.05 V. This can be clearly seen by the presence of pronounced Yoneda wings. Although the Yoneda wings decrease with increasing surface roughness the intensity

at the position of the Yoneda wings increases. Simultaneously the intensity in the vicinity of the specular component decreases. This shows that more intensity is diffusely scattered in off-specular direction due to a rougher electrode surface in accordance with the determined 3D growth mode in this potential regime. The Yoneda wing towards higher 'chi' values, i.e. where α_f equals α_c, exhibits a smaller width than the Yoneda wing towards smaller 'chi' values where the incident angle α_i equals α_c. The difference might be caused by the change in footprint size and of the illuminated surface area. The latter may also account for the deviation in the position of the right Yoneda wing which is not exactly at the expected position (i.e. not at $\alpha_f = \alpha_c$). For more anodic potentials in the (1×1) regime as well as for more cathodic potentials in the reconstructed potential regime significantly lower diffuse scattering is observed which is in agreement with the smoother surface morphology obtained in the layer-by-layer and step-flow growth regimes. Although more extensive diffuse scattering studies at different L positions could not be performed due to the limited beam time, these data demonstrate the possibility of quantitative surface roughness measurements during electrodeposition.

9.9 Deposition Experiments at Enhanced Deposition Rates

High deposition rates are of particular importance for industrial production processes which often require the deposition of several nm thick films over short time periods. Therefore typically applied deposition rates range in the order of 1000 ML/min. This is about 130 to 5000 times higher than all the deposition rates employed in the framework of the present work. It is obvious that crystal growth at such high deposition rates will not or only very localized proceed via 2D- or step-flow mode and that the obtained films will be polycrystalline with lots of grains and a high degree of surface roughness. In order to ensure a homogeneous film thickness and to minimize the surface roughness commercial plating bathes usually contain organic additives, so-called levelers and brighteners. In contrast to industrial fabrication processes we are interested in fundamental aspects of crystal growth carried out in simple electrochemical model systems, i.e. in absence of additives. From this point of view a system which solely exhibits multilayer growth provides not much information. Moreover, the fact that the layer-by-layer growth is non-ideal, as indicated by the decay of growth oscillations in the time-dependent intensity in anti-Bragg position, the performed growth mode studies require the presence of a step-flow growth regime in order to determine 2D dimensional growth. Hence we are restricted in the choice of the deposition rate. In fact, the accessible, maximum deposition rate in regard of the performed SXS experiments is limited by mainly two factors. The growth mode diagram in figure 9.8 shows that the multilayer growth regime extends towards higher deposition rates. Simultaneously, due to the restriction in electrode potential, given by hydrogen evolution at more cathodic potentials on the one hand and by the Nernst equilibrium potential at more anodic potentials on the other hand, the potential regimes of 2D- and step-flow growth narrow. The second limiting factor is the instrumental time resolution. While the latter is of minor importance for the investigation of multilayer and step-flow growth (since these two growth modes result in constant low or high diffracted intensity in anti-Bragg positions, respectively) the instrumental time resolution significantly matters in the investigation of layer-by-layer growth oscillations since the oscillation period
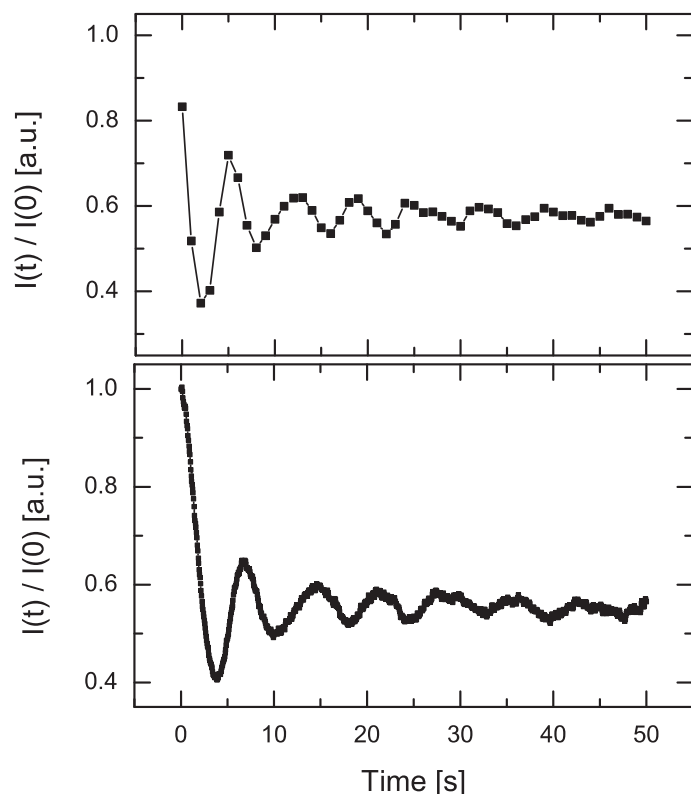
Figure 9.12: Time-dependent intensity recorded at $(1, 1, 0.1)$ parallel to a potential step from $0.75\,V$ to $0.55\,V$. The upper graph shows data recorded via SPEC, the lower graph shows data of the analog detector signal recorded via analog input channel of the potentiostat.

decreases with increasing deposition rate. I will demonstrate in the following that modifications in the experimental setup facilitate the investigation of homoepitaxial growth at deposition rates which are higher than those discussed in the previous sections.

9.9.1 Experimental Observations and Qualitative Discussion

We studied homoepitaxial deposition on Au(100) electrodes in stagnant $0.1\,M\ HCl + 2\,mM$ $HAuCl_4$ solution[1]. Figure 9.12a shows intensity oscillations recorded at the anti-Bragg position $(1, 1, 0.1)$ after stepping the potential from $0.75\,V$ to $0.55\,V$. Six oscillations are recognizable with a comparatively short oscillation period. Obviously the time resolution of the SPEC controlled SXS experiment is almost at the limit as indicated by the small amount of 8 to 10 data points (counting time of $1\,s$ per data point) contributing to each oscillation period. The time resolution could be significantly enhanced by recording the analog detector signal (with a time constant of $0.3\,s$) via analog input channel of the potentiostat. In combination with a data sample rate of $20\,Hz$ well pronounced X-ray intensity oscillations are observed (figure 9.12b). The oscillation period of $T = 7.88\,s$, inferred from the time period between the first two intensity minima, corresponds to a deposition rate of $7.6\,ML/min$. Due to the first integration interval the intensity recorded via SPEC exhibits a delay of exactly one second.

---

[1]As denoted in section 6.5 the concentration near the surface deviates from the nominal concentration of $2\,mM\ HAuCl_4$ due to depletion. The reliable quantity in this study is the deposition rate inferred from X-ray intensity oscillations.
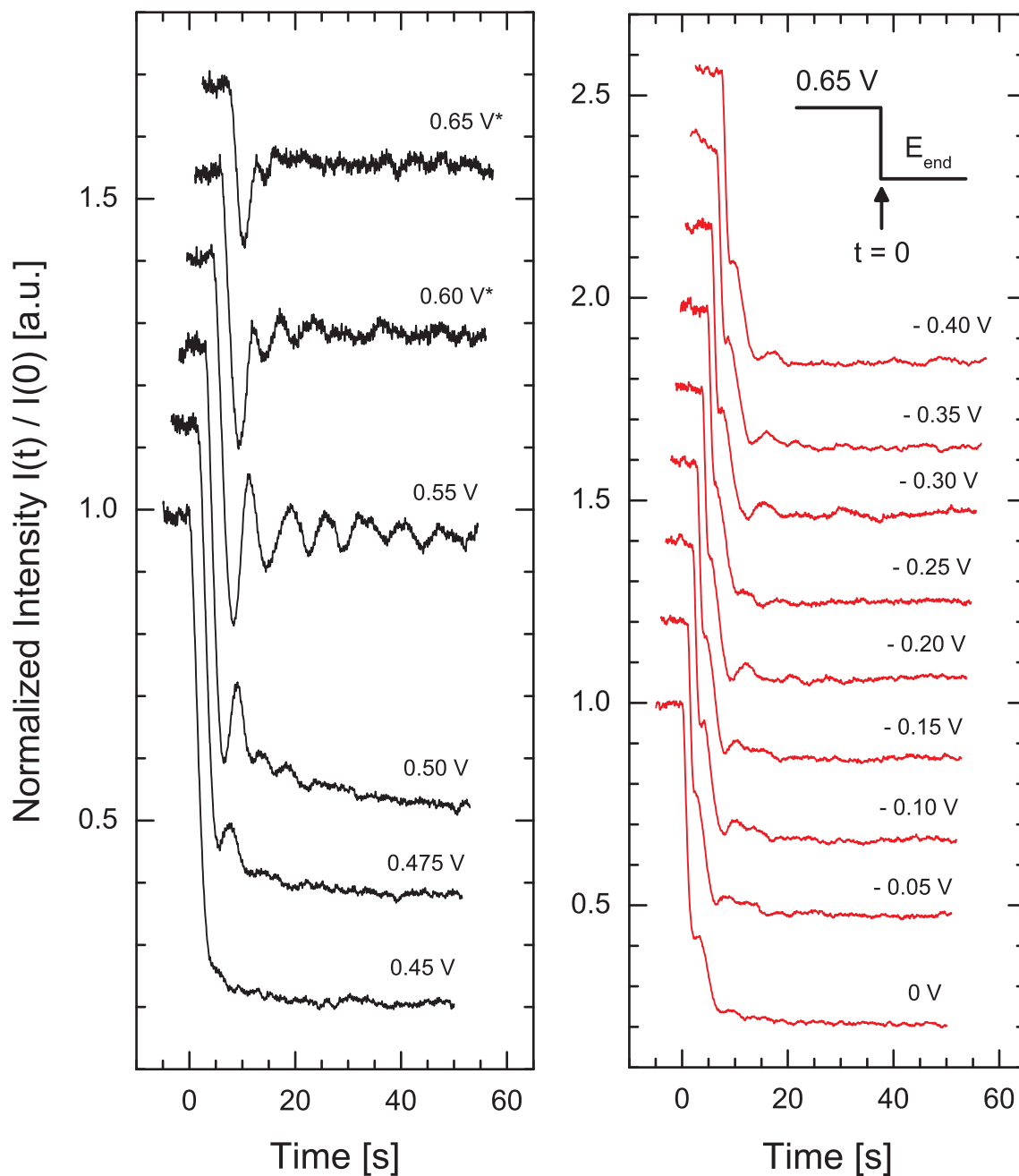
Figure 9.13: Time-dependent X-ray intensity $I(t)$ measured at $(1,1,0.1)$ subsequent to potential steps from $0.65\,\mathrm{V}$ to E_{end} ($*$ denotes potential steps from $0.75\,\mathrm{V}$) in $0.1\,\mathrm{HCl}$ + $2\,\mathrm{mM}$ $HAuCl_4$ solution. For a better time resolution the intensity has been recorded via analog output signal of the X-ray point detector. Different growth modes are observed, specifically multilayer growth in the potential regime from -0.15 V to 0.45 V and layer-by-layer growth from 0.5 V to 0.6 V as well as from -0.3 V to -0.4 V. A high saturation intensity at 0.65 V indicates step-flow growth. The $I(t)$ curves have been normalized to the intensity $I(0)$ before the potential step and are shifted in both axis directions with respect to each other for clarity.

Potential step experiments have been performed from $E_{\text{start}} = 0.65\,\text{V}$ ($0.75\,\text{V}$ for $E_{\text{end}} \geq 0.6\,\text{V}$) to different potentials E_{end} between -0.4 V and 0.75 V in order to determine the growth mode. In parallel $I(t)$ curves were recorded by the potentiostat software via analog detector signal. The obtained $I(t)$ curves are illustrated in figure 9.13. Each curve is normalized to the intensity $I(0)$ before the potential step. As expected according to the growth mode diagram the potential regimes of layer-by-layer and step-flow growth are narrow while the potential regime of multilayer growth is widely extended. In particular, multilayer growth is observed from about -0.15 V to 0.45 V, i.e. near the critical potential in the reconstructed potential regime and in a large part of the unreconstructed potential regime. For potentials $<$ -0.15 V there is a transition from multilayer to a re-entrant layer-by-layer growth regime. Although layering oscillations are not very pronounced, one complete oscillation can be rationalized for transients recorded between -0.3 V and -0.4 V. The potential regime between -0.15 V and -0.25 V cannot be clearly attributed to either of the two growth modes. In the potential regime of the unreconstructed surface phase growth oscillations are seen for potentials between 0.475 V and 0.65 V indicating layer-by-layer growth. The layering oscillations are most pronounced at a potential of 0.55 V where six oscillation periods are found. $I(t)$ curves obtained for 0.475 V and 0.65 V show one oscillation before the intensity saturates at a low and high intensity, respectively. The saturation values indicate that these potentials are close to the growth mode transitions between multilayer and layer-by-layer growth and between layer-by-layer and step-flow growth, respectively. The 3D to 2D growth transition at $\approx$ -0.15 V is in good agreement with the growth mode diagram in figure 9.8. However, the 3D to 2D growth transition at $\approx 0.45\,\text{V}$ and the 2D to step-flow growth transition at $\approx 0.65\,\text{V}$ seem to be shifted towards more positive potentials.

There is a striking feature of $I(t)$ curves in the reconstructed potential regime which is not observed in the unreconstructed potential regime. Within the first 5 seconds the initial intensity $I(0)$ rapidly decreases. While this decay is monotonic in the unreconstructed potential regime, it is interrupted by a plateau of constant intensity in the reconstructed potential regime. A close up view of the plateau in the $I(t)$ transient at -0.4 V is shown in figure 9.14a. It extends over a time period of approximately 1.5 seconds. The relatively short time span explains why the plateau is not observed in the SPEC data since the time resolution of $1\,\text{s}$ per point is insufficient to resolve it. However, in the analog detector signal the plateau is well pronounced with about 30 data points. For all potentials $< 0\,\text{V}$ the normalized intensity at the plateau scatters slightly around a mean value of $I_{\text{plateau}} = 0.55\pm0.05$. The same holds for the first intensity minimum which is found at an average value of $I = 0.28\pm0.02$. An appropriate scale for deposition experiments is the coverage θ_{dep} of the electrode with deposited material. At $t = 0$, i.e. at the time of the potential step, the coverage θ_{dep} is defined to be zero. Figure 9.14b shows the coverages at two positions of the recorded transients, that is 1st) the center of the plateau and 2nd) the first intensity minimum. Both coverages were calculated by multiplication of the time t with the deposition rate of $0.127\,\text{ML/s}$ ($\hat{=}\,7.6\,\text{ML/min}$). At the position of the plateau center $0.25 \pm 0.05\,\text{ML}$ were deposited. This amount accords exactly to the excess of gold atoms in the reconstructed monolayer compared to the unreconstructed one. At the position of the first intensity minimum a total amount of 0.79 ± 0.09 monolayers was deposited, i.e. approximately half a monolayer in addition to the plateau.

9.9.2 Model for the Initial Stage of Deposition after Potential Steps into the Reconstructed Potential Regime

Based on the findings in the previous section a model is proposed which is illustrated in figure 9.14c. At the time $t = 0$ the potential is stepped from $0.65\,\text{V}$ in the unreconstructed potential regime to a potential E_{end} in the reconstructed potential regime. Due to step-flow growth at $0.65\,\text{V}$ the initial surface is smooth. Especially the electron density at the interface is described by a reasonable sharp step function resulting in a high X-ray intensity at the anti-Bragg position $(1, 1, 0.1)$. Then, subsequent to the potential step the deposited gold atoms contribute to the formation of the reconstructed phase of the topmost surface layer. Reconstructed areas spread with ongoing deposition time while simultaneously the fraction of unreconstructed areas decreases. This results in a continuous intensity decrease in the
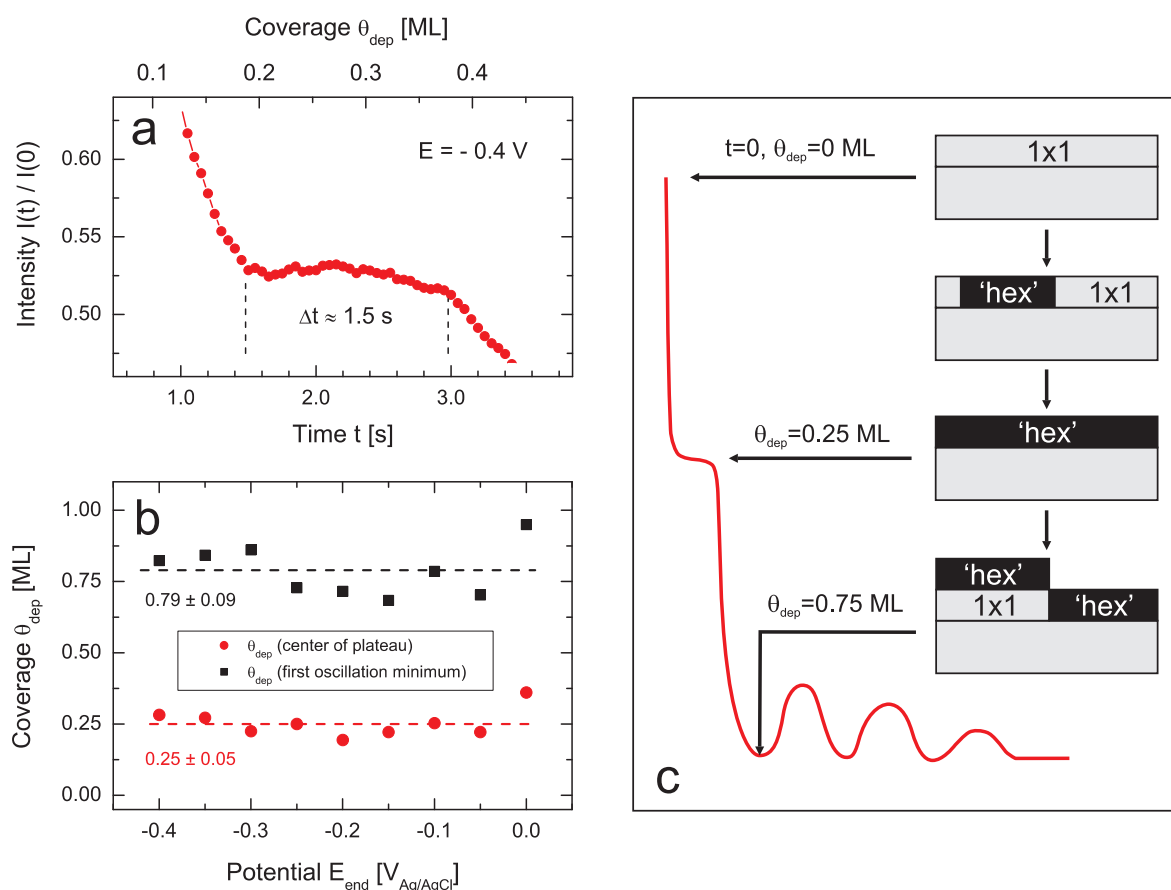
Figure 9.14: a) Intensity plateau observed after potential steps to the reconstructed potential regime. b) Deposited amount of gold at the center of the plateau and in the first oscillation minimum, respectively. c) Proposed model to explain the intensity decrease for potential steps from the unreconstructed to the reconstructed potential regime. The surface reconstructs within the first 3 seconds after the potential step followed by (imperfect) layer-by-layer growth in the 'hex' phase or by multilayer growth.

anti-Bragg position. When θ_{dep} equals 0.25 ML the surface is completely reconstructed. This coverage coincides with the position of the intensity plateau. Between $\theta_{\mathrm{dep}} = 0$ ML and $\theta_{\mathrm{dep}} = 0.25$ ML the intensity continuously decreases. This cannot be explained if the anti-Bragg position is assumed to be exclusively sensitive to the unreconstructed surface structure because then the intensity for $\theta_{\mathrm{dep}} = 0.25$ ML should be equal to the intensity $I(0)$. Hence the reconstructed surface layer must contribute significantly to the observed intensity.

Origin of the plateau is the turning point between the completion of the reconstructed phase, which is equal to the disappearance of unreconstructed areas in the topmost surface layer, and the onset of growth on top of the reconstructed surface. Here two effects influence the diffracted intensity. On the one hand the surface is totally covered with the reconstructed surface phase (in contrast to the situation before), on the other hand the surface below deposited new layers transforms back to the (1×1) bulk structure. Both effects in combination result in a further intensity decrease subsequent to the plateau. The minimum in intensity is taken if the surface is covered by half a monolayer. In this situation θ_{dep} should be equal to 0.75 ML which is the sum of 0.25 ML for the formation of the reconstructed phase and 0.5 ML for the additional half monolayer. Indeed, the measured coverage of 0.79 ± 0.09 ML at the first intensity minimum agrees well with $\theta_{\mathrm{dep}} = 0.75$ ML. For ideal layer-by-layer growth the intensity is expected to oscillate between $I = 0.28$ and $I = 0.55$ in the following. However, the layer-by-layer growth is non-ideal which results in a rapid decay in the oscillation amplitude. The proposed model gets strong support from extensive crystal truncation rod measurements which will be presented in chapter 10.

9.9.3 Thick Film Deposit Morphology

Subsequent to the growth mode studies at $(1, 1, 0.1)$ the in-plane structure of the reconstructed Au(100) surface was characterized at the reciprocal space position $(\Delta_1, \Delta_1, 0.1)$ while the electrode potential was kept at -0.3 V. The inset of figure 9.15 shows a radial scan along the $[110]_c$ direction. Two peaks are recognizable at the reciprocal space positions $(1.215, 1.215, 0.1)$ and $(1.225, 1.225, 0.1)$, respectively. The first of these peaks is most probably related to the hexagonal reconstructed surface layer. The value of $\Delta_1 = 1.215$ is considerably larger than the value of $\Delta_1 = 1.2105$ found in previous in-plane studies at lower deposition rates. This might indicate a dependence of the electrocompression effect on the deposition rate. Unfortunately no detailed study has been carried out to confirm the latter. In order to reveal the origin of the second peak an azimuthal scan has been recorded at $(1.225, 1.225, 0.1)$ which is shown in figure 9.15. A couple of intensity peaks can be seen indicating a powder like structure of the deposit. Between the electrolyte exchange and the in-plane scans a time span of approximately 2 hours passed corresponding to the deposition of an gold amount equivalent to approximately 900 monolayers. For this deposit quantity local growth of crystallites on the surface must be expected. The value $\Delta_1 = 1.225$ corresponds to a scattering vector length of $|\vec{q}| = 2.668 \, \mathring{\mathrm{A}}^{-1}$ and to a netplane spacing of $2.355 \, \mathring{\mathrm{A}}$ in real space. The latter perfectly agrees with the bulk lattice spacing of $(1\,1\,1)$ netplanes $(a_c/\sqrt{3})$. According crystallites are oriented with one of the equivalent $\{\bar{1}\,1\,0\}$ netplanes towards the Au(100) electrode surface. Unfortunately we did not determine the scattered intensity in
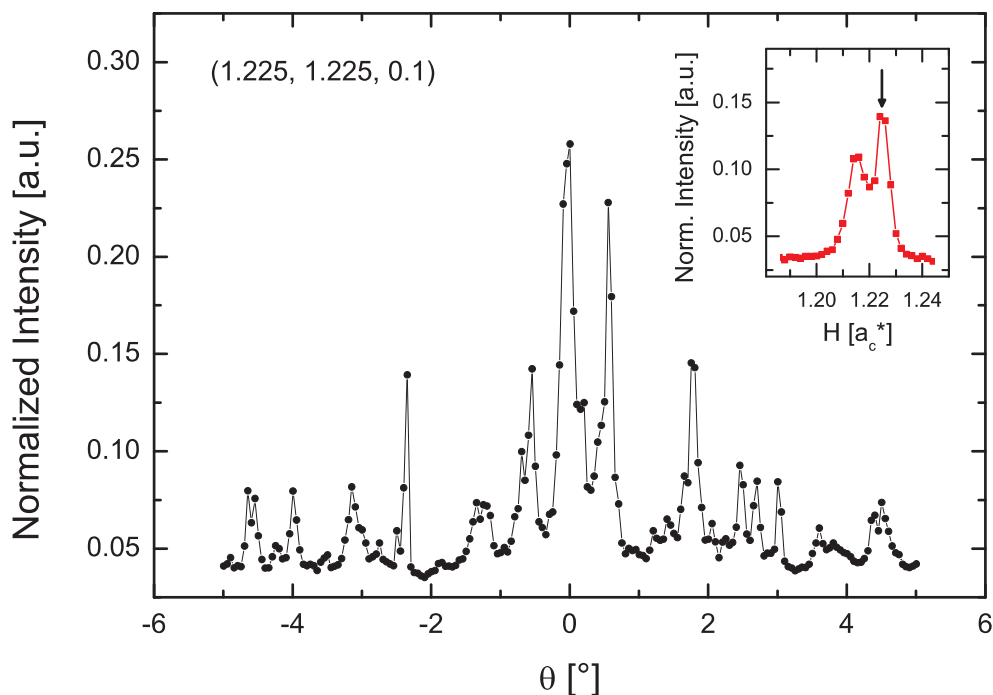
Figure 9.15: Azimuthal scan recorded at the reciprocal space position $(1.225, 1.225, 0.1)$ after deposition of several hundred monolayers. The scattered intensity indicates a powder-like structure of the deposit. The inset shows a radial scan along $\vec{q}_r$ through the $(\Delta_1, \Delta_1, 0.1)$ position with two peaks at $(1.215, 1.215, 0.1)$ and $(1.225, 1.225, 0.1)$, respectively.

L-direction to confirm this orientation. The favorable growth of $(1\,1\,1)$ and $\{\bar{1}\,1\,0\}$ facets is in agreement with growth theory according to Bravais, Friedel, Donnay and Harker. The growth velocity of a facet (hkl) is supposed to be inversely proportional to the lattice spacing d_{hkl} [164] which was found to apply well in the case of simple metal crystals.

9.10 Growth Mode Studies on Au(111) Electrodes

In the framework of the electrodeposition studies homoepitaxial growth has been as well investigated on single crystal Au(111) electrodes. Up to now there is no simple way to predict the presence of certain growth modes in electrochemical environment. This is related to the high complexity of the systems, in particular to the fact that both, the surface diffusion barrier and the step edge barrier are functions of the electrode potential and additionally influenced by ionic species on the solution side of the interface. Although there are attempts to predict growth modes by theoretical approach and yet successful models were reported for the description of growth in UHV [165] similar theoretical works are still rare for electrochemical systems. Thus the only way to obtain fundamental information about crystal growth from the solution phase are experiments. It is known from various MBE studies that fcc(100) metals in general tend to grow smoothly, indicating an effective interlayer mass transport and a low or even vanishing step edge barrier. However, for fcc(111) surfaces

a remarkably different behavior was found, in particular pronounced 3D growth indicating a comparatively large step edge barrier. For the reasons given above these general trends cannot be simply translated to the growth at solid/liquid interfaces. In the following the results of electrodeposition studies on Au(111) electrodes will be summarized briefly in order to shed light on the growth behavior.

9.10.1 Homoepitaxial Growth on Au(111) Electrodes

Homoepitaxial deposition experiments have been performed in a similar manner on Au(111) electrodes in order to characterize the potential-dependent growth behavior. Before the obtained X-ray data is presented the results of previous UHV studies shall be briefly summarized. A real-time X-ray scattering study of epitaxial MBE growth of Au(111) in UHV revealed layer-by-layer growth at sample temperatures between 55 and 145 °C [2] where the surface is reconstructed. This growth mode differs from the behavior expected for homoepitaxy on fcc(111) surfaces and also seems to contradict theoretical calculations which suggest a large Ehrlich-Schwoebel barrier for adatom diffusion [165]. However, Au(111) exhibits a layer-by-layer growth regime while it is for example not observed for Cu(111), Ag(111) and Ni(111) surfaces [1]. An STM study of Au deposition on Au(111) surfaces in UHV indicates three-dimensional growth after deposition of 5 ML at room temperature [166]. The onset of second layer nucleation apparently occurs parallel to coalescence of the first deposited Au layer, suggesting incomplete layer-by-layer growth.

Analog to the electrodeposition studies on Au(100) electrodes we investigated homoepitaxial growth on Au(111) in the onset of deposition as well as in stagnant Au-containing solution. Figure 9.16b shows the diffracted time-dependent X-ray intensity monitored at the reciprocal space position $(0, 1, 0.1)$ close to anti-Bragg (the Au(111) scattering geometry is described in chapter 11) parallel to an electrolyte exchange from 0.1 M HCl to 0.1 M HCl + 0.1 mM HAuCl$_4$ while the electrode potential was kept at 0.6 V. In total 2200 μl were exchanged with a speed of 5 μl/s. Before the initiation of electrolyte flow at $t = 0$ a relatively high intensity of ≈ 0.6 is measured due to a comparatively smooth surface after crystal preparation. In the onset of the exchange process the intensity then rapidly decreases indicating a pronounced growth-induced roughening. The decay sustains until end of the exchange procedure. At the according time, $t = 440$ s, an intensity of ≈ 0.2 is determined. Applying the Au concentration $c_0 = 10^{-7}$ mol cm^{-3}, the diffusion constant $D = 1.1 \cdot 10^{-5}$ cm^2 s^{-1}, the number of Au atoms per monolayer $N_{ML} = 1.387 \cdot 10^{15}$ cm^{-2} and the Nernst diffusion layer thickness $\delta_N \approx 0.012$ cm (as determined for electrolyte flow with a rate of 5 μl/s) to equation 9.4 yields an enhanced deposition rate of $R \approx 2.4$ ML min^{-1} so that in the time span of 440 s during electrolyte exchange an approximate amount of 17.5 ML was deposited. Provided that the growth in electrochemical environment proceeds similar non-ideal as in the aforementioned UHV-STM study the surface will be rough even though the electrode potential of 0.6 V might be in the layer-by-layer regime. Subsequent to the exchange process the intensity partially recovers within a short time period and approaches a saturation value of ≈ 0.3. This partial recovery may be ascribed to a change in the deposition rate. After stop of the exchange process the Nernst diffusion layer extends further into the solution and the deposition rate
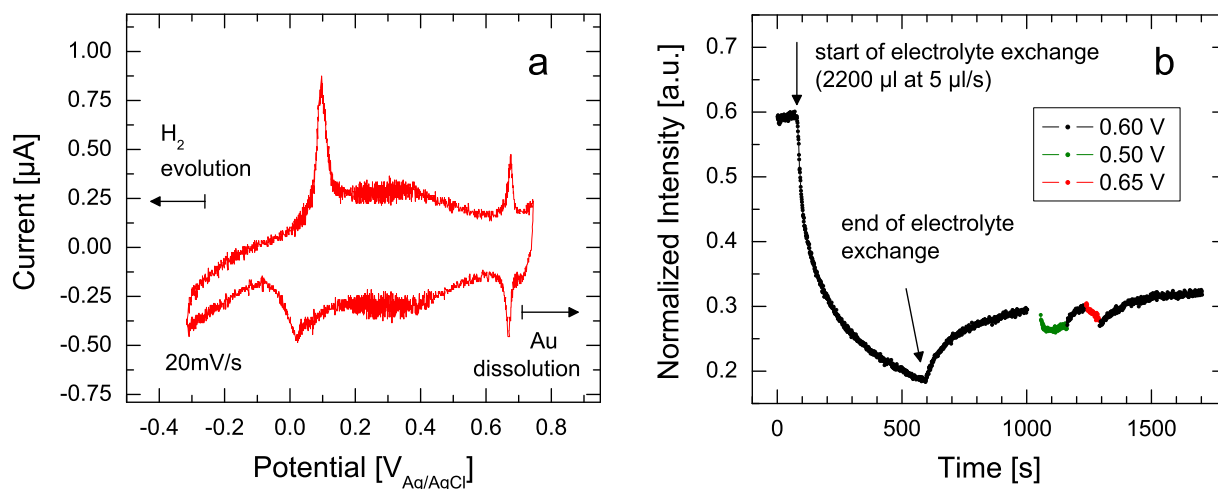
Figure 9.16: a) Cyclic voltammogram of Au(111) in aqueous $0.1\,\mathrm{mM}$ HCl solution. The accessible potential range for deposition experiments lies between the cathodic onset of hydrogen evolution and the anodic onset of Au dissolution. b) X-ray intensity monitored at the reciprocal space position $(0,1,0.1)$ parallel to an electrolyte exchange ($2200\,\mu\mathrm{l}$ at $5\,\mu\mathrm{l/s}$) from $0.1\,\mathrm{M}$ HCl to $0.1\,\mathrm{M}$ HCl + $0.1\,\mathrm{mM}$ HAuCl$_4$. The decrease in intensity indicates either 3D growth or non-ideal layer-by-layer growth.

decreases. Induced by this the nucleation rate will decrease and the accelerating influence of chloride on the mobility of Au adatoms will promote an enhanced intralayer transport. The growth mode at $0.6\,\mathrm{V}$ is either 3D growth or imperfect layer-by-layer growth which cannot be definitely clarified since the surface substantially roughens during the exchange process (3D growth). In fact, the shape of the intensity curve strongly resembles those in exchange experiments on Au(100) electrodes while the potential was kept at a value where layer-by-layer growth is found in stagnant solution.

Subsequent to the exchange process potential step experiments have been performed to different potentials E_{end} in the potential regime between hydrogen evolution and Au dissolution. The latter, i.e. the Nernst potential, may be inferred from the cyclic voltammogram in figure 9.16a which was recorded within the employed (Au-free) base electrolyte. Diffracted intensity for some of the potential steps is shown in figure 9.16b. At the potentials of $0.5\,\mathrm{V}$ and $0.65\,\mathrm{V}$ the intensity slightly decreases while for potential steps back to $0.6\,\mathrm{V}$ the intensity recovers indicating that $0.6\,\mathrm{V}$ is the best potential for growth in this regime. In the whole potential regime between hydrogen evolution and Nernst potential no step-flow growth has been found which strongly limits the growth mode studies on Au(111) electrode surfaces. In addition to $0.1\,\mathrm{M}$ HCl base solution further deposition measurements were carried out in a mixture of $50\,\mathrm{mM}$ H$_2$SO$_4$ and $5\,\mathrm{mM}$ HCl which has been as well employed in Au(111) electrodissolution studies (presented in chapter 11). The results obtained in a mixture of sulfuric and hydrochloric acid are qualitatively identical to the findings in aqueous HCl base solution, i.e. only indications for 3D growth or layer-by-layer growth but no evidence for step-flow growth were found.

Our group also investigated homoepitaxial growth on Au(111) electrodes in 0.01 M HCl by in-situ video STM. These studies were performed by Dr. Wanda Polewska and revealed the formation of nanoscale grooves in the reconstructed potential regime [14]. This is an interesting result which nicely demonstrates that the growth behavior is not only influenced by the solution side but also by the surface structure on the electrode side. Similar reconstruction-induced effects on growth morphology have not been reported before. For thicker Au deposits a very rough deposit morphology has been found with mesa-shaped Au islands in accordance with in-situ SXS data [12]. In the unreconstructed potential regime the STM study revealed a morphology with pyramidal rather than mesa-shaped islands. The pyramidal growth strongly supports 3D growth or non-ideal layer-by-layer growth in agreement with the present SXS study.

The absence of a step-flow growth regime and a pronounced roughening of the surface gives rise to the conclusion that the step edge barrier on Au(111) electrodes in electrochemical environment is significantly larger than on Au(100) electrode surfaces. Thus the growth on gold electrodes of different surface orientations in HCl and Au-containing solutions follows the general trends observed in previous UHV studies. Recent RHEED and Auger Electron Spectroscopic (AES) studies of MBE growth in UHV determined an interesting transition from layer-by-layer to step-flow growth if the Au(111) surface is covered by a submonolayer bismuth which acts as effective surfactant in the Au homoepitaxial growth by the promotion of Au intralayer mass transport [167]. The latter may be utilized in future experiments in order to perform systematic growth mode studies.

9.11 Summary

Our experiments demonstrate that by surface X-ray scattering in transmission geometry direct in-situ studies of the kinetic growth mode are possible for growth at solid-liquid interfaces. As shown here, for homoepitaxial electrodeposition on Au(100), both the solid surface structure, e.g., the Au reconstruction, as well as the solution side of the interface, such as coadsorbed species, can affect the surface transport of the deposited adatoms and by this the growth behavior. With decreasing potential transitions from step-flow to layer-by-layer growth, manifested by layering oscillations in the X-ray intensity, then to multilayer growth, and finally back to layer-by-layer growth were observed. The pronounced step-flow growth at potentials between 0.5 and 0.6 V was found to smoothen even substantially roughened surfaces. Further morphology studies by diffuse scattering revealed an enhanced diffusely scattered intensity in the vicinity of the critical potential for surface reconstruction which is in perfect agreement with the obtained 3D growth mode in this potential regime. On the other hand weak diffuse intensity in the layer-by-layer and step-flow growth regime is in accordance with the lower surface roughness. Growth experiments at enhanced deposition rates (7.6 ML/min) revealed a characteristic plateau in the scattered X-ray intensity for potential steps from the unreconstructed to the reconstructed potential regime. This plateau is related to the formation of the reconstructed phase. Closer analysis of the time-dependent deposit quantity indicates that the first Au amount equal to 0.25 ML is directly incorporated into the topmost surface layer before successive layers grow in the reconstructed phase. Af-

ter the deposition of several hundred monolayers azimuthal in-plane rocking scans indicate a powder-like structure of the deposit, in particular the presence of crystallites which are oriented with one of the equivalent $\{\overline{1}\,1\,0\}$ netplanes towards the Au(100) electrode surface. In addition to systematic growth mode studies in stagnant solution growth experiments have been performed in parallel to a well-defined, constant flow of electrolyte through the electrochemical cell. With increasing flow rate $\mathfrak{F}$ the deposition rate R increases due to a compression of the Nernst diffusion layer δ_N. Data obtained by electrochemical methods and by X-ray scattering are in perfect agreement.

In contrast to homoepitaxial growth on Au(100) electrodes similar studies on Au(111) electrodes reveal only indications for 3D growth or non-ideal layer-by-layer growth, i.e. a significantly larger step edge barrier on the (111) oriented surface. Thus the growth behavior of Au electrodes in chloride containing solution follows the general trends observed in MBE studies under UHV conditions.

10 Influence of Homoepitaxial Growth on the Au(100) Surface Phase Transition

This chapter focuses on the influence of homoepitaxial growth on the Au(100) surface phase transition from the unreconstructed (1×1) phase to the reconstructed 'hex' phase in $0.1\,\mathrm{M}$ HCl + $0.5\,\mathrm{mM}$ HAuCl$_4$ solution. If the electrode potential is stepped from the unreconstructed into the reconstructed potential regime then two processes proceed simultaneously, that is the deposition of gold on the one hand and the formation of the reconstructed surface phase on the other hand. Of particular interest is the behavior in the initial stage after the potential step. We discussed in the previous chapter that X-ray time transients which were recorded at $(1\,,1\,,0.1)$ in parallel to potential steps to E_{end} in the reconstructed potential regime exhibit an intensity plateau after deposition of $0.25\,\mathrm{ML}$ gold. Based on this finding a model was suggested which proposes that the first deposited Au amount of $0.25\,\mathrm{ML}$ becomes directly incorporated into the topmost surface layer and contributes to the formation of the reconstructed phase. Subsequent growth of reconstructed layers was found. In order to investigate the surface phase transition under deposition conditions in more detail and to confirm the simple model of the previous chapter extensive crystal truncation rod measurements have been carried out which will be presented in the following. A systematic extension of SXS measurements allows to construct full Au(100) crystal truncation rods with a time resolution of $\approx 1\,\mathrm{s}$. From these data, a detailed picture of the interface structure at various stages of the growth process can be obtained. After verifying the feasibility of such studies for the particular simple case of layer-by-layer growth on the (1×1) surface, the method will be employed to clarify the influence of gold electrodeposition on the (1×1) to 'hex' transition.

10.1 Potential Step Experiments

In order to investigate the phase transition in presence of homoepitaxial growth potential step experiments were performed as follows. First, the Au crystal was kept at a potential of $0.55\,\mathrm{V}$, where the surface mobility is very high, resulting in rapid surface smoothening. The latter manifests in an increase in X-ray intensity up to a highly reproducible saturation value, even if the surface had been substantially roughened before. Four minutes after saturation had been reached, the potential was changed to $0.35\,\mathrm{V}$ or -0.2 V and the $I(t)$ scan started. Examples of such $I(t)$ curves, obtained at $L = 1.2$ (i.e. close to the anti-Bragg position), are shown in figure 10.1. In these curves, the background intensity, resulting from scattering by the electrolyte, has been subtracted and the intensity has been normalized to the intensity $I(t)$ before the change of potential. After the potential step intensity oscillations are observed at both investigated potentials indicating layer-by-layer growth. These oscillations, which were also found at other reciprocal space positions, disappear after deposition of four to five monolayers (ML) due to increasing roughness. The period Δt of the oscillations equals the time for depositing one monolayer and is 14±2 seconds. This corresponds to a deposition rate of $4.2 \pm 0.2\,\mathrm{ML\,min^{-1}}$, which is in good agreement with the rate obtained from the deposition current density of 40-50 $\mu\mathrm{A\,cm^{-2}}$. The $\approx 12\%$ fluctuation in the deposition rate between different experiments is attributed to slight variations in the hydrodynamic conditions, which are determined by microconvection in the cell and
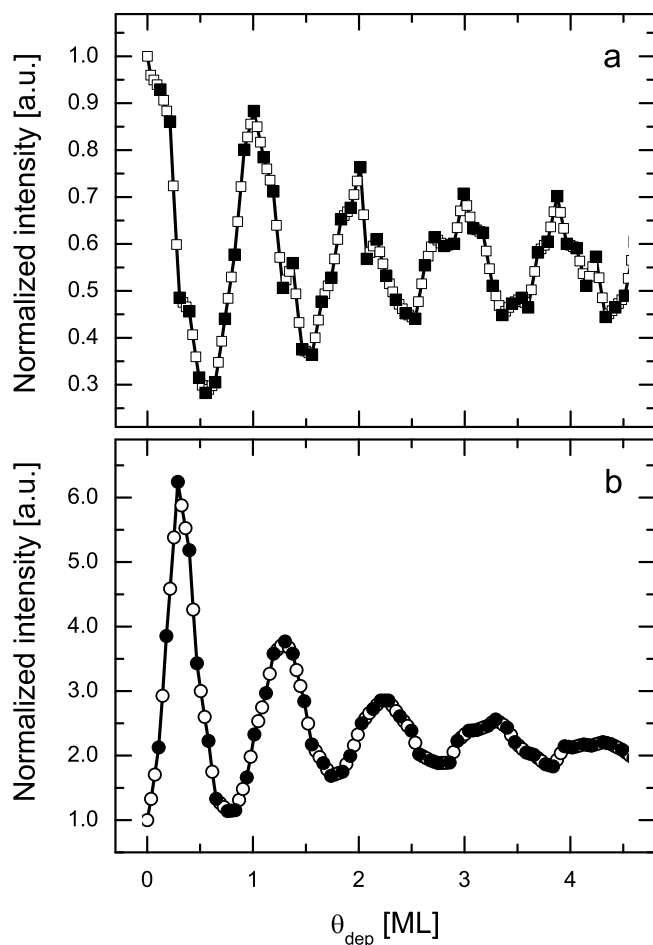
Figure 10.1: Examples of in-situ growth experiments on Au(100) in 0.1 M HCl + 0.5 mM $HAuCl_4$ at a diffusion-limited rate of $4.2\,\mathrm{ML\,min^{-1}}$. The two graphs show the background-subtracted intensity $I(t)$ at $(0,0,1.2)$ versus deposited Au coverage θ_{dep}, after potential steps from $0.55\,\mathrm{V}$ to a) $0.35\,\mathrm{V}$ and b) $-0.2\,\mathrm{V}$. Both curves have been normalized to the intensity at $0.55\,\mathrm{V}$ before the potential jump. Furthermore, in order to obtain the intensity at intermediate coverages, both curves have been interpolated (open symbols).

are consequently not well defined. Furthermore, depletion of the Au concentration in the electrolyte near the surface results in a 1% decrease in deposition rate per minute. Closer inspection of the X-ray transients in figure 10.1 reveals a different initial oscillation phase behavior for potential steps into the unreconstructed and into the reconstructed potential regime. While for potential steps into the unreconstructed regime (figure 10.1a) the intensity first decreases and then oscillates in the range of $0 \leq I(t) \leq I(0)$, the intensity for potential steps into the reconstructed potential regime (figure 10.1b) first increases and then oscillates between $I(0) \leq I(t) \leq I_{\mathrm{max}}(t_{\mathrm{max}})$ with $I_{\mathrm{max}}(t_{\mathrm{max}}) > I(0)$. The latter is a consequence of the $\approx 25\%$ higher electron density in the reconstructed surface layer and is in contrast to the intensity decrease observed at non-specular crystal truncation rods after potential steps into the reconstructed potential regime (cp. section 9.9).

10.2 From X-ray Intensity Transients to Crystal Truncation Rods

From the $I(t)$ data at different L time-dependent specular CTRs can be constructed. For this, first the time axis of each curve at a given deposition potential is multiplied by a correction factor so that the minima in all curves are in phase. This is necessary to ensure

that for all points along the reflectivity curve the same amount θ_{dep} of Au was deposited after the potential step. Since these small differences in deposition rate do not have a major effect on the growth behavior, this correction seems legitimate. Second, the (0 0 L) CTR at a given time t or coverage $\theta_{\text{dep}} = t/\Delta t$, respectively, is constructed by multiplying at each L the intensity $I(t)$ by the rocking curve width and applying the necessary geometry, polarization, and Lorentz correction factors. The rocking curve widths were obtained before the deposition experiments in Au-free HCl solution and were found to be not affected by the growth process. Some of the measured $I(t)$ curves for different L values between the origin at $(0,0,0)$ and the first order Bragg reflection at $(0,0,2)$ are exemplary shown in figure 10.2. Figure 10.3 shows the resulting CTRs for selected coverages at 0.35 V (figure 10.3a) and -0.2 V (figure 10.3b) as well as fits of the data by structural models, which are described in the following. Fits to the crystal truncation rods were performed within the ROD surface crystallography software [168] using a χ^2 minimization method. To keep the models as simple
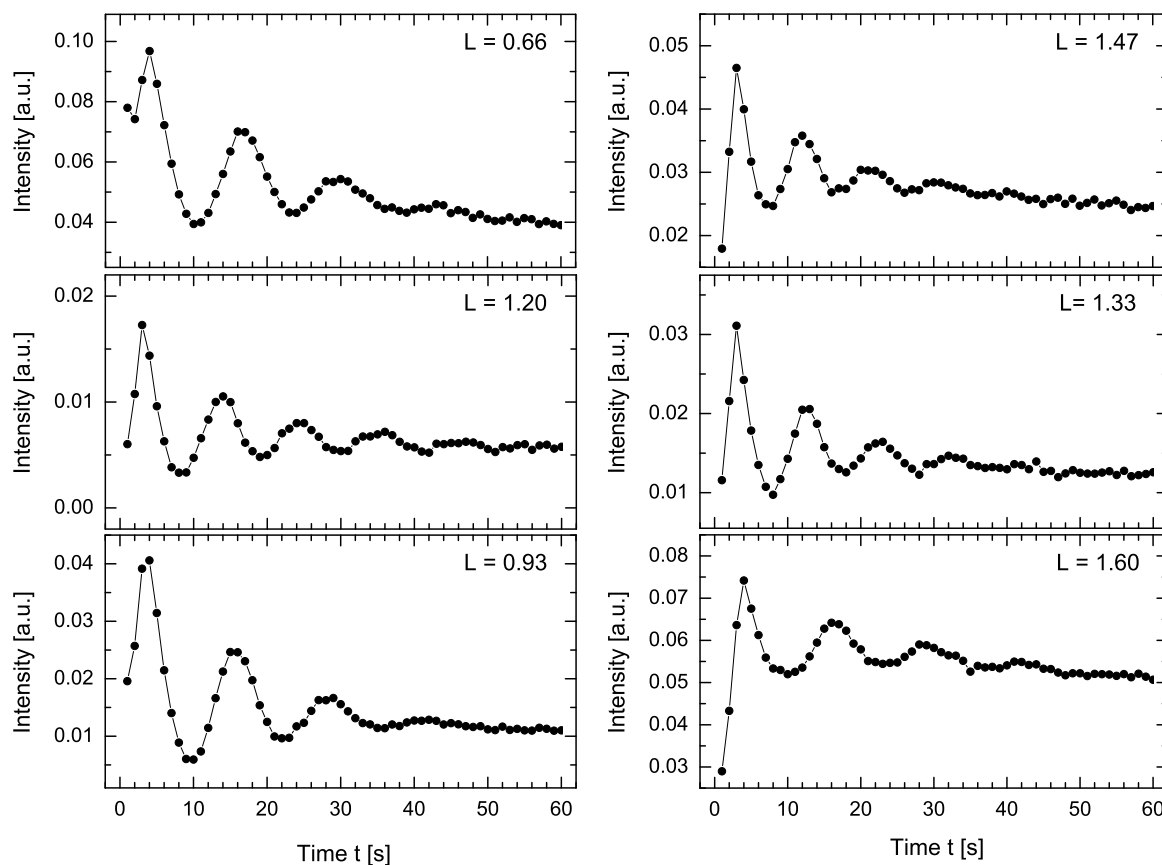
Figure 10.2: In-situ growth experiments on Au(100) in 0.1 M HCl + 0.5 mM HAuCl$_4$ at a diffusion-limited rate of 4.2 ML min^{-1}. Layer-by-layer growth oscillations monitored after potentials jumps from 0.55 V to -0.2 V at different L values on the specular crystal truncation rod. All intensity values are background-subtracted and normalized to the monitor signal. The counting time was 1 s per data point.

as possible, only the submonolayer range of θ_{dep} was quantitatively analyzed in this way. At higher θ_{dep}, more complex models that take the increase in surface roughness into account would be required. The employed method allows to obtain complete crystal truncation rods with the same time resolution as for X-ray time transients recorded at a fixed position in reciprocal space. CTRs with this high time resolution cannot be obtained by conventional recording methods.

10.3 Analysis of Potential Steps into the Unreconstructed Potential Regime

In the case of a potential step from $0.55\,\text{V}$ to $0.35\,\text{V}$, the Au(100) surface is at both potentials in the unreconstructed phase and covered by a $c(\sqrt{2}\times2\sqrt{2})$ Cl adlayer phase. Here the time-dependent CTR data are well described by the model illustrated in figure 10.4a. Immediately after the potential step ($\theta_{\text{dep}} = 0\,\text{ML}$), the CTR can be described by an unreconstructed Au(100) surface in $HClO_4$ solution plus an adsorbed Cl_{ad} adlayer with a coverage of $0.5\,\text{ML}$ (i.e. the coverage of the $c(\sqrt{2}\times2\sqrt{2})$ phase). The vertical relaxation of the topmost Au layer and the Debye-Waller parameters were fixed at the values determined by Ocko et al. [80], the Cl_{ad}-Au spacing was chosen as in $AuCl_4^-$, and the Debye-Waller parameter for Cl_{ad} was set to $10\,\text{Å}^2$. A summary of the fixed parameters is given in table 10.1. The effect of the Cl_{ad} adlayer is small and only slightly improves the fit. To describe the surface at later stages of the growth process ($\theta_{\text{dep}} > 0\,\text{ML}$), scattering from such surface areas (figure 10.4a , right) and areas covered by an additional, unreconstructed Au monolayer (figure 10.4a , left) were coherently superimposed taking into account the chloride adlayer. The surface coverage of the additional monolayer is θ, that of the remaining uncovered Au surface consequently 1-θ. Here, θ is a free fit parameter and not a priori identical to the nominal deposited Au coverage θ_{dep}. However, as shown in table 10.1, the fitted coverage θ is between 0 and $0.5\,\text{ML}$, in good agreement with the nominal coverage θ_{dep} (within the experimental errors). Noticeable deviations are only apparent at $0.7\,\text{ML}$ or higher coverages, where second layer island nucleation is expected. The successful modeling of the data in this particular simple case provides confidence in the method by which these time-dependent CTRs are obtained.

10.4 Analysis of Potential Steps into the Reconstructed Potential Regime

Potential steps to -0.2 V, i.e. into the regime of the surface reconstruction, reveal a more interesting behavior, as can be seen even by a qualitative inspection of the CTRs in figure 10.3b. Contrary to a simple layer growth, the intensity initially increases for all L values (see figure 10.2). At $\theta_{\text{dep}} = 0.25 \pm 0.03\,\text{ML}$, where the $I(t)$ curves reach the first maximum, the CTR is very similar to that found in Au-free electrolyte for a fully 'hex' reconstructed Au(100) surface [80], which has a 25% enhanced packing density in the Au surface layer. The behavior in these early stages of deposition cannot be explained by models that involve the nucleation and growth of reconstructed or unreconstructed Au islands on the (initially unreconstructed) electrode surface. To describe this regime, a model is suggested where
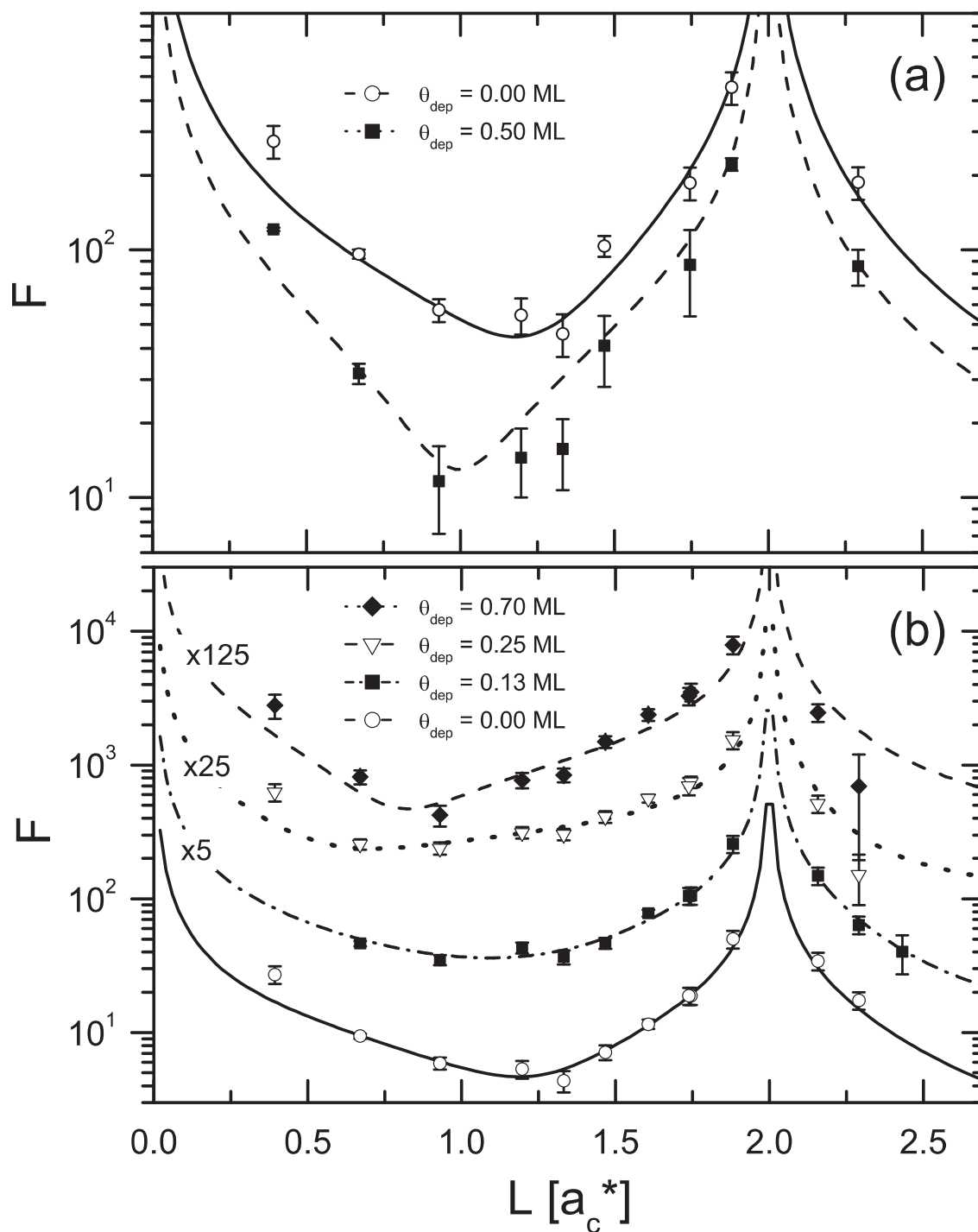
Figure 10.3: Extracted X-ray reflectivity curves (symbols) together with the best fits (lines) after potential steps from 0.55 V, **(a)** to 0.35 V where the Au(100) surface remains unreconstructed, and **(b)** to -0.2 V (i.e. the potential regime of the reconstructed surface). The deposited Au coverages θ_{dep} for which the reflectivity curves were obtained are indicated in the figure. For clarity all CTRs are shifted with respect to each other.

the deposited Au adatoms are incorporated into the Au surface layer (model I), resulting in the rapid growth of domains of the 'hex' reconstruction (figure 10.4b). In this model, reconstructed areas with coverage θ_{dep} and unreconstructed areas with coverage $1 - \theta_{dep}$ are coherently superimposed. The structural parameters of reconstructed and unreconstructed areas were fixed at the values obtained in the previous study by Ocko et al. [80] (table 10.1). Chloride is completely desorbed from the Au surface in this potential regime and does not have to be included in the modeling. As visible in figure 10.3, the CTRs are very well described by this model up to θ_{dep} = 0.25 ML, where the surface is fully reconstructed. Furthermore, the deposited coverage θ_{dep} is approximately $0.25 \cdot \theta_{rec}$ (table 10.1), as it would be expected for this growth model.

At higher coverages, a second model (model II) has to be applied, where reconstructed Au monolayer islands cover the fraction θ of a reconstructed Au surface (figure 10.4c). For θ = 1, the coherent areas are completely covered by a new layer. As in the modeling of the growth at 0.35 V, good agreement between θ_{dep} and the island coverage θ is found up to θ = 0.5 ML. In this case, the fit can be improved by relaxing the spacing parameter of the top layer.

The rapid formation of the reconstruction in the first seconds after the potential jump is in strong contrast to the kinetics of the $(1{\times}1) \rightarrow$ 'hex' transition in the absence of Au electrodeposition. This is illustrated in figure 10.5, where the intensity of the reconstruction peak as a function of time after a potential step from 0.55 V to -0.2 V (i.e., under conditions identical to those of the CTR measurements described earlier) is shown in pure 0.1 M HCl and in 0.1 M HCl containing 0.5 mM $HAuCl_4$. In Au-free solution, the formation of the 'hex' reconstruction is very slow with a characteristic time constant τ of ≈ 1000 seconds. A similar slow $(1{\times}1) \rightarrow$ 'hex' transition was also found in previous electrochemical studies (see chapter 7
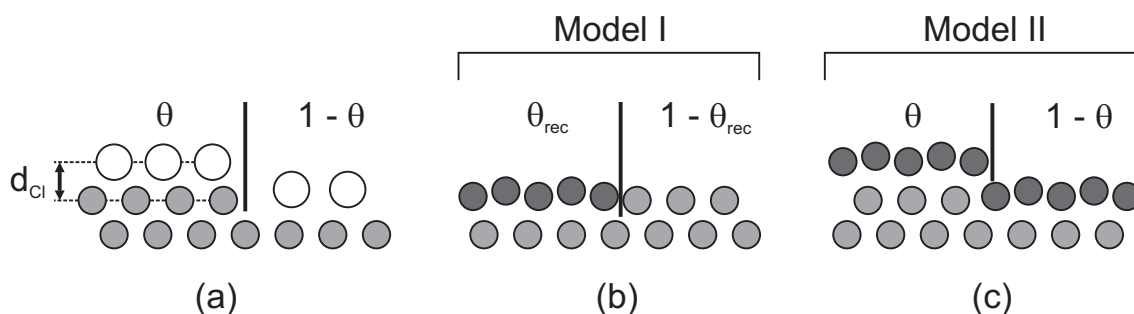
Figure 10.4: Schematic illustration of structural models used for the analysis of the reflectivity data. **(a)** Unreconstructed surface with Au atoms at bulk positions (gray circles) and Cl-adlayer (open circles). θ denotes the surface area fraction covered by the topmost layer. **(b)** Partially reconstructed surface with θ_{rec} denoting the fraction of the reconstructed surface area (Au surface atoms indicated by black filled circles). **(c)** Completely reconstructed surface with reconstructed monolayer islands of coverage θ.

Unreconstructed	Potential	θ_{dep} [ML]	θ [ML]	χ^2
	0.35 V	0.00	0.04 ± 0.04	2.04
		0.50	0.45 ± 0.5	2.72

$d^*_{\mathrm{Au\text{-}Cl}} = 2.07\,\text{Å}$, $d^*_{\mathrm{Au\ Top}} = 2.04\,\text{Å}$, $B^*_{\mathrm{Cl}} = 10\,\text{Å}^2$, $B^*_{\mathrm{Au\ Top}} = 18\,\text{Å}^2$, $\rho^*_{\mathrm{Cl}} = 0.25$

Model I	Potential	θ_{dep} [ML]	θ_{rec} [ML]	χ^2
	-0.2 V	0.00	0.03 ± 0.03	1.04
		0.13	0.44 ± 0.05	1.82

reconstructed areas:　　$d^*_{\mathrm{Au\ Top}} = 2.16\,\text{Å}$, $B^*_{\mathrm{Au\ Top}} = 19\,\text{Å}^2$, $\rho^* = 1.25$

unreconstructed areas:　$d^*_{\mathrm{Au\ Top}} = 2.04\,\text{Å}$, $B^*_{\mathrm{Au\ Top}} = 18\,\text{Å}^2$, $\rho^* = 1$

Model II	Potential	θ_{dep} [ML]	θ [ML]	χ^2
	-0.2 V	0.25	0.03 ± 0.03	2.28
		0.75	0.45 ± 0.05	3.53

$d^*_{\mathrm{Au\ Top}} = 2.16\,\text{Å}$, $B^*_{\mathrm{Cl}} = 19\,\text{Å}^2$, $\rho^* = 1.25$

Table 10.1: Best fit parameters calculated for the models. Displacements are given with respect to the position of the last layer in an ideal bulk termination. Values with $*$ are fixed according to [80] except the values for chloride atoms. $d^*_{\mathrm{Au\ Top}}$ ($d^*_{\mathrm{Au\text{-}Cl}}$) is the distance between the topmost Au layer (the chloride adlayer) and the underlying Au layer. θ_{dep} denotes the deposit amount. θ and θ_{rec} are the coverages of the top Au layer according to model I and model II in figure 10.4, respectively. $B^*_{\mathrm{Au\ Top}}$ and B^*_{Cl} are the Debye-Waller parameters of Au atoms in the topmost layer and of chloride atoms in the adsorbate layer, respectively. ρ^*_{Cl} denotes the chloride coverage in the adsorbate layer. ρ^* denotes the Au coverage in the topmost layer.

and references [73,80,82,90,111,113]). In contrast, in the Au-containing solution the kinetics of this phase transition is two orders of magnitude faster ($\tau = 15s$). In the latter case, the intensity $I(t)$ reaches 90% of the saturation value I_0 after ≈ 40 seconds. The even faster time scale found in the CTR experiments can be partly attributed to ripening of the 'hex' domain distribution, which affects the height of the reconstruction peak, but not the specular CTR. This is demonstrated by angular scans through the reconstruction peak (figure 10.5c), which indicate a decrease in the FWHM of these peaks with increasing time after the potential step. Since ≈ 40 seconds are required for each of these scans (i.e., the peak center in the first scan is recorded ≈ 20 seconds after the potential step), only a qualitative observation of the last stages of this ripening is possible. Nevertheless, a continuous decrease in the FWHM with time could be detected by a series of experiments, where different delay times between the potential step and the start of the scan were employed (figure 10.5d). By multiplication of the peak height I with the FWHM, the integrated peak intensity in azimuthal direction can be obtained, which is a measure of the fraction of the reconstructed surface area. In fact, also the peak broadening along the radial reciprocal space direction would have to be

considered in a similar way to obtain the true integrated peak intensity. However, this effect seems to play a less important role. This correction can largely account for the increase in peak height at $t > 20\,s$. For example, factoring in the $\approx 40\%$ higher FWHM of the data at $t = 20\,s$ as compared to the final value ($\approx 0.9°$), the integrated intensity after this time is 98% of the saturation value. Extrapolating this trend into the inaccessible time regime $t < 20\,s$, the true time constant for the formation of the 'hex' phase could well be in the range of a few seconds, as indicated by the CTR data, and the slower kinetics observed for the reconstruction peak would reflect the 'hex' domain ripening. Indeed, close inspection of figure 10.5b suggests the presence of two time scales, a fast increase up to ~ 4 s, followed by a slow rise in the subsequent 50 s.
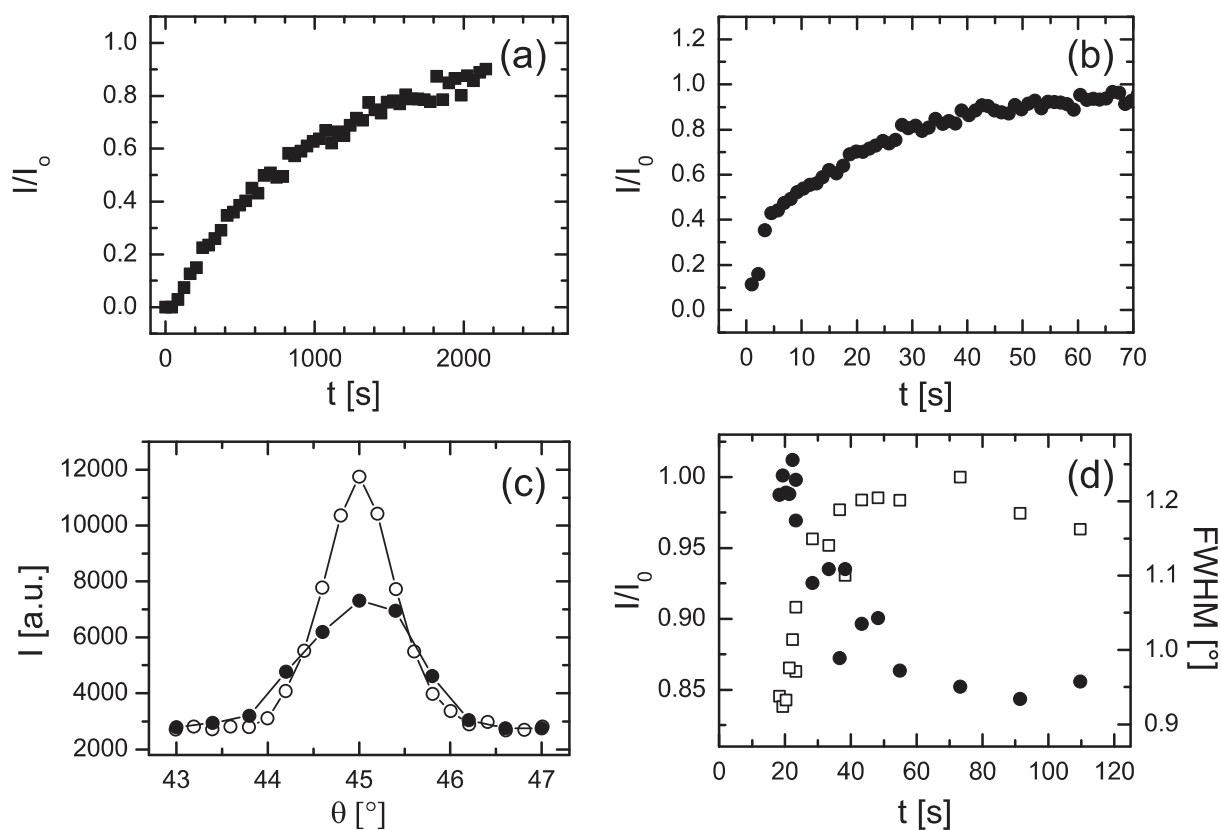
Figure 10.5: **(a,b):** Time-dependent normalized intensity I/I_0 at the position of the in-plane reconstruction peak maximum after potential steps from $0.55\,V$ showing the formation of the reconstruction at -0.2 V (a) in pure 0.1 M HCl (■) and (b) in 0.1 M HCl + 0.5 mM $HAuCl_4$. I_0 corresponds to the saturation value of the completely reconstructed surface. **(c):** In-plane angular scans ($L = 0.1$) through the reconstruction peak after 20 s (●) and 80 s (O) deposition at -0.2 V in 0.1 M HCl + 0.5 mM $HAuCl_4$. **(d):** Normalized time-dependent integrated intensity I/I_0 in azimuthal direction (□) together with the respective in-plane angular FWHM (●) of the data partially shown in (c).

10.5 Comparison with In-plane Data and Growth Mode Studies

The present CTR-analysis in Au-containing solution clearly demonstrates that the first deposit amount of 0.25 ML is directly incorporated into the (initially) unreconstructed topmost surface layer. This finding confirms the growth model in section 9.9.2 which was proposed in order to explain the intensity plateau in anti-Bragg position on the non-specular $(1, 1)$ rod. Furthermore it strongly supports the compression model suggested in section 8.6, i.e. the electrocompressed phase forms subsequent to the initial formation of reconstruction. Thus, in-plane and out-of-plane data are consistent and provide a detailed insight into the growth behavior on unreconstructed and reconstructed Au(100) electrodes, respectively, as well as on the surface phase transition.

10.6 Summary

In the experiment changes in surface structure and morphology of the electrode have been determined during electrochemical growth with subsecond time resolution. Although the method has been applied only to the determination of the specular crystal truncation rod, it can be employed easily well to other points in reciprocal space (e.g., non-specular CTRs), allowing us to further improve the precision of the structure determination. In good agreement with our previous qualitative studies, the data at both studied potentials can be well described by a layer-by-layer growth mechanism, providing confidence in the reliability of this method. In addition, these studies have provided new insight into the mechanisms of electrochemical growth in the potential regime of the hex-reconstructed Au(100) surface. Specifically, CTR and in-plane measurements indicate the formation of a rather disordered 'hex' phase on the (initially unreconstructed) surface within a few seconds, followed by a slower ripening parallel to the layer-by-layer growth of the reconstructed surface. The rapid formation of the reconstruction during Au electrodeposition differs pronouncedly from the very slow kinetics of this process in the absence of Au-species in the solution, suggesting that the barrier for incorporation of the Au atoms into the surface is low and Au surface transport to unreconstructed areas governs the phase transition kinetics. This extended surface model obtained by analysis of the specular CTR includes the influence of coadsorbates and confirms the model inferred from the time-dependent intensity monitored at the anti-Bragg position $(1, 1, 0.1)$ on the non-specular $(1,1)$ rod (cp. section 9.9.2).

11 Electrodissolution of Au(111) Electrodes in Aqueous Chloride Containing Solution

In this chapter the electrodissolution of gold single crystal electrodes in chloride containing solution is discussed. Knowledge about the dissolution mechanism is important for both industrial applications and fundamental science. Even though gold is known to exhibit an excellent chemical stability, it becomes unstable and dissolves in the positive potential region especially in solutions containing complexing agents, such as Cl⁻. This property is used in the modern electronic industry for designing and manufacturing certain thin films and integrated circuits.

Electrodissolution of a metal electrode proceeds positive of the Nernst equilibrium potential and is often considered as the inverse process of electrodeposition. Nevertheless, up to now there are still controversial discussions if both processes are symmetrical, i.e. whether an electrode in an electrochemical system which exhibits a certain growth mode will dissolve in the same mode or not. An experimental or theoretical proof of the latter is extremely difficult due to the complexity of the electrochemical systems and due to high demands on the instrumental method, e.g. a high time resolution. Ideally the deposition and the dissolution behavior have to be investigated within one experiment, i.e. on the same electrode and in the same electrolyte, in order to ensure identical conditions. Simultaneously it is desired that both, the deposition and dissolution processes, are initiated from an originally perfectly flat surface with wide terraces and consequently a low degree of surface roughness. This is in particular difficult as it means that the electrochemical system either has to exhibit a step-flow growth (dissolution) regime at which the surface is able to recover after previous growth (dissolution) in potential regimes with 3D- or imperfect layer-by-layer growth (dissolution) or the electrode surface has to be re-prepared for each potential step experiment which in turn interrupts the experiment and which is time consuming.

Considering the involved atomistic processes there are various analogies between electrodeposition and electrodissolution. In the entire potential regime of cathodic electrodeposition metal atoms are homogeneously deposited onto the crystal surface, followed by surface transport and either nucleus formation or incorporation at kink sites as a final step. In this case the growth mode depends on the deposition rate (adatom flux), on the nucleation rate, on the attachment rate at step edges (incorporation) and on the electrode potential. The latter determines the electric field at the interface and by this the intralayer transport. Furthermore the potential alters the density of anionic adsorbates or induces surface reconstruction which influences the interlayer transport, e.g. due to a different height of the Ehrlich-Schwoebel barrier. Each of these atomic processes has an analog in the electrodissolution process if monoatomar vacancies are considered as counterpart to adatoms. At low anodic overpotentials dissolution predominantly takes place heterogeneously at localized crystal sites where surface atoms are more loosely bonded to the crystal due to a lower coordination number. These sites are kink sites, terrace steps, terrace corners, surface defects and crystal inhomogeneities. Thus the dissolution rate depends in general on the availability of those sites and on their nucleation rates. Due to this behavior step-flow dissolution is often found close to the Nernst potential. In contrast to step-flow growth the according dissolution mode does

not necessarily have to involve surface transport of vacancies from the center of terraces to the step edges. However, migrating vacancies may contribute to the dissolution at step edges provided that they are formed and that they are sufficiently mobile. According to theoretical calculations carried out for Ag(111) surfaces [169] the vacancy step-attachment barrier on (111) oriented surfaces is supposed to be much smaller than the vacancy terrace diffusion energy and thus the incorporation of vacancies into step edges should be favorable in analogy to the incorporation of adatoms at step edges. At high anodic overpotentials many electrochemical systems exhibit a different dissolution behavior. In addition to the step edge sites mentioned above homogeneous nucleation of stable vacancy clusters and subsequent dissolution in the center of terraces is found. This mechanism requires that atoms leave the crystal surface from sites with higher coordination number, i.e. that vacancies are formed on the terraces. Principally, these vacancies are either immobile or they diffuse over the surface. Vacancy diffusion barriers on low-index noble metal surfaces of Cu, Ag and Au have been calculated by a modified analytical embedded-atom method (MAEAM) [170]. According to Zhang et al. the vacancy formation energy (0.494 eV) on Au(111) is predicted to be much lower than the formation energy of an adatom (0.674 eV). On the other hand the vacancy migration energy (0.446 eV) was calculated to be about four times larger than the adatom migration energy (0.112 eV), i.e. the mobility of vacancies is significantly lower. The scenario is more complex at electrochemical interfaces where species in the solution phase affect the migration energies. During the migration process vacancies either encounter and form stable vacancy clusters (nucleation) or they reach step edges. The latter configuration, i.e. vacancies in the vicinity of step edges, has been theoretically analyzed by surface-embedded atom method (SEAM) for low-index Ag surfaces [169] and the existence of a vacancy Ehrlich-Schwoebel (ES_v) barrier was suggested. Haftel determined large ES_v barriers (> 0.2 eV) for vacancies ascending step edges which are enhanced over those of adatoms. Experimental evidences for an ES_v barrier have been as well reported [171, 172]. In analogy to a high adatom ES barrier promoting 3D growth, a high vacancy ES barrier is supposed to promote 3D vacancy island growth, i.e. the formation of surface pitches, as it was for example observed in reference [172]. Vacancy cluster formation and growth of vacancy islands results in an enhanced dissolution rate. In this case the dissolution follows either the multilayer (large ES_v) or the layer-by-layer mode (small ES_v) dependent on the migration energy and the step edge energy. Thus, nucleation and growth of vacancy islands resembles island growth in the deposition experiments. In contrast to electrodeposition, where interlayer transport of adatoms takes place from the upper to the lower terrace, layer-by-layer dissolution requires an uphill transport of vacancies at step edges. In the case of electrodissolution at high anodic overpotentials additional influence on the dissolution rate may arise from the solution side. If complexation is involved the transport of the complexing agent from the solution bulk to the electrode surface might become the rate determining step. This resembles the process of diffusion-limited electrodeposition.

In summary, the growth or dissolution mode strongly depends on energy barriers for adatom and vacancy terrace migration and on the heights of the according ES barriers. Both quantities are usually significantly different for adatoms and vacancies. Furthermore, the deposition or dissolution rates may dependent on the surface site (e.g. different rates for direct depo-

sition/dissolution at step edges and deposition/dissolution in the center of terraces). For these reasons the processes of deposition and dissolution are not necessarily symmetrical, i.e. a certain growth mode may be observed in the deposition regime while it is absent in the dissolution regime. However, due to the complicated nature of interatomic forces the dominance of adatom or vacancy transport is hard to predict in advance and varies from surface to surface. Besides of different energy barriers for adatoms and vacancies the processes of electrodeposition and electrodissolution may result in different shapes of islands and vacancy islands. The unreconstructed Au(111) surface is a nice example which exhibits isotropic homoepitaxial growth [14] but anisotropic dissolution [16,17]. This asymmetry may as well results in an asymmetry of growth and dissolution modes.

11.1 Literature Review

Most studies about electrodissolution were carried out for polycrystalline metals and semiconductors by electrochemical methods. Well studied systems are for example iron, steel, copper, gold and GaAs dissolution because of the technological importance of those materials. Fundamental studies on oriented, single crystal surfaces were mainly carried out by scanning probe techniques and therefore predominantly in potential regimes where the dissolution process is slow, i.e. close to the Nernst equilibrium potential. Compared to gold single crystal electrodes, anodic dissolution of low-index copper single crystal electrodes in Cl^- containing solution has been investigated in great detail [173–176]. Further dissolution experiments were reported on iodine covered, single crystalline palladium [177], silver [178] and nickel [179] electrodes, on sulfur covered nickel electrodes [180] and on platinum electrodes in perchloric acid solution [181]. In most of the latter systems the dissolution process was found to proceed via step-flow mode or layer-by-layer mode. More recently, dissolution studies on gold single crystal electrodes were reported which were performed by electrochemical methods [15] as well as by scanning probe methods [16,17].

Electrochemical STM and AFM are capable to monitor the surface morphology with comparatively low time resolution, i.e. a series of images may indicates a certain growth (dissolution) behavior but real time observations are impossible. Consequently each part of a single image reflects a different stage in the deposition/dissolution process making it especially difficult to obtain information about the growth (dissolution) mode at high deposition (dissolution) rates. Besides of the limited time-resolution scanning probe techniques have more general drawbacks for the investigation of electrodeposition (electrodissolution). On the one hand the deposition (dissolution) rate below the STM tip (AFM cantilever) is typically lower than without the tip due to tip shading effects. Therefore the observed growth (dissolution) mode may differs from the mode present under otherwise identical conditions in absence of the tip. On the other hand a fourth electrode is introduced into the electrochemical system by the metal tip (cantilever) which might influence the deposition (dissolution) process as well. However, surface sensitive X-ray scattering allows to overcome these restrictions. The previous chapters and the following sections demonstrate that the growth (dissolution) process can be probed with high time resolution and without exerting influence on the deposition (dissolution) process. Moreover, compared to scanning probe techniques X-ray scattering

averages over comparatively large surface areas providing more accurate information about the growth (dissolution) mode while it is for example difficult to distinguish layer-by-layer and multilayer growth (dissolution) in case of the former methods which image surface areas of some $1000\,nm^2$ size only. As stated above the local growth does not necessarily need to reflect the growth mode which dominates electrodeposition (electrodissolution) on the total electrode surface. To my knowledge no real-time investigations of layer-by-layer dissolution on single crystal electrodes in solution have been reported up to now, neither for gold nor for other metal surfaces. However, in UHV an interesting real-time SXS study of Argon ion erosion of Au(111) revealed quasi-layer-by-layer removal at sample temperatures of 90-220 °C [2]. This was confirmed by STM studies on ion irradiated Au(111) surfaces which as well suggested a layer-by-layer sputtering regime [182, 183].

Electrodissolution of polycrystalline gold electrodes in chloride containing solutions has been investigated in great detail by various electrochemical methods. These studies provided a fundamental understanding of the involved electrochemical processes and the results will be discussed briefly in section 11.1.1. Of particular interest is a recent STM study of Au(111) electrodissolution carried out by Ye and coworkers [16]. This study allows to compare present results with previous observations and will be summarized in the sections 11.1.2 and 11.1.3. Furthermore, in section 11.1.4, we will introduce the well-known Avrami model which is able to describe the current arising from the deposition of a single monolayer. An appropriate modification of this model will later on allow us to obtain more detailed information about the dissolution process.

11.1.1 Electrodissolution Process of Gold Electrodes in Cl⁻ Containing Solutions

The electrodissolution experiments were performed on Au(111) single crystal surfaces in contact with a mixture of $50\,mM$ H_2SO_4 and $5\,mM$ HCl. If the electrode potential is stepped to potentials more positive than the Nernst equilibrium potential then the Au(111) electrode starts to dissolve. The sulfuric acid increases the electrolyte conductivity and the sulfate ions support the oxidation of metallic gold atoms at the electrode surface. In subsequent reaction steps a stable gold-chloride complex is formed. Heumann and Panesar proposed in 1965 that $1\,e^-$ and $3\,e^-$ oxidation reactions are involved in the gold dissolution from chloride containing solutions [184] according to the reactions

$$Au + 4Cl^- \longrightarrow AuCl_4^- + 3e^- \tag{11.1}$$
$$Au + 2Cl^- \longrightarrow AuCl_2^- + 1e^- \tag{11.2}$$

For potentials $> 1.0\,V_{NHE}$ the forward reactions of (11.1) and (11.2) are favored against the back reactions of Au-deposition. Dissolution is possible only due to complexation as can be seen by the standard potential of the reaction

$$Au^+ + e^- \longleftrightarrow Au \tag{11.3}$$

which is with $1.680\,V_{NHE}$ to $1.830\,V_{NHE}$ even more positive than the potential for oxygen evolution ($1.23\,V_{NHE}$). Thus, in the potential regime accessible with the employed hanging

meniscus cell, every dissolved Au atom would be immediately cathodically redeposited without a complexing agent in the solution. More detailed gold dissolution studies were performed by Gaur and Schmid in $0.1\,M\,HClO_4$ containing 0.2 - $10\,mM\,KCl$ [185]. Significant dissolution was found for potentials between $1.0\,V$ and $1.2\,V$ versus SCE, while for even higher anodic potentials the dissolution was strongly hindered by passivation through gold oxide formation. It was suggested by the authors that gold dissolution and oxide formation are competitive reactions in the positive potential region. Hence, gold is supposed to dissolve as $AuCl_4^-$ only at oxygen-free sites on the electrode surface. A more concentrated Cl^- containing solution was found to destroy the passivation layer in a similar manner as it was observed for stainless steel and nickel in the early 60's of the last century. Since this time several dissolution studies have been carried out by different instrumental methods for polycrystalline Au electrodes in Cl^- containing electrolytes. Rotating ring-disk electrode measurements [186–189], coulometry and atomic absorption spectroscopy [190] and in-situ surface-enhanced Raman spectroscopy (SERS) [191] propose the existence of Au dissolution according to both reaction types mentioned above (11.1 and 11.2). All these studies have in common that reaction 11.2 is found to proceed negative of a critical potential E_c, while reaction 11.1 is supposed to proceed positive of E_c. Obtained values for E_c vary in a wide potential range between $0.8\,V_{SCE}$ and $1.1\,V_{SCE}$ partly related to different experimental conditions. In contrast to the aforementioned studies, an electrochemical quartz crystal microbalance (EQCM) study was employed on the dissolution of single crystal Au(111) electrodes and demonstrated that gold dissolves through a $3\,e^-$ oxidation process in a wide potential region without any evidence for the $1\,e^-$ dissolution process [15]. This EQCM study which also includes cyclic voltammetry provides fundamental information about the dissolution process and will be discussed in more detail in section 11.3. Nevertheless, additional gold-chloride complexes may be formed as intermediate reaction products. In-situ Raman spectroscopic studies identified $AuCl_{ads}^-$ and $[AuCl_2]_{ads}^-$ complexes being involved in the dissolution process [192, 193].

11.1.2 Layer-by-Layer Dissolution of Au(111) Electrodes

The existence of layer-by-layer dissolution of Au(111) electrodes in Cl^- containing solution has been previously demonstrated by in-situ STM investigations [16, 17]. Figure 11.1 shows a series of STM images of an Au(111) electrode in $0.1\,M\,HClO_4 + 1\,mM\,Cl^-$ obtained by Ye et al. for different electrode potentials. The first image (figure 11.1a) was taken at $0.8\,V_{RHE}$ which is more cathodic than the Nernst potential (region 1 in figure 11.4b), i.e. no dissolution takes place and the surface is stable. Wide terraces and monoatomic step lines are seen with sporadic small pits as indicated by circles. When the electrode potential was swept to $1.27\,V_{RHE}$, belonging to the active dissolution regime (region 2 in figure 11.4b), dissolution of the Au(111) surface sets in as visible in figure 11.1b. Gold atoms leave the terraces at the step edges or from preexisting surface vacancy clusters resulting in dissolution of the former and growth of the latter. $1.27\,V_{RHE}$ is close to the Nernst potential (left border of region 2) where the dissolution process is slow and where it can be followed by STM with reasonable time resolution. Images of the surface after $6\,min$ and $40\,min$ at $1.27\,V_{RHE}$ are shown in the figures 11.1c and 11.1d, respectively. It can be clearly seen that terraces which were present at $0.8\,V_{RHE}$ collectively dissolved after $40\,min$ at $1.27\,V_{RHE}$ indicating step-flow dissolution.
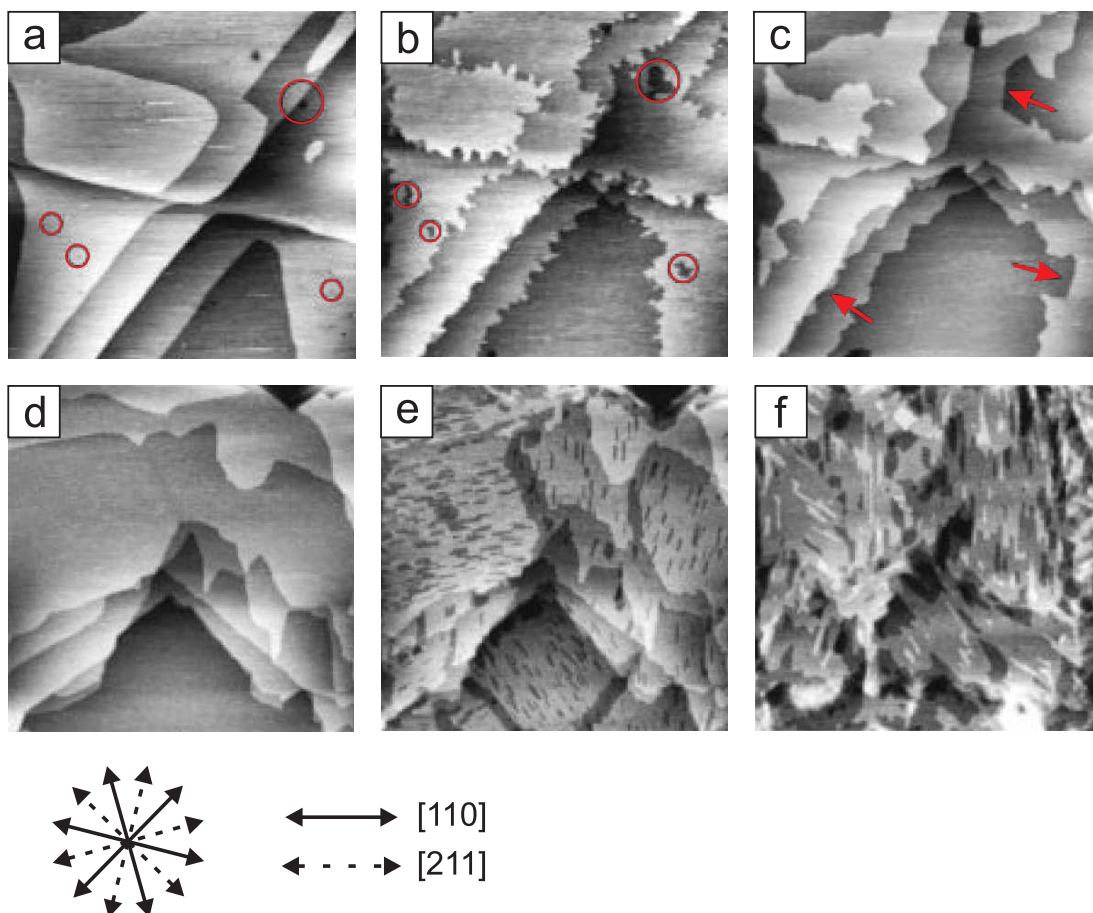
Figure 11.1: Sequence of in-situ STM images ($1{\times}1\,\mu m^2$, $E_{tip} = 1.2\,V$, $i_t = 5\,nA$) of an Au(111) electrode surface in $0.1\,M$ $HClO_4$ solution containing $1\,mM$ Cl^-: a) stable surface at $0.8\,V_{RHE}$, b) surface after a potential sweep from $1.09\,V_{RHE}$ to $1.27\,V_{RHE}$, c) after 6 min at $1.27\,V_{RHE}$, d) after 40 min at $1.27\,V_{RHE}$, e) after a second potential step from $1.27\,V_{RHE}$ to $1.36\,V_{RHE}$ and f) 1 - 2 min after scan e at $1.36\,V_{RHE}$. The compass in the lower left indicates the orientation of the surface. (from ref. [16])

Furthermore the orientation of step edges changed. While in the beginning at $0.8\,V_{RHE}$ the step edges were predominantly oriented along the [110] direction, they are oriented along the [211] direction after dissolution of the topmost monolayer. It was proposed by Ye that the dissolution proceeds anisotropically. Step lines along the [211] direction exhibit the highest chloride adatom concentration. Based on this finding the lateral interaction between the adsorbed chloride and gold was considered to stabilize atom rows along the [211] direction. This results in a lower etching rate in [211] direction and explains the fractal shape of step edges in figure 11.1b. Interestingly the same mechanism has been observed by Suggs and Bard for Cu(111) dissolution in aqueous chloride containing solution [173]. Anisotropic dissolution is also known for other surface orientations of gold, e.g. for the Au(100) surface [17]. If the electrode potential is stepped from $1.27\,V_{RHE}$ to $1.36\,V_{RHE}$, i.e. towards higher anodic overpotentials in the active dissolution regime (close to peak I in

figure 11.4b), the dissolution process significantly changes as shown in figure 11.1e. Now the dissolution is not restricted to kink sites but also takes place on the terraces. Surface vacancy nuclei are homogeneously formed and they anisotropically grow in size along the [211] direction. Image 11.1f was taken about 1 - 2 min subsequent to image 11.1e at the same electrode potential. The topmost monolayer which was observed in image 11.1e is almost completely dissolved and dissolution of the next monolayer already started. This behavior indicates layer-by-layer dissolution. On the basis of the STM images a dissolution rate of approximately $0.34\,ML\,min^{-1}$ is estimated at $1.36\,V_{RHE}$. Finally it should be noted that even at the potential $1.0\,V_{RHE}$ near the chloride order/disorder transition, i.e. more cathodic than the Nernst potential, nucleation of kink sites and very slow dissolution was observed as indicated by serrated step edges. According to reference [194] this effect of etching or migration of atoms at step-edges may be induced by the preferential binding of chloride on a step edge.

11.1.3 Nucleation Mechanism of Au(111) Dissolution

Figure 11.2 shows an STM image of a Au(111) electrode in 0.1M $HClO_4$ + 1 mM HCl containing solution which was recorded by Ye et al [16]. A surface area of $1{\times}1\,\mu m^2$ was rastered by horizontal line scans from the top to the bottom. The whole image was acquired within 50 seconds. From the top of the image to the red line the electrode potential has been kept at $+1.27\,V_{RHE}$ where the dissolution proceeds slowly via step-flow mode. No vacancy cluster or vacancy islands on terraces are observed in this part of the image. At the time marked by the red line, the potential was stepped to $+1.36\,V_{RHE}$ in the layer-by-layer dissolution regime. In the onset of the experiment vacancy clusters nucleate and vacancy islands grow. It is obvious that the density of vacancy cluster and vacancy islands increases with time, i.e. in successional scan lines. This clearly indicates that the nucleation process is progressive and that the number of nuclei is a function of time. Furthermore, it can be seen that the growth of vacancy islands is anisotropic. Nevertheless, the vacancy growth is not restricted to one-
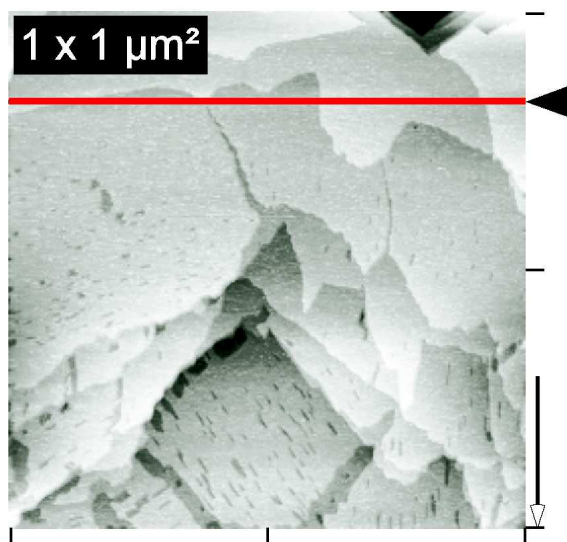
Figure 11.2: In-situ STM image of Au(111) in $0.1\,M$ $HClO_4$ solution containing $1\,mM$ Cl^-. The red line marks the time when the electrode potential was stepped from $+1.27\,V_{RHE}$ in the step-flow dissolution regime to $+1.36\,V_{RHE}$ in the layer-by-layer dissolution regime. At $+1.36\,V$ nucleation of stable vacancy clusters is observed. The density of nuclei increases with time in downward scan direction clearly indicating a progressive nucleation mechanism. The STM image was taken in 50 s. (from ref. [16])

dimensional lines which have the width of a single atom but moreover multiple atom wide, rectangular shaped vacancy islands are observed with an approximate width to length aspect ratio of 1:5. As will be seen below the experimental current-time transients are well fittable by a model function based on two-dimensional, cylindrically growing nuclei with progressive nucleation mechanism while attempts to fit the data with models of different dimensionality or nucleation mechanism were unsuccessful. For this reason we focus on two-dimensional growth of the nuclei in the following.

11.1.4 The Avrami Model

In the layer-by-layer regime the dissolution proceeds via nucleation of stable vacancy clusters and lateral one-dimensional or two-dimensional growth of vacancy islands in addition to the dissolution at step edges. At a certain point the vacancy islands begin to overlap. In order to derive the current density $j(t)$, which depends on the total rim of vacancy islands, the shape of the vacancy islands and the influence of the overlap have to be considered. In this section the discussion will be confined to an isolated monolayer. A first derivation for the analogous case of homoepitaxial deposition has been presented in 1963 by M. Fleischmann and H.R. Thirsk [195]. For a growing **s**ingle and isolated **n**ucleus (i.e. for a growing, isolated island) the current $i_{sn}(t)$ into a surface area $S_{sn}(t)$ is given by

$$i_{sn}(t) = \frac{nF\rho h}{M} \cdot \frac{dS_{sn}(t)}{dt} \tag{11.4}$$

where n is the electron transfer number, F is the Faraday constant, ρ is the mass density of the deposit (g/cm^3), h is the layer height (cm) and M is the molecular weight (g mol^{-1}). The surface area $S_{sn}(t)$, given in cm^2, depends on the shape of the growing nucleus. For the following it is convenient to express the surface area in reference to the unit area. If S_0 is the total surface area, then the dimensionless fraction per unit area being covered by the nucleus is given by

$$S(t) = \frac{S_{sn}(t)}{S_0} \tag{11.5}$$

In addition to $S(t)$ the simultaneous growth of nuclei has to be regarded. Under the presumption that there is a uniform probability with time of converting sites into nuclei the time-dependent number $N(t)$ of nuclei (normalized to S_0 and in units of cm^{-2}) is obtained by the expression

$$N(t) = N_0 \cdot [1 - \exp(-At)] \tag{11.6}$$

where N_0 is the total number of possible nucleation sites (cm^{-2}) and A is the nucleation rate constant (s^{-1}). This equation has two limiting cases dependent on the value of A. If A is assumed to be large then the number of nuclei N is approximated by $N \approx N_0$ and all sites are converted to nuclei instantaneously, which is termed as instantaneous nucleation. However, if A is assumed to be small, then a Taylor expansion of the exponential function yields $N(t) \approx N_0 \cdot A \cdot t$. In this case the nucleation is said to be progressive. The current density $j_{ex}(t)$ results from the two parallel processes of nucleation and nuclei growth and is given by the convolution integral

$$j_{ex}(t) = \int_0^t i_{sn}(u) \left(\frac{dN(\tau)}{d\tau} \right)_{\tau=t-u} du \tag{11.7}$$

where the overlap effect has been still ignored.

In the succeeding stages of deposition (dissolution) the measured current deviates from the one inferred via equation 11.7 due to the overlap of (vacancy) islands. While in real systems the island growth stops at fronts where two islands impinge on each other the island growth continues in the model. As a consequence equation 11.7 predicts too high currents. The overlap effect was first theoretically analyzed by Avrami who developed an appropriate mathematical description [196–198]. If the probability of finding a nucleus growing in two or in three dimensions is uniform in space or over a surface, respectively, and the growth is not limited by the area S_0 of the sample then the overlap problem can be solved exactly for a number of simple cases as demonstrated in [195]. According to the Avrami theorem the electrode area $S(t)$ being covered by overlapping nuclei, is connected with the extended, non-overlapping area $S_{ex}(t)$ by the expression

$$S = 1 - \exp\left(-S_{ex}\right) \tag{11.8}$$

This relationship has two limiting cases. For short times t the nuclei do not overlap and $S_{ex} \ll 1$. Then the expansion of the exponential function yields $S \cong S_{ex}$. However, for large t the extended area tends to infinity, $S_{ex} \to \infty$, and the covered area tends to unity, $S \to 1$. The whole surface is covered by one monolayer.

For example, the instantaneous and progressive nucleation of two-dimensional, cylindrically growing nuclei results in the following extended areas

$$\text{(instantaneous)} \quad S_{ex}(t) \quad = \quad N_0 \pi r^2(t) = \frac{\pi N_0 k^2 M^2}{\rho^2} t^2 \tag{11.9}$$

$$\text{(progressive)} \quad S_{ex}(t) \quad = \quad \frac{A N_0 \pi k^2 M^2}{3\rho^2} t^3 \tag{11.10}$$

where k is the lateral growth rate $(\mathrm{mol\,cm^{-2}\,s^{-1}})$ and $r(t) = Mkt/\rho$ is the average radius of the nuclei [195]. The time-dependent current density $j(t)$ is given by the general expression

$$j(t) \quad = \quad n \cdot e_0 \cdot \frac{dN_{at}(t)}{dt} = \frac{n \cdot h \cdot \rho \cdot F}{M} \cdot \frac{dS(t)}{dt} \tag{11.11}$$

$$= \quad \frac{n \cdot h \cdot \rho \cdot F}{M} \cdot \frac{dS_{ex}(t)}{dt} \cdot \exp[-S_{ex}(t)] \tag{11.12}$$

$$= \quad j_{ex}(t) \cdot \exp[-S_{ex}(t)] \tag{11.13}$$

where e_0 is the elementary charge and

$$N_{at}(t) = \frac{h \cdot \rho \cdot N_A}{M} \cdot S(t) \tag{11.14}$$

is the number of atoms in the growing layer $(\mathrm{cm^{-2}})$ with N_A being the Avogadro constant.

11.2 Out-of-plane Scattering of Au(111) Electrode Surfaces

As convenient coordinate system for the X-ray measurements on Au(111) electrodes a hexagonal unit cell has been chosen with two real space lattice vectors $\vec{a}$ and $\vec{b}$ within the surface plane and a third lattice vector $\vec{c}$ along the surface normal. The lengths of $\vec{a}$ and $\vec{b}$ are equal to the gold nearest-neighbor atomic distance, i.e. $|\vec{a}| = |\vec{b}| = 2.885\text{Å}$, while the length of the third vector is $|\vec{c}| = 7.067\text{Å}$. The angle γ between $\vec{a}$ and $\vec{b}$ is 120°. Figure 11.3a depicts the chosen real space unit cell. According reciprocal space vectors have the lengths $a^* = |\vec{a}^*| = |\vec{b}^*| = 2.52\,\text{Å}^{-1}$ and $c^* = |\vec{c}^*| = 0.89\,\text{Å}^{-1}$, respectively, with $\gamma^*(\vec{a}^*, \vec{b}^*) = 60°$.

The scattering vector $\vec{q}$ is represented in terms of the Miller indices (h, k, l) where

$$\vec{q} = h \cdot \vec{a}^* + k \cdot \vec{b}^* + l \cdot \vec{c}^* \tag{11.15}$$

Along the (111) surface normal direction an ideal fcc crystal is composed of hexagonally close-packed layers separated by $|\vec{c}|/3$ and it follows the stacking sequence ABCABC.... Hence, for the chosen unit cell the atomic basis contains three atoms with translational vectors $\vec{t}_1 = (0,0,0)$, $\vec{t}_2 = (1/3, 2/3, 2/3)$ and $\vec{t}_3 = (2/3, 1/3, 1/3)$. This definition gives rise
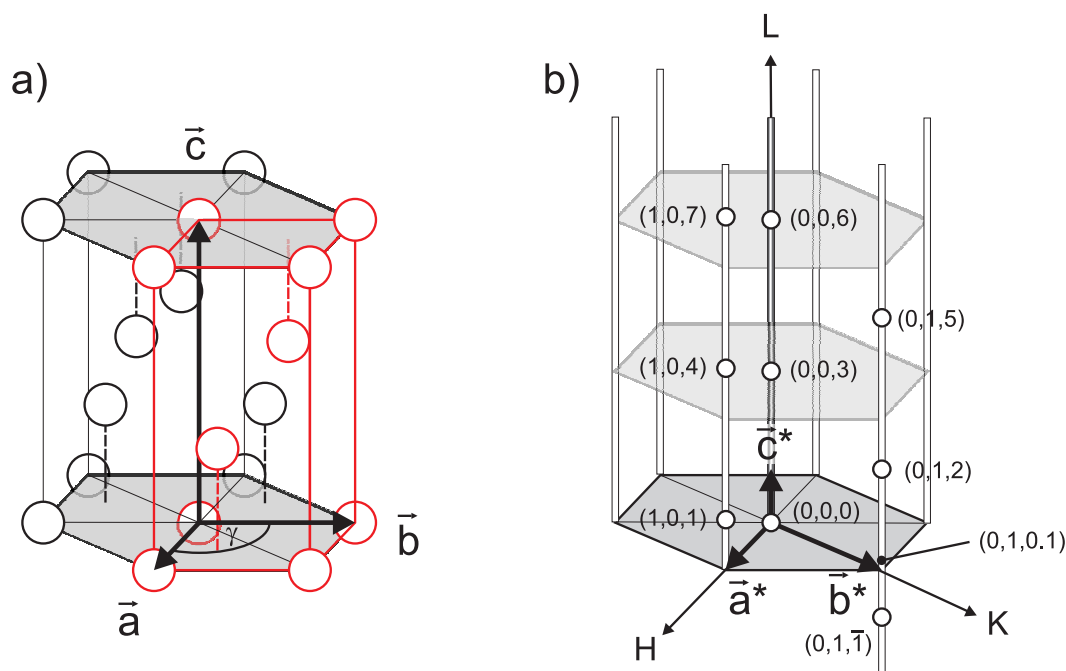
Figure 11.3: a) Hexagonal gold unit cell employed in the SXS measurements. b) Out-of-plane scattering of a Au(111) surface associated with the hexagonal gold unit cell. For clarity only allowed Bragg reflections on the specular (0,0) rod and the non-specular (1,0) and (0,1) rods are shown. Investigations of Au(111) electrodissolution have been carried out at the reciprocal space position $(0,1,0.1)$ which is close to the anti-Bragg position $(0,1,0.5)$.

to the following selection rules for allowed Bragg reflections

$$h + 2k + 2l = 3n_1 \tag{11.16}$$
$$2h + k + l = 3n_2 \tag{11.17}$$

where n_1 and n_2 are natural numbers and which both have to be fulfilled for the same reflection. Figure 11.3b shows a reciprocal space map of the out-of-plane scattering observed for Au(111) electrodes according to the defined real space unit cell. For clarity of the graph only allowed Bragg-reflections on the specular (0,0) rod and the two non-specular (1,0) and (0,1) rods are shown. Superstructure CTRs, which are present in case of surface reconstruction, have not been depicted since the Au(111) electrode surface is unreconstructed in the anodic potential regime of dissolution. Measurements of the electrodissolution process have been carried out at the reciprocal space position $(0\,,1\,,0.1)$ which is situated on the (0,1) rod as marked in figure 11.3b. This position is close to the anti-Bragg position $(0\,,1\,,0.5)$ and therefore very sensitive to effects of surface disorder. In the past surface sensitive X-ray scattering provided detailed information about the surface structure of Au(111) electrodes in Cl$^-$ containing solutions [152,199].

All dissolution experiments were carried out at the European Synchrotron Radiation Facility in Grenoble. An X-ray energy of $E = 22.3$ keV has been used. The footprint size of 2.45×0.4 mm^2 on the sample is defined by presample slits with a horizontal aperture of 0.4 mm and a vertical aperture of 0.01 mm in combination with an incident angle $\alpha_i = 0.234°$ of the X-ray beam. The latter was chosen to be larger than the critical angle $\alpha_c(22.3$ keV$)$ = 0.206° in order to avoid additional effects arising from surface mosaicity. Both detector slits were opened by 3 mm in horizontal and vertical direction, respectively.

11.3 Electrochemical Characterization

Figure 11.4 shows two cyclic voltammograms of a Au(111) electrode in 50 mM H$_2$SO$_4$ + 5 mM HCl solution recorded a) in the double layer regime and b) in the dissolution and passivation regime while the electrochemical system was mounted on the X-ray goniometer. In the double layer regime (figure 11.4a) four peaks are recognizable, two at 0.195 V and 0.725 V in the anodic sweep and two at 0.140 V and 0.723 V in the cathodic sweep. The anodic peak at 0.195 V is an intrinsic characteristic of the Au(111) electrode related to the lifting of the reconstructed ($\sqrt{3} \times 23$) surface [73,152,200,201]. Accordingly the cathodic peak at 0.140 V is related to the reverse process of reconstruction formation. The anodic peak at 0.725 V belongs to a disorder/order transition of adsorbed chloride which forms an ordered, incommensurate superstructure at more positive potentials [199]. The reverse transition occurs in the negative sweep and results in the current peak at 0.723 V. With increasing Cl$^-$ concentration all four peaks shift towards more negative potentials (0.073 V per decade Cl$^-$ concentration). In the more positive potential regime (figure 11.4b) dissolution of the Au(111) electrode and the formation of gold oxide (AuO) proceed according to the reactions

$$Au + H_2O \leftrightarrow AuOH + H^+ + e^- \tag{11.18}$$
$$AuOH \leftrightarrow AuO + H^+ + e^- \tag{11.19}$$

Initially oxidation takes place with the adsorption of OH$^-$ (equation 11.18), followed by a turnover process (equation 11.19), which leads to the formation of a two-atom thick oxide layer [202, 203]. Gold oxide formation on Au(111) and Au(100) electrodes in 50 mM H$_2$SO$_4$ solution without chloride has been studied in detail by in-situ SXS [204]. A comprehensive review of electrochemical oxide film formation on Au electrodes has been published by Conway [205].

The competition of electrodissolution and surface oxidation is a complex process which has been studied in detail by electrochemical quartz crystal microbalance (EQCM) for Au(111) electrodes [15]. The cyclic voltammogram in figure 11.4b was recorded in the present electrochemical system (i.e. in the hanging meniscus cell) containing 50 mM H$_2$SO$_4$ and 5 mM HCl and agrees perfectly with measurements of Ye et al. performed in 0.1 M HClO$_4$ + 10 mM HCl at identical sweep rates of 10 mV/s. We will discuss the present data on the basis of the EQCM study results. Ye divided the potential range in several regions which are denoted by region 1 to region 5 in figure 11.4b. In region 1 no anodic current is observed, i.e. neither dissolution nor gold oxidation takes place. The gold electrode dissolves in region 2 which results in a significant increase in electrochemical current. The dissolution process had been proven with EQCM by the simultaneous decrease of electrode mass. Two peaks are observed in the anodic sweep, denoted by I and II. Peak I at 1.14 V is related to Au dissolution. Peak II at 1.23 V belongs to region 3 and indicates the incipient passivation of the surface by gold oxide formation (reaction 11.19). Consequence of this passivation is a strong decrease in the electrochemical current at even higher anodic electrode potentials. Processes in this potential regime are particularly complicated as passivation and dissolution occur at the same time until the electrode surface is completely passivated. In the onset of a subsequent cathodic sweep, initiated from 1.3 V, region 4 is found. In absence of Cl$^-$ in the solution or for very low
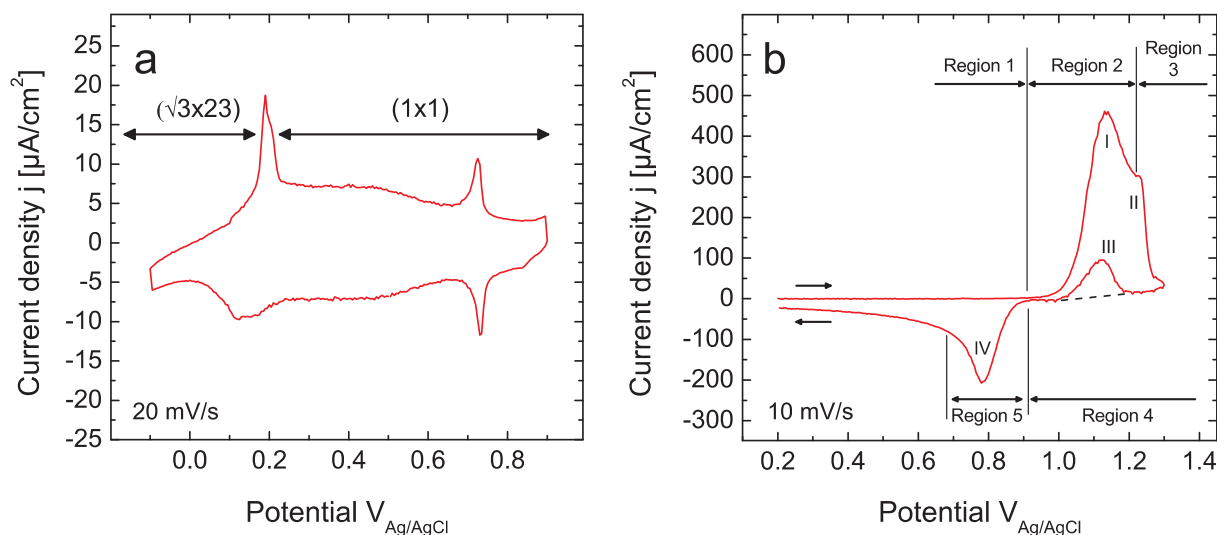
Figure 11.4: Cyclic voltammograms of Au(111) in 50 mM H$_2$SO$_4$ + 5 mM HCl. Shown are a) the double layer regime and b) the dissolution regime at more positive potentials.

chloride concentrations (≤ 1 mM) region 4 is featureless, i.e. no additional current (and no mass decrease) is observed as indicated by the dashed line in figure 11.4b. It was concluded that once a full monolayer oxide is formed the dissolution is completely inhibited. However, for higher chloride concentrations (≥ 1 mM) the shape of region 4 has been found to strongly depend on the potential sweep rate. In particular if the sweep rate is as low as 10 mV/s then an additional broad anodic peak, denoted as peak III, appears. This peak at 1.12 V is associated with a large electrode mass decrease as measured by EQCM and indicates that the gold oxide film is unstable and partly destroyed by a concentrated Cl⁻ solution. Hence the anodic peak is related to a further dissolution of the Au(111) electrode. In region 5 a broad cathodic peak, denoted as peak IV, is found. This peak at 0.78 V is associated with a mass increase of the electrode and is ascribed to the reduction of the dissolved gold species, i.e. it is due to the redeposition of previously dissolved gold. Based on the onsets of dissolution and redeposition the Nernst potential is located at approximately 0.95 V.

The accessible potential regime for dissolution studies, i.e. region 2, is comparatively narrow and ranges from the onset of Au dissolution at about 0.95 V to the onset of gold oxide formation at about 1.2 V for the chosen electrolyte in good agreement with the studies of Gauer and Schmid [185] and with rotating disc electrode studies of Herrera et al. [189]. It should be mentioned that this 250 mV broad regime is much narrower than the potential regime accessible for deposition studies which extends over several hundred millivolt.

11.4 Layer-by-layer Dissolution

In order to investigate the process of electrodissolution in-situ and in real time potential step experiments were performed and current-time transients were recorded. For this the Au(111) electrode was first kept at a potential of 0.5 V which results in a reasonable smooth surface as indicated by a comparatively high X-ray intensity at the reciprocal space position $(0, 1, 0.1)$. Then the electrode potential was stepped to potentials in the dissolution regime while the X-ray intensity as well as the electrochemical current of the electrode were recorded as a function of time. Figure 11.5a shows one data set obtained for a potential step from 0.5 V to 1.1 V. The potential of 1.1 V is about 50 mV more cathodic than peak I but deep in the dissolution regime. In both, the diffracted intensity and the electrochemical current, oscillations are visible. The time-dependent X-ray intensity resembles the growth oscillations measured for homoepitaxial deposition on Au(100) electrodes [65]. In analogy to the latter the oscillation amplitude decreases with time while the oscillation period increases. These oscillations are a clear indication for layer-by-layer dissolution of the Au(111) crystal in accordance with the STM observations. The decrease in amplitude has to be attributed to non-ideal dissolution, i.e. subsequent layers start to dissolve before the dissolution of the topmost layer is completed. By use of the analog X-ray detector signal, as employed in the measurements shown in figure 11.5, the time resolution of the performed SXS experiments (20 data points per second) is sufficient to monitor the dissolution process in real-time, i.e. to resolve oscillations with sub-second oscillation period. In contrast to the deposition experiments the oscillations observed here are not only present in the X-ray intensity but also in the electrochemical current as demonstrated in the lower graph of figure 11.5a. Subsequent

to the potential step a large anodic current spike is measured due to charging of the double layer. This process is very fast and completed within some milliseconds. In the following the current decays on a time scale of several seconds and approaches a saturation value. The shape of the current decay in this time period is determined by the complex interplay between the Au dissolution process and the time-dependent formation of the chloride diffusion layer in front of the electrode. Considering the case that every chloride atom reaching the surface immediately participates in the Au dissolution process then $j(t)$ is described by the Cottrell equation

$$j(t) = \frac{nF\sqrt{D/\pi}(c_0 - c_s)}{\sqrt{t}} \tag{11.20}$$

where n is the charge transfer number, F is the Faraday constant, D is the diffusion constant of Cl$^-$ and c_0 and c_s are the chloride concentrations in the solution bulk and at the electrode surface, respectively. However, as will be pointed out below the surface morphology influences the Au dissolution rate which on his part has an influence on the thickness of the diffusion layer. Thus, the basic shape of the current decay is predominantly determined by equation 11.20 while the dissolution process results in 'superimposed' oscillations. Straight lines in figure 11.5a point out a 180° phase shift between the current oscillation and the intensity oscillation, i.e. the X-ray intensity displays a minimum when the electrochemical
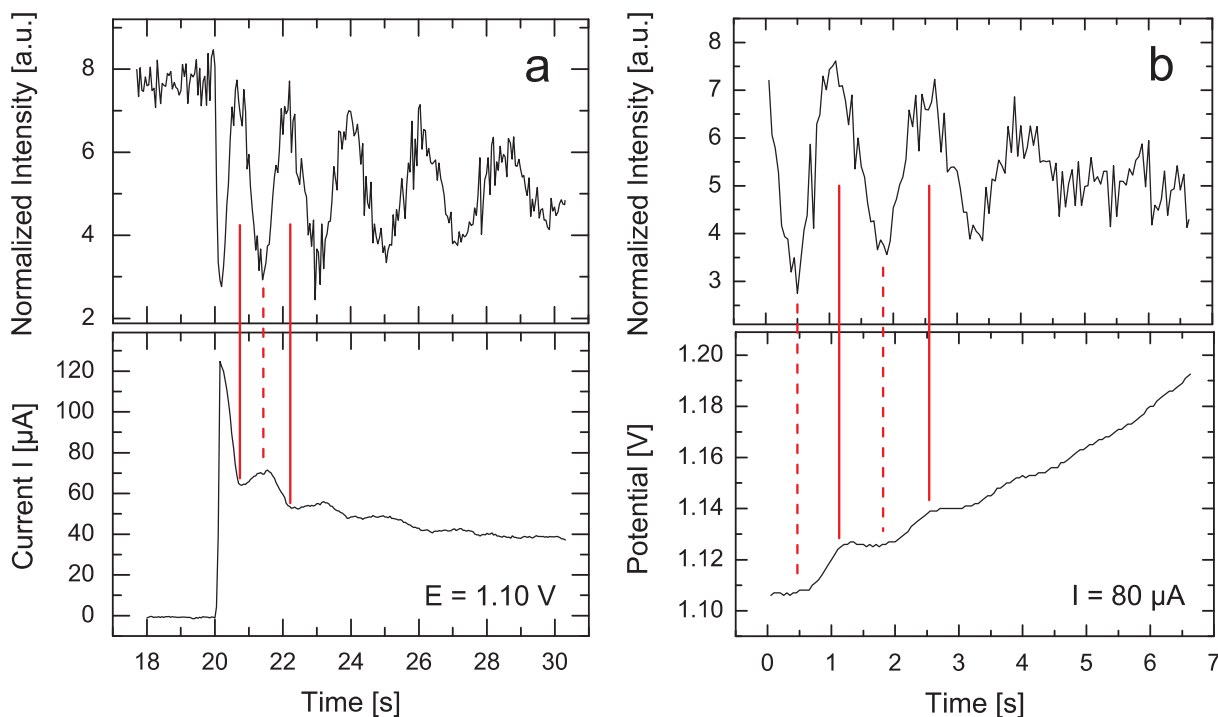
Figure 11.5: Dissolution oscillations in the X-ray intensity at $(1,0,0.1)$ as well as in the current and the electrode potential. The graphs show the results of a) potentiostatic and b) galvanostatic measurements. Solid and dashed lines indicate a) an 180° phase shift observed between X-ray intensity oscillations and current oscillations and b) no phase shift between X-ray oscillations and potential oscillations.

current reaches its maximum and vice versa. This behavior can be qualitatively explained as follows. At the initial potential of 0.5 V the Au(111) surface is predominantly flat with a low degree of surface roughness and wide terraces resulting in a high intensity in anti-Bragg. At the same time no significant electrochemical current is observed as 0.5 V lies within the double layer regime. If subsequently, at $t = t_0$, the potential is stepped to 1.1 V then the crystal starts to dissolve. In the onset of the dissolution process the X-ray intensity decreases until it takes the first intensity minimum if 0.5 ML of the topmost surface layer is dissolved. Then it increases and takes a maximum after dissolution of 1 ML. This intensity behavior is identical to those observed for layer-by-layer deposition and can be expected as the removal of one monolayer is just the reverse process of electrodeposition in view of the scattered X-ray intensity. However, the electrochemical current first rapidly increases subsequent to the potential step (covered by the double layer charging current) and takes a maximum after dissolution of ≈ 0.5 ML followed by a decrease to a current minimum at ≈ 1 ML. Responsible for this characteristics is the interplay of the constant driving force, i.e. the electrode potential, and the available number of dissolution sites. According to the STM studies [16] nucleation of stable vacancy cluster (nuclei) occurs which grow in size with progressing dissolution. At t_0 the amount of available sites for dissolution is comparatively small. As further dissolution proceeds the rim of terraces, islands and vacancy islands increases and by this the amount of kink sites. In turn more kink sites imply higher electrochemical current due to the constant driving force for dissolution under potentiostatic control. According to this consideration and to the measured current data the maximum amount of kink sites exists if ≈ 0.5 ML are dissolved. As dissolution proceeds the adatom islands shrink in size and vacancy islands merge so that the amount of kink sites decreases. This explains the current decrease towards 1 ML. Subsequent monolayers dissolve in the same way leading to repetitive oscillations in the X-ray intensity as well as in the electrochemical current. In total several oscillations are observed while the amplitude in X-ray intensity as well as in electrochemical current decreases with time. It is obvious that the oscillation amplitude decreases faster in current oscillations than in the X-ray intensity. A quantitative analysis of the current transients and of the X-ray intensity will be given in the sections 11.6 and 11.7, respectively. Similar to the deposition studies on Au(100) the Au(111) layer-by-layer dissolution seems to be non-ideal and with time pits are expected to be etched on terraces which results in an increased surface roughness and 3D dissolution. This trend can be also observed in the STM image shown in figure 11.1f.

Besides of potentiostatic control the potential step experiments were performed under galvanostatic control. In this case the dissolution current is kept constant while changes in the electrode potential are measured, i.e. changes in the dissolution driving force. The main advantage of this technique is that the dissolution rate is constant. Thus, even without X-ray oscillations a defined amount of material can be dissolved by knowledge of the surface atom density and the dissolution reaction (electron charge transfer). Galvanostatic experiments have been carried out by the following procedure. First the electrode potential was controlled potentiostatically and set to 0.5 V where the X-ray intensity at $(0\,,1\,,0.1)$ is comparatively high. Then, at $t = t_0$, the potentiostat switched from potentiostatic to galvanostatic control with the current being fixed to a certain value, while changes in the electrode potential were

monitored. Figure 11.5b shows one data set consisting of the time-dependent X-ray intensity and associated electrode potential. The applied current was $80\,\mu A$ corresponding to a current density of $637\,\mu A\,cm^{-2}$. Like for the potentiostatic control discussed above, oscillations are visible in the X-ray intensity as well as in the electrode potential. The interpretation of the X-ray oscillations is the same as given above. The time-dependent potential oscillations are explained as follows. The electrode potential, i.e. the overpotential, has to adopt in a way that the preset current is achieved. Thus in comparison with figure 11.5a the potential exhibits a maximum value if the current under potentiostatic control has a minimum and vice versa. Hence, in this case the potential oscillations are in phase with the X-ray intensity oscillations as indicated by lines in figure 11.5b.

Two differences between potentiostatically and galvanostatically controlled experiments can be seen in the measured X-ray intensities. While under potentiostatic control the oscillation period in the X-ray intensity increases relatively fast with time the first oscillation periods under galvanostatic control are almost identical (cp. figures 11.5a and 11.5b). On the other hand the $I(t)$ curve in the potentiostatic experiment exhibits about six oscillations (figure 11.5a shows only the initial time period after the potential step) while only three oscillations are apparent in the galvanostatic experiment. The latter might be caused by the relatively high current of $80\,\mu A$ in the galvanostatic mode, which expedites non-ideal layer-by-layer dissolution, or by a different pre-treatment of the sample. Electrochemical current and electrode potential show the same qualitative behavior as the according X-ray intensities, i.e. more oscillations are observed in the current transient.

11.5 Potential-Dependence of Au(111) Dissolution

The dissolution behavior of the Au(111) electrode has been probed as a function of electrode potential by SXS and potentiostatic current-time transients. For this the electrode potential was kept for at least $30\,s$ at $0.5\,V$ in order to obtain high X-ray intensity at the reciprocal space position $(0\,,1\,,0.1)$. Subsequently the electrode potential was stepped to a potential E_{end} in the dissolution regime (region 2) or in the passivation regime (region 3). In parallel the X-ray intensity at $(0\,,1\,,0.1)$ as well as the electrochemical current was monitored as a function of time. After each potential step into the dissolution/passivation regime the potential was first kept for 50 to $500\,s$ at $0.85\,V$ close to the Nernst equilibrium potential. At this potential the dissolved gold is redeposited with a moderate deposition rate. Subsequently the potential was stepped back to $0.5\,V$. At the latter electrode potential the X-ray intensity in anti-Bragg position recovered with time. This effect is related to the presence of Cl⁻ anions in the solution which is known to increase the mobility of gold atoms on the electrode surface. Trevor et al. found that the terraces of Au(111) surfaces in a $HClO_4$ solution which contains a trace amount of Cl⁻ were smoother than those in a Cl⁻ free solution after the formation and reduction of gold oxide [156]. Honbo et al. reported that pits were formed after the reduction of gold oxide on Au(111) surfaces in a Cl⁻ free solution but not in a Cl⁻ containing solution [206]. Thus, the presence of chloride results in a smoothening of the surface by Ostwald ripening of adatom islands and by filling of surface pits.

11.5.1 Qualitative Analysis of the X-ray Intensity Transients

Figure 11.6 summarizes the obtained $I(t)$ intensity curves and the current-time transients $j(t)$ for potential steps from $0.5\,\mathrm{V}$ to different electrode potentials E_{end}. In the time-dependent X-ray intensity clear oscillations are observed for potentials between $1.05\,\mathrm{V}$ and $1.20\,\mathrm{V}$. While the oscillation period is comparatively long with approximately $12\,\mathrm{s}$ at $1.05\,\mathrm{V}$ it shortens towards higher anodic potentials as expected according to the Butler-Volmer equation. The data acquisition via SPEC is sufficient to resolve the dissolution oscillations reasonably up to a potential of $1.07\,\mathrm{V}$ with a counting time of $0.5\,\mathrm{s}$ per data point. For the potential of $1.09\,\mathrm{V}$ the time resolution is at the limit as indicated by the small amount of data points contributing to each oscillation period in the respective $I(t)$ curve. For even higher anodic potentials, i.e. for $1.10\,\mathrm{V}$ to $1.25\,\mathrm{V}$, the diffracted intensity was recorded via the analog X-ray detector signal with an integration time constant of $0.1\,\mathrm{s}$ and a sampling rate of $20\,\mathrm{Hz}$. In doing so even oscillations with sub-second oscillation period could be resolved. For example the transient at $E_{end} = 1.2\,\mathrm{V}$ exhibits an oscillation period of $0.72\,\mathrm{s}$ in the initial time period after the potential step. No clear oscillations have been found for potentials of $1.0\,\mathrm{V}$ and $1.25\,\mathrm{V}$, respectively. The potential of $1.0\,\mathrm{V}$ belongs to the cathodic border of region 2 (see figure 11.4b) and is located close to the onset of dissolution. The observed $I(t)$ curve resembles half an oscillation with an estimated oscillation period of $\geq 20\,\mathrm{s}$. Because no complete oscillation period is recognizable the dissolution at this potential is not categorized into the layer-by-layer mode regime. In fact the shape of the recorded intensity-time transient is similar to the one observed after potential steps to the step-flow growth regime in the Au(100) electrodeposition experiments (cp. figure 9.6b, dashed line). The intensity $I(t)$ first decreases and then recovers, approaching an approximately constant intensity that is comparable to the initial intensity I_0 before the potential step. In analogy with the deposition experiments, this behavior is likely attributed to 2D dissolution of the first monolayer, followed by step-flow dissolution. However, in contrast to the deposition experiments, the initial 2D dissolution of the topmost monolayer is presumably not caused by nucleation of stable vacancy clusters (which is expected for higher overpotentials) but rather by the growth of preexisting vacancy clusters and vacancy islands. An interesting behavior is seen at $1.25\,\mathrm{V}$. This potential belongs to region 3, i.e. to the passivation regime. Subsequent to the potential step to $1.25\,\mathrm{V}$ the X-ray intensity at $(0,1,0.1)$ rapidly decreases within 1.5 seconds and saturates at very low intensity which is close to the background intensity level. The intensity decay is not monotonic but small superimposed intensity oscillations are recognized as indicated by arrows in figure 11.6. These oscillations have an estimated period of $T < 0.5\,\mathrm{s}$. This behavior is in accordance with the STM studies of Ye et al. which reported a competitive coexistence of layer-by-layer dissolution and gold oxide formation in the onset of region 3. It is conceivable that this mechanism results in local formation of etch pits at positions where the surface passivates at later times.

For all acquired $I(t)$ curves a more or less pronounced time-dependent intensity increase is observed subsequent to the potential step which influences the dissolution oscillations. The origin of this increase is unclear but might be related to a raise in the background intensity due to diffuse scattering induced by a slow but continuous roughening of the electrode
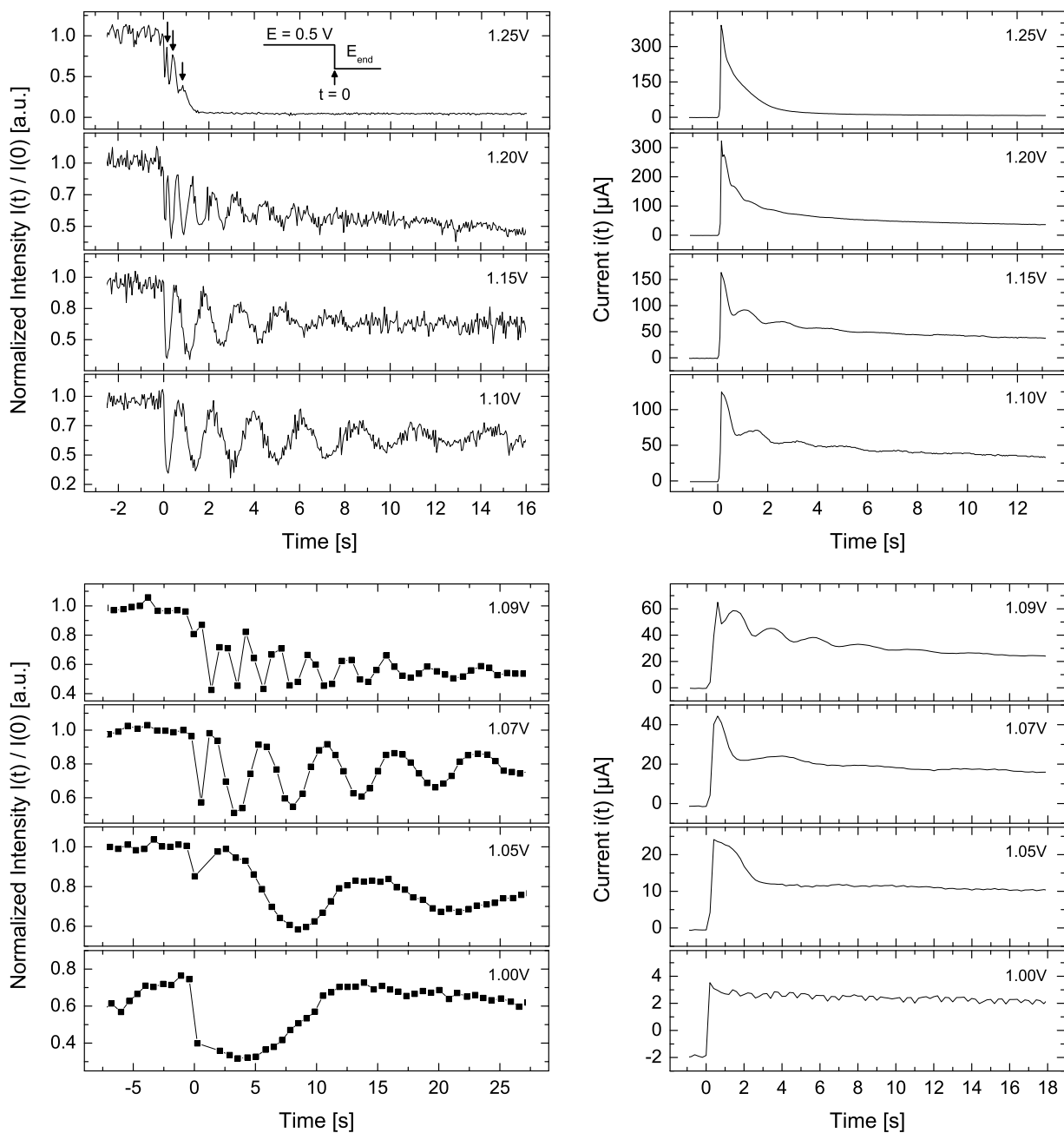
Figure 11.6: Diffracted intensity $I(t)$ at the reciprocal space position $(0, 1, 0.1)$ and electrochemical current-time transients for potential steps from $0.5\,\mathrm{V}$ to E_{end} in the dissolution potential regime. The lower graphs show $I(t)$ curves recorded via SPEC, while the upper graphs show $I(t)$ curves of the analog detector signal. In the X-ray intensity clear dissolution oscillations are seen for potentials from $1.05\,\mathrm{V}$ to $1.20\,\mathrm{V}$. Oscillations in the electrochemical current are less pronounced but can be realized between $1.07\,\mathrm{V}$ and $1.20\,\mathrm{V}$. For clarity of the graph only a selection of the measured transients is shown.
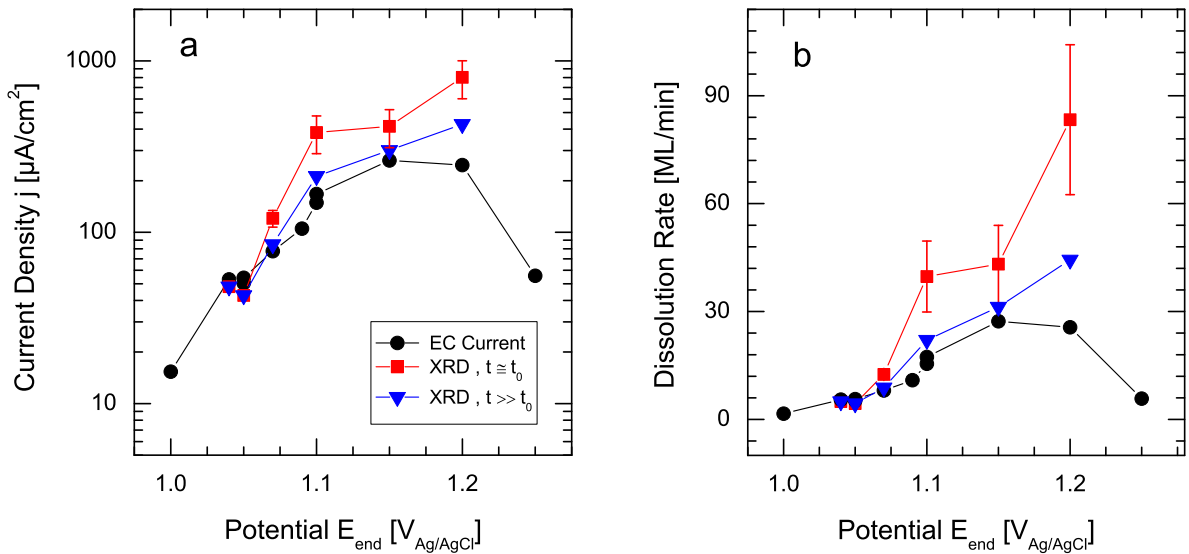
Figure 11.7: a) Au(111) steady state current densities j and b) dissolution rates determined subsequent to potential steps from 0.5 V to different potentials E_{end} in the dissolution and passivation regime. The data was obtained from X-ray intensity transients (squares and triangles) at the reciprocal space position $(0, 1, 0.1)$ and from current-time transients (circles), respectively. Squares (triangles) were determined from the 1st and 2nd (3rd and 4th) intensity oscillation subsequent to the potential step.

surface during the dissolution process. Unfortunately, the background signal as well as the peak profile could not be determined parallel to the intensity-time transient due to the high demands on the time resolution and due to the usage of an X-ray point detector. Future measurements with one-dimensional X-ray detectors are planned. However, azimuthal intensity profiles revealed that the background intensity is about 4% of the peak intensity. This may also be seen in the analog detector signal recorded subsequent to the potential step to 1.25 V where a low saturation value is observed in the passivation regime. Thus the background contribution to the intensity profiles is small and has been neglected in the further analysis. The time periods of the X-ray intensity oscillations provide information about the potential-dependent dissolution rates. In order to determine the latter the first two intensity oscillations in the onset of each potential step have been fitted by a decaying sinus function. Figure 11.7b summarizes the results (squares). As expected the dissolution rate increases towards higher anodic overpotentials. Due to a concurrent shortening of the oscillation periods the error bars, which are provided by the non-linear least square algorithm, increase as well. Close to the Nernst equilibrium potential the Au(111) electrode surface dissolves comparatively slow. The lowest determined dissolution rate is approximately 6 ML/min at 1.04 V. However, at the highest measured anodic potential in the active dissolution regime (1.20 V) a dissolution rate of 84 ML/min was found. It has to be considered that the rates obtained in this manner reflect the dissolution process for small times t subsequent to the potential step, where the chloride concentration near the electrode surface is comparatively high. We deter-

mined as well the dissolution rates under approximately diffusion-limited conditions. For this we applied the same fit procedure to the 3rd to 4th oscillation period of each intensity transient, where the stationary Nernst diffusion layer is to a large extent established. Triangles in figure 11.7b show the according dissolution rates. In the diffusion-limited regime dissolution rates of $5\,\mathrm{ML\,min^{-1}}$ and $44.4\,\mathrm{ML\,min^{-1}}$ have been determined for the potentials of $1.04\,\mathrm{V}$ and $1.20\,\mathrm{V}$, respectively. It is remarkable that even for such high dissolution rates several distinct X-ray intensity oscillations are observed, i.e. that the dissolution still proceeds via layer-by-layer mode. From the dissolution rates the electrochemical current densities have been calculated via equation 2.25. The results are shown as squares and triangles in figure 11.7a corresponding to the two curves shown in figure 11.7b. For low overpotentials, i.e. from $0.95\,\mathrm{V}$ to $\approx 1.1\,\mathrm{V}$ the current increases exponentially. The logarithmic plots yield Tafel slopes of $0.053\,\mathrm{V}$ (XRD, $t \approx t_0$) and $0.072\,\mathrm{V}$ (XRD, $t \gg t_0$) per decade in good agreement with the Tafel slope of $0.054\,\mathrm{V}$ per decade determined by Ye et al. [16] and in accordance with the results of previous works [184, 188, 190]. For higher anodic overpotentials, i.e. between $1.1\,\mathrm{V}$ and $1.2\,\mathrm{V}$, the calculated values deviate from the initial Tafel behavior and the slope is significantly lower, indicating diffusion-limited conditions. In the passivation regime (e.g. for $1.25\,\mathrm{V}$) no meaningful current densities are obtainable even though intensity oscillations superimpose the intensity decay. The influence of the passivation process cannot be easily estimated since the oscillation amplitude of all intensity transients decreases with time. Thus for potentials close to the passivation regime (e.g. $1.20\,\mathrm{V}$) the oscillation periods may lead to overestimated current densities.

11.5.2 Qualitative Analysis of the Electrochemical Current-Time Transients

In the electrochemical current data clear oscillations are observed for potentials between $1.09\,\mathrm{V}$ and $1.15\,\mathrm{V}$. The current transient at $1.07\,\mathrm{V}$ shows weak current oscillations with a long oscillation period and the transient at $1.20\,\mathrm{V}$ weak oscillations with a short oscillation period. However, for potentials $< 1.07\,\mathrm{V}$ and for potentials $> 1.20\,\mathrm{V}$ no current oscillations are observed. Moreover, with the exception of the transient measured at $1.0\,\mathrm{V}$ all other current transients exhibit a pronounced Cottrellian decay. We determined the potential-dependence of the anodic current at times when the dissolution process is diffusion-controlled, i.e. when the Nernst diffusion layer almost achieved a time-independent thickness. Each current density was taken at the time $t = 30\,\mathrm{s}$ after the potential step. The result is summarized by circles in figure 11.7a. In the potential regime between $1.0\,\mathrm{V}$ and $1.1\,\mathrm{V}$ the current-overpotential relationship shows Tafel behavior ($\log j \propto \eta$). This is in qualitative agreement with the ECQM studies by Ye et al. [16, 17] which as well reported Tafel behavior in a $100\,\mathrm{mV}$ wide potential regime next to the onset of dissolution for Au(111) electrodes in $0.1\,\mathrm{M}\ HClO_4 + 5\,\mathrm{mM}$ Cl^- containing solution. The Tafel slope inferred from the electrochemical current data is $0.109\,\mathrm{V}$, i.e. two times larger than previously reported values of $0.054\,\mathrm{V}$ per decade. Since there is a significant statistical spread in the current data (partly related to minor deviations in the surface morphology) the according Tafel slope has to be considered to be afflicted with a rather large error. In regard of these errors comparable Tafel slopes have been determined. The electrochemical current densities are in good agreement with those inferred from the 3rd to 4th X-ray intensity oscillation. For potentials $< 1.20\,\mathrm{V}$ the latter are only 10%

to 15% larger due to the Cottrell behavior. In the more positive potential region between 1.1 V and 1.2 V the current density is more or less potential-independent which indicates that the dissolution process is diffusion-controlled. This is as well in agreement with the ECQM studies and has been also found in rotating disk electrode studies [185, 188, 190]. The current drop at 1.25 V is related to the passivation of the electrode surface. Summarized, the overall $j(\eta)$ relationship is in agreement with the data of Ye et al. From the electrochemical current density the dissolution rate has been determined using equation 2.25. Resulting rates are shown as circles in figure 11.7b. Under diffusion-limited conditions dissolution rates of 5.5 ML min^{-1} and 25.6 ML min^{-1} were determined for the potentials of 1.04 V and 1.2 V, respectively. Since electrochemical current and dissolution rate are proportional to each other the latter increases exponentially in the potential regime between Nernst potential and approximately 1.10 V.

In conclusion of this section we want to emphasize an important difference between the STM studies of Ye et al. and the present SXS measurements. The series of STM images given in figure 3 of reference [16] allows to estimate the dissolution rate at a potential of 1.36 V$_{\mathrm{RHE}}$ during the tunneling process. A value of 0.33 ± 0.05 ML min^{-1} is found in 0.1 M HClO$_4$ + 1 mM Cl$^-$ solution. In contrast the according cyclic voltammogram in figure 1 of reference [16] yields an estimated current density of $\approx 117 \, \mu$A cm^2 and thus a dissolution rate of ≈ 10.5 ML min^{-1} at the same electrode potential. Hence the dissolution rate below the STM tip is a factor of $\approx$32 lower. This suggests that the dissolution process is strongly hampered by instrumental limitations. Presumably the transport of chloride from the solution bulk to the electrode surface is shaded by the STM tip in a similar manner as it is known for metal complexes during electrodeposition. Thus scanning probe methods are principally incapable to investigate the dissolution behavior under real reaction conditions. However, in the case of the performed SXS experiments the X-ray intensity and the electrochemical data yield almost identical current densities (figure 11.7a). Consequently the dissolution process can be followed in real-time and with unrestricted mass transport of chloride and AuCl$_4^-$ at the interface.

11.6 Quantitative Analysis of the Current Dissolution Oscillations

In this section I will first present a standard two-dimensional growth model which is based on the Avrami model. Then I will adequately extend the standard model in order to apply it to current-time transients which were recorded subsequent to potential steps into the dissolution regime. The section concludes with a quantitative analysis of the current oscillations based on the extended model. This analysis provides information about the layer-by-layer dissolution process and about the surface morphology.

11.6.1 Two-dimensional Standard Model

For simultaneous two-dimensional, cylindrical growth of nuclei, the following two expressions are valid (equations 11.12 and 11.8 applied on 11.9 and 11.10) which describe the time-
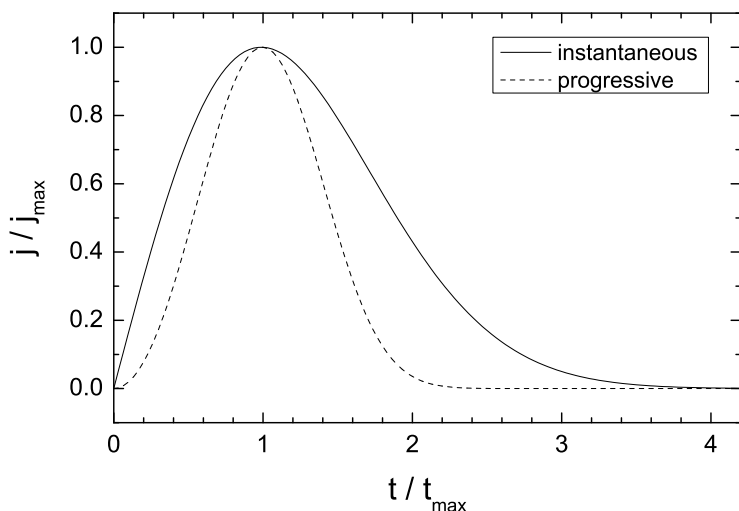
Figure 11.8: Shape of theoretical current-time transients for instantaneous and progressive nucleation in the case of two-dimensional, cylindrical growth of the nuclei.

dependence of the electrochemical current density j in case of instantaneous nucleation

$$j(t) = \left(\frac{2nF\pi hMN_0k^2}{\rho}\right) \cdot t \cdot \exp\left(\frac{-\pi M^2 N_0 k^2}{\rho^2} \cdot t^2\right) \tag{11.21}$$

and progressive nucleation

$$j(t) = \left(\frac{nF\pi hMAN_0k^2}{\rho}\right) \cdot t^2 \cdot \exp\left(\frac{-\pi M^2 AN_0 k^2}{3\rho^2} \cdot t^3\right). \tag{11.22}$$

For current-time transients recorded at constant electrode potential and provided that the mass transport is fast the lateral growth rate k and the nucleation rate A can be assumed to be time-independent. The pre-exponential terms in (11.21) and (11.22) describe the overall current-time relationship for simultaneous two-dimensional, cylindrical growth and nucleation without overlap of the growing nuclei according to equation 11.7. The latter is taken into account by the exponential terms which represent the overlap effect and which act as correction terms. Hence, in case of homoepitaxial growth and constant electrode potential the current density j is a pure function of time while all other contributions are constant. Thus, both equations can be written as

$$\text{(instantaneous)} \qquad j(t) \;=\; C_1 \cdot t \;\cdot \exp\left(-C_2 \cdot t^2\right) \tag{11.23}$$
$$\text{(progressive)} \qquad j(t) \;=\; C_1 \cdot t^2 \cdot \exp\left(-C_2 \cdot t^3\right) \tag{11.24}$$

where C_1 ($C\,cm^{-2}\,s^{-2}$ for instantaneous and $C\,cm^{-2}\,s^{-3}$ for progressive nucleation) and C_2 (s^{-2} for instantaneous and s^{-3} for progressive nucleation) are constants containing material specific quantities, the lateral growth rate k as well as the nucleation rate A in the case of progressive nucleation (cp. with equations 11.21 and 11.22). Figure 11.8 depicts the basic shapes of these two curves. In the case of Au(111) electrodes in Cl$^-$ containing solution the deposition (dissolution) of one monolayer requires a total charge transfer of

$$Q_{ML} = \frac{nFh\rho}{M} = 666\,\mu C \tag{11.25}$$

whereupon $n = 3$ electrons are transfered per gold atom according to reaction 11.1. The constants C_1 and C_2 are coupled via Q_{ML} as demonstrated by the ratios

$$\text{(instantaneous)} \qquad \frac{C_1}{C_2} = \frac{2nFh\rho}{M} = 2 \cdot Q_{\text{ML}} \qquad (11.26)$$

$$\text{(progressive)} \qquad \frac{C_1}{C_2} = \frac{3nFh\rho}{M} = 3 \cdot Q_{\text{ML}} \qquad (11.27)$$

Far more relevant for X-ray scattering and a more intuitive quantity to describe the deposition (dissolution) of one monolayer is the coverage θ which is directly related to the charge transfer. The charge $Q(t)$ transfered in the time interval from $t' = 0$ to $t' = t$ is given by the following integrals

$$\text{(instantaneous)} \quad Q(t) \;=\; \int_0^t j(\tau)d\tau = Q_{ML} \cdot \left(1 - \mathrm{e}^{-C_2 \cdot t^2}\right) \qquad (11.28)$$

$$\text{(progressive)} \quad Q(t) \;=\; \int_0^t j(\tau)d\tau = Q_{ML} \cdot \left(1 - \mathrm{e}^{-C_2 \cdot t^3}\right) \qquad (11.29)$$

With (11.25), (11.28) and (11.29) the coverage $\theta(t)$ of the considered single monolayer at the time t is defined as

$$\text{(deposition)} \qquad \theta_{\text{dep}}(t) \;=\; \frac{Q(t)}{Q_{ML}} \qquad (11.30)$$

$$\text{(dissolution)} \qquad \theta_{\text{diss}}(t) \;=\; 1 - \frac{Q(t)}{Q_{ML}} \qquad (11.31)$$

11.6.2 Extended Two-dimensional Model

In order to fit the current-time transients, which were recorded in the onset of Au(111) electrodissolution after previous potential steps, the equations 11.23 and 11.24 for instantaneous and progressive growth, respectively, have been applied to the dissolution data. Although these equations have been derived for the case of deposition the formulae can be used for dissolution. Nucleation and growth of stable vacancy clusters as well as overlap of vacancy islands must result in current densities identical to those of island growth and island overlap in deposition experiments. In the previous section we introduced the current arising from deposition (dissolution) of a single monolayer. The according equations base on the assumption that the transport of species from the solution bulk to the surface or vice versa is infinitely rapid, i.e. that the incorporation of adatoms to the step-edges of islands is reaction-controlled. Only under these conditions the lateral dissolution rate k and the nucleation rate A can be assumed to be time-independent. As mentioned before this situation is fulfilled for constant electrode potentials. However, in the present studies we performed potential step experiments. A sudden change in the electrode potential induces non-stationary conditions until a new equilibrium is achieved. Principally two processes affect the electrochemical current in the according time period, that is the double layer charging process and the development of the Nernst diffusion layer. The first process results in a large current spike directly after the potential step and is completed within milliseconds. The second process

causes a current decay over a longer time period and is correlated to a change in the deposition/dissolution rate. The standard model of the previous section does not account for either of the two effects and has to be modified. Since to my knowledge no current oscillations due to layer-by-layer dissolution of single crystal electrodes have been reported up to now the extended model proposed in the following is unique and has never been applied before.

In the present system chloride ions diffuse from the solution bulk to the surface where the $AuCl_4$ complex is formed. Therefore k must depend on the surface near chloride concentration and thus becomes time-dependent. Since according to Cottrell the current is proportional to $1/\sqrt{t}$ we propose a similar time-dependence for the lateral dissolution rate, i.e.

$$k^*(t) = k_c \cdot \frac{1}{\sqrt{t}} \tag{11.32}$$

where k_c ($mol\,cm^{-2}\,s^{-1/2}$) is a constant arising from the Cottrellian behavior. The numerical value of the constant k_c represents the dissolution rate one second after the potential step. For reasons given below equation 11.32 has to be considered as an approximation of the true time-behavior in k. Besides of k the nucleation rate A potentially becomes time-dependent since the formation process of vacancies likewise requires chloride ions. However, in the model proposed below the nucleation rate is assumed to be constant. This approach is necessary since the time-dependence of A is entirely unknown. Nevertheless, the extended model with constant A is able to describe the current-time transients and from this point of view the approach of a constant nucleation rate seems to be legitimate. A time-dependent change in nucleation rate would affect the shape of the current curve for progressive nucleation (dashed line in figure 11.8). For increasing A the current curve more and more approaches the shape of the current curve for instantaneous nucleation (solid line in figure 11.8). Since the current-time transients could not be fitted by a model function based on instantaneous nucleation the time-dependence in A must be small.

In order to model the recorded current-time transients the constant dissolution rate k has to be replaced by a time-dependent dissolution rate $k(t)$. However, an analytical derivation of expressions similar to those given in the equations 11.21 and 11.22 is extremely difficult. This is related to the fact that equation 11.12 (in combination with the Avrami-equation) and the Cottrell-equation base on contrary assumptions. The Cottrell equation presumes that the transport of the deposition species from the solution to the surface is the rate-determining step while all surface processes like surface transport and charge transfer are rapid. In strict contrast equation 11.12 assumes that the deposition (dissolution) rate is constant and that surface transport and charge transfer are the rate-determining steps. This situation gives rise to integral differential equations with nonconstant coefficients which probably can only be solved numerically. Fleischmann and Thirsk mentioned in their review article about metal deposition that a theoretical modeling of this problem has not been attempted until their article was published in 1969 [195] and to my knowledge no appropriate solution exists so far. Due to these difficulties we took a different approach to model the measured data. We exploit that the oscillation period of the current oscillations is narrow compared to the $1/\sqrt{t}$ decay, i.e. the time constant for dissolution of a single monolayer, τ_{ML} is much smaller than

the time constant τ_{Cottrell} for the evolution of the stationary Cl$^-$ concentration profile. In this manner we can consider the Nernst diffusion layer to be approximately constant in the time period when a single monolayer dissolves. Instead of incorporating the dissolution rate $k^*(t)$ we choose discrete time values t_i for each of the i topmost surface layers so that the constant dissolution rate of the i-th layer is given by

$$k_i = k^*(t_i) = k_c \cdot \frac{1}{\sqrt{t_i}} \tag{11.33}$$

There are various possibilities to choose these discrete time values. With regard to the fitting process it makes sense to refer each t_i to a fixed point of reference to keep the amount of parameters small. Unfortunately the time t_{max} of the theoretical current curve depends on t_i (see below) so that it is no appropriate choice for the latter. The t_i may be chosen with respect to the starting point of dissolution for the i-th layer, e.g. either in form of a constant shift or in form of a more complicated function of time. However, an additional fit parameter is required. For now we want to consider the current arising from a single monolayer with t_c being the according constant time value related to the Cottrellian decay. If we replace the dissolution rate k in (11.23) and (11.24) by the dissolution rate $k^*(t_c)$ then we obtain the following model equations

$$(\text{instantaneous}) \qquad j(t) = \begin{cases} \dfrac{C_1^*}{t_c} \cdot t \cdot \exp\left(-\dfrac{C_2^*}{t_c} \cdot t^2\right) & t \geq 0 \\ 0 & t < 0 \end{cases} \tag{11.34}$$

and

$$(\text{progressive}) \qquad j(t) = \begin{cases} \dfrac{C_1^*}{t_c} \cdot t^2 \cdot \exp\left(-\dfrac{C_2^*}{t_c} \cdot t^3\right) & t \geq 0 \\ 0 & t < 0 \end{cases} \tag{11.35}$$

where the two constants C_1^* (C cm^{-2} s^{-1} for instantaneous and C cm^{-2} s^{-2} for progressive nucleation) and C_2^* (s^{-1} for instantaneous and s^{-2} for progressive nucleation) are related to the previous constants C_1 and C_2

$$C_1^* = \frac{C_1}{k^2} \cdot k_c^2 \tag{11.36}$$

$$C_2^* = \frac{C_2}{k^2} \cdot k_c^2 \tag{11.37}$$

The two equations 11.34 and 11.35 describe the current density originating from a single monolayer and allow to include the Cottrell behavior by appropriate choice of the time t_c. The current density maximum, $j_{\max}$, and the according point in time, $t_{\max}$, are given by the following expressions

$$(\text{instantaneous}) \qquad t_{\max} = \sqrt{\frac{t_c}{2 \cdot C_2^*}} \quad , \quad j_{\max}(t_{\max}) = \frac{C_1^*}{2} \sqrt{\frac{2}{t_c \cdot C_2^* \cdot e}} \tag{11.38}$$

$$(\text{progressive}) \qquad t_{\max} = \sqrt[3]{\frac{2 \cdot t_c}{3 \cdot C_2^*}} \quad , \quad j_{\max}(t_{\max}) = \frac{C_1^*}{t_c} \left(\frac{2 \cdot t_c}{3 \cdot C_2^* \cdot e}\right)^{2/3} \tag{11.39}$$

where e is the Euler number.

11.6.3 Current Fit Function

For simplicity only the case of progressive nucleation is discussed in the following. The fit function for instantaneous nucleation is obtained in an analogous way by replacing t^2 by t in the pre-exponential term and by replacing t^3 by t^2 in the exponential term. Both, instantaneous and progressive nucleation have been considered in the data analysis (see below). The measured current is the sum of contributions of several monolayers whose dissolution starting points are shifted in time versus each other. For progressive nucleation the following function has been fitted to the data

$$
j(t) = \underbrace{\frac{C_1^*}{TS_0 + SHIFT_0} \cdot (t - TS_0)^2 \cdot \exp\left(-\frac{C_2^*}{TS_0 + SHIFT_0} \cdot (t - TS_0)^3\right)}_{\text{topmost monolayer}}
$$
$$
+ \underbrace{\sum_{i=1}^{N} \frac{C_1^*}{TS_i + SHIFT} \cdot (t - TS_i)^2 \cdot \exp\left(-\frac{C_2^*}{TS_i + SHIFT} \cdot (t - TS_i)^3\right)}_{\text{successive monolayers}} \quad (11.40)
$$

where C_1^* and C_2^* are the constants introduced above, TS_i are the points in time at which the i-th monolayer starts to dissolve and $t_i = TS_i + SHIFT$ are the discrete time values to incorporate the Cottrellian behavior of the evolving chloride diffusion layer. Thus in the present case the discrete time values t_i are chosen to be shifted by a constant amount $SHIFT$ versus the dissolution starting points TS_i of each monolayer. The times t_i basically determine the widths of the contributing current curves, which broaden with time due to the Cottrellian effect. Free model fit parameters are C_1^*, C_2^*, TS_1, $SHIFT$, TS_0, $SHIFT_0$ and an additional parameter called MLF (Monolayer Fraction). The latter describes to which fraction the i-th monolayer has to be dissolved until the dissolution of the '$i+1$'-th layer sets in (onset of second layer nucleation), i.e. it constitutes the overlap of the contributing current (coverage) curves. MLF can be expressed in terms of transfered charge by the following ratio

$$
MLF = \frac{Q_{MLF}}{Q_{ML}} \quad (11.41)
$$

where Q_{MLF} is a constant fraction of Q_{ML}. Hence, MLF basically varies between zero (maximum overlap) and unity (no overlap). The smaller MLF the shorter is the oscillation period in the current-time transient and the smaller is the oscillation amplitude. It is obvious that small values of MLF are attributed to 3D dissolution while for large MLF the electrode dissolves in the layer-by-layer mode (MLF equals unity for perfect 2D dissolution). This parameter is usually compared with the critical coverage θ_c which determines the 2D-3D growth mode transition [1]. Figure 11.9 illustrates the meaning of the model parameters for an arbitrarily chosen value of $MLF = 0.5$.

The starting times $TS_2, TS_3, ... TS_n$ of the third to the n-th layer are recursively determined from the two fit parameters TS_1 and MLF according to the recursion formula

$$
TS_{i+1} = TS_i + \sqrt[3]{-\frac{t_i}{C_2^*} \ln(1 - MLF)} \quad (11.42)
$$
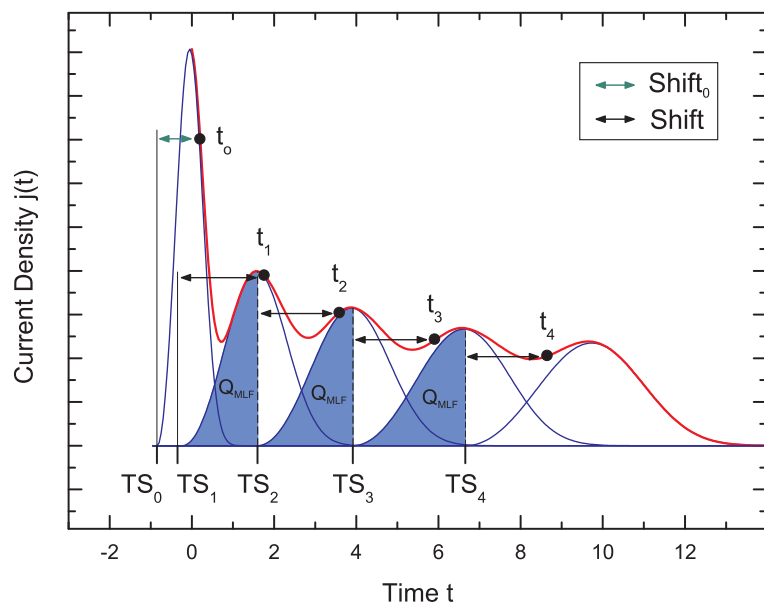
Figure 11.9: Illustration of the model parameters. The blue curve depicts the current arising from single monolayers while the red curve shows the current sum of all contributing monolayers. Exemplary a value of $MLF = Q_{MLF}/Q_{ML} = 0.5$ has been chosen. Shaded areas point out Q_{MLF}.

The latter was derived from the equations 11.29 and 11.41. Equation 11.42 furthermore determines in combination with the fit parameter $SHIFT$ the time values t_i. The topmost surface layer has been modeled by a separate parameter set consisting of the starting time TS_0 and $SHIFT_0$. Particularly within the first second after the potential step double layer charging contributes to the electrochemical current and the time-dependent change in the lateral dissolution rate k is high (Cottrell). The latter is not in agreement with the model assumption that k is only weakly time-dependent for the time period of the dissolving monolayer. Thus it is convenient to decouple the first monolayer from the residual parameter set. An interpretation of current contributions from the topmost surface layer is not straightforward and the discussion will be postponed to section 11.7. In addition to the aforementioned fit procedure the data has been modeled with a reduced parameter set by replacing the constant C_1^* by C_2^* according to equation 11.27. For reasons given below the reduced parameter set was only partially suited to fit the measured current-time transients. Appendix A.5 lists the software implementation of function 11.40 in Origin[1] C which has been fitted to the data by non-linear least-square method.

At this point it is worth to mention that the expressions C_1^*/t_i and C_2^*/t_i contain the product $A \cdot k(t_i)$ and thus neither informations about the nucleation rate A nor about the dissolution rates $k^*(t_i)$ are accessible by the fit of current-time transients. In principle STM images, such as the one shown in figure 11.2, would allow to determine the nucleation rate, so that the dissolution rate may be estimated. Unfortunately, the time-resolution as well as the spatial resolution of the STM images are insufficient to infer the nucleation rate.

---

[1]OriginLab, Origin Pro 7.5, Scientific Graphing and Analysis Software

11.6.4 Fit of the Extended Model to the Measured Current-Time Transients

Figure 11.10 shows the best fit of the model function 11.40 to a measured current-time transient, recorded parallel to a potential step from $0.5\,\mathrm{V_{Ag/AgCl}}$ in the double layer regime to $1.1\,\mathrm{V_{Ag/AgCl}}$ in the active dissolution regime. From all acquired current transients this dataset exhibits the most pronounced dissolution oscillations. In order to fit the current data seven contributing monolayers (I to VII) have been included, each of them is illustrated by a solid or dashed blue curve in the graph. The topmost surface layer (layer I) was modeled by two independent parameters TS_0 and $SHIFT_0$. All obtained parameter values are summarized in table 11.1 in the row denoted by transient 'A$_a$'.

Apparently the obtained $j(t)$ curve is capable to describe the acquired data, i.e. the dissolution oscillations as well as the Cottrellian decay are well reproduced. Furthermore the time-dependent increase in the oscillation period is accurately fit by the model. According to the resulting constants, $C_1^* = 419.281\,\mathrm{C\,cm^{-2}\,s^{-3}}$ and $C_2^* = 0.199\,\mathrm{s^{-3}}$, the total charge transfer per monolayer is $Q_{\mathrm{ML}} = 702.3\;\mu\mathrm{C\,cm^{-2}}$. This value is only about 5% larger than the expected value of $666\,\mu\mathrm{C\,cm^{-2}}$ and shows that the theoretical model quantitatively describes the experimental data. In addition the relatively small deviation and the pronounced current oscillations indicate that the electrode surface is smooth. For potential steps to different potentials E_{end} larger Q_{ML} were determined with a maximum value of $830.3\,\mu\mathrm{C\,cm^{-2}}$, corresponding to a rather large deviation of 25%. This discrepancy may be explained by a constant contributing current caused by either additional electrochemical reactions or more likely by an increased surface roughness (see below). The lower graph in figure 11.10 shows the attributed, time-dependent coverages of the seven surface layers determined via equation 11.31. Every coverage curve has the typical sigmoidal shape as it is known from the deposition model, but in the present dissolution studies the coverage curves are mirrored about the horizontal axis due to the removal of atoms from an initially filled monolayer. The intersections of the sigmoidal coverage curves at $t = 0$ basically provide information about the coverages of the atomic layers present before the potential step. Nevertheless, as stated above the interpretation of the topmost surface layer is complicated by means of the current transient and will be therefore discussed on the basis of the X-ray data (section 11.7).

Of particular interest is the fit parameter MLF which is 0.439 for the considered current-time transient. Hence, the $n + 1$-th monolayer starts to dissolve if $\approx 44\%$ of the previous n-th monolayer is dissolved. According to this second layer nucleation sets in comparatively early. However, closer inspection of the coverage curves in figure 11.10 reveals that the n-th layer is already $>90\%$ dissolved while the $(n + 1)$-th layer has a coverage of $0.95\,\mathrm{ML}$. This behavior is related to the slow initial dissolution of a monolayer and clearly demonstrates that the electrode dissolves via layer-by-layer mode. We compare the MLF value of 0.439 with those predicted for deposition experiments. Rosenfeld et al. proposed a critical coverage $\theta_c = 0.66$ which is used as criterion to decide if homoepitaxial growth will follow the 2D ($\theta_c > 0.66$) or 3D ($\theta_c < 0.66$) growth mode [1]. This value coincides with coalescence of islands and has been derived on the basis of typical literature values for critical nucleus sizes and capture numbers. The determined value of $MLF = 0.44$ in the present electrodissolution experiment
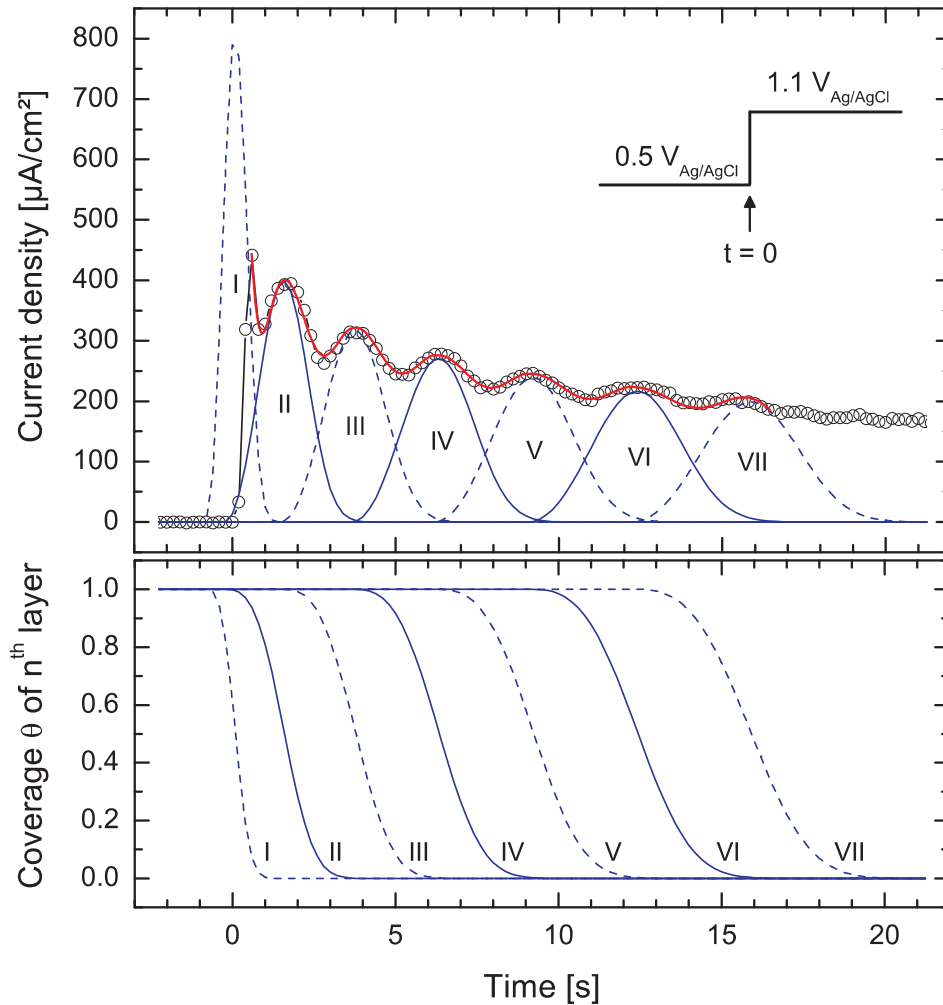
Figure 11.10: Current-time transient (open circles) which was recorded parallel to a potential step ($t = 0$) from $0.5\,\mathrm{V_{Ag/AgCl}}$ in the double layer regime to $1.1\,\mathrm{V_{Ag/AgCl}}$ in the active dissolution regime and its best fit based on the model function 11.40 (red line). The fit curve is the sum over current contributions from seven monolayers, denoted by I to VII (blue lines, solid and dashed). The lower graph shows the according time-dependent coverages.

is much lower than $\theta_c = 0.66$, i.e. second layer nucleation of stable vacancy clusters takes place before significant coalescence of vacancy islands sets in. Nevertheless, despite the relatively small MLF value pronounced current oscillations are observed which clearly prove layer-by-layer dissolution and which indicate that the transition to 3D growth probably occurs at even smaller MLF values. It is not clear if interlayer transport of vacancies plays an important role in layer-by-layer dissolution of Au(111) electrodes. Even though interlayer mass transport is a necessary premise for layer-by-layer growth in deposition experiments it is conceivable that the anisotropic dissolution on Au(111) electrodes may hinders second layer nucleation until a certain fraction of the first layer is dissolved. This fraction may be sufficient to result in layer-by-layer dissolution. The comparatively small critical coverage

in our dissolution experiments may be explained by such a mechanism. In this regard the absence of a layer-by-layer growth regime during homoepitaxial deposition may be related to isotropic growing islands as indicated by STM studies of W. Polewska [14]. However, the existence of interlayer vacancy transport cannot be excluded, neither from a theoretical point of view nor from our experimental data. Provided that vacancy interlayer transport is involved the small MLF value indicates either a very high vacancy migration energy, a high vacancy Ehrlich-Schwoebel barrier or a combination of both.

The overlap of the coverage curves indicates that the dissolution process is predominantly restricted to the two topmost monolayers, respectively, if the deviation of 5% in Q_{ML} is neglected. Thus, at least for the initial time after the potential step, the layer-by-layer dissolution results in a low degree of surface roughness. In order to quantify the latter the root-mean-square roughness has been calculated according to the definition

$$\sigma_{RMS} = \sqrt{\frac{1}{P \cdot Q} \sum_{q=1}^{Q} \sum_{p=1}^{P} \left[z(x_p, y_q) - \langle z \rangle \right]^2} \tag{11.43}$$

where $P \cdot Q$ is the number of atoms per cm^2, $z(x_p, y_q)$ is the height of the atom at the position (x_p, y_q) in reference to the surface nearest bulk monolayer with complete coverage and $\langle z \rangle$ is the average over all z. Equation 11.43 can be written in terms of the time-dependent layer coverages which yields

$$\sigma_{RMS}(t) = \sqrt{\underbrace{\theta_1(t) \cdot \left[(N-1) \cdot h - \langle z \rangle \right]^2}_{\text{topmost layer}} + \underbrace{\sum_{i=2}^{N} \left[\theta_i(t) - \theta_{i-1}(t) \right] \cdot \left[(N-i) \cdot h - \langle z \rangle \right]^2}_{\text{2nd to } N \text{th layer}}} \tag{11.44}$$

with

$$\langle z \rangle = \underbrace{\theta_1(t) \cdot (N-1) \cdot h}_{\text{topmost layer}} + \underbrace{\sum_{j=2}^{N} \left[\theta_j(t) - \theta_{j-1}(t) \right] \cdot (N-j) \cdot h}_{\text{2nd to } N \text{th layer}}$$

In equation 11.44 the summations are carried out over the N topmost layers present at the time t, while layer N is the surface nearest layer with complete coverage. The resulting rms curve is plotted in figure 11.11 together with the coverage curves of figure 11.10. For $t > 0$ σ_{RMS} oscillates in the range between 0.36 and 0.5 in units of the Au(111) layer thickness h. While the rms maxima always equal 0.5·h the rms minima moderately raise with each oscillation period. The latter is related to the Cottrellian behavior which induces a broadening of the contributing current curves. A maximum roughness of 0.5·h conforms to a perfectly terminated bulk crystal being covered by exactly half a monolayer. This is in agreement with the coverage curves as projections of the rms maxima point out. At the according times $t_{\text{rms,max}}$ the topmost monolayer exhibits almost exactly the coverage $\theta = 0.5$ while the upper layer is completely dissolved and the lower layer is fully filled. Due to the overlap of the coverage curves the rms roughness does not approach zero, i.e. the crystal is never ideally terminated during the dissolution process.
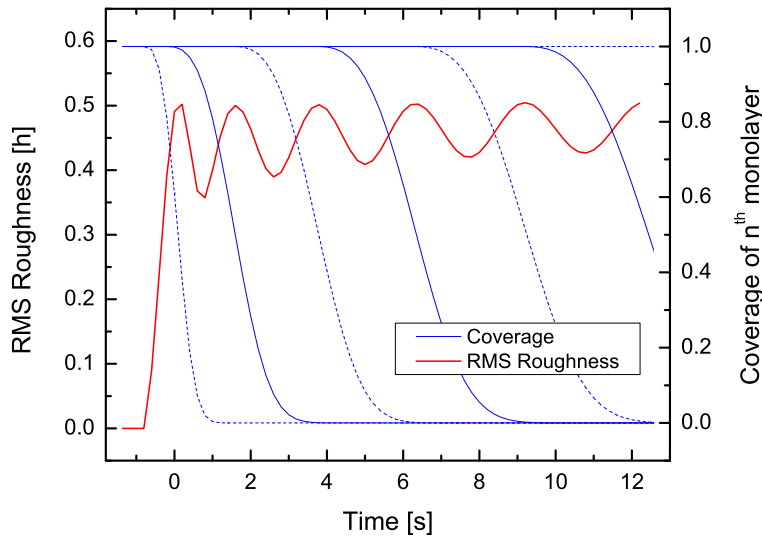
Figure 11.11: Time-dependence of the rms roughness during Au(111) electrodissolution in 50 mM H_2SO_4 + 5 mM HCl solution. At $t = 0$ the electrode potential has been stepped from $0.5\,V_{Ag/AgCl}$ to $1.1\,V_{Ag/AgCl}$. (transient A)

A second fit of the same dataset has been accomplished by replacing C_1^* with C_2^* according to the relationship $C_1^* = 3 \cdot Q_{ML} \cdot C_2^*$ with $Q_{ML} = 666\,\mu C$ (equation 11.25). The resulting $j(t)$ curve is shown in figure 11.12 A_b and the according fit parameters are summarized in table 11.1. It describes the measured current-time transient less precise than the previous fit as can be clearly seen for large times t where the oscillation period of the model function runs out-of-phase with the measured oscillations in the current-time transient. This is also indicated by an increased χ^2 value of the fit, $\chi^2(A_b) = 73.41$, which is more than twice as large as $\chi^2(A_a) = 28.66$ in the case of independently fit constants C_1^* and C_2^*. Besides of the observed discrepancy in the oscillation period the obtained fit parameter $MLF = 0.443$ is similar to the one determined in the framework of the first fit (cp. transients A_a and A_b in table 11.1). Thus, MLF seems to be less sensitive to the fitting process. The reduced parameter set is appropriate to fit the current-time transients in the potential regime between 1.09 V and 1.10 V whereas at all other potentials the independency of the variables C_1^* and C_2^* is essential, being related to the comparatively large deviation in Q_{ML}.

In an analogous way the fit procedure has been applied to several current-time transients which were recorded parallel to potential steps from 0.5 V to different potentials E_{end} in the active dissolution regime. In detail the extended model could be fitted to the acquired data in the potential regime between 1.07 V and 1.15 V. The resulting $j(t)$ curves are shown in figure 11.12 and the according best fit parameters are summarized in table 11.1. However, the model could not be fitted to the current-time transient recorded at 1.2 V even though weak oscillations are existent. This may be either related to the pronounced Cottrelian decay, i.e. the model assumption $\tau_{ML} \ll \tau_{Cottrell}$ does not hold anymore although the oscillation period is comparatively short, or to an influence of the incipient passivation process. In addition to the model based on two-dimensional, progressive nucleation it has been tried to fit an alternative model based on two-dimensional, instantaneous nucleation to the data. The analysis revealed that for all of the measured current-time transients no appropriate fit was possible
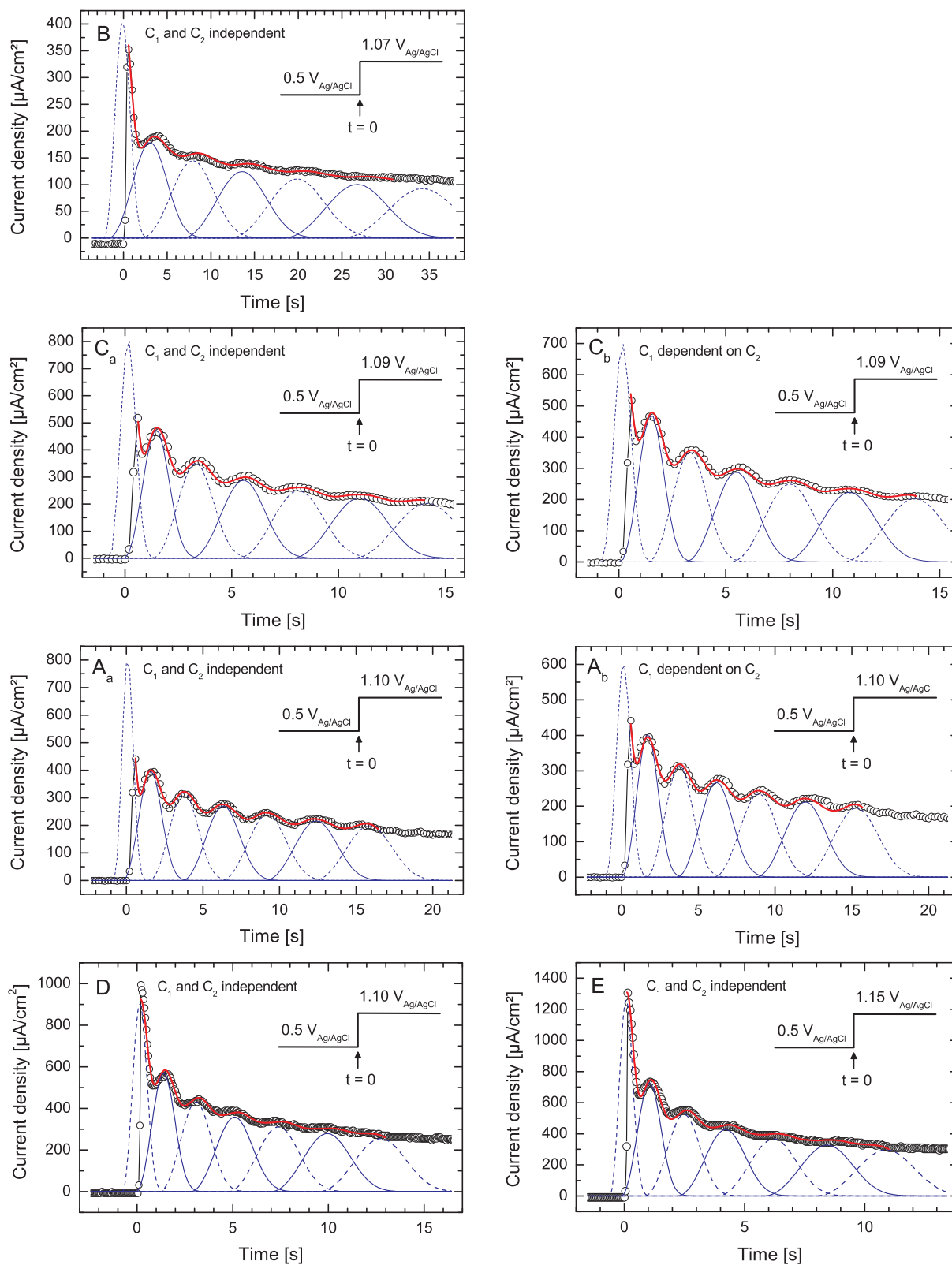
Figure 11.12: Best fits of the extended model function to the measured current-time transients. The graphs are ordered by the potential E_{end}.

Transient	E_{end} [$V_{\text{Ag/AgCl}}$]	C_1^* [$C\,cm^{-2}\,s^{-3}$]	C_2^* [s^{-3}]	MLF	Q_{ML} [$\mu C/cm^2$]
B	1.07	66.178	0.027	0.286	817.0
C_a	1.09	374.742	0.181	0.377	690.1
C_b	1.09†	$3{\cdot}Q_{ML}{\cdot}C_2$	0.197	0.383	667.2
A_a	1.10	419.281	0.199	0.439	702.3
A_b	1.10†	$3{\cdot}Q_{ML}{\cdot}C_2$	0.220	0.443	667.2
D	1.10‡	571.779	0.239	0.349	797.5
E	1.15‡	595.309	0.239	0.311	830.3

Transient	E_{end} [$V_{\text{Ag/AgCl}}$]	TS_1 [s]	SHIFT [s]	TS_0 [s]	$SHIFT_0$ [s]
B	1.07	-1.713	6.021	-2.212	2.585
C_a	1.09	-0.033	0.929	-0.727	0.909
C_b	1.09†	+0.061	0.837	-0.811	1.089
A_a	1.10	-0.234	1.994	-0.804	1.013
A_b	1.10†	-0.072	1.808	-1.025	1.478
D	1.10‡	-0.132	1.324	-0.747	1.006
E	1.15‡	-0.125	0.702	-0.592	0.699

Table 11.1: Best fit parameters of the model function 11.40 applied on electrodissolution current oscillations which were obtained by potentiostatic potential step experiments from $0.5\,V$ in the double-layer regime to different potentials E_{end} in the active dissolution regime. † indicates fits with a reduced parameter set according to the relationship $C_1^* = 3Q_{ML}\cdot C_2^*$. ‡ indicates measurements which were carried out subsequent to previous potential cycling into the passivation regime and by a simultaneous fit of electrochemical current and X-ray intensity (see section 11.7).

with the result that the nucleation mechanism must be progressive in the whole potential regime of layer-by-layer dissolution.

11.6.5 Interpretation of the Fit Results

An interpretation of the obtained parameter values is difficult since the shape of the current-time transients strongly depends on the history of the sample, i.e. on the morphology of the electrode surface before the potential step. This can be clearly seen by direct comparison of the transients A and D in figure 11.12 which both were recorded after potential steps to $1.1\,V$. In transient D less pronounced current oscillations and higher current densities are observed. Both affects the parameter values Q_{ML} and MLF (table 11.1). The surface morphology may be particularly influenced by two effects, that is a) the surface roughening in the dissolution and passivation regime and b) the redeposition of previously dissolved gold. Although these effects complicate the interpretation of the results useful informations are inferred from the chronological sequence of the potential step experiments which is schematically shown in figure 11.13. In the graph all potentials E_{end} with evaluable current transients in the layer-

by-layer dissolution regime were indexed by capitals which correspond to the denotations in table 11.1 and in figure 11.12. Prior to the main potential step experiments the electrode surface was characterized by cyclic voltammetry and cyclic diffractograms in the double layer regime and by a 30 s long potential step to 1.1 V. These investigations were carried out in a time span of 2 hours and 40 minutes. Then the first potential step was performed from 0.5 V to 1.1 V (transient A) according to the procedure shown in the inset of figure 11.13. The potential step to 1.1 V in this experiment defines the origin $t = 0$ of the employed time scale. We recall that the fit of transient A provides a charge transfer of $Q_{ML} = 702.3\,\mu C\,cm^{-2}$ in the dissolution of individual monolayers and a vacancy island coverage of $MLF = 43.9\%$ for the onset of 2nd layer nucleation. Since Q_{ML} is close to the theoretical value and pronounced current oscillations are apparent the electrode surface is smooth. Subsequent to transient A the potential was stepped to potentials of 1.0 V, 1.05 V, 1.07 V (B), 1.09 V (C), 1.04 V, 1.3 V (CV into passivation regime, figure 11.4b), 1.1 V (D), 1.15 V (E), 1.2 V and 1.25 V , respectively. After approximately every second to third potential step a cyclic voltammogram was recorded in the double layer regime in order to ensure the stability of the reference electrode on the basis of the chloride order/disorder peaks. Since the dissolution rates are comparatively high for potentials > 1.1 V an amount of 1.5 ml electrolyte was manually exchanged between the potential steps to 1.3 V and 1.1 V (D) as well as between 1.15 V (E) and 1.2 V in order to rule out an accumulation of dissolved gold in the solution.

Figure 11.14a exemplary shows the time-dependent, normalized peak intensity measured at the anti-Bragg position $(0,1,0.1)$ parallel to the potential step procedure with $E_{end} = 1.09$ V. The initial intensity at 0.5 V is comparatively high indicating a smooth surface. Subsequently the potential was changed into the dissolution regime. At 1.09 V oscillations are observed and the intensity saturates at a lower value indicating an increased roughness of the electrode
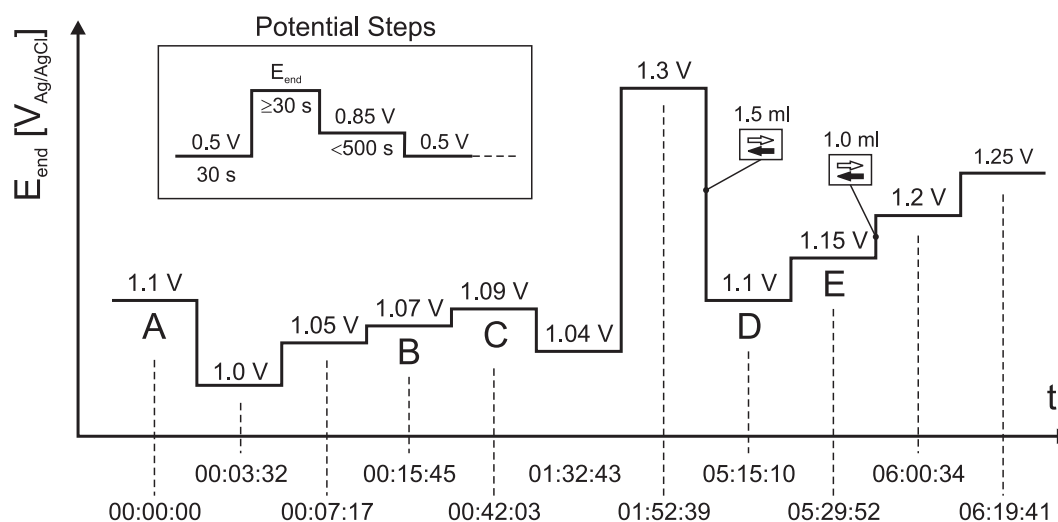
Figure 11.13: Timeline of the performed potential step experiments from 0.5 V to different potentials E_{end} in the active dissolution regime. Potential steps denoted by capitals exhibit pronounced current oscillations and could be fitted by the model function.

surface. In the following the potential was stepped to 0.85 V in order to stop the dissolution process. At this potential the previously dissolved gold is redeposited with a moderate deposition rate. The latter in presence of adsorbed Cl⁻ anions causes a smoothening of the roughened surface as it was reported in STM studies [156, 206]. Consequently the intensity increases, but, since no step-flow growth was found on Au(111) electrodes, the intensity does not fully recover to the original value. In the final potential step back to 0.5 V the intensity again decreases. This effect has to be likely attributed to fast redeposition of remaining gold in the solution which is connected to surface roughening. According to the integrated charge of 1609 μC during the dissolution process an amount of ≈ 19 ML was dissolved in the 80 s time period at 1.09 V. From this quantity only ≈ 2.8 ML have been redeposited at 0.85 V as estimated by the transferred charge during the 120 s deposition time. The remaining ≈ 16.2 ML (minus the Au amount which diffused deeper into the solution bulk [189]) were deposited at 0.5 V with presumably higher deposition rate.

The X-ray intensities for potential steps to all employed potentials E_{end} are summarized in figure 11.14b. Each potential step procedure basically shows the same behavior as exemplified before. Some exceptions will be discussed in the following. An intensity decrease after potential steps from 0.5 V to E_{end} is observed in all experiments and it is particularly pronounced for potentials E_{end} in (or close to) the passivation regime. The passivated Au(111) surface is well known to be rough [156, 202–204, 207, 208]. At the intermittent holding potential of 0.85 V the intensity increases in all experiments as a consequence of slow redeposition and enhanced surface mobility of Au adatoms due to the presence of chloride ions. Figure 11.14c shows the amount of gold which has been dissolved in the dissolution process at E_{end}, and for comparison the amount which has been redeposited during the holding time at 0.85 V. For the employed holding times, ranging from 40 to 175 s, 5 to 30% of the dissolved gold was redeposited at 0.85 V. It is remarkable that even after potential steps to E_{end} in the passivation regime the initial intensity is almost fully recovered. This is in agreement with STM studies of Au(111) electrodes which reported monoatomar deep pits and monoatomic high islands after stepping the potential into the passivation regime and back [208], i.e. a similar surface morphology as it arises from the dissolution process. Nevertheless, for increased chloride concentrations in the solution the enhanced dissolution in competition with oxide layer formation potentially results in a surface roughening by local formation of 3-dimensional etch pits. Since the chloride concentration in the present study is about one to two orders of magnitude higher than those commonly employed in the STM studies an additional roughening caused by the potential cycle to 1.3 V cannot be fully excluded. The intensity saturation values after the final potential step back to 0.5 V either agree with the values which were achieved at 0.85 V beforehand or they decrease due to preceding redeposition. Only for potential steps to 1.05 V and 1.1 V (D) a further increase was observed. Especially if the time Δt at 0.5 V between two subsequent potential step experiments to different potentials E_{end} is too short then the redeposition process after the first potential step experiment determines the intensity at the start of the second potential step experiment. This can be seen in the first four experiments in figure 11.14b where the initial intensities are lower than the final intensities in the previous experiments. For all other experiments Δt is > 10 min and the intensity recovers.
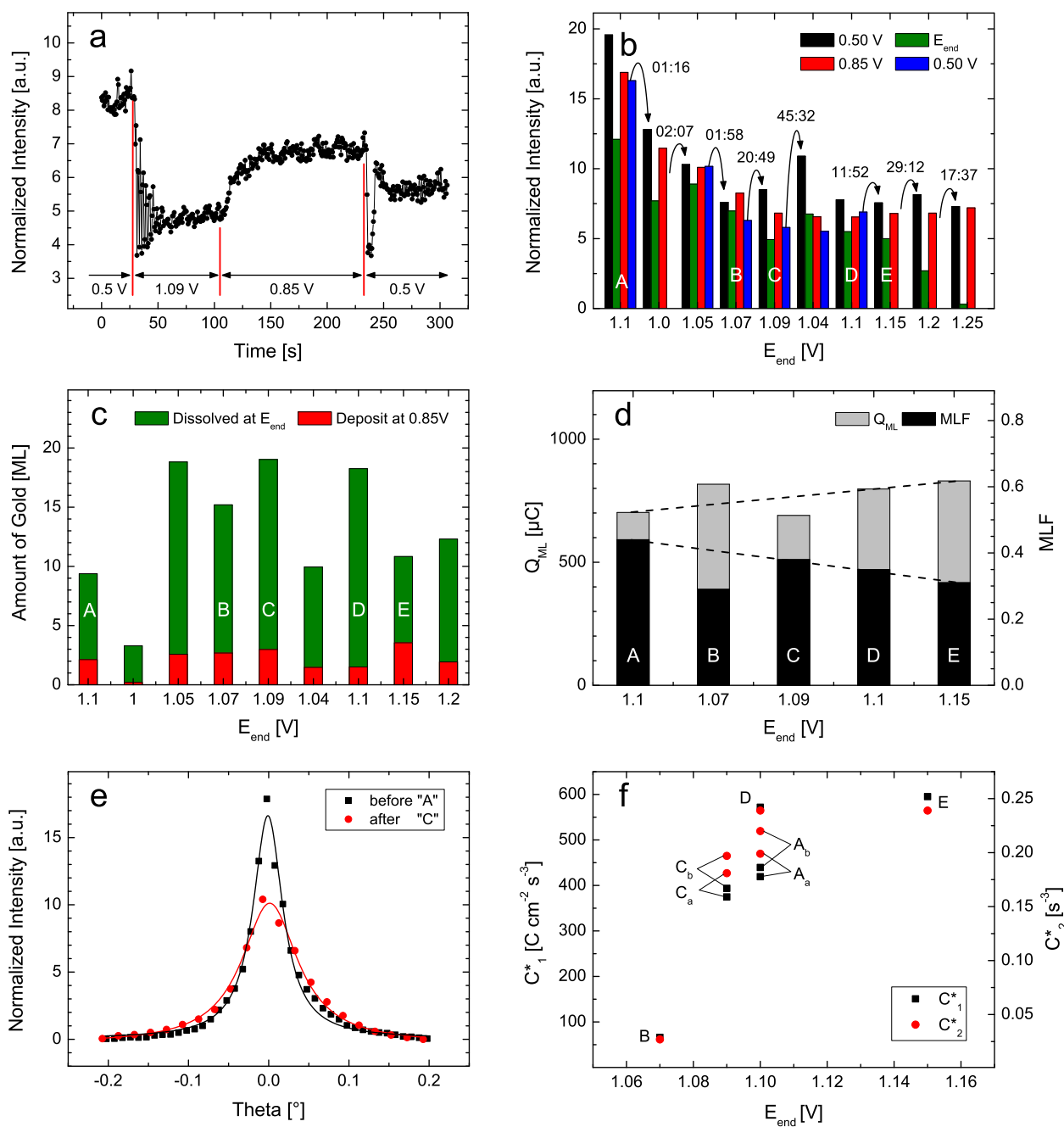
Figure 11.14: a) Time-dependent peak intensity at $(0\,,1\,,0.1)$ measured parallel to the potential step procedure with $E_{end} = 1.09\,\text{V}$. **b)** Saturation values of the intensity at different potentials in chronological sequence of the experiment. The times, given in minutes, denote the holding times at $0.5\,\text{V}$ between two experiments. **c)** Gold amount dissolved at E_{end} and the redeposited amount at $0.85\,\text{V}$. **d)** Q_{ML} and MLF determined by the fit procedure in chronological sequence of the experiments. Dashed lines point out the trends in both quantities. **e)** Azimuthal intensity profiles at $(0\,,1\,,0.1)$ recorded prior to transient A and subsequent to transient C. **f)** Potential-dependence of C_1^* and C_2^*.

The overall decrease of the peak intensity in anti-Bragg position corroborates a roughening of the electrode surface induced by repeated potential steps into the dissolution regime. Figure 11.14e shows two azimuthal intensity profiles monitored at $(0\,,1\,,0.1)$ before transient A and after transient C, respectively. The decrease in peak intensity and simultaneous increase in the FWHM from 0.045° to 0.085° (integrated intensity is approximately constant) is a clear evidence that after transient C more intensity is diffusely scattered by the rougher electrode surface. This is in agreement with the determined parameter values of Q_{ML} and MLF which are plotted in chronological sequence of the potential step experiments in figure 11.14d. The transfered charge per monolayer (Q_{ML}) increases with each experiment. This is related to the fact that the model function 11.40 does not take into account a significant initial surface roughness. If more than the two topmost surface layers have fractional coverage prior to the potential step to E_{end} then each current curve attributed to a single monolayer contains contributions of the dissolution of underlying layers. The parameter MLF decreases with the amount of potential step experiments, i.e. the contributing current curves exhibit a larger overlap. As stated above small MLF values are connected to 3D dissolution. The tendency for 3D dissolution can be also seen in the current-time transients by means of lower oscillation amplitudes in later experiments (figure 11.12). The behavior in the transients B and C differs from the general trend. In the case of transient B the relatively short holding times at 0.5 V between the previous three potential step experiments apparently results in an increased surface roughness and thus in a high Q_{ML} value and in a small MLF value. However, in the ≈ 20 min holding time at 0.5 V between transient B and transient C the surface obviously smoothened since the Q_{ML} value in transient C is close to the theoretical value and the MLF value is significantly higher than for transient B. The current oscillations are well pronounced in transient C with a comparatively high oscillation amplitude. Due to the gradual roughening of the electrode surface no informations about the potential-dependence of the critical coverage MLF can be inferred from the performed experiments. The most reliable informations about MLF are obtained from current-time transients with Q_{ML} close to the theoretical value, i.e. from transient A and transient C. Thus, in order to determine the potential-dependence more systematic studies are required.

Figure 11.14f shows the potential-dependence of the constants C_1^* and C_2^* which both contain the product $k_c^2 \cdot A$. As already demonstrated by figure 11.7 the overall dissolution rate increases with the applied overpotential in agreement with the Butler-Vollmer equation. The same is supposed to hold for the lateral dissolution rate k_c as well as for the nucleation rate A, so that the aforementioned product is expected to increase towards higher positive overpotentials. This behavior is confirmed by the fit of the model function to the measured data as demonstrated in figure 11.14f. Furthermore, for potentials > 1.1 V the slope of the curve decreases in agreement with the current-overpotential relationship in figure 11.7a, i.e. in the onset of the diffusion-controlled potential regime.

The series of acquired current-time transients clearly demonstrates that Au(111) dissolution in Cl⁻ containing solution proceeds via layer-by-layer mode. This layer-by-layer dissolution is not perfect and surface roughening is observed after repeated potential steps into the dissolution regime. The decay in X-ray intensity oscillations strongly resembles those observed for

layer-by-layer growth in homoepitaxial deposition experiments on Au(100) (chapter 9). Nevertheless, even though an amount of ≈ 120 monolayers has been dissolved in several potential step experiments the electrode surface remains comparatively smooth. This layer-by-layer mode in presence of chloride ions allows the controlled dissolution of single monolayers up to homogeneous abrasion of several Ångstroem thick surface layers. Appropriate experiments will be presented in section 11.8.

11.7 Analysis of the Scattered X-ray Intensity

Parallel to the potential step experiments the scattered X-ray intensity was monitored at the reciprocal space position $(0, 1, 0.1)$ close to anti-Bragg. We apply kinematic theory to describe the data. The structure factor $F_{\text{sum}}(\vec{q})$ of the Au(111) electrode is given by the interference sum of contributions from the surface layers, $F_{\text{surf}}(\vec{q})$, and from the crystal bulk, $F_{\text{bulk}}(\vec{q})$. Since the intensity was measured at a fixed position in reciprocal space all correction factors (Lorentz-factor, polarization factor, absorption factor, geometry factor, . . .) are constant and the detected X-ray intensity is proportional to the square modulus of $F_{\text{sum}}(\vec{q})$, i.e.

$$I(\vec{q}) \propto |F_{\text{sum}}(\vec{q})|^2 = |F_{\text{bulk}}(\vec{q}) + F_{\text{surf}}(\vec{q})|^2 \tag{11.45}$$

We will now derive expressions for $F_{\text{bulk}}(\vec{q})$ and $F_{\text{surf}}(\vec{q})$. The bulk structure factor is given by

$$F_{\text{bulk}}(\vec{q}) = \sum_{\vec{r}_u} F_u \cdot \mathrm{e}^{2\pi i \vec{q} \cdot \vec{r}_u} \tag{11.46}$$

where F_u is the structure factor of the employed Au(111) unit cell, $\vec{q} = (q_x, q_y, q_z) + i\vec{\alpha}$ is an arbitrary scattering vector including absorption via $\vec{\alpha} = (\alpha_x, \alpha_y, \alpha_z)$ and $\vec{r}_u = (x_u, y_u, z_u)$ is the position vector of the u-th unit cell in the crystal bulk. The sum is carried out over all unit cells of the crystal. For the present system it is convenient to separate the in-plane and the out-of-plane components in the exponential term which yields

$$F_{\text{bulk}}(\vec{q}) = \sum_{z_u} F_u \cdot \underbrace{\mathrm{e}^{2\pi i q_z \cdot z_u} \cdot \mathrm{e}^{-2\pi \alpha_z z_u}}_{\text{out-of-plane}} \cdot \sum_{x_u, y_u} \underbrace{\mathrm{e}^{2\pi i (q_x \cdot x_u + q_y \cdot y_u)} \cdot \mathrm{e}^{-2\pi \alpha_x x_u - 2\pi \alpha_y y_u}}_{\text{in-plane}} \tag{11.47}$$

$$\approx \sum_{z_u} F_u \cdot \mathrm{e}^{2\pi i q_z \cdot z_u} \cdot \mathrm{e}^{-2\pi \alpha_z z_u} \cdot \sum_{x_u=-\infty}^{\infty} \sum_{y_u=-\infty}^{\infty} \mathrm{e}^{2\pi i q_x x_u} \cdot \mathrm{e}^{2\pi i q_y y_u} \tag{11.48}$$

$$= \sum_{z_u} F_u \cdot \mathrm{e}^{2\pi i q_z \cdot z_u} \cdot \mathrm{e}^{-2\pi \alpha_z z_u} \cdot \delta(q_x - H) \cdot \delta(q_y - K) \tag{11.49}$$

where H and K are Miller indices and integer values. The approximation is based on the assumption that q_x and q_y are real, i.e. that absorption is negligible. In this case the infinite sums over x_u and y_u in (11.48) can be written as product of the two delta distributions $\delta(q_x - H)$ and $\delta(q_y - K)$. Hence, the structure factor F_{bulk} is nonzero if the in-plane components of the scattering vector match the Laue conditions, i.e. if $q_x = H$ and $q_y = K$, respectively. Then only the L-dependence in the bulk structure factor has to be considered. For now we maintain the absorption term $\exp(-2\pi \alpha_z z_u)$ in order to evaluate the sum in equation 11.49. We assume that the in-plane Laue-conditions are fulfilled and carry out the sum from $z_u = 0$
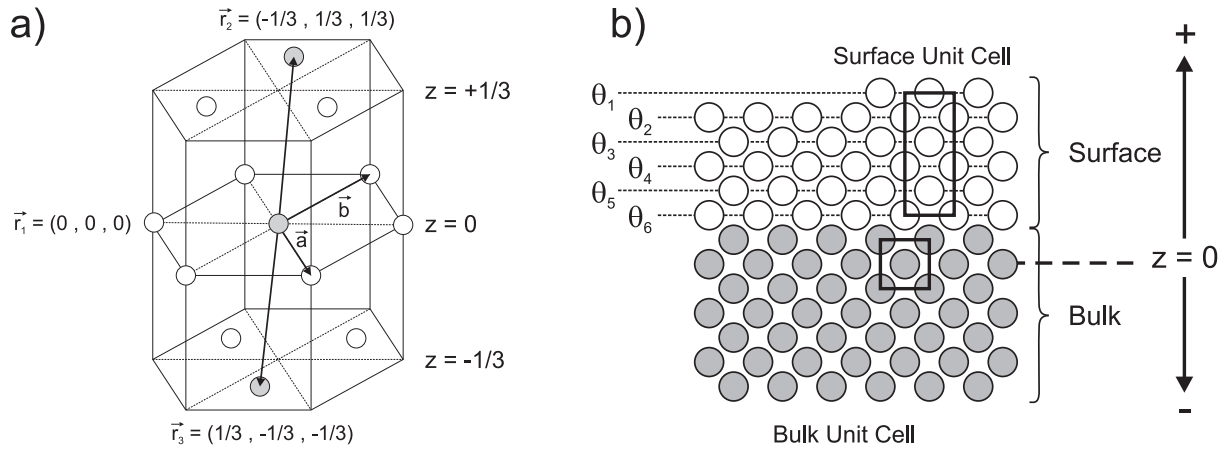
Figure 11.15: Structural model of the Au(111) electrode. a) Definition of the atomic basis. b) Model of the Au(111) electrode surface. The surface morphology during electrodissolution is described by the time-dependent change in the coverages $\theta_1, \ldots, \theta_6$ of the six topmost atomic layers.

to $-\infty$. Equation 11.49 reduces to

$$F_{\text{bulk}} = \sum_{z_u=0}^{-\infty} F_u \cdot e^{2\pi i L z_u} \cdot e^{-2\pi \alpha_z z_u}. \tag{11.50}$$

whereupon q_z was replaced by the Miller index L. In contrast to H and K the index L is not restricted to integer values. The structure factor F_u of the primitive gold unit cell is given by

$$F_u = \sum_{j=1}^{N} f_{Au} \cdot e^{2\pi i \vec{q} \cdot \vec{r}_j} = f_{Au} \left\{ 1 + 2 \cdot \cos\left(2\pi \cdot \frac{-H+K+L}{3}\right) \right\} \tag{11.51}$$

where $\vec{r}_j$ are the position vectors of the N atoms in the unit cell[2] and f_{Au} is the atomic form factor of gold. The employed unit cell consists of three Au atoms and is depicted in figure 11.15a. If equation 11.51 and

$$a \cdot \sum_{n=0}^{\infty} x^n = \frac{a}{1-x} \qquad \text{for} \quad |x| < 1 \tag{11.52}$$

are applied on equation 11.50 then the following expression results for the bulk scattering factor

$$
\begin{aligned}
F_{\text{bulk}} &= F_u \cdot \sum_{z_u=0}^{\infty} e^{-2\pi i L z_u + 2\pi \alpha_z z_u} & (11.53) \\
&= f_{Au} \cdot \left[1 + 2\cos\left(2\pi \cdot \frac{-H+K+L}{3}\right) \right] \cdot \frac{1}{1 - e^{-2\pi i L + 2\pi \alpha_z}} & (11.54) \\
&\approx f_{Au} \cdot \left\{ \frac{1 + 2\cos(2\pi \cdot \frac{-H+K+L}{3})}{1 - e^{-2\pi i L}} \right\} & (11.55)
\end{aligned}
$$

---

[2]Equation 11.51 makes use of the geometrical relation $2 \cdot \cos(z) = \exp(iz) + \exp(-iz)$.

whereupon the absorption term $\exp(2\pi\alpha_z)$ has been neglected after evaluation of the geometric series. This is justified since the penetrated slab of surface layers is comparatively thin in grazing incidence geometry. The structure factor F_{surf} of the topmost layers is given by

$$F_{\text{surf}} = \sum_{j=0}^{M} \theta_j \cdot f_{Au} \cdot \underbrace{e^{-0.5 \cdot q_z^2 \cdot \sigma_j}}_{\text{Debye Waller}} \cdot e^{2\pi i(Hx_j + Ky_j + Lz_j)} \tag{11.56}$$

where (x_j, y_j, z_j) are the coordinates of atom j in the surface unit cell (in fractional real space lattice units), σ_j are the Debye-Waller parameters including dynamical and static displacements and θ_j are the occupancy parameters of the j surface layers. The summation is carried out over all M atoms in the surface unit cell. If single surface layers are partially covered by overlying layers then σ_j has to be modified.

11.7.1 X-ray Model Function

In order to describe the scattered X-ray intensity $I(t)$ which was measured in the electrodissolution process the following model function has been applied to the data

$$
\begin{aligned}
I(t) &= AZ \cdot (F_{\text{sum}} \cdot F_{\text{sum}}^*) \\
&= AZ \cdot \Bigg| \underbrace{\frac{1 + 2 \cdot \cos\left(2\pi \cdot \frac{-H+K+L}{3}\right)}{1 - e^{-2\pi iL}} \cdot e^{-0.5 \cdot q_z^2 \cdot \sigma_{\text{bulk}}^2}}_{\text{bulk contribution}} + \underbrace{\theta_1(t) \cdot e^{-0.5 \cdot q_z^2 \cdot \sigma_1^2} \cdot e^{2\pi i \vec{q} \cdot \vec{r}_1} \ldots}_{\text{surface contribution of 1st ML}} \\
&\quad \ldots + \underbrace{\sum_{j=2}^{6} \left[\{\theta_j(t) - \theta_{j-1}(t)\} \cdot e^{-0.5 \cdot q_z^2 \cdot \sigma_1^2} + \theta_{j-1} \cdot e^{-0.5 \cdot q_z^2 \cdot \sigma_{\text{bulk}}^2} \right] \cdot e^{2\pi i \vec{q} \cdot \vec{r}_j}}_{\text{surface contribution of 2nd to 6th ML}} \Bigg|^2
\end{aligned} \tag{11.57}
$$

where σ_{bulk} is the dynamical bulk root mean square (rms) displacement amplitude representing thermal vibrations of atoms in the crystal bulk, σ_1 is a displacement parameter for surface atoms regarding static as well as dynamic displacements, $\vec{r}_j$ are vectors pointing to surface unit cell atoms in the j-th surface layer and AZ is a scale factor which includes the atomic form factor f_{Au} of gold. Since the diffracted intensity was measured at a fixed position in reciprocal space all correction terms are constant and were incorporated into AZ. The surface is described by six atomic layers with according coverages $\theta_1(t), \ldots, \theta_6(t)$ which are placed in direct continuation of the crystal bulk (see figure 11.15b). Six surface layers are sufficient to model the initial stage of electrodissolution where clear oscillations are observed in the electrochemical current as well as in the scattered X-ray intensity. The origin of the coordinate system perpendicular to the surface, $z = 0$, is defined by the position of the second atomic layer in the bulk (figure 11.15b). Adsorbate layers consisting of Cl$^-$, AuCl$_4^-$ or other gold-chloride complexes have not been considered in the model. It is difficult to include the adlayer structure without detailed knowledge about its structural composition particularly for reciprocal space positions on non-specular crystal truncation rods. Furthermore the adlayer structure is expected to permanently change with time during the electrodissolution process since adsorbed chloride ions participate in the formation of gold-chloride complexes and leave the electrode surface.

Specular crystal truncation rod measurements of Au(111) electrodes in 0.01 M NaCl solution revealed that there is no apparent relaxation of the gold-gold layer spacing for the topmost gold layer (within 0.5%) in the unreconstructed (1×1) phase at positive electrode potentials [152]. Thus, all static distances between the gold layers have been fixed to the bulk value of $c/3 = 2.356\,\text{Å}$ in our model. For the rms displacement amplitude σ_1 of atoms in the topmost gold layer a value of $\sigma_1 = 0.12\,\text{Å}$ was determined in 0.01 M NaCl solution [152]. We assume a similar displacement for Au surface atoms in the present HCl containing solution. The vibrational amplitude of atoms in the crystal bulk of gold was measured by electron spectroscopy for chemical analysis (ESCA) which provided a value of $\sigma_{bulk}=0.084\,\text{Å}$ [22].

During the electrodissolution process the surface morphology permanently changes with time, i.e. certain fractions of a few surface near atomic layers are in direct contact with the electrolyte. According surface atoms have to be described by σ_1 while covered Au atoms in lower layers are exclusively afflicted with the bulk Debye-Waller factor based on σ_{bulk}. This behavior has been incorporated into the fit procedure in order to model the correct Debye-Waller factors for all times t of the dissolution process. The initial topmost layer (layer I) solely consists of surface atoms, thus the second summand in equation 11.57 contains a Debye-Waller factor based on σ_1. Underlying layers may either be fully or partially covered. The coverage of the n-th monolayer is always smaller or equal to the coverage of the $(n+1)$-th monolayer. Thus the fraction of the $(n+1)$-th monolayer being exposed to the electrolyte is given by $\theta_{n+1} - \theta_n$ while the fraction being covered by the n-th monolayer equals the coverage θ_n of the overlaying layer. An Origin C implementation of the fit function 11.57 is listed in appendix A.5.

11.7.2 Fit of the X-ray Model Function to the Measured Intensity Data

The experimental X-ray data was recorded parallel to the electrochemical current-time transients at the fixed reciprocal space position $(0\,,1\,,0.1)$. For this, data was acquired via SPEC control software and additionally by the analog detector signal which was fed into an analog voltage input channel of the Iviumstat potentiostat. The latter technique has two advantages. First, as noted before the time resolution is significantly higher compared to conventional X-ray detection via SPEC ($\approx 0.5\,\text{s}$ per data point in SPEC). In the case of analog signal recording the time resolution is approximately given by the detector time constant which was set to 0.1 s. Accordingly a sampling rate of 20 Hz was used. Second, the X-ray data monitored via potentiostat is accurately time synchronized with the current data, while there is always an inevitable, small timeshift between SPEC data and electrochemical current data. For normalization the monitor signal was recorded by use of a second analog input channel of the potentiostat. Since the monitor intensity was constant in all potential step experiments we desist from monitor normalization. Unfortunately, analog X-ray detector signals were only measured for all scans subsequent to potential step 'D' in figure 11.13, i.e. in a potential regime ranging from 1.1 V to 1.25 V. However, for two reasons X-ray data acquired via SPEC could not be fitted by the model function. Due to the low time resolution each measured SPEC data point represents an integrated intensity over a time period of 0.5 s. Especially for high dissolution rates ($E_{end} \geq 1.10\,\text{V}$) this insufficient time resolution would

allow to fit oscillations with arbitrary oscillation period to the data on the one hand and it complicates the time synchronization of X-ray data and electrochemical current data on the other hand. For low dissolution rates ($E_{end} \leq 1.07\,\text{V}$) the time resolution of the SPEC data was sufficient but no pronounced oscillations were observed in the current-time transients. Thus, we focus on the X-ray data recorded via analog detector signal in the following. In order to maximize the time resolution no normalization scans were recorded during the dissolution process at anodic overpotentials so that the model function has been applied to the unnormalized intensity data. Sporadically taken azimuthal scans at $0.5\,\text{V}$ in the double layer regime revealed a comparatively low background intensity ($\leq 4\%$ peak intensity) and thus background contributions were safely disregarded in the fitting process.

The model function 11.57 has been fitted to the X-ray data. For this it is necessary to know the time-dependence of the coverages $\theta_n(t)$. One possibility is to simulate the coverages. However, in the present case we benefit from the recorded current-time transients. Thus, both the X-ray data and the electrochemical current data have been fitted simultaneously by non-linear least square method. This procedure is expected to provide more accurate and reliable information about the Au(111) electrode surface during the layer-by-layer dissolution process than an exclusive modeling of the electrochemical data. In detail, the complete parameter set of the current fit function is used within the least-square fit procedure to calculate the currents $j_i(t)$ via equation 11.35 and the coverages $\theta_i(t)$ via equation 11.31 for each monolayer at the time t. The resulting total current $j(t) = \sum j_i(t)$ and the resulting coverages are used within the same iteration step to simultaneously fit the two model functions 11.40 and 11.57 to the current-time transient and the X-ray data, respectively. Hence, for $t > 0$ the parameter set of the combined fit consists of all parameters of the current fit function extended by the additional parameter AZ. For all times $t < 0$ the surface morphology is static and the X-ray intensity is constant. It became evident during the fitting process that the scaling factor AZ is not capable to fit the intensities $I(t < 0)$ based on the coverages of the n layers at $t = 0$. This effect probably has to be related to the non-steady state conditions induced by the potential step, e.g. by a sudden change of the chloride adlayer structure. Therefore we applied a different scale factor $AZ2$ for all times $t < 0$. The scaling parameters AZ and $AZ2$ provide no important information and will not be discussed in the following.

Figure 11.16 shows the combined fit of dataset 'D' which was recorded in parallel to a potential step from $0.5\,\text{V}$ to $1.1\,\text{V}$. Obviously, the simultaneous fit accurately describes the electrochemical current data (figure 11.16a) and the X-ray intensity (figure 11.16c). The obtained time-dependent coverage curves of the n surface layers are shown in figure 11.16b. All fit parameters, besides of the scaling factors AZ and $AZ2$, are summarized in table 11.1 in the row denoted by transient D. Concerning the X-ray intensity all characteristic features of the acquired data are well reproduced, i.e. the increase in oscillation period and the time-dependent decay of the oscillation amplitude. Particularly the first intensity minimum in direct onset of the dissolution process is reasonably described by the model curve. However, the calculated intensity in the first maximum is larger than the measured data and a further deviation between the fit curve and measured X-ray intensity can be seen in the fourth and
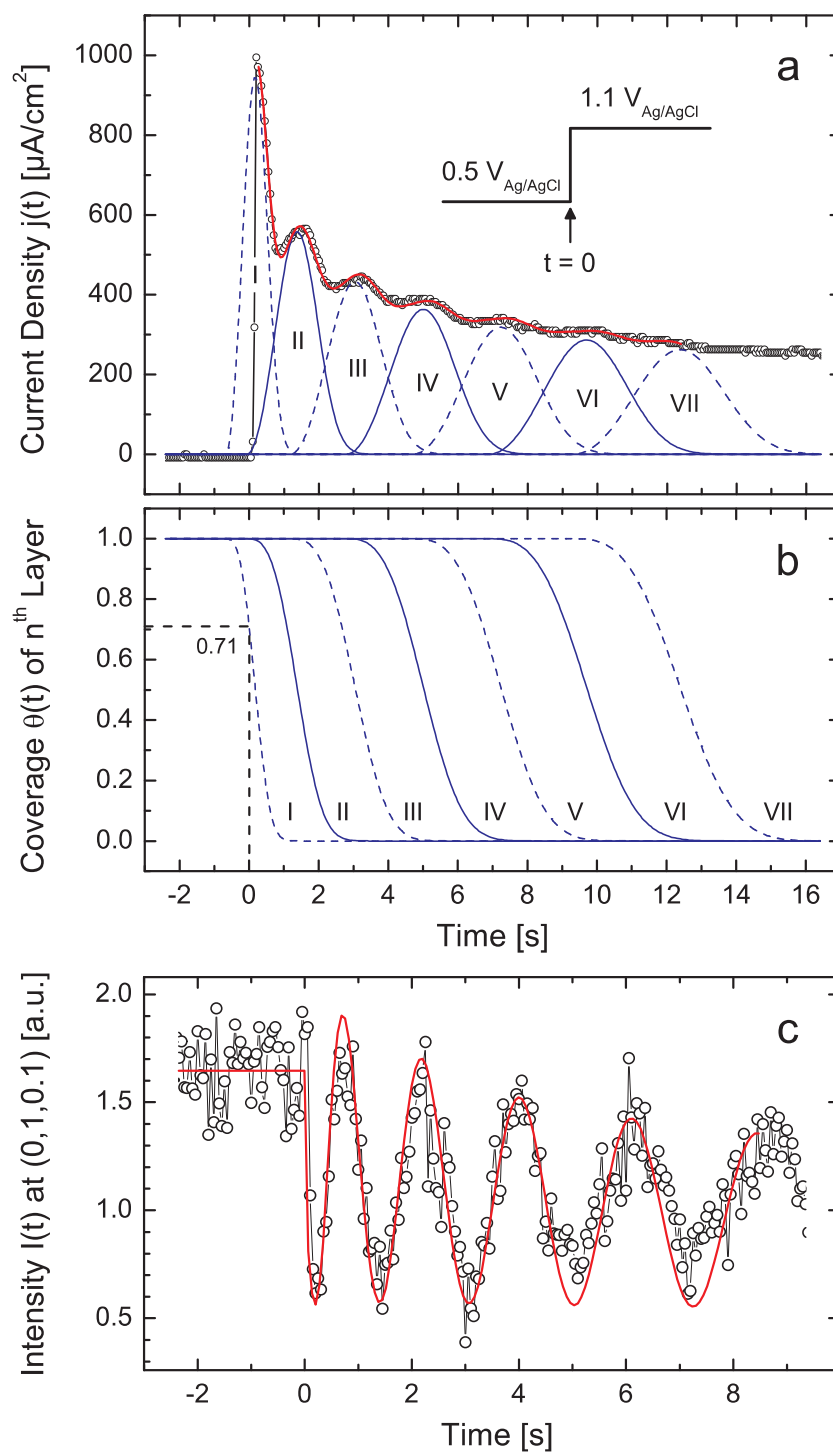
Figure 11.16: Combined fit of Au(111) dissolution oscillations observed in a) the electrochemical current and c) the scattered X-ray intensity at the reciprocal space position $(0, 1, 0.1)$. Figure b shows the time-dependent coverages $\theta_1(t)$ to $\theta_7(t)$ of the seven topmost surface layers. The data has been acquired parallel to a potential step from $0.5\,\mathrm{V}$ to $1.1\,\mathrm{V}$.

fifth oscillation period where the data points in the oscillation minima do not match well with the modeled intensities. These discrepancies most probably have to be attributed to diffuse scattering which increases with time due to a moderate progressive roughening of the electrode surface. The intensity increase is relatively small in the considered dataset but it is existing in more pronounced form in other potential step experiments. The same behavior of increasing intensity has been observed in homoepitaxial electrodeposition experiments on Au(100) electrodes (figure 9.7). Nevertheless, despite these deviations the modeled X-ray intensity agrees with the measured data. Since the X-ray intensity is directly linked to the current data via the time-dependent coverages $\theta_n(t)$ the simultaneous fit confirms that the simple current model based on discretization of k is well suited to describe the layer-by-layer dissolution process and it provides confidence in the obtained model parameters. This is particularly true for $t \gg 0$ when the electrochemical system approaches stationary conditions (second and further monolayers).

In the following we focus on the critical time period subsequent to the potential step ($0 \leq t \leq 1\,s$), when non-stationary conditions at the electrochemical interface strongly influence the electrochemical current and the dissolution process. Even though the incorporation of layer I to the model function 11.40 allows to fit the current-time transient and the X-ray data the information content of layer I remains unclear for mainly two reasons. First, the premise that k is only weakly time-dependent during dissolution of a single monolayer is obviously not fulfilled for layer I in the respective time period. Hence it is questionable if the dissolution of layer I is describable by a current based on equation 11.35. Second, the current contribution of the double layer (DL) charging process cannot be separated from the current contribution related to the dissolution of layer I. This is a consequence of the unknown time constant τ_{DL} of the exponentially decaying charging current and of the very similar shape of the decaying part of the current model curve 11.35. In this regard the measured current in the time period between $t = 0$ and $t \approx 1\,s$ may be determined by one of the following cases

1. regard of DL charging current ($\tau_{DL} \gg 0$) and disregard of layer I ($\theta_1 = 0$)

2. disregard of DL charging current ($\tau_{DL} \approx 0$) and regard of dissolution of layer I ($\theta_1 > 0$)

3. regard of DL charging current ($\tau_{DL} > 0$) and regard of dissolution of layer I ($\theta_1 > 0$)

Case 3 is very complex and has not been modeled. However, we tried to fit the current-time transient according to case 1 by including an exponentially decaying function for the DL charging process. The fit procedure could not describe the measured data so that layer I is supposed to give significant contributions to the current. Case 2 has been modeled in all of our fits based on the assumption that the current of layer I is well described by equation 11.35. At this point we tentatively assume that the modeled current curve of layer I approximates the real current contribution. At the time $t = 0$ a coverage of $\theta_1(t = 0) = 0.71$ is inferred from the coverage curves in figure 11.16b while all other layers have full coverage. Analog fractional coverages $\theta_1 = 0.61, 0.46, 0.68, 0.71$ and 0.63 were determined for the transients A, B, C, D and E, respectively. Thus the fractional coverages θ_1 predominantly range
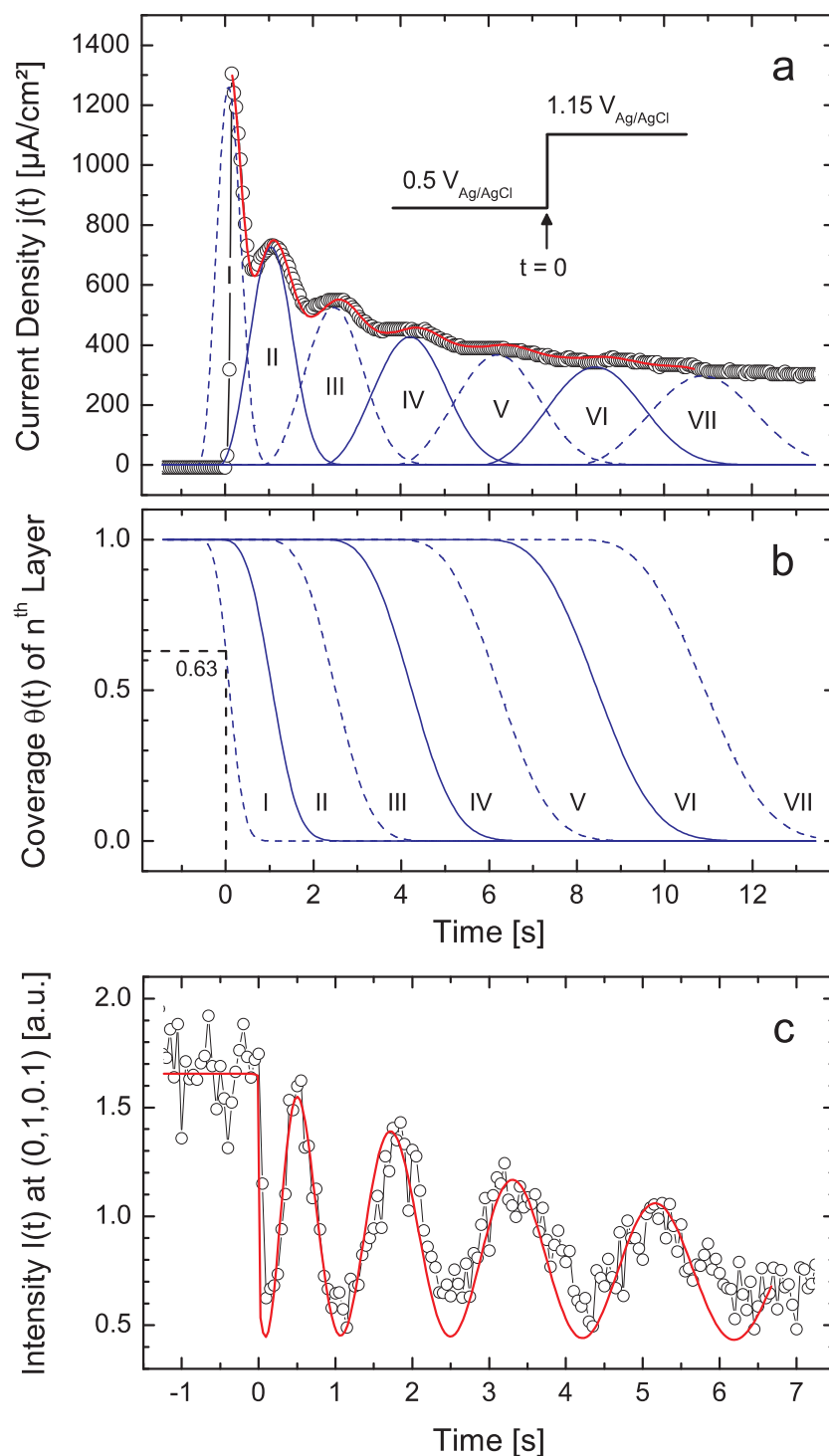
Figure 11.17: Combined fit of Au(111) dissolution oscillations observed in a) the electrochemical current and c) the scattered X-ray intensity at the reciprocal space position $(0, 1, 0.1)$. Figure b shows the time-dependent coverages $\theta_1(t)$ to $\theta_7(t)$ of the seven topmost surface layers. The data has been acquired parallel to a potential step from 0.5 V to 1.15 V. In order to fit the X-ray data an intensity slope subsequent to the potential step has been corrected.

from 0.6 to 0.7. Interestingly, controlled dissolution experiments, which are presented in section 11.8, as well indicated initial coverages of $\theta_1 \approx 0.75$ in the topmost surface layer. The similarity of both values may be either coincidental or it indicates that the current curve of layer I contains some true information about the topmost surface layer. However, due to the very complex situation within the first second after the potential step no definite conclusion can be drawn.

The second dataset which could be fitted by the X-ray model function is dataset E and was recorded parallel to a potential step from 0.5 V to 1.15 V. In contrast to dataset D the latter exhibits a more pronounced intensity increase subsequent to the potential step (cp. figure 11.6). Since the X-ray model is unable to describe the intensity increase we subtracted it so that all intensity minima are leveled on the same baseline. Obviously this procedure is not quite correct but a fit to the data will provide at least a more accurate oscillation period. Figure 11.17 shows the combined fit of the electrochemical current and the X-ray intensity. The current oscillations are accurately described by the model function. The X-ray fit is less precise but changes in the oscillation period are well reproduced up to the fourth oscillation period. As expected the model curve deviates most notably in the oscillation minima and maxima. Nevertheless, electrochemical and X-ray data are in basic agreement.

11.8 Controlled Electrodissolution of Au(111) Electrodes

The controlled dissolution of single surface layers plays an important role in semiconductor device fabrication, e.g. for ultra large scale integrated circuits (ULSI), and it will be of importance in future fabrication of microelectromechanical systems (MEMS). The development of etching and epitaxy technology with atomic scale controllability is thus highly desirable. One of the best studied systems is the 'digital etching' of GaAs either photo-assisted via tunable deep ultraviolet (DUV) laser in an etching gas atmosphere [209, 210] or from the solution phase (wet etching) [211]. Digital etching is a technology which involves self-limiting mechanisms, i.e. the etching rate is exactly controlled in atomic scale without any precise control of etching parameters. Hence, the etching rate is independent of etching time and etchant gas flow rate. It is clear that this premise is not fulfilled in the present system because the amount of dissolved material is a function of time. Nevertheless, by appropriate time control of the applied electrode potential in the layer-by-layer dissolution regime the same result is achieved. In contrast to step-flow dissolution, the layer-by-layer dissolution can be followed by variations in the scattered X-ray intensity and thus the dissolved amount of gold can be easily determined. The present system is of particular interest since most grown Au films are (111)-oriented.

The layer-by-layer dissolution found for Au(111) electrodes in chloride containing solution allows to repetitively etch off single surface layers. Based on the results of the previous sections we performed well controlled dissolution experiments. For this we employed two methods. The etching process was either controlled by the applied electrode potential in potentiostatic mode or by the applied electrochemical current in galvanostatic mode. In parallel to the dissolution process the surface morphology was monitored by the scattered

X-ray intensity at the reciprocal space position $(0, 1, 0.1)$. Figure 11.18 shows the data of two experiments which were carried out on Au(111) electrodes in 50 mM H_2SO_4 + 5 mM HCl. The results are discussed in the following.

11.8.1 Potentiostatic Experiments

In potentiostatic experiments the electrode potential was first kept at an electrode potential of 0.5 V where the surface morphology is static and where a maximum in X-ray intensity is achieved at the reciprocal space position $(0, 1, 0.1)$. Then the electrode potential was stepped for a time Δt_1 to a potential E_{end} in the dissolution regime. After this time period an electrode potential of 0.95 V was applied in order to freeze the surface morphology. As can be seen by the cyclic voltammogram in figure 11.4b the potential of 0.95 V is close to the Nernst equilibrium potential and significant redeposition of the previously dissolved gold is avoided. In the scattered X-ray intensity now a minimum is observed. Subsequent to a certain resting time at 0.95 V the potential was stepped a second time to the potential E_{end} in order to continue the dissolution process. It is observed that the time necessary to achieve the original X-ray intensity, Δt_2, usually differs from the time Δt_1 applied in the first potential pulse. Δt_2 is the time required to dissolve half a monolayer $(\Delta t_{\mathrm{ML}/2})$ and depends on the dissolution rate at the respective potential E_{end}. The meaning of Δt_1 will
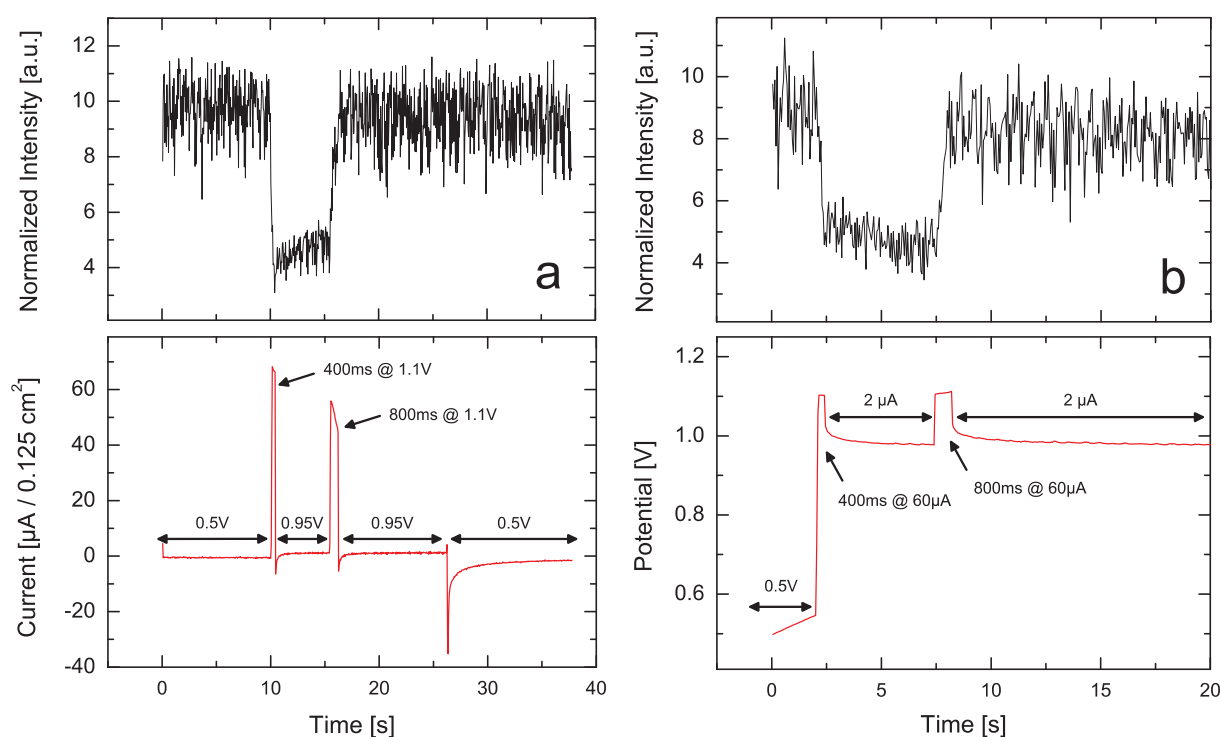
Figure 11.18: Controlled etching of a Au(111) electrode in 50 mM H_2SO_4 + 5 mM HCl solution. Consecutively two half monolayers have been etched from the electrode surface under a) potentiostatic and b) galvanostatic control. The etching process was followed by the scattered X-ray intensity at the reciprocal space position $(0, 1, 0.1)$.

be explained below. After the second pulse the potential was stepped back to 0.95 V. The success of the controlled etching process depends on the exact choice of the dissolution times Δt_1 and Δt_2. The best conditions have been found by experimentally.

Figure 11.18a shows X-ray data and current data which were acquired by the procedure described above. The first amount of gold was dissolved by a temporary potential step to 1.1 V with a pulse duration of $\Delta t_1 = 400$ ms. Parallel to this potential step a drop in X-ray intensity is observed. In the subsequent time period of 5 seconds the potential has been kept at 0.95 V. Besides of a marginal slope the X-ray intensity stays more or less constant. The small intensity increase must be either attributed to redeposition of gold (further dissolution of the electrode) which would indicate that 0.95 V is a bit more cathodic (anodic) than the Nernst potential or it has to be attributed to a surface smoothening promoted by adsorbed chloride ions. Subsequently half a monolayer was dissolved in a further potential step to 1.1 V with a pulse duration of $\Delta t_2 = 800$ ms. This pulse length is twice as long as the previous one. The difference has to be most likely attributed to the coverage θ_1 of the topmost surface layer prior to the first potential step. In the previous section initial coverages of 60 to 70% have been determined for θ_1. Thus instead of 0.5 ML only about 0.1 to 0.2 ML have to dissolve in order to observe the first X-ray intensity minimum. In this regard an initial coverage of $\theta_1 \approx 0.75$ ML would explain the factor of two in both pulse durations. Basically the topmost surface layer exhibits an arbitrary coverage between 0 and 100% so that the choice of Δt_1 is critical for the initiation of the controlled dissolution process. However, once the dissolution process is successfully started further monolayers can be etched off by repeated Δt_2 pulses (see section 11.8.3). Parallel to the second potential pulse the X-ray intensity increased to its initial value. According to the present experiment the total time for the dissolution of ≈ 0.75 ML at 1.1 V is $\Delta t_1 + \Delta t_2 = 1.2$ s corresponding to a time $\Delta t_{ML} = 1.6$ s for one complete monolayer. This value agrees with $t_{ML} = 1.5$ s inferred from X-ray intensity oscillations (figure 11.7). The latter is a further evidence that Δt_1 depends on the initial coverage of the topmost surface layer while $\Delta t_2 = 800$ ms is the expected value for the dissolution time of 0.5 ML.

11.8.2 Galvanostatic Experiments

In galvanostatic experiments the electrode potential was first kept at 0.5 V via potentiostatic control. Then the potentiostat switched to galvanostatic control and a current of 60 μA was applied for a time Δt_1 in order to start the dissolution process and to achieve a minimum in the scattered intensity. Subsequently the current was fixed to a value of 2 μA which accords to a potential close to the Nernst potential. After a resting time of 5 seconds at 2 μA a second current pulse of 60 μA was applied. The changes in the recorded X-ray intensity are similar to those in the potentiostatically controlled experiments. Figure 11.18b shows the X-ray data and the potential data which was acquired by the procedure described above. The first and second current pulses had durations of 400 ms and 800 ms, respectively. These times are identical to the times in the potentiostatic experiments since the current value of 60 μA was chosen on the basis of the observed current in the potentiostatic experiments. This can be also seen by means of the measured electrode potential which is ≈ 1.1 V during the

dissolution process. The two current pulses correspond to charge transfers of $Q(\Delta t_1) = 24 \, \mu\text{C}$ and $Q(\Delta t_2) = 48 \, \mu\text{C}$, respectively. Normalizing these values to the unit area of $1 \, \text{cm}^2$ yields $Q(\Delta t_1) = 191 \, \mu\text{C cm}^{-2}$ and $Q(\Delta t_2) = 382 \, \mu\text{C cm}^{-2}$. The latter is in reasonable agreement with the nominal charge $Q_{ML/2} = 333 \, \mu\text{C cm}^{-2}$ (cp. equation 11.25) which is expected for the dissolution of half a monolayer.

11.8.3 Mixed Mode Experiments

The employed potentiostat (Iviumstat) allows alternating measurements under potentiostatic and galvanostatic control. This had been utilized to repeatedly dissolve half monolayers of the Au(111) electrode. In order to freeze the surface morphology the potential was set to 0.95 V via potentiostatic mode. The Nernst potential is easily obtained via cyclic voltammetry so that the potentiostatic mode provides best control of the resting potential. For the dissolution of the crystal the galvanic mode was used and the current was fixed to $60 \, \mu\text{A}$ during the current pulses. The galvanostatic mode is best suited for control of the dissolution process since it allows to predefine the dissolving gold amount by the pulse duration.

Figure 11.19 shows the X-ray data and electrochemical data of an experiment in which repeatedly half monolayers were dissolved. In total 3 monolayers were etched off from the electrode surface. During this procedure current pulses of $60 \, \mu\text{A}$ were applied for $\Delta t_{ML/2} = 900 \, \text{ms}$. In contrast to the previously discussed dissolution experiments now all pulse durations are
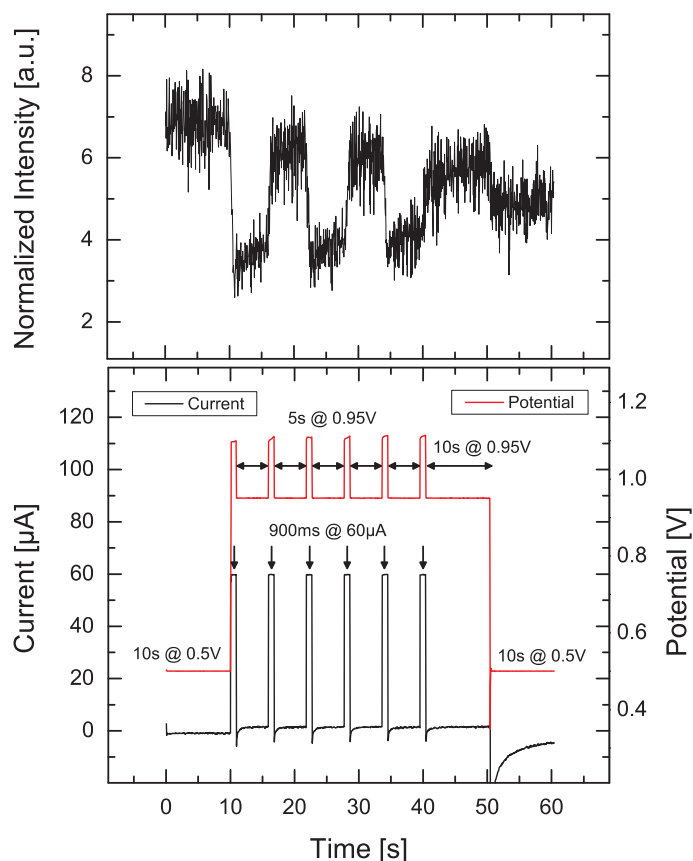
Figure 11.19: Repetitive dissolution of single monolayers. Half monolayers are dissolved by galvanostatically controlled current pulses of $60 \, \mu\text{A}$ and a pulse duration of 900 ms. Between single dissolution processes the electrode potential has been kept at the resting potential of 0.95 V via potentiostatic mode.

identical. Apparently the electrode surface was almost perfectly terminated prior to the experiment. The X-ray intensity measured at 0.95 V changes with each dissolution cycle, i.e. the intensity maxima decrease while the intensity minima increase. This indicates that the time $\Delta t_{ML/2}$ was inaccurately chosen and that it does not accord to the dissolution of half a monolayer. A 60 μA current pulse of 900 ms duration corresponds to a charge transfer of 54 μC with respect to the surface area or to 430 μC cm^{-2} with respect to unit area. Thus, according to equation 11.25 each current pulse resulted in the dissolution of ≈ 0.65 ML. Furthermore, since the holding times at 0.95 V between two current pulses were rather short with 5 seconds no pronounced surface smoothening could proceed so that the electrode surface is expected to roughen with time. Nevertheless, the experiment nicely demonstrates that controlled etching of Au(111) electrodes is in principal possible over several atomic surface layers. The dissolution process can be still optimized by appropriate choice of the pulse duration, of the holding potential and the according holding time and of the dissolution rate (via chloride concentration and via choice of the anodic overpotential).

11.9 Summary

The performed experiments demonstrate that in agreement with previous STM studies of Ye et al. [16, 17] the electrodissolution of Au(111) in Cl$^-$ containing solution proceeds via step-flow mode close to the Nernst potential (0.95 V) and via layer-by-layer mode at higher anodic overpotentials in the active dissolution regime. However, while for scanning probe techniques (e.g. STM and AFM) the 'real' dissolution behavior is inaccessible at high anodic overpotentials due to tip shading effects and due to an insufficient time-resolution the present SXS study clearly shows layer-by-layer dissolution until the surface passivates at sufficiently anodic electrode potentials ($\gtrsim 1.2$ V). No distinct multilayer dissolution has been found on initially smooth surfaces. The layer-by-layer dissolution process manifests in X-ray intensity oscillations and in oscillations in the electrochemical current. The latter is particularly interesting since current oscillations due to layer-by-layer dissolution of single crystal metal electrodes have not been reported up to now. Even at comparatively high dissolution rates of ≈ 26 ML min^{-1} in the diffusion-limited potential regime several oscillations in the electrochemical current and in the X-ray intensity have been observed. However, it is important to note that attempts to reproduce the data indicate a strong dependence of the current oscillations on the initial surface quality. We estimate on the basis of our data analysis that in order to observe current oscillations only the topmost two or three surface layers are allowed to exhibit incomplete coverage while all underlying layers have to be fully filled. Thus a very low degree of surface roughness over the total area of the electrode/electrolyte interface is required which is a tremendous challenge in terms of surface preparation.

Current-time transients were measured parallel to potential steps into the layer-by-layer dissolution regime and have been quantitatively analyzed. For this a two-dimensional standard growth model which describes the current arising from the deposition of a single monolayer under steady state conditions has been modified and applied to the dissolution data. The extended model includes the Cottrellian current decay due to the time-dependent evolution of the Nernst diffusion layer. This simple model successfully describes the current data in

almost the entire potential regime of layer-by-layer dissolution. Simultaneous fits to the electrochemical data and to the corresponding structure-sensitive X-ray data provides confidence in the current model and in the model parameters. The analysis reveals that layer-by-layer dissolution proceeds exclusively via progressive nucleation and growth of stable vacancy clusters in addition to the dissolution at step edges.

The characteristics of the current oscillations are dependent on the sample history. Transients which were recorded directly after preparation of the electrode surface exhibit the most pronounced current oscillations. Especially for those transients the model fit parameters provide a total charge transfer per monolayer which agrees well with the theoretical value of $Q_{ML} = 666\,\mu\mathrm{C\,cm^{-2}}$. A potential step to $1.1\,\mathrm{V}$ indicates that second layer nucleation sets in when $MLF = 44\%$ of the previous layer is dissolved. This value is smaller than the critical coverage of $\theta_c \approx 0.66$ which was theoretically predicted to determine the 2D-3D transition in homoepitaxial electrodeposition experiments [1]. Nonetheless dissolution proceeds via layer-by-layer mode which likely has to be attributed to the anisotropy of the dissolution process. For subsequent potential steps into the dissolution regime the model provides increasing values for the charge transfer per monolayer and decreasing MLF-values for second layer nucleation. This is a clear evidence for surface roughening. Accordingly the current-time transients exhibit weaker oscillations with lower oscillation amplitudes. Since the determined charge transfer per monolayer is larger than the theoretical value the current of a single monolayer now contains contributions from underlying layers and thus the model parameters do not precisely reflect the dissolution process. Therefore, no clear information about the potential-dependence of single model parameters (e.g. the onset of second layer nucleation) could be inferred from the series of current-time transients. Nevertheless, even though the surface is not very smooth the measured X-ray intensity could be well fitted based on the layer coverages. Thus the obtained model parameters at least approximate the dissolution behavior. The surface roughening has to be ascribed to mainly two processes that is the (imperfect layer-by-layer) dissolution process and the redeposition of previously dissolved gold. An additional surface roughening after potential steps into the passivation regime cannot be excluded but for the employed chloride concentration the influence of an oxidation-reduction cycle on the surface morphology seems to be small. Increased surface roughness was also observed in the scattered X-ray intensity. Azimuthal intensity profiles taken at $(0\,,1\,,0.1)$ broadened with the amount of performed dissolution experiments indicating an enhanced diffuse scattering. In the presence of adsorbed chloride ions rough surfaces smoothened at a holding potential of $0.5\,\mathrm{V}$ in the double layer regime. Sufficiently extended holding times of more than 10 minutes resulted in an almost full recovery of the X-ray intensity in anti-Bragg.

The analysis shows that Au(111) electrodes predominantly dissolve in the layer-by-layer mode while for homoepitaxial growth on Au(111) electrodes only indications for 3D growth or very non-ideal layer-by-layer growth were found. This demonstrates that electrodeposition and electrodissolution do not have to be symmetrical processes. We utilized the layer-by-layer dissolution mode to perform well controlled dissolution experiments which allow the stepwise etching of single surface layers.

12 Summary

The structure and surface morphology of Au(100) and Au(111) electrodes in gold and chloride containing solutions was investigated in-situ by surface-sensitive X-ray scattering (SXS). Utilizing the high time resolution and the high surface sensitivity of the SXS technique structural changes in the potential regimes of electrodeposition and electrodissolution were determined. Moreover, for the first time homoepitaxial growth and electrodissolution on single crystal electrodes could be studied under real reaction conditions, i.e. with unrestricted mass transport in the electrochemical cell. Operating in the diffusion-limited potential regime, i.e. at constant deposition rate (which is determined by the Au concentration in the electrolyte), the growth behavior was studied as a function of the electrode potential and deposition rate. This allowed to clarify the complex relationship between the atomic-scale structure of the solid-liquid interface, the growth behavior and the resulting surface morphology.

A novel X-ray transmission cell has been developed for the SXS experiments. In this cell the X-ray beam penetrates through a free-standing electrolyte meniscus which is established between the electrochemical cell and the electrode surface. The special design of the electrochemical cell allows to rapidly replace the solution. For this a remote-controlled electrolyte exchange system was developed based on two motor-driven syringe pumps. Our new experimental setup, which meanwhile has been copied by other groups, is perfectly suited for electrodeposition and electrodissolution studies as it simultaneously allows to obtain high quality electrochemical data and SXS data, respectively, and to control the electrolyte. The setup facilitates more complicated deposition experiments so that similar studies may help to clarify other fundamental as well as applied problems, e.g., the role of organic additives in electrodeposition or biomineralization processes.

The lateral surface structure and the surface morphology of Au(100) electrodes in Au-free and in Au-containing 0.1 M HCl solution has been investigated in-situ by SXS. It is well-known that the Au(100) electrode surface reconstructs from the (1×1) bulk structure to a quasi-hexagonal 'hex' structure at sufficiently negative electrode potentials. A characterization of the reconstructed surface layer in Au-free 0.1 M HCl solution shows that the 'hex' layer is characterized by a surface strain (area contraction) of $\epsilon = $ -19.90%. Reconstructed domains are preferentially rotated by an angle of $\Delta\theta = 0.72° \pm 0.05°$ with respect to the $[110]_c$ direction of the unreconstructed substrate. In almost the entire potential regime of the reconstructed phase (< 0.15 V) neither the size of the surface unit cell nor the rotation angle $\Delta\theta$ exhibits a pronounced potential-dependence. The (1×1) → 'hex' surface phase transition in 0.1 M HCl is a comparatively slow process. The electrode surface was found to be 90% reconstructed approximately 17 min subsequent to a potential step into the reconstructed potential regime. On the basis of these results the influence of homoepitaxial growth was investigated.

In-plane scans which were performed in parallel to an electrolyte exchange from Au-free to Au-containing solution revealed that the homoepitaxial growth induces an enhanced compression of the reconstructed surface layer as well as an alignment of rotated 'hex' domains along the $[110]_c$ direction. Both effects are strongly potential-dependent and reversible: the 'hex' layer compresses linearly towards more negative potentials while simultaneously an almost linear rotational transition from rotated domains to aligned domains is observed.

A similar effect of linear electrocompression has been previously found in our group for homoepitaxial growth on reconstructed Au(111) electrodes [12]. The compressed, reconstructed Au(100) surface layer at the most negative investigated electrode potential (E = -0.4 V) is characterized by a surface strain of ϵ = -20.52 % which is significantly lower than in Au-free solution. The data is in agreement with a perfect uniaxial compression perpendicular to the reconstruction stripes (in 'x5' direction) although due to significant error bars a biaxial compression (i.e. perpendicular and parallel to the reconstruction stripes) cannot be fully excluded. The electrocompression effect can be described by a simple theoretical continuum model which was first proposed by R.C. Cammarata [133]. Refering the compressed surface layers of Au(100) and Au(111) in Au containing solution to their uncompressed, reconstructed surfaces in Au-free solution the resulting potential-dependent changes in surface strain, $\epsilon(E)$, can be well reproduced. Although our data does not allow to determine the driving forces for reconstruction on both surfaces the applied continuum model indicates that within the reconstructed potential regime the main driving force for electrocompression of Au(111) electrode surfaces is the release of tensile surface stress while for Au(100) electrode surfaces the gain in surface energy is the dominating factor. An analysis of in-plane and out-of-plane data provided a deeper insight in the (1×1) → 'hex' surface phase transition under deposition conditions. Subsequent to potential steps from the unreconstructed to the reconstructed potential regime the first deposited 0.25 monolayer (ML) are directly incorporated in the unreconstructed Au(100) surface which results in an uncompressed, reconstructed 'hex' layer exhibiting a similar structure as potential-induced, reconstructed surfaces in Au-free electrolyte. Here an enhanced surface compression seems to be hindered by kinetic limitations since the initial formation of reconstruction requires the insertion of Au adatoms into the existing surface layer. The 'hex' phase forming within a few seconds on the (initially unreconstructed) surface ($\theta \leq 0.25$ ML) is rather disordered. Parallel to the proceeding layer-by-layer growth a slower ripening of the reconstructed surface is observed. The compressed phase forms with the deposition of the successive monolayer and is almost completed after a total deposit amount of 1.25 ML. In this stage of the deposition process the growth proceeds via attachment of adatoms to island step edges and no significant barrier exists for attaining the energetically preferred in-plane spacing. Consequently further layers grow in the electrocompressed phase. The rapid formation of the reconstruction during Au electrodeposition differs pronouncedly from the very slow kinetics of this process in the absence of Au-species in the solution, suggesting that the barrier for incorporation of the Au atoms into the surface is low and Au surface transport to unreconstructed areas governs the phase transition kinetics.

For the first time ever the SXS technique was utilized to monitor time-dependent changes in the surface morphology parallel to electrochemical growth under real reaction conditions. Intensity-time transients which were recorded at selected reciprocal space positions as a function of electrode potential and Au concentration revealed an interesting growth behavior on Au(100) electrodes. With decreasing potential transitions from step-flow to layer-by-layer growth, manifested by layering oscillations in the X-ray intensity, then to multilayer growth, and finally back to layer-by-layer growth were observed. The presence of all three kinetic growth modes substantiates the existence of an Ehrlich-Schwoebel barrier in electrochemical environment which was for a long time subject to speculations. Furthermore it is demon-

strated that in contrast to similar studies of MBE-growth (molecular beam epitaxy) under ultrahigh vacuum (UHV) conditions the growth behavior in electrochemical environment can be controlled by the applied electrode potential which alters energy barriers for surface adatom diffusion and for step edge diffusion. Particularly interesting is the re-entrant layer-by-layer growth in the reconstructed potential regime which demonstrates the important role of the solid surface structure on the growth behavior and on the resulting film morphology. On the other hand the pronounced step-flow growth at very positive potentials demonstrates the influence of the solution side on the growth behavior as adsorbed chloride ions promote the surface mobility of gold adatoms. Even substantially roughened surfaces were found to smoothen rapidly in the step-flow potential regime. In contrast to homoepitaxial growth on Au(100) electrodes respective studies on Au(111) electrodes provided only indications for 3D growth or non-ideal layer-by-layer growth which indicates a significantly larger step edge barrier on the (111) oriented surface. Thus the growth behavior of Au electrodes in chloride containing solution follows the general trends observed in MBE studies under UHV conditions.

Besides of electrodeposition the inverse process of electrodissolution has been studied in-situ by SXS. Our experiments demonstrate that in agreement with previous STM studies of Ye et al. [16, 17] the electrodissolution of Au(111) in Cl⁻ containing solution proceeds via step-flow mode close to the Nernst potential (0.95 V) and via layer-by-layer mode at higher anodic overpotentials in the active dissolution regime. However, while for scanning probe techniques (e.g. STM and AFM) the region of high anodic overpotentials is inaccessible due to tip shading effects and insufficient time-resolution the present SXS study clearly shows layer-by-layer dissolution until the surface passivates at a sufficiently anodic electrode potential ($\approx 1.2\,\mathrm{V}$) [185, 204]. No distinct multilayer dissolution has been found on initially smooth surfaces. The layer-by-layer dissolution process manifests in X-ray intensity oscillations and in oscillations in the electrochemical current. The latter is particularly interesting since current oscillations due to layer-by-layer dissolution of single crystal, metal electrodes have not been reported up to now. Even at comparatively high dissolution rates of $\approx 26\,\mathrm{ML\,min^{-1}}$ in the diffusion-limited potential regime several oscillations in the electrochemical current and in the X-ray intensity were observed. Current-time transients in the layer-by-layer dissolution regime have been quantitatively analyzed. For this a two-dimensional standard growth model which describes the current arising from the deposition of a single monolayer under steady state conditions has been modified and applied to the dissolution data. The model successfully describes the current data in almost the entire potential regime of layer-by-layer dissolution. Electrochemical data and SXS data could be simultaneously fitted which provides confidential information about the surface structure during the dissolution process. The analysis revealed that layer-by-layer dissolution exclusively proceeds via progressive nucleation. In the layer-by-layer dissolution regime second layer nucleation sets in when approximately 35 to 40% of the previous layer is dissolved. These values are smaller than the critical coverage of $\theta_c \approx 0.66$ which was theoretically predicted to determine the 2D-3D transition in homoepitaxial electrodeposition experiments [1]. Nonetheless dissolution proceeds via layer-by-layer mode which likely has to be attributed to the anisotropy of the dissolution process. The layer-by-layer dissolution mode has been utilized to perform well controlled dissolution experiments.

A Appendix

A.1 Beamline ID32 : X-ray Source Characteristics and X-ray Optics

Table A.1 summarizes the X-ray source characteristics and the X-ray optics of beamline ID32 at the European Synchrotron Radiation Facility. The data describes the configuration in the years between 2004 to 2008.

X-ray Source Characteristics			
	1st undulator	2nd undulator	3rd undulator
magnet period	35 mm	35 mm	42 mm
K_{max}	2.3957	2.3246	3.2025
field B_{max}	2.08 T	2.01 T	1.95 T
total power	1.8 kW at 0.2 A	1.8 kW at 0.2 A	3.2 kW at 0.2 A
max. power density at 30 m	90 W mm^{-2}	90 W mm^{-2}	90 W mm^{-2}
source size	0.900×0.02 mm^2 (H × V) FWHM		
beam divergence	0.030×0.02 mrad^2 (H × V) FWHM at 10 keV		
peak flux at 25 m	7×10^{14} ph s^{-1} mm^{-2}, 0.1% bandwidth, 0.2 A		
polarization	95% horizontal, 5% vertical		

X-ray Optics	
at 30 m	Monochromator: Si(111) cryo-genically cooled
at 41 m	Mirror: 450 mm long 3 regions depending on photon energy used: SiO$_2$, Ni and Pd (formerly Ru) coated
beam size at sample (H × V)	0.9×0.05 mm^2 with 16 CRLs and E $=$ 18.2 keV
spectral range	min E $=$ 2.5 keV ; max E $=$ 30 keV
resolution in $\Delta E/E$	$\geq 10^{-4}$
flux at sample	$\approx 10^{13}$ ph s^{-1} at low energy (10^{-4} bandwidth, 0.1 A) $\approx 10^{12}$ ph s^{-1} at high energy (10^{-4} bandwidth, 0.1 A)

**Table A.1:** X-ray source characteristics and X-ray optics at ID32.

A.2 Uniaxial and Biaxial Compression

The geometrical relationship between two selected netplane distances $d(\Delta_1)$ and $d(\Delta_2)$ is shown in figure A.1 for the case of an unsheared, quasi-hexagonal surface structure. Quasi-hexagonal means that the basic structure is near hexagonal but the distance t can differ from the distance a, i.e. the structure might be already compressed along t or perpendicular to t. In this case the hexagon is composed of six triangles of the same area A. Thus, the total area is given by

$$A_h = 6 \cdot A = 6 \cdot d(\Delta_1)^2 \cdot \tan \alpha \tag{A.1}$$

A.2.1 Uniaxial Compression Parallel to d(Δ_1)

If the structure becomes uniaxially compressed (or expanded) in the direction of $d(\Delta_1)$ then the second netplane distance changes from $d(\Delta_2)$ to $d_U(\Delta_2)$. Here and in the following the index 'U' denotes values that belong to the final uniaxial compressed structure. In the considerations given below any shearing of the structure shall be excluded.
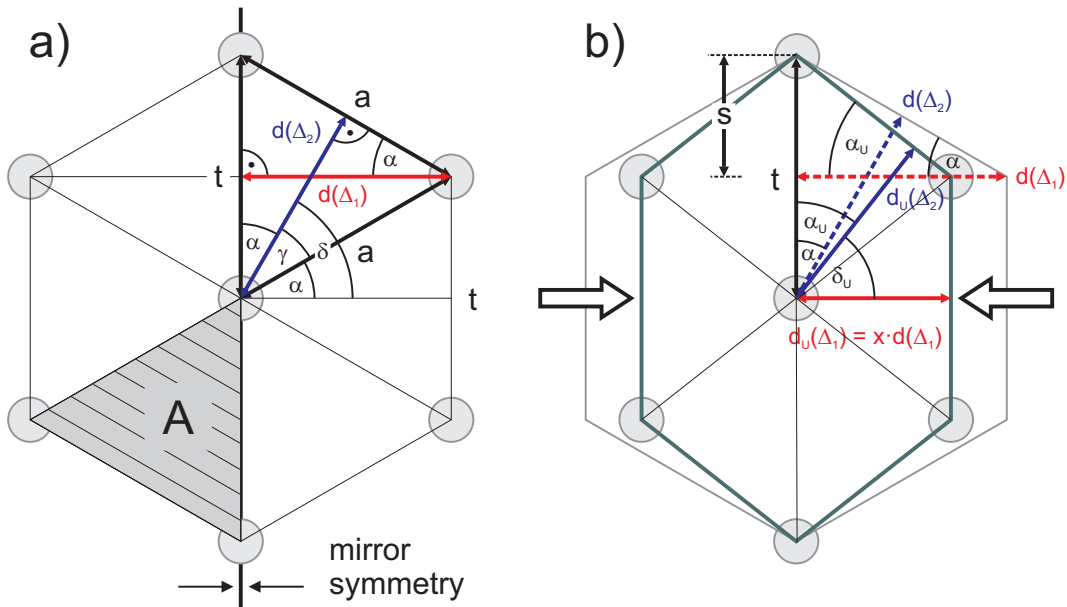
Figure A.1: a) Geometry of an unsheared, quasi-hexagonal surface structure. A denotes the area of one sixth of the total hexagonal structure. b) Additional uniaxial compression along $d(\Delta_1)$. As a consequence of the compression the second netplane distance $d(\Delta_2)$ shortens and the angle δ decreases to δ_U.

From geometrical relations the angles α, α_U and δ are obtained as a function of the netplane distances $d(\Delta_1)$ and $d(\Delta_2)$ before the compression and $d_U(\Delta_1)$ after compression. One obtains $\cos \alpha = d(\Delta_1)/a = d(\Delta_2)/t$ and $\sin \alpha = 0.5 \cdot t/a$ from figure A.1a which allows to

express α in terms of $d(\Delta_1)$ and $d(\Delta_2)$

$$\alpha = \arcsin \frac{d(\Delta_2)}{2\,d(\Delta_1)} \tag{A.2}$$

A similar expression is found for the angle δ which is defined by $\delta = 90° - \alpha$. The identity $\arccos(x) = 90° - \arcsin(x)$ leads to

$$\delta = 90° - \alpha = \arccos \frac{d(\Delta_2)}{2\,d(\Delta_1)} \tag{A.3}$$

The relations $\tan\alpha = s/d(\Delta_1)$ and $\tan\alpha_U = s/d_U(\Delta_1)$ in figure A.1b provide the angles α_U and δ_U after uniaxial compression

$$\alpha_U \;=\; \arctan\left(\frac{d(\Delta_1)}{d_U(\Delta_1)}\tan\alpha\right) \tag{A.4}$$

$$\delta_U \;=\; 90° - \arctan\left(\frac{d(\Delta_1)}{d_U(\Delta_1)}\tan\alpha\right) \tag{A.5}$$

Regarding furthermore the relations $\cos\alpha = d(\Delta_2)/t$ and $\cos\alpha_U = d_U(\Delta_2)/t$, the new value of $d(\Delta_2)$ is given by

$$d_U(\Delta_2) = \frac{d(\Delta_2)}{\cos\alpha}\cos\alpha_U = \frac{d(\Delta_2)}{\cos\alpha}\cdot\cos\left[\arctan\left(\frac{d(\Delta_1)}{d_U(\Delta_1)}\tan\alpha\right)\right] \tag{A.6}$$

Alternatively, $d_U(\Delta_1)$ can be expressed by a scaling factor x with

$$d_U(\Delta_1) = x\cdot d(\Delta_1). \tag{A.7}$$

The structure compresses for $x < 1$ while it expands for $x > 1$. By replacing $d_U(\Delta_1)$ in equation A.6 and by additional use of the trigonometrical relations

$$\tan(\arcsin x) = \frac{x}{\sqrt{1-x^2}} \qquad \cos(\arctan x) = \frac{1}{\sqrt{1+x^2}} \qquad \cos(\arcsin x) = \sqrt{1-x^2} \tag{A.8}$$

the equations A.6 and A.5 can be written as follows

Uniaxial Compression Parallel to $d(\Delta_1)$ (Real Space)

$$d_U(\Delta_2) \;=\; \frac{2\cdot|x|\cdot d(\Delta_1)\cdot d(\Delta_2)}{\sqrt{4\cdot x^2\cdot d(\Delta_1)^2 + (1-x^2)\cdot d(\Delta_2)^2}} \tag{A.9}$$

$$\delta_U \;=\; 90° - \arctan\left(\frac{1}{x}\cdot\frac{d(\Delta_2)}{\sqrt{4\cdot d(\Delta_1)^2 - d(\Delta_2)^2}}\right) \tag{A.10}$$

The compression shortens $d(\Delta_1)$ to $d_U(\Delta_1)$ as well as $d(\Delta_2)$ to $d_U(\Delta_2)$. Simultaneously the angle δ between both netplanes decreases to δ_U.

The equations A.7, A.9 and A.10 can be transferred from real space to reciprocal space by use of the relations $d(\Delta_1) = a_c/(\sqrt{2} \cdot \Delta_1)$ and $d(\Delta_2) = a_c/(\sqrt{2} \cdot \Delta_2)$ where a_c denotes the real space lattice constant. One obtains for $\Delta_{1,U}$, $\Delta_{2,U}$ and $\delta_{U,r}$ in reciprocal space

Uniaxial Compression Parallel to d(Δ_1) (Reciprocal Space)

$$\Delta_{1,U} \;=\; \frac{1}{x} \cdot \Delta_1 \tag{A.11}$$

$$\Delta_{2,U} \;=\; \frac{\sqrt{x^2 \cdot (4 \cdot \Delta_2^2 - \Delta_1^2) + \Delta_1^2}}{2 \cdot x} \tag{A.12}$$

$$\delta_{U,r} \;=\; 90° - \arctan\left(\frac{1}{x} \cdot \frac{\Delta_1 \cdot \Delta_2}{\sqrt{4 \cdot \Delta_2^4 - \Delta_1^2 \cdot \Delta_2^2}} \right) \tag{A.13}$$

In order to calculate $\Delta_{2,U}$ from the given pair Δ_1 and $\Delta_{1,U}$ the factor x might be replaced by $x = \Delta_1/\Delta_{1,U}$.

A.2.2 Uniaxial Compression Perpendicular to d(Δ_1)

Besides of an uniaxial compression along d(Δ_1) we now consider an uniaxial compression in the perpendicular direction. As the derivation is independent from the original dimensions of the unsheared structure and for reasons which will be given below, the structure defined by $d_U(\Delta_1)$, $d_U(\Delta_2)$ and α_U shall be taken as starting point for the following compression without loss of generality. The according geometry is shown in figure A.2. Analog to the previous case the strength of compression (or expansion) shall be described by a scaling factor called y. The angles α_U and δ_U are given by

$$\alpha_U = \arcsin\left(\frac{d_U(\Delta_2)}{2 \cdot d_U(\Delta_1)} \right) \tag{A.14}$$

and

$$\delta_U = 90 - \alpha_U = \arccos\left(\frac{d_U(\Delta_2)}{2 \cdot d_U(\Delta_1)} \right) \tag{A.15}$$

The two geometrical relations $\tan\alpha_B = 0.5 \cdot y \cdot t / d_U(\Delta_1)$ and $\cos\alpha_U = d_U(\Delta_2)/t$ in combination with equation A.15 determine the angles α_B and δ_B after compression

$$\alpha_B \;=\; \arctan\left[\frac{y \cdot d_U(\Delta_2)}{2 \cdot d_U(\Delta_1)} \cdot \frac{1}{\cos\alpha_U} \right] \tag{A.16}$$

$$\delta_B \;=\; 90° - \alpha_B = 90° - \arctan\left(\frac{y \cdot d_U(\Delta_2)}{2 \cdot d_U(\Delta_1)} \cdot \frac{1}{\cos\alpha_U} \right) \tag{A.17}$$

A second pair of relations, $\cos\alpha_{\mathrm{B}} = d_{\mathrm{B}}(\Delta_2)/(y\cdot t)$ and $\cos\alpha_{\mathrm{U}} = d_{\mathrm{U}}(\Delta_2)/t$, allows us to obtain the netplane distance $d_{\mathrm{B}}(\Delta_2)$ after the perpendicular (second) compression

$$
\begin{aligned}
d_{\mathrm{B}}(\Delta_2) &= y\cdot d_{\mathrm{U}}(\Delta_2)\cdot\frac{\cos\alpha_{\mathrm{B}}}{\cos\alpha_{\mathrm{U}}} \\[2mm]
&= y\cdot d_{\mathrm{U}}(\Delta_2)\cdot\frac{\cos\left[\arctan\left(\frac{y\cdot d_{\mathrm{U}}(\Delta_2)}{2\cdot d_{\mathrm{U}}(\Delta_1)}\cdot\left[\cos\left(\arcsin\frac{d_{\mathrm{U}}(\Delta_2)}{2\cdot d_{\mathrm{U}}(\Delta_1)}\right)\right]^{-1}\right)\right]}{\cos\left[\arcsin\left(\frac{d_{\mathrm{U}}(\Delta_2)}{2\cdot d_{\mathrm{U}}(\Delta_1)}\right)\right]}
\end{aligned}
\tag{A.18}
$$

The equations A.17 and A.18 can be rewritten by use of the mathematical identities in (A.8). The new length of the second netplane and δ_B is given by

---

<div align="center">

Uniaxial Compression Perpendicular to d(Δ_1) (Real Space)

</div>

$$
d_{\mathrm{B}}(\Delta_1) = d_{\mathrm{U}}(\Delta_1) \tag{A.19}
$$

$$
d_{\mathrm{B}}(\Delta_2) = \frac{2\cdot y\cdot d_{\mathrm{U}}(\Delta_1)\cdot d_{\mathrm{U}}(\Delta_2)}{\sqrt{4\cdot d_{\mathrm{U}}(\Delta_1)^2 + (y^2-1)\cdot d_{\mathrm{U}}(\Delta_2)^2}} \tag{A.20}
$$

$$
\delta_B = 90° - \arctan\left(\frac{y\cdot d_{\mathrm{U}}(\Delta_2)}{\sqrt{4\cdot d_{\mathrm{U}}(\Delta_1)^2 - d_{\mathrm{U}}(\Delta_2)^2}}\right) \tag{A.21}
$$

A compression perpendicular to $d_{\mathrm{U}}(\Delta_1)$ does not change $d_{\mathrm{U}}(\Delta_1)$ but it compresses $d_{\mathrm{U}}(\Delta_2)$ to $d_{\mathrm{B}}(\Delta_2)$. Simultaneously the angle δ_{U} increases to δ_{B}, i.e. changes in the opposite direction as in the previous uniaxial compression parallel to $d(\Delta_1)$.

Reciprocal space expressions of the equations A.20 and A.17 are obtained in the same way as described above

---

<div align="center">

Uniaxial Compression Perpendicular to d(Δ_1) (Reciprocal Space)

</div>

$$
\Delta_{1,B} = \Delta_{1,U} \tag{A.22}
$$

$$
\Delta_{2,B} = \frac{\sqrt{4\cdot\Delta_{2,U}^2 + (y^2-1)\cdot\Delta_{1,U}^2}}{2\cdot y} \tag{A.23}
$$

$$
\delta_{B,r} = 90° - \arctan\left(\frac{y\cdot\Delta_{1,U}}{\sqrt{4\cdot\Delta_{2,U}^2 - \Delta_{1,U}^2}}\right) \tag{A.24}
$$
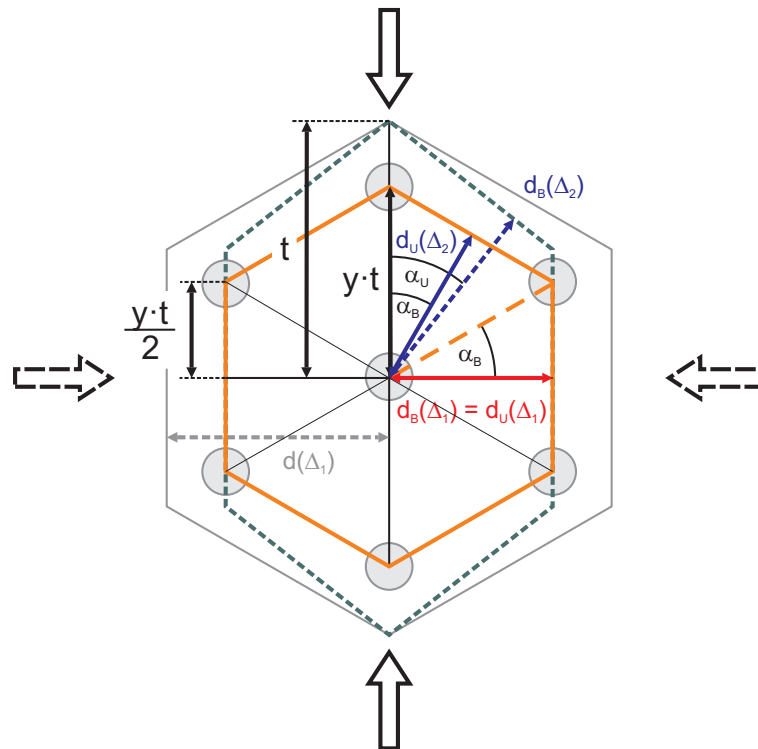
Figure A.2: Uniaxial compression perpendicular to $d_U(\Delta_1)$ of an unsheared, quasi-hexagonal structure. The netplane distance shortens from $d_U(\Delta_2)$ to $d_B(\Delta_2)$ and the angle δ_U increases to δ_B.
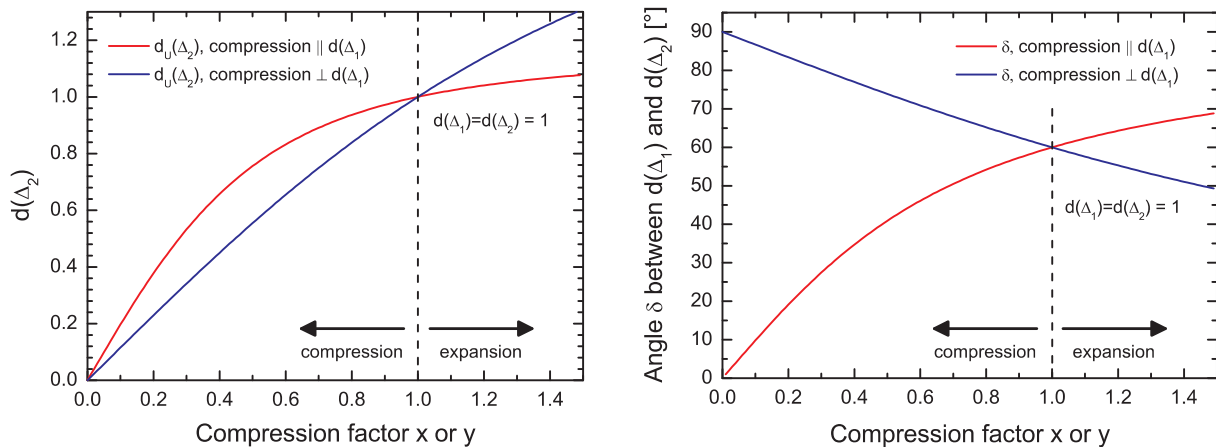
Figure A.3: Change of the netplane distance $d(\Delta_2)$ and of the angle δ dependent on uniaxial compression of the structure in direction of $d(\Delta_1)$ (red curve) or perpendicular to it (blue curve).

Figure A.3 illustrates the changes in $d(\Delta_2)$ for the two cases of uniaxial compression along $d(\Delta_1)$ and perpendicular to $d(\Delta_1)$, respectively. As initial structure a perfect hexagonal structure has been chosen with $d(\Delta_1) = d(\Delta_2) = 1$. This way the ordinate of the left graph shows the new length of $d(\Delta_2)$ in percentage of the original length. It can be inferred from the left graph of figure A.3 that for all scaling factors (where $x = y$) a perpendicular compression (expansion) decreases (increases) $d(\Delta_2)$ stronger than a compression (expansion) along $d(\Delta_1)$.

A.2.3 Biaxial Compression

The two equations A.7 and A.9 inserted in equation A.20 determine the new netplane distance $d(\Delta_2)$ after a biaxial compression. This is justified because each composition of the two steps of compression results in the same final structure. The latter is given by

<div align="center">

Biaxial Compression (Real Space)

</div>

$$d_B(\Delta_1) \quad = \quad x \cdot d(\Delta_1) \tag{A.25}$$

$$d_B(\Delta_2) \quad = \quad \frac{2 \cdot x \cdot y \cdot d(\Delta_1) \cdot d(\Delta_2)}{\sqrt{4 \cdot x^2 \cdot d(\Delta_1)^2 + (y^2 - x^2) \cdot d(\Delta_2)^2}} \tag{A.26}$$

$$\delta_B \quad = \quad 90° - \arctan\left(\frac{y \cdot d(\Delta_2)}{x \cdot \sqrt{4 \cdot d(\Delta_1)^2 - d(\Delta_2)^2}}\right) \tag{A.27}$$

in real space or by

<div align="center">

Biaxial Compression (Reciprocal Space)

</div>

$$\Delta_{1,B} \quad = \quad \frac{1}{x} \cdot \Delta_1 \tag{A.28}$$

$$\Delta_{2,B} \quad = \quad \frac{\sqrt{4 \cdot x^2 \cdot \Delta_2^2 + (y^2 - x^2) \cdot \Delta_1^2}}{2 \cdot x \cdot y} \tag{A.29}$$

$$\delta_{B,r} \quad = \quad 90° - \arctan\left(\frac{y \cdot \Delta_1}{x \cdot \sqrt{4 \cdot \Delta_2^2 - \Delta_1^2}}\right) \tag{A.30}$$

in reciprocal space. Here the index 'B' denotes values that belong to a biaxial compressed structure. The same index 'B' has been used in the second uniaxial compression because it leads to an identical final structure after the preceding first uniaxial compression. If x and y are selectively set to unity the equations A.25 to A.30 transform to the equations of the uniaxial compression parallel and perpendicular to $d(\Delta_1)$, respectively.

A.3 Error Statistics of Anarod

The Anarod program [168] consists of three separate programs called ANA, AVE and ROD. ANA serves as data analysis program and allows to fit measured intensity profiles, to subtract the background, to normalize the intensity to the monitor signal and to integrate the peak intensity. From the integrated intensities I and corresponding errors ΔI, the structure factors f_i and errors Δf_i are calculated for each reflection.

There are two ways to obtain reflectivity data. The first one is with a rocking scan of the surface normal within the scattering plane. Depending on the diffractometer, this can be done using an alignment cradle, the angle of incidence, or another appropriate degree of freedom. The second type of reflectivity scan is a ridge scan. The detector and sample are rotated simultaneously such that the specular reflectivity condition is continuously maintained. One stays 'on top of the peak'. In order to find the background in this case, the scan needs to be repeated with an offset on either side of the reflectivity profile (offset scan). ANA provides functions to calculate I and ΔI for both methods.

The way from measured intensities to structure factors and their errors consists of 4 steps which will be described in the following.

1a) ΔI **from Rocking Scans** If rocking scans are available the integrated intensity I and error ΔI are provided by the fitting procedure. The error $\Delta\{PAR\}_{\mathrm{fit}}$ for each fit parameter $\{PAR\}$ is computed by finding the value for which χ^2 increases by an amount $\Delta\chi^2$. From these values ΔI is calculated specifically for the chosen fitting function. Table A.2 summarizes the calculations for different types of fitting functions.

Fitting Function	Integrated Intensity I	Error of Integrated Intensity ΔI
Gaussian	$I = I_{\max} \cdot \mathrm{FWHM} \cdot 0.5\sqrt{\frac{\pi}{\ln 2}}$	$\Delta I = I \cdot \sqrt{\left(\frac{\Delta I_{\max,\mathrm{fit}}}{I_{\max}}\right)^2 + \left(\frac{\Delta\mathrm{FWHM}_{\mathrm{fit}}}{\mathrm{FWHM}}\right)^2}$
Lorentzian	$I = I_{\max} \cdot \mathrm{FWHM} \cdot \frac{\pi}{2}$	$\Delta I = I \cdot \sqrt{\left(\frac{\Delta I_{\max,\mathrm{fit}}}{I_{\max}}\right)^2 + \left(\frac{\Delta\mathrm{FWHM}_{\mathrm{fit}}}{\mathrm{FWHM}}\right)^2}$

Table A.2: Values of I and ΔI provided by the Levenberg-Marquardt least-square fitting method dependent on the fitting function. The intensity profile has to be normalized to the monitor signal prior to the fitting process. $I_{\max}$ denotes the height of the background subtracted profile and FWHM the according full width at half maximum of the profile.

1b) Δ**I from Ridge Scans** In case of reflectivity scans without additional rocking scans for intensity integration the original rod data $I_{\mathrm{ROD}}(\mathrm{L})$ and the offset scan data $I_{\mathrm{BG}}(\mathrm{L})$ are imported into ANA. After determination of the errors σ_I and σ_{BG} from the rod scan and offset scan, respectively, the offset scan is subtracted from the rod scan. The total error of

the obtained intensity I = I$_{ROD}$ − I$_{BG}$ is given by

$$\Delta I = \sqrt{\sigma_I^2 + \sigma_{BG}^2} \tag{A.31}$$

where $\sigma_I = \sqrt{I}$ (Poisson statistics) is the error of the monitored intensity and $\sigma_{BG} = \sqrt{I_{BG}}$ the error of the background intensity.

2) Structure Factors During the calculation of the structure factors necessary correction factors (CF) such as Lorentz-factor, polarisation factor and geometry factor are applied. This leads to the following expressions for the f_i and Δf_i of a single reflection.

$$\begin{aligned} f_i &= \sqrt{\text{CF} \cdot I} \tag{A.32} \\ \Delta f_i &= \sqrt{\text{CF} \cdot (I + \Delta I)} - f_i \tag{A.33} \end{aligned}$$

Table A.3 summarizes correction factors for a 6-circle diffractometer.

6-Circle Diffractometer	
Lorentz factor rocking scan	$\frac{1}{\sin \delta \cos \beta_{in} \cos \gamma}$
Lorentz factor stationary mode	$\frac{1}{\sin \beta_{out}}$
Lorentz factor reflectivity rocking scan	$\frac{1}{\sin 2\beta_{in}} = \frac{1}{\sin 2\beta_{out}}$
Rod interception	$\frac{2 \cos \beta_{in} \cos \gamma}{\cos \alpha + \cos(\alpha - 2\beta_{in}) + \sin(2\alpha - 2\beta_{in}) \sin \gamma + 2 \sin^2(\alpha - \beta_{in}) \cos \delta \cos \gamma}$
Linear γ table	$\cos \gamma$
Polarisation factor	$P = p_h P_{hor} + (1 - p_h) P_{ver}$
Horizontal polarisation P_{hor}	$1 - (\sin \alpha \cos \delta \cos \gamma + \cos \alpha \sin \gamma)^2$
Vertical polarisation P_{ver}	$1 - \sin^2 \delta \cos^2 \gamma$
Transmission incoming beam	$T_{0,in}\left(\frac{1}{\cos \alpha} - 1\right)$
Transmission outgoing beam	$T_{0,out}\left(\frac{1}{\cos \gamma} - 1\right)$
Area correction	$\frac{1}{\sin \delta \cos(\alpha - \beta_{in})}$
Beam profile and finite sample size	Calculated numerically in ANA. See [62]

Table A.3: Correction factors for a 6-circle diffractometer. For area correction the footprint size and sample size have been ignored. Table taken from [61].

ANA produces a data file which contains the structure factors f_i and the errors Δf_i. The data file can be imported to the AVE program. AVE sorts and averages the data based on the plane group symmetry. By default, AVE uses the Friedel rule to sort data into rods with both positive and negative L-values. All symmetry-equivalent reflections f_i are grouped

together and the average structure factor $\overline{f_{\text{hkl}}}$

$$\text{Weighting Factors} \qquad \omega_i \;=\; \frac{1}{(\Delta f_i)^2} \qquad\qquad \text{(A.34)}$$

$$\text{Average Structure Factors} \qquad \overline{f_{\text{hkl}}} \;=\; \frac{\sum_{i=1}^{E} f_i \cdot \omega_i}{\sum_{i=1}^{E} \omega_i} \qquad\qquad \text{(A.35)}$$

$$\overline{f_{\text{hkl}}^2} \;=\; \frac{\sum_{i=1}^{E} f_i^2 \cdot \omega_i}{\sum_{i=1}^{E} \omega_i} \qquad\qquad \text{(A.36)}$$

, the variance (called σ_1) and the statistical error (called σ_2)

$$\text{Variance} \qquad \sigma_1 \;=\; \sqrt{\frac{E}{E-1}\left(\overline{f_{\text{hkl}}^2} - \overline{f_{\text{hkl}}}^{\,2}\right)} \qquad \text{(A.37)}$$

$$\text{Statistical Error (SIGMA2MODE 0)} \qquad \sigma_2 \;=\; \sqrt{\frac{1}{\sum_{i=1}^{E} \omega_i}} \qquad \text{(A.38)}$$

$$\text{Statistical Error (SIGMA2MODE 1)} \qquad \sigma_2 \;=\; \frac{1}{E}\sum_{i=1}^{E} \Delta f_i \qquad \text{(A.39)}$$

$$\text{Statistical Error (SIGMA2MODE 2)} \qquad \sigma_2 \;=\; \sqrt{\frac{E}{\sum_{i=1}^{E} \omega_i}} \qquad \text{(A.40)}$$

are calculated, where the summations run over all equivalent reflections and where E denotes the total number of equivalent reflections. By default, the standard deviation of the statistical average is used in the calculation of σ_2 (SIGMA2MODE 0). The two additional modes SIGMA2MODE 1 and SIGMA2MODE 2 can be used if the standard deviation is considered to be unrealistically small.

3) Agreement Factor AVE also calculates the overall agreement factor $\overline{\epsilon}$ of the data. This is done as follows. For each reflection of which more than one symmetry-equivalent reflection is contained in the data set, the variance σ_1 is calculated. The ϵ_{hkl} of this reflection is the variance divided by the averaged structure factor.

$$\epsilon_{\text{hkl}} = \frac{\sigma_1}{\overline{f_{\text{hkl}}}} \qquad\qquad \text{(A.41)}$$

The ϵ_{hkl}'s of all non-equivalent reflections are averaged into the overall agreement factor $\overline{\epsilon}$ that is a measure of the systematic errors in the data set

$$\overline{\epsilon} = \frac{1}{\mu}\sum_{k=1}^{\mu} \overline{\epsilon_{\text{hkl}}} \qquad\qquad \text{(A.42)}$$

where μ is the number of non-equivalent reflections. A reflection is of sufficient quality if its average is larger than a certain cutoff value times the statistical error σ_2 ($\overline{f_{\text{hkl}}} > \text{Cutoff} \cdot \sigma_2$). The default cutoff is 2.

Note: For specular data no equivalent reflections exist. In this case the average agreement factor $\bar{\epsilon}$ has to be set manually to a reasonable value. In earlier in-plane experiments on Au(100) electrodes $\bar{\epsilon}$ has been determined as 0.08. This value has been used for all specular CTRs within the present work. The agreement factor of a data set typically varies from 0.03 to 0.15.

4) Error of the Structure Factors   As final step the appropriate error that is assigned to a reflection is calculated by

$$
\sigma_f = \begin{cases} \sqrt{\sigma_1^2 + \sigma_2^2} & E > E_{\min} \\[2ex] \sqrt{\bar{\epsilon}^2 \bar{f}^2 + \sigma_2^2} & E < E_{\min} \end{cases}
\tag{A.43}
$$

If the number of equivalent reflections of a particular reflection is less than $E_{\min}$ then $\bar{\epsilon}$ is used to estimate the error. The error of a particular structure factor f is thus the square sum of the average agreement factor of the entire data set and its own statistical error. In this way, also reflections of which no symmetry-equivalent ones have been measured, get a realistic error. Often the systematic error dominates.

A.4 Instrumental Resolution

In this section the instrumental resolution is derived for a (001)-surface of a cubic crystal. The real space unit cell shall be defined by the two perpendicular vectors $\vec{a}$ and $\vec{b}$ within the surface plane ($|\vec{a}| = |\vec{b}|$) and by the vector $\vec{c}$ along the surface normal. $\vec{a^*}$, $\vec{b^*}$ and $\vec{c^*}$ are the associated vectors in reciprocal space.

The slit sizes Δs_{hg} and Δs_{vg} of the vertical and horizontal detector slits, respectively, define the part of reciprocal space seen by the X-ray point detector. In the following the out-of-plane resolution ΔL, the in-plane resolution ΔR and the angular resolution $\Delta \theta$ will be determined. For this we consider the geometry of a diffraction experiment which is shown in figure A.4a. The incident wave vector $\vec{k}_i$, the diffracted wave vector $\vec{k}_f$ and the momentum transfer $\vec{q}$ are depicted. The scattering vector $\vec{q}$ can be expressed by

$$\vec{q} = H \cdot \vec{a^*} + K \cdot \vec{b^*} + L \cdot \vec{c^*} \tag{A.44}$$

where H, K and L are Miller indices. Furthermore $\vec{q}$ can be decomposed in a component parallel to the surface, $\vec{q}_\parallel$, and in a component perpendicular to the surface, $\vec{q}_\perp$. The length of $\vec{q}_\parallel$ is given by the peak position $(H, K, 0)$, i.e.

$$|\vec{q}_\parallel| = \sqrt{H^2 + K^2} \cdot |\vec{a^*}| \tag{A.45}$$

or as a function of the motors δ and γ

$$
\begin{aligned}
|\vec{q}_\parallel| &= k \cdot \sqrt{(\cos\gamma \sin\delta)^2 + (1 - \cos\gamma \cos\delta)^2} \\
&= k \cdot \sqrt{\cos^2\gamma - 2 \cdot \cos\gamma \cdot \cos\delta + 1}
\end{aligned} \tag{A.46}
$$

The projection of all vectors onto the surface plane is shown in figure A.4b. The angles ϕ, δ and α are connected via

$$\phi = 90° - (90° - \delta) - \alpha = \delta - \alpha \tag{A.47}$$

which allows together with equation A.46 to obtain the following relation

$$
\begin{aligned}
|\vec{q}_\parallel| \cdot \cos\phi &= |\vec{q}_\parallel| \cdot \cos(\delta - \alpha) \\
&= |\vec{q}_\parallel| \cdot (\cos\delta \cos\alpha + \sin\delta \sin\alpha) \\
&= \cos\delta \cdot (|\vec{q}_\parallel| \cdot \cos\alpha) + \sin\delta \cdot (|\vec{q}_\parallel| \cdot \sin\alpha) \\
&= \cos\delta \cdot k \cdot \cos\gamma \cdot \sin\delta + \sin\delta \cdot k(1 - \cos\delta \cdot \cos\gamma) \\
&= k \cdot \sin\delta
\end{aligned} \tag{A.48}
$$

The detector-sample distance is about $1\,\mathrm{m}$ for the ID32-diffractometer and thus the angular acceptances in γ and δ are given by

$$\Delta\gamma = \frac{\Delta s_{vg}}{1\,\mathrm{m}} \tag{A.49}$$

$$\Delta\delta = \frac{\Delta s_{hg}}{1\,\mathrm{m}} \tag{A.50}$$

A.4.1 Out-of-Plane Resolution

The out-of-plane resolution ΔL in reciprocal lattice units is given by

$$\Delta L = \Delta L_0 \cdot \cos(\gamma) = \Delta\gamma \cdot \frac{k}{|\vec{c^*}|} \cdot \cos(\gamma) \underset{\text{A.49}}{=} \frac{\Delta s_{vg}[m]}{1m \cdot \lambda} \cdot |\vec{c}| \cdot \cos(\gamma) \qquad (A.51)$$
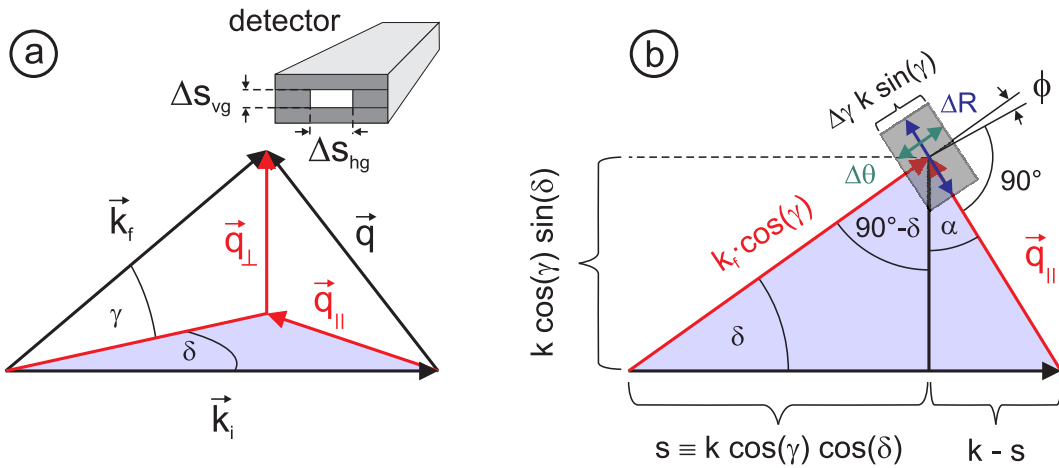
where ΔL_0 is the resolution in the L-direction ($\gamma \approx 0$) and $k = 2\pi/\lambda$ is the wave number.

A.4.2 In-plane Resolution

For the resolution on the scan directions parallel to the sample surface, $\Delta\theta$ and ΔR, the in-plane (the plane described by $\vec{Q}_\parallel$ and $\vec{k}_i$) projection of $\vec{k}_f$ has to be considered. The part of this plane seen by the detector is depicted by a gray rectangle in figure A.4b and the resolution in the direction of a rocking scan, $\Delta\theta$, and in radial direction, ΔR are shown. The latter are given by

$$\Delta\theta[°] = \frac{\Delta\gamma \cdot k \cdot \sin\gamma}{|\vec{q}_\parallel| \cdot \cos\phi} \underset{\text{A.48}}{=} \frac{\Delta\gamma \cdot \sin\gamma}{\sin\delta} \underset{\text{A.49}}{=} \frac{\Delta s_{vg}[m]}{1m} \cdot \frac{\sin\gamma}{\sin\delta} \qquad (A.52)$$

$$\Delta R = \frac{\Delta\delta \cdot k}{|\vec{a^*}| \cdot \cos\phi} \underset{\text{A.48}}{=} \frac{\Delta\delta \cdot |\vec{q}_\parallel|}{|\vec{a^*}| \cdot \sin\delta} \underset{\text{A.50}}{=} \frac{\Delta s_{hg}[m]}{1m} \cdot \frac{|\vec{q}_\parallel|}{|\vec{a^*}| \cdot \sin\delta} \qquad (A.53)$$

Figure A.4: Geometry of a grazing incidence scattering experiment. a) The incident vector $\vec{k}_i$, the scattered vector $\vec{k}_f$ and the scattering vector $\vec{q}$. The scattering vector $\vec{q}$ has a component parallel to the surface, $\vec{q}_\parallel$, and a component perpendicular to the surface, $\vec{q}_\perp$. b) In-plane projection of the geometry shown in a. The gray rectangle depicts the reciprocal space area seen by the detector.

A.5 Electrodissolution: Software Implementation of Current and X-ray Model

The source code listed below is written in Origin C and contains the implementation of the current model function (equation 11.40) and of the X-ray model function (equation 11.57). Both models are simultaneously fitted via least-square method to a measured dataset consisting of electrochemical current data and scattered X-ray data. The implementation presumes the electrodissolution of Au(111) electrodes. By default the X-ray intensity is expected to be measured at the fixed reciprocal space position $(0, 1, 0.1)$ on the basis of the unit cell being defined in section 11.7.1. For convenience the rms displacement amplitude σ_1 of surface atoms (static and dynamic contributions) is expressed by $\sigma_1^2 = \sigma_{\mathrm{bulk}}^2 + \sigma_{\mathrm{top}}^2$, where σ_{bulk} is the thermal bulk vibrational amplitude and σ_{top} is an 'extra' amplitude. This definition allows to factorize the Debye Waller (DW) term

$$\underbrace{\mathrm{e}^{-0.5 \cdot q_z^2 \cdot \sigma_1^2}}_{\text{DW surface}} = \underbrace{\mathrm{e}^{-0.5 \cdot q_z^2 \cdot \sigma_{\mathrm{bulk}}^2}}_{\text{DW bulk}} \cdot \underbrace{\mathrm{e}^{-0.5 \cdot q_z^2 \cdot \sigma_{\mathrm{top}}^2}}_{\text{extra z vibration}} \tag{A.54}$$

and to incorporate the bulk DW factor into the scale factor AZ. According to experimental values of $\sigma_1 = 0.12\,\text{Å}$ [152] and $\sigma_{\mathrm{bulk}} = 0.084\,\text{Å}$ [22] the extra z vibration for Au(111) surface atoms is given by $\sigma_{\mathrm{top}} = 0.086\,\text{Å}$. The X-ray part of the source code has been adopted from reference [212] with appropriate modifications.

Listing A.1: Non-linear Least Square Fit Function to Model Current Oscillations and X-ray Intensity Oscillations of Anodic Au(111) Electrodissolution by Use of OriginLAB v.7.5 Pro

```
1
2   #include <stdio.h>
3   #include <Origin.h>
4   #include <wksheet.h>
5   #include <data.h>
6   #include <math.h>
7   #include <utilities.h>
8   #include <OCN_s.h>
9
10
11  //----------------------------------------------------------
12  //
13  void _nlsfDifflim(
14  /* Fit Parameter(s):*/
15  double TS, double MLFraction, double C1, double C2, double AZ,
16  double Shift, double TS0, double Shift0, double AZ0,
17  /* Independent Variable(s): */
18  double t,
19  /* Dependent Variable(s): */
20  double& y, double& Xray)
21  {
22
```

```
23    /* Variables for current */
24    double Current0 ,Current1 ,Current2 ,Current3 ,Current4 ,Current5 ,Current6 ;
25    /* Variables for shift in time */
26    double z0,z1,z2,z3,z4,z5,z6;
27    /* Variables for Cottrell 1/sqrt(t) decay */
28    double t0,t1,t2,t3,t4,t5,t6;
29    /* Variable for charge per monolayer */
30    double QPerML;
31    /* Variables for dissolution onset of nth monolayer */
32    double TS2,TS3,TS4,TS5,TS6;
33
34
35    // ###########################################################################
36    // Electrochemical  Current  Model  ##########################################
37    // ###########################################################################
38
39    /* Total charge per monolayer */
40    QPerML = C1/(3*C2);
41
42    /* Iterative calculation of TS2 to TS6 from the first monolayer (TS) */
43    TS2 = pow(-(TS+Shift) *ln(1-(3*C2*MLFraction*QPerML/C1))/C2, 1.0/3.0)+TS ;
44    TS3 = pow(-(TS2+Shift)*ln(1-(3*C2*MLFraction*QPerML/C1))/C2, 1.0/3.0)+TS2;
45    TS4 = pow(-(TS3+Shift)*ln(1-(3*C2*MLFraction*QPerML/C1))/C2, 1.0/3.0)+TS3;
46    TS5 = pow(-(TS4+Shift)*ln(1-(3*C2*MLFraction*QPerML/C1))/C2, 1.0/3.0)+TS4;
47    TS6 = pow(-(TS5+Shift)*ln(1-(3*C2*MLFraction*QPerML/C1))/C2, 1.0/3.0)+TS5;
48
49    /* Definition of the timeshifts for each monolayer */
50    z0 = t - TS0;   z1 = t - TS;   z2 = t - TS2;
51    z3 = t - TS3;   z4 = t - TS4;  z5 = t - TS5;
52    z6 = t - TS6;
53
54    /* Definition of the time values for the Cottrell decay */
55    t0 = TS0 + Shift0;  t1 = TS  + Shift;   t2 = TS2 + Shift;
56    t3 = TS3 + Shift;    t4 = TS4 + Shift;   t5 = TS5 + Shift;
57    t6 = TS6 + Shift;
58
59    // ########## Choose Nucleation model ################################
60
61
62    // Model A) progressive nucleation
63
64    /* disable by demand */
65    if (z0<0) {Current0=0;} else {Current0 = (C1*z0*z0/t0)*exp(-C2*z0*z0*z0/t0)};
66    if (z1<0) {Current1=0;} else {Current1 = (C1*z1*z1/t1)*exp(-C2*z1*z1*z1/t1)};
67    if (z2<0) {Current2=0;} else {Current2 = (C1*z2*z2/t2)*exp(-C2*z2*z2*z2/t2)};
68    if (z3<0) {Current3=0;} else {Current3 = (C1*z3*z3/t3)*exp(-C2*z3*z3*z3/t3)};
69    if (z4<0) {Current4=0;} else {Current4 = (C1*z4*z4/t4)*exp(-C2*z4*z4*z4/t4)};
70    if (z5<0) {Current5=0;} else {Current5 = (C1*z5*z5/t5)*exp(-C2*z5*z5*z5/t5)};
71    if (z6<0) {Current6=0;} else {Current6 = (C1*z6*z6/t6)*exp(-C2*z6*z6*z6/t6)};
72
73    // Model B) instantaneous nucleation
74
75    /* enable by demand
```

```
76    if (z0<0) {Current0=0;} else {Current0 = (C1*z0/t0)*exp(-C2*z0*z0/t0)};
77    if (z1<0) {Current1=0;} else {Current1 = (C1*z1/t1)*exp(-C2*z1*z1/t1)};
78    if (z2<0) {Current2=0;} else {Current2 = (C1*z2/t2)*exp(-C2*z2*z2/t2)};
79    if (z3<0) {Current3=0;} else {Current3 = (C1*z3/t3)*exp(-C2*z3*z3/t3)};
80    if (z4<0) {Current4=0;} else {Current4 = (C1*z4/t4)*exp(-C2*z4*z4/t4)};
81    if (z5<0) {Current5=0;} else {Current5 = (C1*z5/t5)*exp(-C2*z5*z5/t5)};
82    if (z6<0) {Current6=0;} else {Current6 = (C1*z6/t6)*exp(-C2*z6*z6/t6)};
83    */
84
85    // ################# MAIN CURRENT FIT FUNCTION #########################
86
87    y =  Current0 + Current1 + Current2 + Current3 + Current4 + Current5
88       + Current6;
89
90
91    // ####################################################################
92    // ###### X-ray Model #################################################
93    // ####################################################################
94
95    double MaxCoverage;
96    double MomCoverage0,MomCoverage1,MomCoverage2,MomCoverage3,MomCoverage4,
97           MomCoverage5;
98
99    /* Determine total charge transfer for one monolayer */
100   MaxCoverage = C1/(3*C2);
101
102   double InitialCov;
103   InitialCov = C1/(3*C2)*(-exp(-C2*(0.0-TS0)*(0.0-TS0)*(-0.0-TS0)/t0) + 1);
104
105
106   /* Calculate momentary charges of n-th monolayer */
107   MomCoverage0 = C1/(3*C2)*(- exp(-C2*(t-TS0)*(t-TS0)*(t-TS0)/t0) + 1);
108   MomCoverage1 = C1/(3*C2)*(- exp(-C2*(t-TS) *(t-TS) *(t-TS)/t1) + 1);
109   MomCoverage2 = C1/(3*C2)*(- exp(-C2*(t-TS2)*(t-TS2)*(t-TS2)/t2) + 1);
110   MomCoverage3 = C1/(3*C2)*(- exp(-C2*(t-TS3)*(t-TS3)*(t-TS3)/t3) + 1);
111   MomCoverage4 = C1/(3*C2)*(- exp(-C2*(t-TS4)*(t-TS4)*(t-TS4)/t4) + 1);
112   MomCoverage5 = C1/(3*C2)*(- exp(-C2*(t-TS5)*(t-TS5)*(t-TS5)/t5) + 1);
113
114   /* Calculate Coverages */
115   if (t>=0) {MomCoverage0 = 1-(MomCoverage0/MaxCoverage)}
116   else      {MomCoverage0 = InitialCov/MaxCoverage;};
117
118   if (t>=TS) {MomCoverage1 = 1-(MomCoverage1/MaxCoverage)}
119   else       {MomCoverage1 = 1};
120
121   if (t>=TS2) {MomCoverage2 = 1-(MomCoverage2/MaxCoverage)}
122   else        {MomCoverage2 = 1};
123
124   if (t>=TS3) {MomCoverage3 = 1-(MomCoverage3/MaxCoverage)}
125   else        {MomCoverage3 = 1};
126
127   if (t>=TS4) {MomCoverage4 = 1-(MomCoverage4/MaxCoverage)}
128   else        {MomCoverage4 = 1};
```

```
129
130    if (t>=TS5) {MomCoverage5 = 1-(MomCoverage5/MaxCoverage)}
131    else        {MomCoverage5 = 1};
132
133
134    complex one, rms_surf;
135    complex aa, aamin, a1, num;
136    complex A1,SUM;
137    double sn_alp;
138    double qq,qz,hh[3],rms,;
139
140    /* Au(111) and X-ray properties */
141    double TWOPI  = 2*Pi;
142    double AuLat  = 4.0786;
143    double Lambda = 0.55614;
144    double TWO_K  = 4 * Pi * Lambda;
145    double Z_Au   = 79;
146
147    /* Bulk rms [Kolb, Ber. Bunsenges. Phys. Chem. 87,1108] */
148    double RMS     = 0.084;
149
150    /* Anti-Bragg position (0 , 1 , 0.1) */
151    double HHH = 0.0;
152    double KKK = 1.0;
153    double L   = 0.1;
154
155    double nhat[3];
156    nhat[0] = nhat[1] = nhat[2] = 1.0 / sqrt(3.0);
157
158    /* Expansion of topmost layers */
159    /* no significant toplayer expansion in Cl containing solution */
160    /* [Wang, Ocko, Phys. Rev. B. (46), 10321] */
161    double EPS_0 = 0.0;
162    double EPS_1 = 0.0;
163    double EPS_2 = 0.0;
164
165    /* Debye Waller, extra z vibration of 1st monolayer */
166    /* sigma_1^2 = rms_bulk^2 + rms_surface^2 */
167    /* sigma_1 = 0.12A (Wang, PRB 46,16) */
168    /* rms_bulk=0.084A --> rms_surface = 0.086A */
169    double RMS_0 = 0.086;
170
171    /* no extra z vibrations for subjacent layers */
172    double RMS_1 = 0.0;
173    double RMS_2 = 0.0;
174    double RMS_3 = 0.0;
175    double RMS_4 = 0.0;
176    double RMS_5 = 0.0;
177
178    /* H,K,L */
179    hh[0] = 0.0; hh[1] = 1.0; hh[2] = 0.1;
180
181    /* hextocube */
```

```
182    hh[0] = -4 * hh[0]/3 - 2 * hh[1]/3 + hh[2]/3;
183    hh[1] =  2 * hh[0]/3 - 2 * hh[1]/3 + hh[2]/3;
184    hh[2] =  2 * hh[0]/3 + 4 * hh[1]/3 + hh[2]/3;
185
186    /* scattering vector */
187    qq = TWOPI * sqrt(hh[0] * hh[0] + hh[1]*hh[1] + hh[2]*hh[2])/AuLat;
188    rms = exp(-RMS * RMS * qq * qq);
189
190    /* sin(alpha) */
191    sn_alp = (nhat[0] * hh[0] + nhat[1] * hh[1] + nhat[2] * hh[2]) * qq;
192    sn_alp /= sqrt(hh[0]*hh[0] + hh[1]*hh[1] + hh[2]*hh[2]) * TWO_K;
193    sn_alp = fabs(sn_alp);
194
195    /* z-component of scattering vector */
196    qz  = TWO_K * sn_alp;
197
198    one.m_re = 1.0;
199    one.m_im = 0.0;
200
201    aa.m_im = 2 * L * TWOPI;
202    aamin.m_im = - L * TWOPI;
203    aamin.m_re = aa.m_re = a1.m_re = 0.0;
204    rms_surf.m_im = 0.0;
205
206    /* Extra rms of the topmost surface layer */
207    complex rms_TopLayer;
208    rms_TopLayer.m_re = exp(-0.5 * qz * qz * RMS_0 * RMS_0);
209
210    /* 1st Layer (C) percent expansion and structure factor */
211    a1.m_im = (L * EPS_0 / 3 + (-HHH+KKK+L) / 3) * TWOPI;
212    /* the complete 1st layer is topmost */
213    A1 = MomCoverage0 * rms_TopLayer * exp(a1);
214
215    /* 2nd layer (B) percent expansion and structure factor */
216    a1.m_im = L * EPS_1 * TWOPI / 3;
217    rms_surf.m_re = exp(-0.5 * qz * qz * RMS_1 * RMS_1);
218    A1 = A1 + MomCoverage0 * rms_surf * exp(a1);
219    A1 = A1 + (MomCoverage1 - MomCoverage0) * rms_TopLayer * exp(a1);
220
221    /* 3rd layer (A) percent expansion and structure factor */
222    a1.m_im = (L * EPS_2 / 3 + (HHH-KKK-L) / 3) * TWOPI;
223    rms_surf.m_re = exp(-0.5 * qz * qz * RMS_2 * RMS_2);
224    A1 = A1 + MomCoverage1 * rms_surf * exp(a1);
225    A1 = A1 + (MomCoverage2 - MomCoverage1) * rms_TopLayer * exp(a1);
226
227    /* 4th layer (C) percent expansion and structure factor */
228    a1.m_im = (-L + (-HHH+KKK+L) / 3) * TWOPI;
229    rms_surf.m_re = exp(-0.5 * qz * qz * RMS_3 * RMS_3);
230    A1 = A1 + MomCoverage2 * rms_surf * exp(a1);
231    A1 = A1 + (MomCoverage3 - MomCoverage2) * rms_TopLayer * exp(a1);
232
233    /* 5th layer (B) percent expansion and structure factor */
234    a1.m_im = (-L) * TWOPI;
```

```
235    rms_surf.m_re = exp(-0.5 * qz * qz * RMS_4 * RMS_4);
236    A1 = A1 + MomCoverage3 * rms_surf * exp(a1);
237    A1 = A1 + (MomCoverage4 - MomCoverage3) * rms_TopLayer * exp(a1);
238
239    /* 6th layer (A) percent expansion and structure factor */
240    a1.m_im = (-L+(HHH-KKK-L)/3) * TWOPI;
241    rms_surf.m_re = exp(-0.5 * qz * qz * RMS_5 * RMS_5);
242    A1 = A1 + MomCoverage4 * rms_surf * exp(a1);
243    A1 = A1 + (MomCoverage5 - MomCoverage4) * rms_TopLayer * exp(a1);
244
245    /* bulk contribution */
246    num.m_re = 1 + 2 * cos(TWOPI * (-HHH+KKK+L)/3);
247    num.m_im = 0;
248
249    /* Calculate intensity I = |F F*| */
250    SUM = num/(one - exp(aamin)) + exp(aa)*(A1);
251    SUM = SUM * Conj(SUM);
252
253    // ################# MAIN X-RAY FIT FUNCTION #########################
254
255    /* Additional scale factor for t<0 */
256    double AddFacAZ;
257
258    if (t>0) {AddFacAZ = 1} else {AddFacAZ = AZ0};
259
260    Xray = AddFacAZ * AZ * SUM.m_re;
261
262    /* scale factor AZ includes bulk rms, normalization, transmission,
263       atomic form factor of gold, Lorentz correction */
264
265    }
```

B Bibliography

[1] Rosenfeld, G., Poelsema, B., and Comsa, G. *Growth and Properties of Ultrathin Epitaxial Layers*, volume 8. Elsevier Science, Amsterdam, (1999).

[2] RamanaMurty, M. V., Curcic, T., Judy, A., Cooper, B. H., Woll, A., Brock, J. D., Kycia, S., and Headrick, R. L. *Phys. Rev. B* **60**, 16956 (1999).

[3] Venables, J., Spillert, G., and Hanbücken, M. *Rep. Prog. Phys.* **47**, 399–459 (1984).

[4] Günther, S., Kopatzki, E., Bartelt, M. C., Evans, J. W., and Behm, R. J. *Phys. Rev. Lett.* **73**, 553 (1994).

[5] Günther, S. *Mikroskopische Aspekte beim Wachstum dünner Metallfilme*. PhD thesis, Universität Ulm, (1995).

[6] Divisek, J., Steffen, B., Stimming, U., and Schmickler, W. *J. Electroanal. Chem.* **440**, 169 (1997).

[7] Skylar, O., Treutler, T. H., Vlachopoulos, N., and Wittstock, G. *Surf. Sci.* **597**, 181 (2005).

[8] Nagy, Z. and You, H. *Electrochim. Acta* **47**, 3037 (2002).

[9] Magnussen, O. M. *Chem. Rev.* **102**, 679 (2002).

[10] Nagy, Z., Yonco, R. M., Melendres, C. A., Yun, C. A., and Maroni, V. A. *Electrochim. Acta* **36**, 209 (1991).

[11] Tamura, K., Ocko, B. M., Wang, J. X., and Adzic, R. R. *J. Phys. Chem. B* **106**, 3896 (2002).

[12] Ayyad, A., Stettner, J., and Magnussen, O. *Phys. Rev. Lett.* **94**, 066106 (2005).

[13] Kolb, D., Lehmpfuhl, G., and Zei, M. *J. Electroanal. Chem.* **179**, 289 (1984).

[14] Polewska, W. and Magnussen, O. *Surf. Sci.* **601**, 4657–4661 (2007).

[15] Ye, S., Ishibashi, C., Shimazu, K., and Uosaki, K. *J. Electrochem. Soc.* **145**, 1614 (1998).

[16] Ye, S., Ishibashi, C., and Uosaki, K. *Langmuir* **15**, 807–812 (1999).

[17] Ye, S., Ishibashi, C., and Uosaki, K. *Electrochemical Society Proceedings* **PV-2000-35**, 133–147 (2001).

[18] Hamann, C. H. and Vielstich, W. *Elektrochemie*. Wiley-VCH, (1998).

[19] Bockris, J., Conway, B., and Yeager, E. *Comprehensive treatise of electrochemistry*, volume 1. Plenum Press, (1980).

[20] Bard, A. J. and Faulkner, L. R. *Electrochemical Methods.* John Wiley & Sons, Inc., (1980).

[21] Habib, M. *Specific adsorption of anions.* Plenum Press, (1980).

[22] Kolb, D., Rath, D., Wille, R., and Hansen, W. *Ber. Bunsenges. Phys. Chem.* **87**, 1108 (1983).

[23] Reeves, R. *Comprehensive treatise of electrochemistry*, volume 1. Plenum Press, (1980).

[24] Zelenay, P. and Wieckowski, A. *Electrochemical Interfaces.* VCH, (1991).

[25] Butler, J. A. V. *Proc. Roy. Soc. A* **112**, 129 (1926).

[26] Guggenheim, E. A. *J. Phys. Chem.* **33**, 842 (1929).

[27] Wilkinson, P. *Gold Bull.* **19(3)**, 75–81 (1986).

[28] Rich, R. and Taube, H. *J. Phys. Chem.* **58**, 6 (1954).

[29] Chen, J., Qiu, L., and An, K. *Acta Chimica Sinica* **46**, 360–363 (1988).

[30] Bauer, E. *Z. Kristallogr.* **110**, 372–394 (1958).

[31] Reif, F. *Fundamentals of statistical and thermal physics.* McGraw-Hill, New York, (1965).

[32] Wulff, G. *Z. Krist. Min.* **34**, 449 (1901).

[33] Vollmer, M. *Kinetik der Phasenumwandlung.* Steinkopffverlag, (1939).

[34] Burton, W., Cabrera, N., and Frank, F. *Philos. Trans. Roy. Soc. London A* **243**, 299 (1951).

[35] Kossel, W. *Nachr. Ges. Wiss. Göttingen, math.-phys. Klasse* , 135 (1927).

[36] Stranski, I. N. *Z. Phys. Chem.* **136**, 259 (1928).

[37] Basset, D. and Webber, P. R. *Surf. Sci.* **70**, 520 (1978).

[38] Feibelman, P. J. *Phys. Rev. Lett.* **65**, 729 (1990).

[39] Kellogg, G. L. and Feibelman, P. J. *Phys. Rev. Lett.* **64**, 3143 (1990).

[40] Tsong, T. T. and Chen, C. L. *Nature* **355**, 328 (1992).

[41] Ehrlich, G. and Hudda, F. *J. Chem. Phys.* **44(3)**, 1039–49 (1966).

[42] Schwoebel, R. L. *J. Appl. Phys.* **40(2)**, 614–18 (1969).

[43] Haftel, M. and Rosen, M. *Phys. Rev. B* **68**, 165402 (2003).

[44] He, Y. and Borguet, E. *Faraday Discuss.* **121**, 17–25 (2002).

[45] Parratt, L. *Phys. Rev.* **95(2)**, 359–369 (1954).

[46] Als-Nielsen, J. *Physica A* **140**, 376–389 (1986).

[47] Dosch, H. *Phys. Rev. B* **35**, 2137–2143 (1987).

[48] Sinha, S., Sirota, E., Garoff, S., and Stanley, H. *Phys. Rev. B* **38**, 2297 (1988).

[49] Robinson, I. *Phys. Rev. B* **33**, 3830 (1986).

[50] Feidenhans'l, R. *Surf. Sci. Rep.* **10**, 105 (1989).

[51] Marra, W., P.Eisenberger, and Cho, A. *J. Appl. Phys.* **50**, 6927 (1979).

[52] Eisenberger, P. and Marra, W. *Phys. Rev. Lett.* **46**, 1081 (1981).

[53] Warren, B. *X-ray diffraction.* Addison-Wesley Pub. Co., (1990).

[54] Guinier, A. *X-ray Diffraction.* W.H. Freeman & Co, (1956).

[55] Robinson, I. and Tweet, D. *Rep. Prog. Phys.* **55**, 599 (1992).

[56] Robinson, I. *Handbook of Synchrotron Radiation*, 221. Elsevier Science Publishers (1991).

[57] Fuoss, P. and Brennan, S. *Annu. Rev. Mater. Sci.* **20**, 365 (1990).

[58] Toney, M. and Melroy, O. *In-Situ Studies of Electrochemical Interfaces.* VCH Verlag Chemical, (1991).

[59] Toney, M. F., Gordon, J., and Melroy, O. *SPIE Proc.* **1550**, 140 (1991).

[60] Ocko, B. and Wang, J. *Synchrotron Techniques in Interfacial Electrochemistry.* Kluwer Academic Publishers.

[61] Vlieg, E. *From beam time to structure factors*, (2002).

[62] Vlieg, E. *J. Appl. Cryst.* **30**, 532 (1997).

[63] Robinson, K. and O'Grady, W. *Rev. Sci. Instrum.* **64**, 1061 (1993).

[64] Kaminski, D., Krug, K., Golks, F., Stettner, J., and Magnussen, O. M. *J. Phys. Chem. C* **111**, 17067–17071 (2007).

[65] Krug, K., Stettner, J., and Magnussen, O. *Phys. Rev. Lett.* **96**, 246101 (2006).

[66] DeVilbiss, J., Wang, J., Ocko, B., Tamura, K., Adzic, R., Vartanyants, I., and Robinson, I. *Electrochim. Acta* **47**, 3057–3064(8) (2002).

[67] Clavilier, J. *J. Electroanal. Chem.* **107**, 211 (1980).

[68] Müller, K. *Ber. Bunsenges. Phys. Chem.* **90**, 184 (1986).

[69] Hove, M. V., Koestner, R., Stair, P., Biberian, J., Kesmodel, L., Bartos, I., and Somorjai, G. *Surf. Sci.* **103(1)**, 218 (1981).

[70] Bertel, E. and Netzer, F. *Surf. Sci.* **97(2-3)**, 409 (1980).

[71] Hamelin, A., Gao, X., and Weaver, M. *J. Electroanal. Chem.* **323**, 361 (1992).

[72] Yeager, E., Homa, A., Cahan, B., and Scherson, D. *J. Vac. Sci. Technol.* **20**, 628 (1982).

[73] Kolb, D. M. and Schneider, J. *Surf. Sci.* **162(1-3)**, 764 (1985).

[74] Zei, M. S., Lehmpfuhl, G., and Kolb, D. M. *Surf. Sci.* **221(1-2)**, 23 (1989).

[75] D'Agostino, A. T. and Ross, P. N., J. *Surf. Sci.* **185(1-2)**, 88 (1987).

[76] Skoluda, P. and Kolb, D. *Surf. Sci.* **260**, 229 (1992).

[77] Santos, E. and Schmickler, W. *Chem. Phys. Lett.* **400**, 26–29 (2004).

[78] Feng, Y., Bohnen, K., and Chan, C. *Phys. Rev. B* **72**, 125401 (2005).

[79] Haftel, M. and Rosen, M. *Surf. Sci.* **523**, 118–124 (2003).

[80] Ocko, B., Wang, J., Davenport, A., and Isaacs, H. *Phys. Rev. Lett.* **65**, 1466 (1990).

[81] Wang, J., Davenport, A., Isaacs, H., and Ocko, B. *Science* **255**, 1416 (1991).

[82] Gao, X., Hamelin, A., and Weaver, M. *Phys. Rev. Lett.* **67**, 618 (1991).

[83] Gao, X., Hamelin, A., and Weaver, M. *J. Chem. Phys.* **95**, 6993 (1991).

[84] Gao, X., Hamelin, A., and Weaver, M. *Phys. Rev. B* **44**, 10983 (1991).

[85] Haiss, W., Lackey, D., Sass, J., and Besocke, K. *J. Chem. Phys.* **95**, 2193 (1991).

[86] Tao, N. and Lindsay, S. *Surf. Sci.* **274**, L546 (1992).

[87] Magnussen, O., Wiechers, J., and Behm, R. *Surf. Sci.* **289**, 139 (1993).

[88] Magnussen, O., Hotlos, J., Behm, R., Batina, N., and Kolb, D. *Surf. Sci.* **296(3)**, 310–332 (1993).

[89] Magnussen, O. *In-Situ Rastertunnelmikroskop-Untersuchungen zu Rekonstruktion, Anionenadsorption und Unterpotentialabscheidung auf Goldelektroden.* PhD thesis, Universität Ulm, (1993).

[90] Labayen, M. and Magnussen, O. *Surf. Sci.* **573(1)**, 128–139 (2004).

[91] Jacob, T. *Electrochim. Acta* **52(6)**, 2229–2235 (2007).

[92] Venkatachalam, S., Kaghazchi, P., Kibler, A., Kolb, D., and Jacob, T. *Chem. Phys. Lett.* **455(1-3)**, 47–51 (2008).

[93] Simeone, F., Kolb, D., Venkatachalam, S., and Jacob, T. *Angewandte Chemie*, chapter The Au(111)/electrolyte interface: a tunnel-spectroscopic and DFT investigation., 8903–8906. Wiley-VCH (2007).

[94] Abernathy, D., Gibbs, D., Grübel, G., Huang, K., Mochrie, S., Sandy, A., and Zehner, D. *Surf. Sci.* **283**, 260 (1993).

[95] Wendelken, J. and Zehner, D. *Surf. Sci.* **71**, 178 (1978).

[96] Fedak, D. and Gjostein, N. *Surf. Sci.* **8**, 77–97 (1967).

[97] Ercolessi, F., Tosatti, E., and Parrinello, M. *Phys. Rev. Lett.* **57**, 719 (1986).

[98] Wang, X. *Phys. Rev. Lett.* **67**, 3547 (1991).

[99] Dunn, D., Zhang, J., and Marks, L. *Surf. Sci.* **260**, 220–228 (1992).

[100] Rieder, K., T.Engel, Swendsen, R., and Manninen, M. *Surf. Sci.* **127**, 223 (1983).

[101] Ocko, B., Gibbs, D., Huang, K., Zehner, D., and Mochrie, S. *Phys. Rev. B* **44**, 6429 (1991).

[102] Ercolessi, F., Parinello, M., and Tosatti, E. *Surf. Sci.* **177**, 314 (1986).

[103] Gibbs, D., Ocko, B., Zehner, D., and Mochrie, S. *Phys. Rev. B* **42**, 7330 (1990).

[104] Nomura, M. and Wang, X.-Q. *Phys. Rev. Lett.* **81**, 2739 (1998).

[105] Zehner, D. and Appelton, B. *J. Vac. J. Technol.* **12**, 454 (1975).

[106] Zehner, D., Mochrie, S., Ocko, B., and Gibbs, D. *J. Vac. Sci. Technol. A* **9(3)**, 1861 (1991).

[107] Cuesta, A. and Kolb, D. *Surf. Sci.* **465**, 310–316 (2000).

[108] Dakkouri, A. *Solid State Ionics* **94**, 99–114 (1997).

[109] Batina, N., Dakkouri, A., and Kolb, D. *J. Electroanal. Chem.* **370**, 87–94 (1994).

[110] Gao, X., Hamelin, A., and Weaver, M. *Phys. Rev. B* **46**, 7096 (1992).

[111] Schneider, J. and Kolb, D. *Surf. Sci.* **193**, 579 (1988).

[112] Kolb, D. *Prog. Surf. Sci.* **51**, 109–173 (1996).

[113] Labayen, M., Ramirez, C., Schattke, W., and Magnussen, O. *Nature Materials Letters* **2**, 783 (2003).

[114] Gao, X. and Weaver, M. *J. Phys. Chem.* **97**, 8685 (1993).

[115] Tidswell, I., Markovic, N., Lucas, C., and Ross, P. *Phys. Rev. B* **47**, 16542 (1993).

[116] Mochrie, S., Zehner, D., Gibbs, D., and Ocko, B. *Phys. Rev. Lett.* **64**, 2925 (1990).

[117] Hamilton, J. *Phys. Rev. Lett.* **88**, 126101(1–4) (2002).

[118] Okwamoto, Y. and Bennemann, K. *Surf. Sci.* **179**, 231–242 (1987).

[119] Krug, K. Master's thesis, Christian-Albrechts-Universität Kiel, (2004).

[120] Nichols, R. J., Magnussen, O. M., Hotlos, J., Twomey, T., Behm, R. J., and Kolb, D. M. *J. Electroanal. Chem.* **290**, 21 (1990).

[121] Ikemiya, N., Nishide, M., and Hara, S. *Surf. Sci.* **340**, L965 (1995).

[122] Kubo, K., Hirai, N., and Hara, S. *Appl. Surf. Sci.* **237**, 301 (2004).

[123] Giesen, M., Beltramo, G., Dieluweit, S., Müller, J., Ibach, H., and Schmickler, W. *Surf. Sci.* **595**, 127 (2005).

[124] Ocko, B. M., Gibaud, A., and Wang, J. *J. Vac. Sci. Technol. A* **10(5)**, 3019 (1992).

[125] Huang, K., Gibbs, D., Zehner, D., Sandy, A., and Mochrie, S. *Phys. Rev. Lett.* **65**, 3317 (1990).

[126] Lucas, C. *J. Phys. D - Appl. Phys.* **32**, A198 (1999).

[127] Lucas, C. *Surf. Sci.* **425**, L381 (1999).

[128] Bombis, C. and Ibach, H. *Surf. Sci.* **564**, 201–210 (2004).

[129] Watson, G. M., Gibbs, D., Zehner, D., Yoon, M., and Mochrie, S. *Surf. Sci.* **407**, 59–72 (1998).

[130] Wang, J., Watson, G. M., and Ocko, B. M. *Physica A* **200**, 679–687 (1993).

[131] Wang, J., Adzic, R. R., and Ocko, B. M. *J. Phys. Chem.* **98**, 7182–7190 (1994).

[132] Wang, J. X., Adzic, R. R., Magnussen, O. M., and Ocko, B. M. *Surf. Sci.* **344**, 111–119 (1995).

[133] Cammarata, R. C. *Surf. Sci.* **279**, 341 (1992).

[134] Needs, R., Godfrey, M., and Mansfield, M. *Surf. Sci.* **242**, 215 (1991).

[135] Mansfield, M. and Needs, R. *J. Phys. (Condensed Matter)* **2**, 2361 (1990).

[136] Cammarata, R. *Surf. Sci. Lett.* **273**, L399 (1992).

[137] Ibach, H. *Surf. Sci. Rep.* **29**, 193–263 (1997).

[138] Cammarata, R. and Sieradzki, K. *Annu. Rev. Mater. Sci.* **24**, 215–234 (1994).

[139] Haiss, W. *Rep. Prog. Phys.* **64**, 591–648 (2001).

[140] Gibbs, J. W. *The Scientific Papers of J. Willard Gibbs* **1**, 55 (1906).

[141] Ibach, H. *J. Vac. Sci. Technol. A* **12**, 2240–3 (1994).

[142] Shuttleworth, R. *Proc. Phys. Soc. A* **63**, 445 (1950).

[143] Herring, C. *The Physics of Powder Metallurgy.* New York: McGraw-Hill, (1951).

[144] de Launey, J. *Solid State Phys.* **2**, 220 (1956).

[145] Grafov, B. M. *J. Electroanal. Chem.* **471(2)**, 105–108 (1999).

[146] Frenkel, J. and Kontorova, T. *Phys. Z. Sowjetunion* **13**, 1 (1938).

[147] Bach, C. E., Giesen, M., Einstein, T. L., and Ibach, H. *Phys. Rev. Lett.* **78**, 4225–4228 (1997).

[148] Needs, R. and Mansfield, M. *J Phys.: Condens. Matter* **1**, 7555–63 (1989).

[149] Feibelman, P. *Phys. Rev. B* **50**, 1908–11 (1994).

[150] Feibelman, P. *Phys. Rev. B* **51**, 17867–75 (1995).

[151] Sandy, A., Mochrie, S., Zehner, D., Huang, K., and Gibbs, D. *Phys. Rev. B* **43**, 4667 (1991).

[152] Wang, J., Ocko, B., Davenport, A., and Isaacs, H. *Phys. Rev. B* **46**, 10321 (1992).

[153] Toney, M., Gordon, J., Samant, M., Borges, G., and Melroy, O. *J. Phys. Chem.* **99**, 4733 (1995).

[154] Ibach, H., Santos, E., and Schmickler, W. *Surf. Sci.* **540**, 504–507 (2003).

[155] Toney, M., Gordon, J., Samant, M., Borges, G., Melroy, O., Kau, L., Wiesler, D., Yee, D., and Sorensen, L. *Phys. Rev. B* **42**, 5594 (1990).

[156] Trevor, D. J., Chidsey, C. E. D., and Loiacono, S. N. *Phys. Rev. Lett.* **62**, 929 (1989).

[157] Tersoff, J., van der Gon, A. D., and Tromp, R. M. *Phys. Rev. Lett.* **72**, 266 (1994).

[158] Rottler, J. and Maass, P. *Phys. Rev. Lett.* **83**, 3490 (1999).

[159] Krug, J., Politi, P., and Michely, T. *Phys. Rev. B* **61**, 14037 (2000).

[160] Albery, W. and Brett, C. *J. Electroanal. Chem.* **148**, 201–210 (1983).

[161] Yoneda, Y. *Phys. Rev.* **131**, 2010 (1963).

[162] Kortright, J. *J. Appl. Phys.* **70**, 3620 (1991).

[163] Russel, T. *Mat. Sci. Rep.* **5**, 171 (1990).

[164] Donnay, J. and Harker, D. *Am. Mineral.* **22**, 446 (1937).

[165] DePristo, E. and Li, Y. *Surf. Sci.* **351(1)**, 189–199 (1996).

[166] Lang, C., Dovek, M., Nogami, J., and Quate, C. *Surf. Sci. Lett.* **224**, L947–L955 (1989).

[167] Kamiko, M., Mizuno, H., Chihaya, H., Xu, J., Kojima, I., and Yamamoto, R. *Appl. Surf. Sci.* **252(2)**, 364–371 (2005).

[168] Vlieg, E. *J. Appl. Cryst.* **33**, 401 (2000).

[169] Haftel, M. *Phys. Rev. B* **64**, 125415 (2000).

[170] Zhang, J., Song, X., Zhang, X., Xu, K., and Ji, V. *Surf. Sci.* **600**, 1277–1282 (2006).

[171] Pai, W. and Reutt-Robey, J. *Phys. Rev. B* **53**, 15997 (1996).

[172] Constantini, G., Rusponi, R., Gianotti, R., Boragno, C., and Valbusa, U. *Surf. Sci.* **416**, 245 (1998).

[173] Suggs, D. and Bard, A. *J. Am. Chem. Soc.* **116**, 10725 (1994).

[174] Suggs, D. and Bard, A. *J. Phys. Chem.* **99**, 8349 (1995).

[175] Vogt, M., Moeller, F., Schilz, C., Magnussen, O., and Behm, R. *Surf. Sci.* **367**, L33 (1996).

[176] Vogt, M., Lachenwitzer, A., Magnussen, O., and Behm, R. *Surf. Sci.* **399**, 49 (1998).

[177] Sashikata, K., Matsui, Y., and Itaya, K. *J. Phys. Chem.* **100**, 20027–20034 (1996).

[178] Teshima, T., Ogaki, K., and Itaya, K. *J. Phys. Chem. B* **101**, 2046–2053 (1997).

[179] Müller, P., Ando, S., Yamada, T., and Itaya, K. *J. Electroanal. Chem.* **467**, 282–290 (1999).

[180] Ando, S., Suzuki, T., and Itaya, K. *J. Electroanal. Chem.* **412**, 139 (1996).

[181] Komanicky, V., Chang, K., Menzel, A., Markovic, N., You, H., Wang, X., and Myers, D. *J. Electrochem. Soc.* **153**, B446–B451 (2006).

[182] Michely, T., Besocke, K., and Comsa, G. *Surf. Sci. Lett.* **230**, L135 (1990).

[183] Reimann, K., Rehmet, A., Bolse, W., and Geyer, U. *Mater. Res. Soc. Symp. Proc.* **439**, 361 (1997).

[184] Heumann, T. and Panesar, H. *Z. Phys. Chem.* **229**, 84 (1965).

[185] Gauer, J. and Schmid, G. *J. Electroanal. Chem.* **279**, 1970 (1970).

[186] Cadle, S. and Bruckenstein, S. *J. Electroanal. Chem.* **48**, 325 (1973).

[187] Lovrecek, B., Moslavac, K., and Matic, D. *Electrochim. Acta* **26**, 1087 (1981).

[188] Diaz, M., Kelsall, G., and Welham, N. *J. Electroanal. Chem.* **361**, 25 (1993).

[189] Herrera, J., Castellano, C., Calandra, A., and Arvia, A. *J. Electroanal. Chem.* **66**, 207–230 (1975).

[190] Horikoshi, T., Yoshimura, S., Kubota, N., and Sato, E. *Nippon Kagakukaishi* , 1118 (1983).

[191] Loo, B. *J. Phys. Chem.* **86**, 433 (1982).

[192] Watling, K., Hope, G., and Woods, R. *J. Electrochem. Soc.* **152(6)**, D103–D108 (2005).

[193] Li, Z., Wu, T., Niu, Z., Huang, W., and Nie, H. *Electrochemistry Communications* **6**, 44–48 (2004).

[194] Baker, T., Friend, C., and Kaxiras, E. *Chem. Phys.* **129**, 104702 (2008).

[195] Fleischmann, M. and Thirsk, H. *Advances in Electrochemistry and Electrochemical Engineering*, volume 3, chapter 3. Metal Deposition and Electrocrystallization, 123–210. Interscience Publishers (1963).

[196] Avrami, M. *J. Chem. Phys.* **7**, 1103 (1939).

[197] Avrami, M. *J. Chem. Phys.* **8**, 212 (1940).

[198] Avrami, M. *J. Chem. Phys.* **9**, 177 (1941).

[199] Magnussen, O., Ocko, B., Adzic, R., and Wang, J. *Phys. Rev. B* **51**, 5510 (1995).

[200] Scherson, D. and Kolb, D. *J. Electroanal. Chem.* **76**, 353 (1984).

[201] Shi, Z. and Lipkowski, J. *J. Electroanal. Chem.* **403**, 225 (1996).

[202] Angerstein-Kozlowska, H., Conway, B., Hamelin, A., and Stoicoviciu, L. *Electrochim. Acta* **31**, 1051 (1986).

[203] Angerstein-Kozlowska, H., Conway, B., Hamelin, A., and Stoicoviciu, L. *J. Electroanal. Chem.* **228**, 429 (1987).

[204] Kondo, T., Morita, J., Hanaoka, K., Takakusagi, S., Tamura, K., Takahasi, M., Mizuki, J., and Uosaki, K. *J. Phys. Chem. C* **111**, 13197–13204 (2007).

[205] Conway, B. *Prog. Surf. Sci.* **49**, 331–452 (1995).

[206] Honbo, H., Sugawara, S., and Itaya, K. *Anal. Chem.* **62**, 2424 (1990).

[207] Schneeweiss, M. and Kolb, D. *Solid State Ionics* **94**, 171–179 (1997).

[208] Gao, X. and M.J, W. *J. Electroanal. Chem.* **367**, 259 (1994).

[209] Meguro, T. and Aoyagi, Y. *Inst. Phys. Chem. Res.* **19**, 13–15 (1997).

[210] Aoyagi, Y. and Meguro, T. *Electrochemical Society Proceedings* , 66–72 (1997).

[211] DeSalvo, G., Bozada, C., Ebel, J., Look, D., Barette, J., Cerny, C., Ross, R., Gillespie, J., and et al., C. H. *J. Electrochem. Soc.* **143(11)**, 3652–3656 (1996).

[212] Sandy, A. R. *X-ray scattering studies of metal surfaces.* PhD thesis, McGill University, (1986).

List of Acronyms

AES	Auger Electron Spectroscopy
AFM	Atomic Force Microscope
CD	Cyclic Diffractogram
CE	Counter Electrode
CTR	Crystal Truncation Rod
CV	Cyclic Voltammogram
DFT	Density Functional Theory
EQCM	Electrochemical Quartz Crystal Microbalance
ESB	Ehrlich-Schwoebel Barrier
ESCA	Electron Spectroscopy for Chemical Analysis
ESRF	European Synchrotron Radiation Facility
FWHM	Full Width Half Maximum
GID	Grazing Incidence Diffraction
HASYLAB	Hamburger Synchrotronstrahlungslabor
LEED	Low Energy Electron Diffraction
MAEAM	Modified Analytical Embedded-Atom Method
MBE	Molecular Beam Epitaxy
MD(S)	Molecular Dynamics (Simulation)
MEED	Medium Energy Electron Diffraction
ML	Monolayer
NHE	Normal Hydrogen Electrode
OCP	Open Circuit Potential
OPD	Over-Potential Deposition
PCTFE	Poly-Chloro-Tri-Fluoro-Ethylene, KEL-F
PICS	Positive Ion Channeling Spectrocopy
RE	Reference Electrode
RHE	Reversible Hydrogen Electrode

RHEED   Reflection High Energy Electron Diffraction

SCE   Saturated Calomel Electrode
SEAM   Surface Embedded Atom Model
STM   Scanning Tunneling Microscope
SXRD   Surface X-Ray Diffraction
SXS   Surface X-ray Scattering

TDB   Terrace Diffusion Barrier

UHV   Ultra High Vacuum
UPD   Under-Potential Deposition

WE   Working Electrode

XRD   X-ray Diffraction
XRV   X-ray Voltammetry

Scientific Contributions

Publications

- 'In Situ Surface X-Ray Diffraction Studies of Homoepitaxial Electrochemical Growth on Au(100)'
  K. Krug, J. Stettner and O.M. Magnussen
  Phys. Rev. Lett. 96, 246101 (2006)

- 'Grazing incidence X-ray diffraction studies of the in-plane surface structure of Au(001) electrodes during gold electrodeposition'
  K. Krug, J. Stettner and O.M. Magnussen
  to be published

- 'Real-time surface X-ray scattering study of Au(111) electrochemical dissolution'
  K. Krug, D. Kaminski, F. Golks, J. Stettner, O.M. Magnussen
  to be published

- 'Microscopic growth kinetics of gold electroplating'
  K. Krug, J. Stettner and O.M. Magnussen
  ESRF Highlights (2006)

- 'Time-Dependent Diffraction Studies of Au(100) Electrode Surface During Deposition'
  D. Kaminski, K. Krug, F. Golks, J. Stettner and O.M. Magnussen
  J. Phys. Chem. C, 111, 17067-17071 (2007)

- 'In situ diffraction studies of electrode surface structure during gold electrodeposition'
  O.M. Magnussen*, K. Krug, A.H. Ayyad, J. Stettner
  Electrochimica Acta, 53(9), 3449-3458 (2008)

- 'Study of Bi UPD structures on Au(100) using in situ Surface X-ray Scattering'
  S.H. Zheng, K. Krug, F. Golks, D. Kaminski, S. Morin and O.M. Magnussen
  to be published

- 'Structure and redox behavior of azobenzene-containing monolayers on Au (111): A combined STM, x-ray reflectivity, and voltammetry study'
  U. Jung, B. Baisch, D. Kaminski, K. Krug, A. Elsen, T. Weineisen, D. Raffa, J. Stettner, C. Bornholdt, R. Herges, O.M. Magnussen
  Journal of Electroanalytical Chemistry, 619-620, 152-158, (2008)

Oral Presentations

- 'Studies of surface structures by Grazing Incidence Diffraction (GID)'
  Joint Solid State Physics Seminar
  Sehlendorf, 2005

- 'In-situ diffraction studies of homoepitaxial electrochemical growth on Au(100)'
  DPG Frühjahrstagung
  Dresden, 2006
  K. Krug, D. Kaminski, J. Stettner, A. Ayyad, O.M. Magnussen

Poster Presentations

- 'In-situ Video-STM Untersuchungen des (1x1) → '"hex"'-Phasenüberganges an Au(100)-Elektrodenoberflächen'
  DPG Frühjahrstagung
  Regensburg, 2004
  K. Krug, M. Labayen, O.M. Magnussen

- 'In-situ X-ray investigation of the electrodeposition of Au on Au single crystal surfaces'
  DPG Frühjahrstagung
  Berlin, 2005
  K. Krug, A. Ayyad, K. Kölln, J. Stettner, O.M. Magnussen

- 'In-situ x-ray investigation of the electrodeposition of Au on Au single crystal surfaces'
  6th Autumn School on X-ray scattering from surfaces and thin layers
  Smolenice, 2005
  K. Krug, J. Stettner, O.M. Magnussen

- 'In-situ surface x-ray investigation of the electrodeposition of Au on Au(100)'
  Hasylab User Meeting
  Hamburg, 2005
  K. Krug, A. Ayyad, K. Kölln, J. Stettner, O.M. Magnussen

- 'In-situ diffraction studies of Au(100) electrode surface structure during Au electrodeposition'
  Deutsche Tagung für Forschung mit Synchrotronstrahlung, Neutronen und Ionenstrahlen an Großgeräten 2006
  Hamburg, 2006
  D. Kaminski, K. Krug, J. Stettner, A. Ayyad, O.M. Magnussen

- 'In-situ diffraction studies of homoepitaxial electrochemical growth on single crystal electrodes'
  International Conference on Electrified Interfaces (ICEI)
  Sahoro (Japan), 2007
  K. Krug, D. Kaminski, F. Golks, J. Stettner, O.M. Magnussen

Awards

- PCCP Poster Prize
  International Conference on Electrified Interfaces (ICEI)
  Sahoro (Japan), 2007

Curriculum Vitæ

Klaus Gerold Krug

Date of Birth	Jannuary 7th 1977, Nürnberg
	son of Karl Krug
	and Ursula Gelbke (née Kämmerer)
Nationality	German
Marriage Status	unmarried
Children	none

School

1983-1985	Elementary school, Wertheim/Dertingen
1985-1989	Elementary school, Dielingsgrund (Berlin)
1989-1990	High school, Eckener Gynmasium (Berlin)
1990-1996	High school, Ernst-Barlach-Gymnasium (Kiel)
05/1996	Abitur

Civilian Service

08/1996 - 08/2002	Medic for Arbeiter-Samariter-Bund Kiel

Studies

10/1996 - 10/2004	Major in physics at the Christian-Albrechts-Universität Kiel. Diploma thesis with the title 'Integration einer Temperaturregeleinheit in ein bestehendes elektrochemisches Hochgeschwindigkeits-Rastertunnelmikroskop und erste temperaturvariable Messungen an Au(100)-Elektroden' at the department for surfaces and interfaces of the Institute of Experimental and Applied Physics (IEAP) University Kiel, supervised by Prof. Dr. Olaf Magnussen.
10/2004	Diplom (M.Sc.)
since 11/2004	Work on dissertation at the department for surfaces and interfaces of the Institute of Experimental and Applied Physics (IEAP), University Kiel.

Kiel, July 14, 2009

Acknowledgement

Eidesstattliche Erklärung

Hiermit erkläre ich, dass ich die vorgelegte Arbeit selbständig verfasst und keine anderen als im Literaturverzeichnis angegebenen Quellen benutzt habe. Dies gilt für alle Quelltypen. Ich habe alle Passagen und Sätze der Arbeit, die wortwörtlich oder sinngemäß anderen veröffentlichten und nicht veröffentlichten Werken entnommen sind, unter Angabe der Herkunft der Quelle deutlich als Entlehnung gekennzeichnet. Die Arbeit ist in gleicher oder ähnlicher Form noch nicht eingereicht worden. Mir ist bekannt, dass Zuwiderhandlungen gegen diese Erklärung und gewusste Täuschungen den Ausschluss von der Prüfung zur Folge haben können.

Ort, Datum	Klaus Krug